# Aerothermal Investigation of the Flow around an Airfoil with Endwall Cooling Air Injection

*Aerothermische Untersuchung einer Profilumströmung unter dem Einfluss von Kühllufteinblasung an der Endwand*

Master Thesis of Constantin Völzel, B. Sc.
Matriculation number: 1949319
Date of submission: 12th June 2018

1st Reviewer: Prof. Dr.-Ing. Heinz-Peter Schiffer
2nd Reviewer: Tom Ostrowski, M.Sc.

TECHNISCHE
UNIVERSITÄT
DARMSTADT

Aerothermal Investigation of the Flow around an Airfoil with Endwall Cooling Air Injection
*Aerothermische Untersuchung einer Profilumströmung unter dem Einfluss von Kühllufteinblasung an der Endwand*

Master Thesis of Constantin Völzel, B. Sc.
Matriculation number: 1949319

1st Reviewer: Prof. Dr.-Ing. Heinz-Peter Schiffer
2nd Reviewer: Tom Ostrowski, M.Sc.

Date of submission: 12th June 2018

# Thesis Statement

I herewith formally declare that I, Constantin Völzel, have written the submitted thesis independently. I did not use any outside support except for the quoted literature and other sources mentioned in the paper. I clearly marked and separately listed all of the literature and all other sources which I employed when producing this academic work, either literally or in content. This thesis has not been handed in or published in the same or similar form.

In the submitted thesis the written copies and the electronic version for archiving are identical in content.

Darmstadt, 12th June 2018


_____

(Constantin Völzel)

# Master–Thesis

Nr.: 384/19/17

von Herrn **Constantin  V ö l z e l**

**Thema:**

**Aerothermische Untersuchung einer Profilumströmung unter dem Einfluss von Kühllufteinblasung an der Endwand**

**Aerothermal Investigation of the Flow around an Airfoil with Endwall Cooling Air Injection**

**TECHNISCHE UNIVERSITÄT DARMSTADT**

Fachgebiet Gasturbinen,
Luft- und Raumfahrtantriebe

GLR

Prof. Dr.-Ing. H.-P. Schiffer
Otto-Berndt-Str. 2
64287 Darmstadt
Tel. +49 6151 16 - 22100
Fax +49 6151 16 - 22108
schiffer@glr.tu-darmstadt.de

**Aufgabenbeschreibung:**

Der Turbinenprüfstand "Large Scale Turbine Rig" (LSTR) wird um Wärmeübergangsmesstechnik an der nabenseitigen Rotorendwand erweitert. Hierbei kommt die flächig hochauflösende Infrarotthermographie zum Einsatz, um Temperaturverteilungen auf der Endwand zu vermessen und hierdurch Rückschlüsse auf den lokalen Wärmeübergang sowie die Filmkühleffektivität ziehen zu können. Die Strömung im Bereich der Endwand wird durch die Interaktion zwischen Hauptstrom und Sperrluft dominiert. Im Rahmen einer Vorstudie zu den geplanten Messungen am LSTR soll in dieser Masterthesis die Umströmung eines symmetrischen Profils im institutseigenen rechteckigen Windkanal experimentell untersucht werden. Um Sperrlufteinblasung zu modellieren, kann stromauf der Vorderkante ein Modul mit entsprechender Spaltgeometrie eingebracht werden. In einer Parameterstudie soll die Interaktion zwischen Kühlluft und Hauptstrom detailliert untersucht werden und deren Einfluss auf den Wärmeübergang sowie die Filmkühleffektivität quantifiziert werden. Neben einer Variation der Einblaserate soll die Integrationszeit der Kamera soweit reduziert werden, dass eine Ähnlichkeit zu den geplanten Messungen im rotierenden System des LSTR gegeben ist.

Bei der Bearbeitung der Masterthesis ergeben sich folgende Teilaufgaben:
- Aerodynamische Untersuchung des Strömungsfelds im Gebiet der eingeblasenen Sperrluft sowie der Profilvorderkante
- Wärmeübergangsmessungen unter Variation der Einblaserate
- Wärmeübergangsmessungen unter Variation der Integrationszeit
- Auswertung der Messdaten inklusive der Betrachtung von Messunsicherheiten

Bestandteile der Arbeit sind eine ausführliche schriftliche Ausarbeitung sowie ein Zwischen- und Abschlusskolloquium.

Betreuer:        Tom Ostrowski, M.Sc.

Darmstadt, 30. November 2017

Prof. Dr.-Ing. H.-P. Schiffer

# Contents

# List of Figures

# List of Tables

# Nomenclature

**Abbreviations**

| | |
|---|---|
| CCD | charge-coupled device |
| CFD | Computational Fluid Dynamics |
| CMOS | complementary metal-oxide-semiconductor |
| $CO_2$ | carbon dioxide |
| CV | corner vortex |
| DC | digital counts |
| DSNU | dark signal non-uniformity |
| HV | horseshoe vortex |
| ICAO | International Civil Aviation Organization |
| PRNU | pixel response non-uniformity |
| FPA | focal plane array |
| GLR | Institute for Gas Turbines and aerospace Propulsion |
| HTCVal1.7 | in-house evaluation routine for adiabatic heat transfer coefficients in MATLAB |
| IR | infrared |
| KWK | small flow channel (Kleiner Windkanal) |
| LSTR | Large Scale Turbine Rig |
| NACA | National Advisory Committee for Aeronautics |
| $NO_x$ | nitrogen oxide |
| NUC | non-uniformity correction |
| mu | substitutional for microsecond |
| PIV | particle image velocimetry |
| px | pixel |
| RQL | Rich-Burn-Quick-Quench-Lean-Burn |
| SFC | specific fuel consumption |
| SNR | signal-to-noise ratio |
| SV | secondary vortex |
| TU Darmstadt | Technische Universität Darmstadt |
| TV | tertiary vortex |

**Latin**

| | | |
|---|---|---|
| $A$ | $\mathrm{m^2}$ | surface area |
| $a$ | — | absorption coefficient |
| $BR$ | — | blowing rate |
| $c$ | $\frac{\mathrm{m}}{\mathrm{s}}$ | speed of light |
| $c_p$ | $\frac{\mathrm{J}}{\mathrm{kgK}}$ | isobaric heat capacity |
| $d$ | m | diameter |
| $e$ | — | Euler's Constant |
| $\dot{e}$ | $\frac{\mathrm{W}}{\mathrm{m^2}}$ | specific radiative power |
| $Ec$ | — | Eckert number |
| $f$ | — | control variable |
| $\hat{f}$ | — | recovery factor |

| | | |
|---|---|---|
| $g$ | — | control variable |
| $h$ | Js | Planck's Constant |
| $HTC$ | $\frac{W}{m^2K}$ | (adiabatic) heat transfer coefficient |
| $I$ | — | momentum ratio |
| $\hat{I}$ | — | image intensity |
| $i$ | — | control variable |
| $J$ | $\frac{W}{m^3}$ | radiative intensity |
| $j$ | — | control variable |
| $K$ | — | calibration coefficient |
| $L$ | m | slot length |
| $Ma$ | — | Mach number |
| $MFR$ | — | mass flow ratio |
| $\dot{m}$ | $\frac{kg}{s}$ | mass flow |
| $n$ | $\frac{1}{min}$ | rotational speed |
| $Nu$ | — | Nusselt number |
| $p$ | Pa | pressure |
| $Pr$ | — | Prandtl number |
| $\dot{Q}$ | W | radiative power |
| $\dot{q}$ | $\frac{W}{m^2}$ | specific heat flux |
| $R$ | — | value of cross-correlation function |
| $r$ | m | radius |
| $\hat{R}$ | $\frac{J}{kgK}$ | specific gas constant |
| $Re$ | — | Reynolds number |
| $Res$ | m | resolution |
| $S$ | m | slot width |
| $s$ | m | thickness |
| $St$ | — | Stanton number |
| $T$ | $°C, K$ | temperature |
| $t$ | s | time |
| $Tu$ | — | turbulence intensity |
| $U$ | — | camera output signal |
| $u$ | $\frac{m}{s}$ | velocity |
| $X$ | m | x-coordinate in the heating plate coordinate system |
| $x$ | m | x-coordinate |
| $Y$ | m | y-coordinate in the heating plate coordinate system |
| $y$ | m | y-coordinate |
| $Z$ | m | Z-coordinate in the heating plate coordinate system |
| $z$ | m | z-coordinate |

## Greek

| | | |
|---|---|---|
| $\alpha$ | $\frac{W}{m^2K}$ | heat transfer coefficient |
| $\gamma$ | — | isentropic exponent |
| $\varepsilon$ | — | emissivity |
| $\zeta$ | — | refraction index |
| $\eta$ | — | cooling effectiveness |
| $\rho$ | $\frac{kg}{m^3}$ | density |
| $\kappa$ | $\frac{W}{m^2K^4}$ | Boltzmann's Constant |
| $\Lambda$ | $\frac{W}{mK}$ | wavelength |
| $\lambda$ | $\frac{W}{mK}$ | thermal conductivity |
| $\Theta$ | — | dimensionless temperature |

| $\xi$ | $-$ | reflection coefficient |
| $\sigma$ | $-$ | standard deviation |
| $\tau$ | $-$ | transmission coefficient |
| $\Phi$ | $^{\circ}$ | slot injection angle |
| $\omega$ | $\frac{1}{s}$ | vorticity |

## Indices

| | |
|---|---|
| 0 | reference case without secondary air injection |
| ad | adiabatic |
| amb | ambient |
| atm | atmospheric |
| aux | auxiliary wall |
| b | black body |
| cav | cavity |
| coat | coating |
| cond | conductive |
| conv | convective |
| D | diameter |
| F | fluid |
| hg | hot gas |
| int | integration |
| l | lens |
| LE | leading edge |
| N | normalized |
| NACA | National Advisory Committee for Aeronautics, reference to airfoil contour |
| NGV | nozzle guide vane |
| mean | average |
| obj | object |
| off | offset |
| PIV | Particle Image Velocimetry |
| prim | primary, reference to primary flow |
| rec | recovery |
| rel | relative value |
| RIDN | rear inner discharge nozzle |
| rotorendwall | rotor endwall |
| sec | secondary, reference to secondary flow |
| stat | static |
| tot | total |
| U | camera signal |
| u | reference to velocity |
| w | wall |

# 1 Introduction

Prospects for the future volume of air traffic predict high growths in the numbers of passengers and in the carriage of goods. The International Civil Aviation Organization (ICAO) forecast average annual growths of 6.3 % for the passenger-kilometres performed and 4.1 % for the tonne-kilometres performed in the freight traffic in the period from 2014 to 2016 [1]. However, the development of fundamentally different aircraft propulsion systems competing with turbojet engines is not expected to take place at the same pace. What is more, the current fleet of aircraft in use is expensive and can hardly be exchanged in a whole at once.

Reducing costs of the operation of the predominant turbojet engines is therefore a key factor for airlines and other aircraft carriers. On top of that, environmental legislation based on propositions by the ICAO constantly seeks to lower emissions of carbon dioxide ($CO_2$) or detrimental residuals like nitrogen oxides ($NO_x$) caused by air traffic. The same applies to the operation of stationary gas turbines in the energy sector as well. Increasing requirements regarding the ability for load changes are crucial for gas turbines in power plants today when it comes to energy production on a profitable level.

One major leverage to increase the efficiency of turbojet engines is to raise the turbine entry temperature which results in a reduction of the specific fuel consumption (SFC). As can be seen in figure 1.1 this development has proceeded for many decades, exhibiting a distinct step around the time when active blade cooling was introduced in turbojet engines [2, p. 1085].
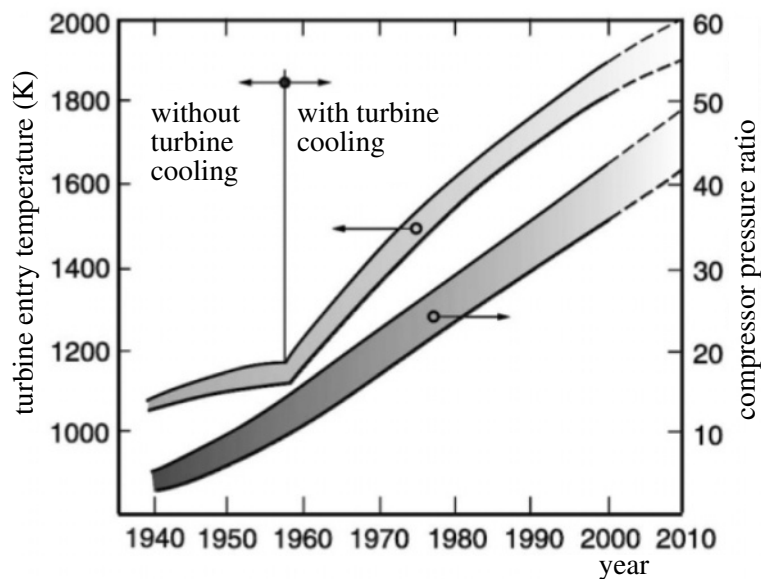


**Figure 1.1:** Historical development of the turbine entry temperature in turbojet engines, adapted from [2]

Implications of rising temperatures are a negative impact on the durability of components in the combustion chamber and in the subsequent turbine as well as higher $NO_x$ emissions. The highest production of $NO_x$ emissions occurs in regions with equivalence ratios near the stochiometric proportion and elevated temperatures. Currently established combustion concepts feature both rich and lean burn zones in the combustion chamber which is achieved by a staged air supply. They are referred to as Rich-Burn-Quick-Quench-Lean-Burn combustors (RQL). However, at some point the stochiometric equivalence ratio and consequently a region of increased $NO_x$ production is passed between the rich zone enabling a stable ignition and the lean burn zone after the additional air injection. Operating the combustion process at higher air excess, a so-called lean burn, has the potential to significantly reduce harmful $NO_x$ emissions. Figure 1.2 illustrates the occurrence of $NO_x$ emissions in dependence on the equivalence ratio.
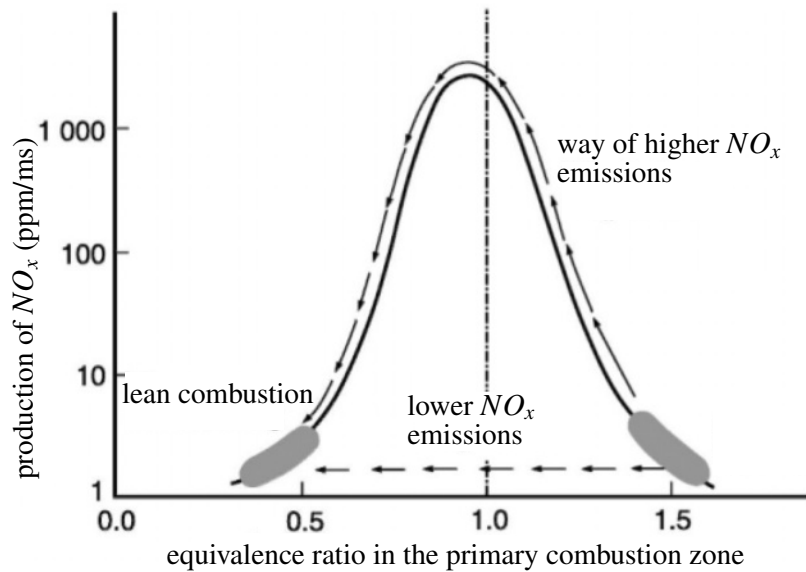
**Figure 1.2:** Generation of $NO_x$ emissions with varying equivalence ratios in a turbojet engine, adapted from [2]

As research has shown that lean-burn concepts flatten the radial temperature profile in the turbine, the hub side endwall and the casing are exposed to higher heat loads in comparison to conventional burn concepts [3]. The cooling of the turbine blades and the hub side endwall is realised with air tapped from the compressor and injected through holes or slot configurations. This secondary air flow is also guided through cavities in the rotor and used as sealing air between the spinning rotor and the fixed stator in order to avoid a penetration of hot gas into the hub. The secondary air has a significantly lower temperature than the primary flow through the turbine and does not contribute to the energy conversion at the same level. High overall efficiencies with an active cooling of the turbine therefore also require a minimum amount of cooling air and elaborate cooling methods [2, p. 1105].

## Aims of this work

At the Institute of Gas Turbines and Aerospace Propulsion of Technische Universität Darmstadt the usability of sealing air between a stator and a rotor stage for cooling purposes on the rotor endwall is planned to be examined. The measurements shall be conducted at a scaled turbine test bench with the help of infrared thermography as a non-intrusive optical measurement technique for surface temperatures.

In the present work important preliminary investigations are conducted. The flow in front of a symmetrical airfoil with Reynolds similarity to a rotor blade at the turbine test rig is examined in a flow channel. An upstream slot simulates the cavity for the sealing air at the turbine test rig. Typical flow configurations upstream of the leading edge are resolved in aerodynamic measurements of the flow field and their impact on the endwall heat transfer is derived from infrared-thermographic measurements. The integration time of the infrared camera system is reduced to a level so that a comparability to the future application at the turbine test bench is ensured. An assessment of the influence of lowered integration times on the uncertainty in results for heat transfer coefficients and film cooling effectiveness is given. Furthermore, a variation of mass flow rates of the sealing air is performed in the thermal and in the aerodynamic measurements in order to analyse respective changes in the endwall heat transfer.

# 2 Theoretical foundations

This chapter summarizes the most relevant information required for the understanding of the measurements conducted in this thesis. It focusses on the topics of infrared thermography and particle image velocimetry as the two measurement techniques applied in the context of this work.

## 2.1 Heat transfer

Heat transfer describes thermodynamic processes in which the transport of energy results in temperature differences between an observed system and its surroundings [4, p. 1]. Within a single and static medium heat is transferred by conduction. Assuming temperature-independent material properties, the specific heat flux $\vec{q}$ grows proportionally with the temperature gradient within the medium which is expressed by *Fourier's Law* in equation 2.2. $\lambda$ denotes the thermal conductivity of the medium.

$$\vec{q}_{cond} = -\lambda \nabla T \tag{2.1}$$

In the presence of flows heat is transferred by means of conduction and additionally by the transport of enthalpy and kinetic energy. This is referred to as convective heat transfer. For technical applications a correlation between the temperature $T_F$ of the fluid far from the influence of a neighbouring surface with another temperature and the temperature $T_w$ at the surface itself is useful. The complex relation between the local heat flux normal to the surface and the temperature and velocity distribution is therefore reduced to the following combination which defines the local heat transfer coefficient $\alpha$.

$$\dot{q}_{conv} = \alpha (T_w - T_F) \tag{2.2}$$

Another form of heat transfer is radiative heat transfer which will be addressed in section 2.2.1 in the context of infrared thermography.

### 2.1.1 Adiabatic heat transfer coefficient and adiabatic film cooling effectiveness

A major issue in quantifying convective heat transfer is the choice of the reference temperature for the fluid which runs above a surface and exchanges heat. The thickness of the thermal boundary layer grows with proceeding running length [5, p. 470]. The approach in equation 2.2 does not incorporate the fact that local surface temperatures $T_w$ are affected by surface temperatures at upstream locations. In case $(T_w - T_F)$ changes, $\alpha$ changes as well.
In order to isolate the effect of flow characteristics on the heat transfer between surface and overflowing media adiabatic parameters ensure a uniform reference temperature, the adiabatic wall temperature $T_{w,ad}$. This is the temperature that the surface takes on with vanishing heat flux. The corresponding adiabatic heat transfer coefficient $\alpha_{ad}$ is independent from thermal boundary conditions and a function of the flow characteristics and the geometry [6]. It will further be denoted as $\alpha_{ad}$ or $HTC$.

$$\dot{q}_{conv} = \alpha_{ad} (T_w - T_{w,ad}) \tag{2.3}$$

In cooling applications the effectivity of the coolant flow configuration is assessed by a dimensionless description of the adiabatic wall temperature. This adiabatic cooling effectiveness relates the adiabatic wall temperature to both the primary flow temperature $T_{prim}$ and the coolant flow temperature $T_{sec}$ [2, p. 1116]. A low cooling performance results in surface temperatures close to the primary flow temperature, the minimum $\eta_{ad} = 0$ leading to $T_{w,ad} = T_{prim}$. Higher cooling performances push the surface temperature near the temperature of the coolant flow with the limiting case of $\eta_{ad} = 1$ and $T_{w,ad} = T_{sec}$.

$$\eta_{ad} = \frac{T_{prim} - T_{w,ad}}{T_{prim} - T_{sec}} \tag{2.4}$$

The experimental determination of $HTC$ is not always possible due to the adiabatic boundary condition. This also applies to the experimental setup of the present work. Based on the linearity of $\alpha$ with the dimensionless surface temperature $\Theta$ (compare equation 2.5) Gritsch [7] discusses another more practical way to determine adiabatic parameters.

$$\Theta = \frac{T_{prim} - T_{sec}}{T_{prim} - T_w} \tag{2.5}$$

A linear regression of measurement pairs of surface temperatures $\Theta$ and corresponding heat transfer coefficients $\alpha$ in the definition of equation 2.2 enables to determine $HTC$ and $\eta_{ad}$. The linear correlation of these two adiabatic quantities that is discussed in detail by Eckert [8] is illustrated in figure 2.1(a). The adiabatic heat transfer coefficient $HTC$ corresponds to the interception with the ordinate at zero heat flux whereas the reciprocal of the adiabatic cooling effectiveness $\eta_{ad}$ is given as the interception with the abscissa. Theoretically, two measurement pairs are sufficient to properly determine these adiabatic parameters [7]. Another depiction of the regression method is given on the right side in figure 2.1(b) where the slope of the fit represents $HTC$ [9]. In the absence of coolant flow, the non-dimensional formulation of the adiabatic cooling effectiveness is not possible, but this representation of the regression method generates the adiabatic heat transfer coefficient $HTC$.



(a) Regression of $HTC$ and $\eta_{ad}$      (b) Regression of $\dot{q}_w$ and $T_{w,ad}$
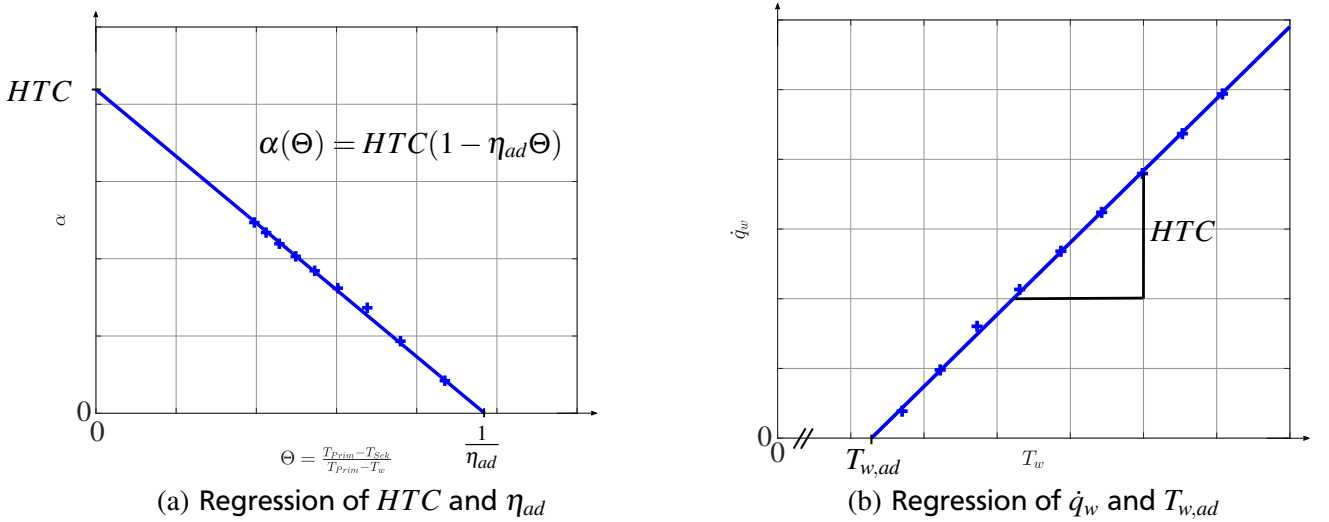
**Figure 2.1:** Linear regression method to determine adiabatic parameters from temperature-dependent heat transfer coefficients

According to Gritsch [7] this linear relation can only be made use of when the consistency of certain boundary conditions is ensured. These are condensed in the Stanton number $St$ as a dimensionless expression for the heat transfer coefficient. It is a function of the dimensionless surface temperature $\Theta$, the blowing rate $BR$, the momentum rate $I$, the turbulence intensity $Tu$ of the flows, the Reynolds number $Re$, the Eckert number $Ec$ and the geometry.

$$St = f(\Theta, BR, I, Tu, Re, Ec, geometry) \tag{2.6}$$

The variation of Θ supplies at least two different measurement pairs as explained earlier in this section. Therefore, only two ways are suitable from a practical point of view to keep the flow characteristics expressed by the other parameters constant: varying the surface temperature or varying both the primary flow temperature and the coolant flow temperature simultaneously [7]. The experiments conducted in the course of this thesis focus on the former alternative. Adiabatic heat transfer coefficients are later expressed in terms of Stanton numbers according to the definition in equation 2.7 with a characteristic velocity $u$, the density $\rho$ of the flow medium and its isobaric heat capacity $c_p$. These parameters are referred to constant conditions at the inlet of the flow channel (compare to the beginning of section 4.3). The Stanton number is commonly used in American literature related to cooling applications on turbine endwalls and vanes.

$$St = \frac{HTC}{u\rho c_p} \tag{2.7}$$

The Nusselt number $Nu$ can be derived from the Reynolds number $Re$, the Prandtl number $Pr$ and the Stanton number $St$ of the heat transfer problem in the following way [4, p. 24]:

$$Nu = StRePr \tag{2.8}$$

## 2.2 Infrared thermography

Infrared thermography describes an optical measurement technique for qualitative and quantitative temperature measurements on surface. The signal acquisition is based on the temperature-dependent radiation of objects in the infrared spectrum between 780 nm and 1 mm.

### 2.2.1 Fundamentals

Radiative power is transferred by electromagnetic waves. It can be reflected, absorbed or transmitted by bodies. The total radiative power is split into respective fractions represented by the reflection coefficient $\xi$, the absorption coefficient $a$ and the transmission coefficient $\tau$ [4, p. 29].

$$\xi + a + \tau = 1 \tag{2.9}$$

*Planck's Law* in equation 2.10 describes the intensity $J_b$ emitted by a black body as a function of the wavelength $\Lambda$ and the temperature $T$. In this equation, $h$ is Planck's Constant, $c$ is the speed of light in vacuum, $\zeta$ represents the refraction index in the path of the radiation and $\kappa$ is Boltzmann's Constant.

$$J_b(\Lambda, T) = \frac{2\pi c^2}{\zeta^2 \Lambda^5 \left(e^{\frac{hc}{n\Lambda\kappa T}} - 1\right)} \tag{2.10}$$

In figure 2.2 *Planck's Law* is pointed out. It can be seen that the positions of local intensity maxima move towards shorter wavelengths when the object temperature rises according to *Wien's Law*.

An integration of equation 2.10 over all wavelengths leads to the total radiation of a black body known as *Boltzmann's Law* in equation 2.11. $\dot{e}_b$ represents the specific intensity of the radiation expressed in radiation power $\dot{Q}$ per area $A$ which is independent from the wavelength. For an arbitrary body, the specific intensity is given by multiplying $\dot{e}_b$ with the emissivity $\varepsilon(T)$. In case the emissivity is independent from wavelength and temperature, the body is denoted as a grey body and its emissivity is identical with the absorption coefficient [4].
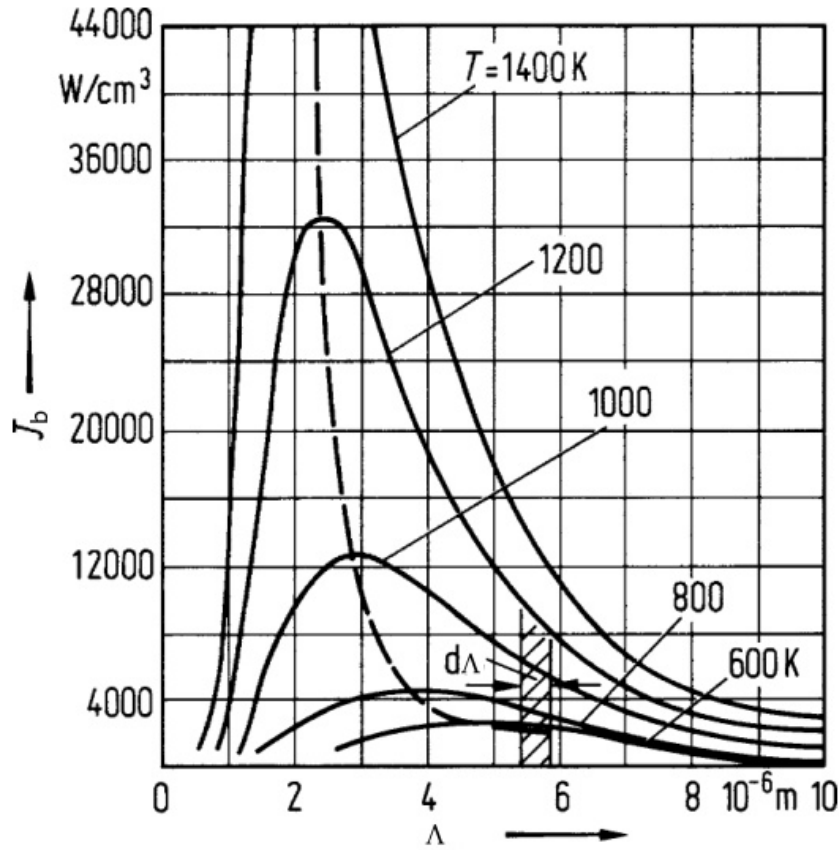
**Figure 2.2:** *Wien's Law* illustrating the shift of local intensity maxima to shorter wavelengths with higher object temperature, adapted from [10]

$$\dot{e}_b = \frac{\dot{Q}}{A} = \zeta^2 \kappa T^4 \tag{2.11}$$

Infrared thermography systems operate in certain ranges of infrared wavelengths with respect to the sensitivity of the detector.[1] *Short-wave* infrared relates to wavelengths from $0,9\,\mu$m to $1,7\,\mu$m, *mid-wave* infrared covers the range from $3\,\mu$m and *long-wave* infrared refers to $7\,\mu$m to $14\,\mu$m. With reference to *Wien's Law* in figure 2.2 it is obvious that these ranges of wavelengths cover certain temperature limits within which the best sensitivity is achieved. At higher temperatures the intensity maximums rise which implies that a digital collector in an infrared camera may saturate at shorter times of exposure to the source of radiation. Observing large dynamic object temperature ranges or small ranges at low temperatures may require the use of filters and additional amplification methods [11].

## 2.2.2 Calibration of the infrared imaging system

Infrared camera systems are composed of the camera optics and a detector field, fabricated as a CMOS chip or a CCD chip and referred to as the focal plane array *FPA*. They produce a pixelwize digital output signal proportional to the incident radiation. In the present work an in-situ calibration process is performed to gain temperature values from the digital output signal in the specific measurement setup. It is based on the existing calibration procedure in the evaluation routine *HTCVal1.7* in *Matlab* introduced by Steinhausen [12] and edited by Wiemer [13]. The importance of an in-situ calibration for quantitative thermographic measurements is pointed out by the exemplary setup given in figure 2.3.

---

[1] Infrared systems are further divided into photon-detector based systems and thermal detector based systems. All following explanations refer to photon-detector based sytems as the infrared camera FLIR X6540sc used at the institute GLR works with this principle. The measurement range is $2,5 - 5,1\,\mu$m.

$U_l$: radiation from lens system
$U_{hg}$: radiation from hot gas
$U_s$: radiation from surrounding surface
$U_w$: radiation from optical window
$U_{obj}$: radiation from target object
$U_{amb}$: radiation from abience
$\tau_l$: transmissivity of lens system
$\tau_{hg}$: transmissivity of hot gas
$\tau_w$: transmissivity of optical window
$\tau_{atm}$: transmissivity of atmosphere
$T_{hg}$: temperature of hot gas
$T_{obj}$: temperature of target object
$T_{atm}$: temperature of atmosphere
$\varepsilon_{obj}$: emissivity of target object

**Figure 2.3:** Optical path for infrared thermographic measurements in an exemplary setup [14]

Only the radiative intensity $U_{obj}$ emitted by the target object is directly related to the temperature of the object. The resulting radiative intensity reaching the camera changes with every modification of the optical path. Dependencies of transmission coefficients on ambient temperatures as well as dependencies of reflection coefficients on the surface composition can alter the resulting radiative intensity gathered by the detector. These dependencies can be summarised as an offset $U_{off}$ added to the actual radiative intensity $U_{obj}$ coming from the temperature distribution on the target object surface. The total intensity reaching the camera detector can then be expressed as follows:

$$U_{tot}(T_{obj}, T_{amb}, ...) = U_{obj}(T_{obj}) + U_{off}(T_{obj}, T_{amb}, ...). \tag{2.12}$$

As it is not possible to adequately describe these dependencies expressed in the offset $U_{off}$ analytically the calibration of the camera signal has to be performed within the exact same setup and with the same surrounding conditions as the measurements. In order to relate the reference temperatures to the correspondent output signals of the camera, calibration functions are used. Usually, polynomial functions, exponential functions or logarithmic approaches are applied [11]. Both the number of nodes, defined by the amount of pairs of temperature values and camera output signals, and the dynamic range of the camera determine an adequate function to be used. The calibration function currently implemented in the evaluation routine *HTCVal1.7* is given in equation 2.13 where $U$ represents the camera output signal. The coefficients $K_0$, $K_1$, $K_2$ and $K_3$ are calculated with a least-squares fit.

$$T = K_3 U^3 + K_2 U^2 + K_1 U + K_0 \tag{2.13}$$

The approach by Ochs [14] addresses the fact that a dependency on wavelength and temperature of the transmissivity for infrared radiation exists within the optical path in the presence of hot gas flows. Schulz [15] confirms the usability of this calibration method in film cooling applications. Wiemer implemented further changes to the calibration procedure in the evaluation programme *HTCVal1.7* [13]. In the present setup surface temperature data and corresponding camera signals are acquired at distinct spots where reference thermocouples are installed and measure the surface temperature. These value pairs are gathered from the same recordings used as measurement images to account for the dependencies of the transmissivity. The calibration coefficients are subsequently scattered across the whole detector field by means of interpolation and extrapolation methods. An additional precalibration is not necessary any more as the coefficients from the in-situ calibration data are available at each pixel.

## 2.2.3 Influence of integration time

Most current infrared imaging systems are designed as photon detectors. Incident radiation is converted into a change of the concentration of free charge carriers which is subsequently interpreted as a digital output signal [11, p. 83]. As the energy of incident radiation is dependent on the wavelength, any additional internal release of charge carriers due to thermal effects results in random noise in the camera signal. Photon detectors working in the midwave infrared spectrum of $3-5\,\mu m$ are therefore cooled to reduce the dark current noise induced by the detector itself [11, p. 91]. Another form of noise is fixed pattern noise. It is characterized as spatial noise which can produce column-wize oscillations on the FPA dependent on the reading algorithm implemented in the detector electronics. Offsets between signals of single pixels that are detectable in absence of background noise from the surroundings are referred to as *Dark Signal Non-Uniformity DSNU*. Deviations in the response behaviour of pixels on the FPA are called *Pixel Response Non-Uniformity PRNU*. DSNU can be corrected by subtracting the oscillations from a dark image recorded at the respective integration time with a uniformly tempered coverage in front of the optics. This *one-point non-uniformity correction* (NUC) deteriorates fixed differences in the output signals of single pixels. Figure 2.4 opposes an image without NUC on the left side to an image after a NUC is applied on the right side.
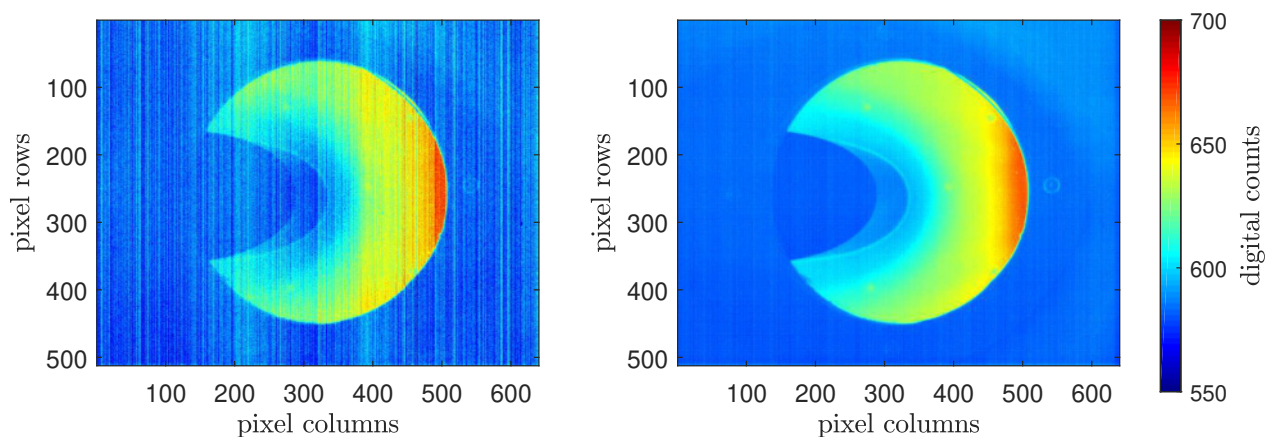


**Figure 2.4:** Raw camera images from the same scene taken with $50\,\mu s$ without NUC on the left and with NUC on the right

Both images are the average of 1000 frames taken with an integration time of $50\,\mu s$. They show the same scene from the experimental setup for the heat transfer measurements explained in section 3.2.1. The influence of the NUC on the final adiabatic results of the heat transfer measurements is presented in section 4.3.1.

With reference to the calibration curves mentioned in section 2.2.2 another aspect of shorter integration times has to be observed. Figure 2.5 displays sensitivity curves for three different integration times. They are derived from exemplary calibration curves at the location of reference thermocouple 5 which is situated directly under the black body surface (compare section 3.2.1). The temperature sensitivity relates to the temperature difference which is theoretically generated by the minimal input variation of one digital count in the camera raw signal. It can be seen that sensitivities decrease with rising temperatures as well as with higher integration times.

In summary, two major influences of lower integration times on the noise development in thermographic recordings need to be considered in the course of the measurements:

- Shorter integration times lead to lower camera output signals because the time span for discharging electrons as free charge carriers is shortened. Reducing the integration time of an infrared camera is therefore liable to increase the proportion of detector-related noise and non-uniformities in the camera output signal.

- The calibration curve matches temperature values to correspondent camera output signals. Its sensitivity rises with lower integration times. This effect magnifies the minimal detectable temperature difference. One expected implication is that the contribution of wall temperatures and camera signals, accordingly, to the uncertainty in adiabatic results increases with reduced integration times. Reducing the statistical fluctuation of the average camera output signal also reduces the uncertainty of correspondent temperatures.
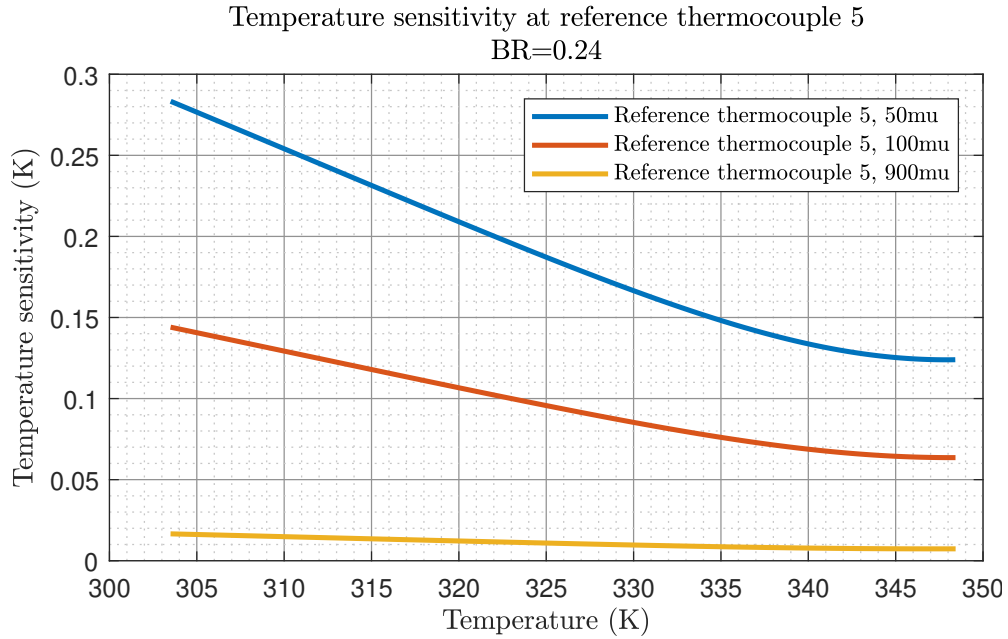
**Figure 2.5:** Temperature sensitivity of reference thermocouple 5 for measurements at three different integration times

## 2.3 Particle Image Velocimetry

Another optical measurement technique applied in the course of this thesis is *particle image velocimetry* (PIV). It is a widely used non-intrusive method to visualise flow movements and to produce quantitative descriptions of flow characteristics. This is achieved by the use of adequate software during the post-processing. It is based on the statistical evaluation of the movements of particles in the flow.

### 2.3.1 Fundamentals of PIV

The following explanations are based on information from [16]. The setup of a PIV system consists of a light source, equipped with geometric optics in order to produce a thin light sheet in the flow channel, one or more cameras which generally provide imaging optics and an image plane as well as the tracer particles themselves unless they are not imminent in the flow and have to be produced with a seeding generation system [16, p. 72]. Laser systems can be used as light sources as they emit monochromatic light with high intensities. Monochromatic light contributes to a homogeneous illumination of all particles in the physical object plane. Figure 2.6 shows a typical PIV setup and its components.

The tracer particles in the flow scatter the incident light from the light source which is subsequently collected by the cameras in the setup. For approximately spherical particles with diameters $d_P$ larger than the wavelength $\Lambda$ of the light, Mie's scattering describes the spatial distribution of the scattered light intensity [16, p. 13]. The number of local maxima and their relative spatial orientation to the incident light is dependent on the normalized diameter $d_N$ of the particles, which is defined by

$$d_N = \frac{\pi d_P}{\Lambda}.$$ 
(2.14)

As the intensity of the scattered light increases with greater particle diameters, but the efficiency of the scattering also increases with a higher ratio of the refractive index of the particles to that of the fluid, smaller particles can be used in seeded air flows than in seeded water flows for example. A compromise has to be found between particles which are small enough to follow the main flow sufficiently well and bigger particles to increase the scattering efficiency. Figure 2.7 shows that the
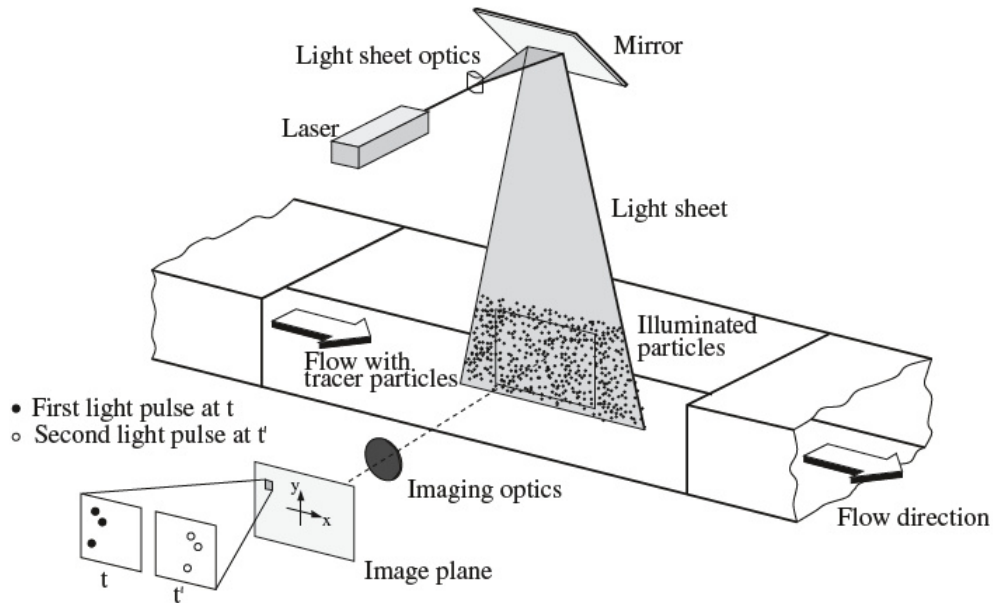
**Figure 2.6:** PIV setup with flow channel, light source, light sheet and imaging optics [16]

proportion of forward scattering (at $180°$) increases with the particle diameter. This implies that recording the scattered light is most efficient at an angle of $180°$ relatively to the incident light.



(a) Light scattered by a $1\,\mu$m oil particle

(b) Light scattered by a $10\,\mu$m oil particle
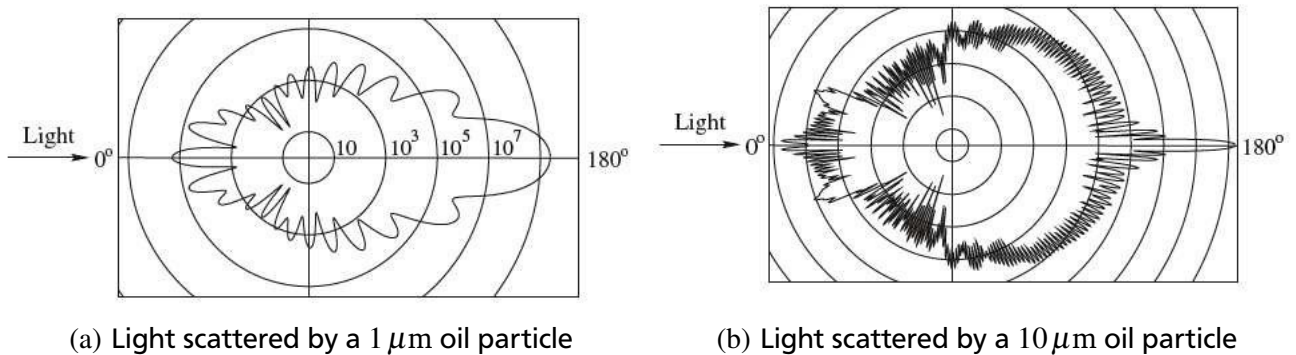
**Figure 2.7:** Spatial intensity distribution of Mie's scattering by oil particles in air, logarithmic intensity scale [16]

However, in practical applications recording takes place at an angle of nearly $90°$ considering the available space and the difficulties in preventing the light sheet from passing the imaging optics. Besides, in stereo-PIV recordings it is advantageous to position two cameras at an angle of $90°$ relatively to each other in order to gain as much information as possible about the displacement vectors of particles. This will be explained in section 2.3.2.

The light sheet is illuminated twice with very short light pulses to ensure that the particles do not move during the exposure. Most contemporary systems produce two separate digital images from these illuminations, so-called double-frames. A digital image is further divided up into several interrogation areas. The size of these areas is strongly dependent on the average flow velocity, accordingly on the time delay between two illuminations and on the smallest turbulent structures to be visualised. It is assumed that all particles within an interrogation area execute the same homogeneous movement and have a constant displacement vector. Thus, the size of the interrogation areas also determines the number of independent velocity vectors. Correspondent interrogation areas in two subsequent frames are then cross-correlated to detect the displacement of identical particles by statistical means. A cross-correlation sums up the products of discrete pixelwize intensities which is pointed out in the general form of a discrete cross-correlation in equation 2.15. The cross-correlation function features a maximum located where the average displacement within an interrogation area in the light sheet evolves. Thus, the location of this

maximum indicates the average in-plane displacement when transferred to the physical geometry of the object plane. $R$ represents the discrete cross-correlation function, $\hat{I}_1$ and $\hat{I}_2$ are the intensities in two correlated images at the locations $(i,j)$ and $f$ and $g$ represent variables for the spatial displacement by which to determine the displacement for a maximum of $R$. The cross-correlation is identical with a convolution of two functions in the image space, namely $\hat{I}_1$ and $\hat{I}_2$ in this example [17, p. 27]. The terms with $i \neq j$ give the correlation of stochastically distributed particles which generates Gaussian noise whereas the terms with $i = j$ hold relevant information about the displacement of identical particles.[2]

$$R(a,b) = \sum_i \sum_j I_1(i,j) \cdot I_2(i+f,j+g) \tag{2.15}$$

Components of the velocity vectors are calculated from the known time step between two images and the displacement of particles which is transferred to the physical coordinate system of the illuminated object plane.

Reliable results from PIV recordings can only be obtained if the correlation of images is successful and shows a distinct maximum. This maximum can usually be assessed visually in the measurement acquisition and processing software inside double-frame recordings. One necessary precondition for striking correlation maximums is the reduction of *in-plane losses* and *out-of-plane losses*. In-plane losses occur if particles enter or exit the interrogation area between two recordings. They can be diminished by a reduction of the time delay which reduces the possible resolution of the velocity gradients, though. The time delay should not be too short to discriminate particle locations from each other in a double-frame recording. As a thumb rule the shift of a single particle in the image should not exceed $1/4$ of the size of the interrogation area.

Out-of-plane losses arise if particles enter or exit perpendicularly to the light sheet. These can be observed in highly three-dimensional and turbulent flows. Increasing the thickness of the light sheet is one possible solution. Though, an unadvantageous intensity distribution in the direction normal to the light sheet plane and a deteriorated spatial resolution are the consequences [16, p. 36]. Besides, increasing the thickness of the laser sheet results in a greater amount of illuminated particles which can prevent a successful correlation of particles if the particle density is too high. A shorter time delay between the recordings can reduce the out-of-plane losses as well in this case.

The use of statistical methods to extract the information about the displacement vectors of the particles only yields probabilities of the current movement of these particles. Absolute values cannot be obtained and other measurements with exactly the same boundary conditions may show different results due to the stochastical approach. This is why any additional dynamic information in the recordings such as reflection phenomena, a very dense particle distribution, noise from the detector system and the aforementioned in-plane losses and out-of-plane losses reduce the relevant information in the images.

### 2.3.2 Stereo-PIV

The reconstruction of a three-dimensional velocity vector can be quite defective if only one camera with a fixed point-of-view is used for PIV recordings. As it is explained in section 2.3.1 the scattered light is often recorded with camera optics positioned at an angle of $90°$ relative to the light sheet. The thickness of the light sheet expands in the direction of the optical axes of the camera and movements of particles in this direction cannot be resolved properly. Stereo-PIV makes use of two cameras which have different perspectives at the light sheet. Figure 2.8 shows the geometric construction of a vector which is observed from two different angles in a stereo-PIV setup.

Whereas the information from recordings of a single camera can only project velocity vectors into the plane of the light sheet, the third component of the velocity vector normal to the light sheet can be derived when the positions of two cameras are known. An accurate knowledge of the positions and the relative angles of the cameras can be obtained through a calibration process with a specially designed calibration target of known geometry. This procedure is explained in section 2.3.3.

In case the angle between the light sheet and the optical axes of the camera is not $90°$ as it is often handled in stereo-PIV applications, the region of interest along the light sheet exhibits different object distances. According to the *Scheimpflug criterion* the object plane, the lens plane and the image plane need to intersect in one line to achieve a focus on the whole

---

[2]   There are PIV systems that work with a double illumination of the same recording which requires an auto-correlation method to extract this information. Regarding the vast applications chips with high refresh rates nowadays this techniques is of no importance any more.
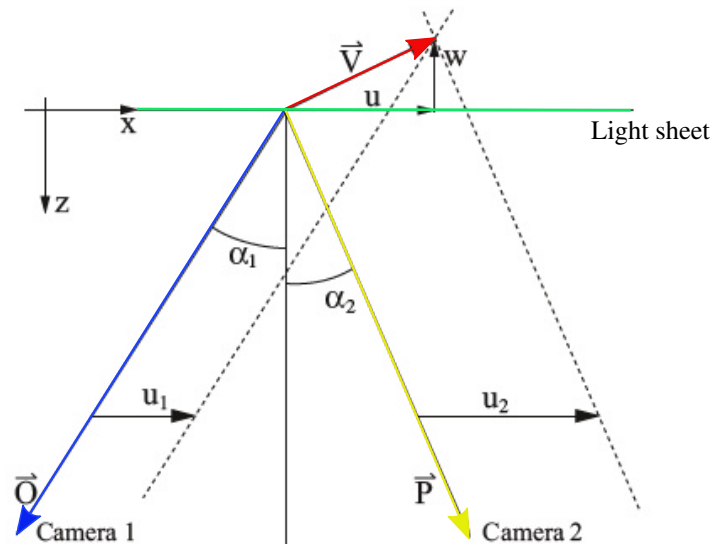
**Figure 2.8:** Reconstruction of three-dimensional velocity vector with two cameras in a stereo-PIV setup [16]

region within the field of view in the object plane [16, p. 212]. This can be realised with an adaptable angular displacement of the image plane relative to the lens plane which is exemplified in figure 2.9.
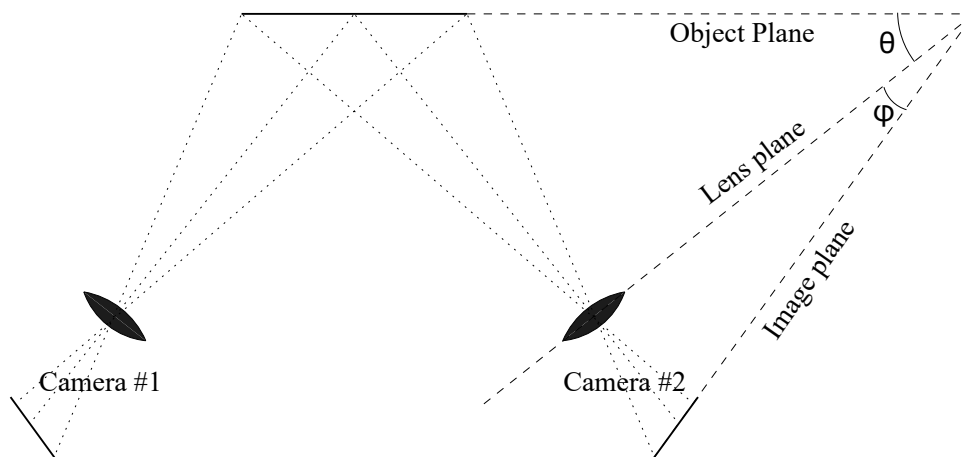


**Figure 2.9:** Fulfillment of Scheimpflug criterion by angular displacement of the image plane [16]

## 2.3.3  Calibration procedure

The calibration procedure for PIV systems requires geometric reference points within the light sheet. These are located on a specially manufactured calibration target whose geometry is known to the software. Calibration images are recorded while the target is illuminated homogeneously by a diffuse light source to spot the distinct locations of reference points on the target. These reference points in the calibration images are further used to create a global coordinate system in the software starting from an origin reference point specified by the user. Two additional points need to be defined in the camera images in order to create the x- and y-axes of the coordinate system. An automated search algorithm based on an assumed ideal geometry of the target finds all reference points on the first plane of the target. This defines the x-y-plane to which all additional planes on the target are related. The target is positioned parallely in the plane of the light sheet inside the region of interest for the measurements. Incident laser light therefore illuminates particles in the x-y-plane of the calibration target. Figure 2.10 shows

an exemplary grid on the calibration target generated from the reference points. The respective x- and y-axis start from the manually specified origin of the PIV coordinate system.
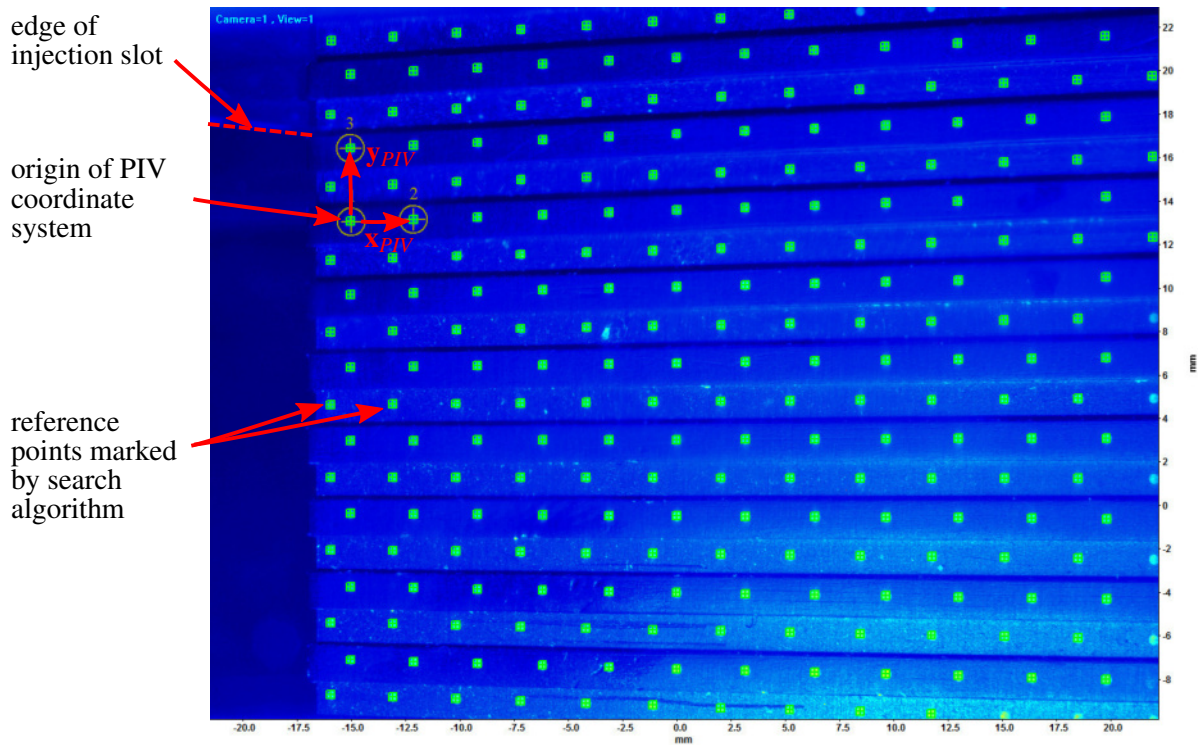


**Figure 2.10:** Grid points on the calibration target marked by the search algorithm

Stereo-PIV systems determine the positions of the cameras within this coordinate system by means of the different planes on the calibration target. In case the cameras are directed at the target from two sides, the target needs reference points on either side. The distance between the sides has to be known in order to enable the algorithm to accurately reconstruct the velocity component in the z-plane perpendicular to the target (compare figure 2.8). A manual measurement of the distances and angles of the cameras relative to the target is possible, but this procedure is restricted to the available space and accuracy. The transformation from the object plane to the image plane with consideration of the imaging optics is performed with a physical *pinhole-model* of the camera. Other approaches based on third-grade polynomial fits are more advantageous when obstructions and complex geometries like cylinders distort the optical path [18].

Once the coordinate system and the respective positions of the cameras are defined from calibration images the measurement recordings can be transformed into this coordinate system of physical dimensions and vector fields are calculated.

## 2.4 Film cooling

Cooling methods in gas turbines and aircraft engines have become a crucial aspect in past decades. Rising turbine entry temperatures are one of the implications when it comes to raising the overall efficiency of a turbine engine. A compromise has to be found between the increasing need for cooling air tapped from the last stages of the compressor and higher turbine entry temperatures which makes the efficient distribution of cooling air yet more important. Usually, only the first two stages of a turbine need to be exposed to cooling air. Stator and rotor blades as well as the endwall in this section are cooled with several internal and external cooling methods. Extensive film cooling is achieved when the cooling air forms a complete film above the components which are to protect against hot gas flows [2, p. 185]. The cooling of the blades is achieved with hole configurations on the blade surface. In contrast, the inner endwall features more accesses to eject air like the combustor-turbine gap or the stator-rotor gap through which the sealing air is led.

In the context of film cooling and the respective parameters for its investigation, the *mass flow rate*, the *blowing rate* and the *momentum rate* are commonly used to define operating points. The mass flow rate *MFR* is the ratio of coolant mass flow $\dot{m}_{sec}$ to primary mass flow $\dot{m}_{prim}$. In order to take different cross sections at the injection position for both flows into account, the

blowing rate $BR$ relates the MFR to the respective cross-sectional areas. Herein, $\rho$ represents the density and $u$ is the averaged velocity.

$$MFR = \frac{\dot{m}_{sec}}{\dot{m}_{prim}} \qquad BR = \frac{\rho_{sec} u_{sec}}{\rho_{prim} u_{prim}} \qquad I = \frac{\rho_{sec} u_{sec}^2}{\rho_{prim} u_{prim}^2} \qquad (2.16)$$

The momentum rate $I$ gives the ratio between the momentum of the injected coolant flow and the primary flow.
Geometric factors influencing secondary flow phenomena and their contribution to heat transfer to the endwall can be identified as the distance between the injection position and the leading edge of the airfoil, the injection angle, the width of an injection slot and its shape.

### 2.4.1 Secondary flow phenomena

The flow approaching a stator or a rotor vane features various secondary flow phenomena. Secondary flow phenomena inside a turbine passage have been subject to investigations for a long time which has led to multiple models summarising the characteristic flow phenomena induced by lateral pressure gradients and the flow around the leading edge of an airfoil. The model of the three-dimensional flow in the endwall region proposed by Goldstein and Spores [19] is exemplified in figure 2.11.
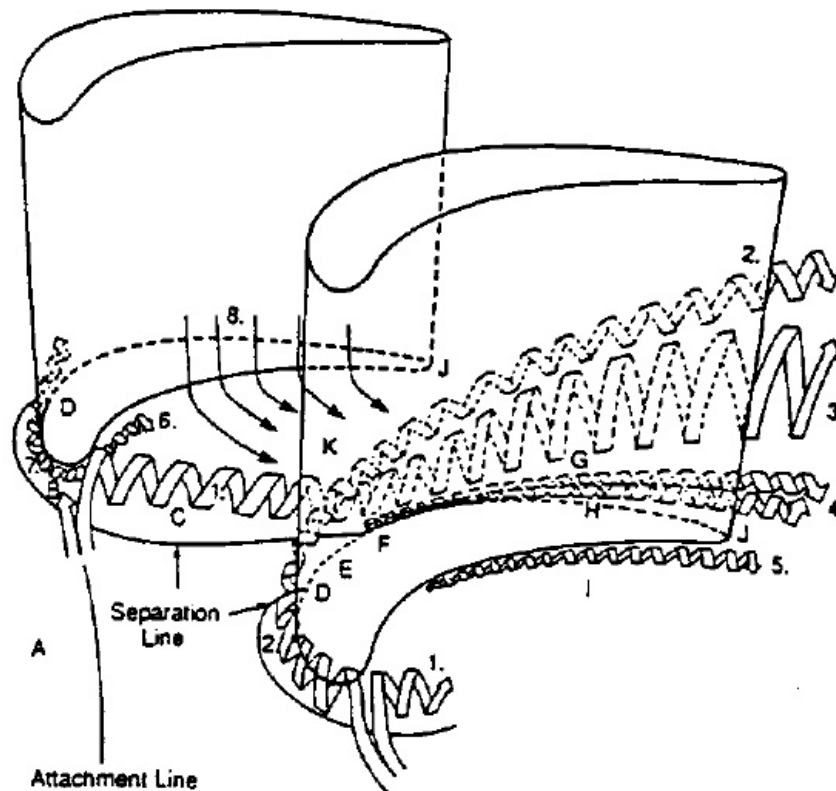


**Figure 2.11:** Secondary flow model by Goldstein and Spores [19]

Downstream of the three-dimensional separation line the horseshoe vortex lifts off and both its pressure-side branch (1)and its suction-side branch (2) enter the turbine passage. The pressure-side branch is deflected by the pressure gradient between the pressure side and the suction side of the neighbouring vane. Directly in front of the leading edge a corner vortex forms and is divided into two branches (6,7) as well. Farther upstream the normally thick and turbulent boundary layer detaches from the endwall under the influence of a rising pressure in front of the stagnation point and rolls up into the horseshoe vortex [20]. According to the literature survey by Friedrichs [20] the differences between models explaining the secondary flows in a

turbine passage focus on the propagation of the suction-side branch of the horseshoe vortex. Furthermore, Friedrichs identifies several regions of increased heat transfer to the endwall from his survey on investigations of passage flows. Increased heat transfer between the separation line and the leading edge is accounted for by the horseshoe vortex bringing hot main flow to the endwall. This is confirmed in the study by Kang et al. [21] who interpret the flow field upstream of the airfoil stagnation point in conjunction with heat transfer measurements on the endwall in this region. Praisner [22] attributes the gain in heat transfer coefficients to quasi-periodic transitions of the vortex structure which induce an additional downwash of fluid upstream of the horseshoe vortex. Independently from Reynolds numbers it is found that heat transfer coefficients rise beginning at the assumed location of the separation line in front of the leading edge and the horseshoe vortex. Downstream of the separation line the newly formed boundary layer is thin and laminar as stated before which reinforces high heat transfer to the endwall. Flow field visualisations show that fluid from regions above the vortex are washed down onto the endwall between the vortex and the leading edge. Farther downstream in the passage the flow is accelerated which leads to increased heat transfer in the throat and in the pressure side and suction side corners with the endwall in this region. Additionally, high velocities and turbulence at the trailing edge cause elevated heat transfer levels in this part [20]. These regions of increased heat transfer are illustrated in figure 2.12.
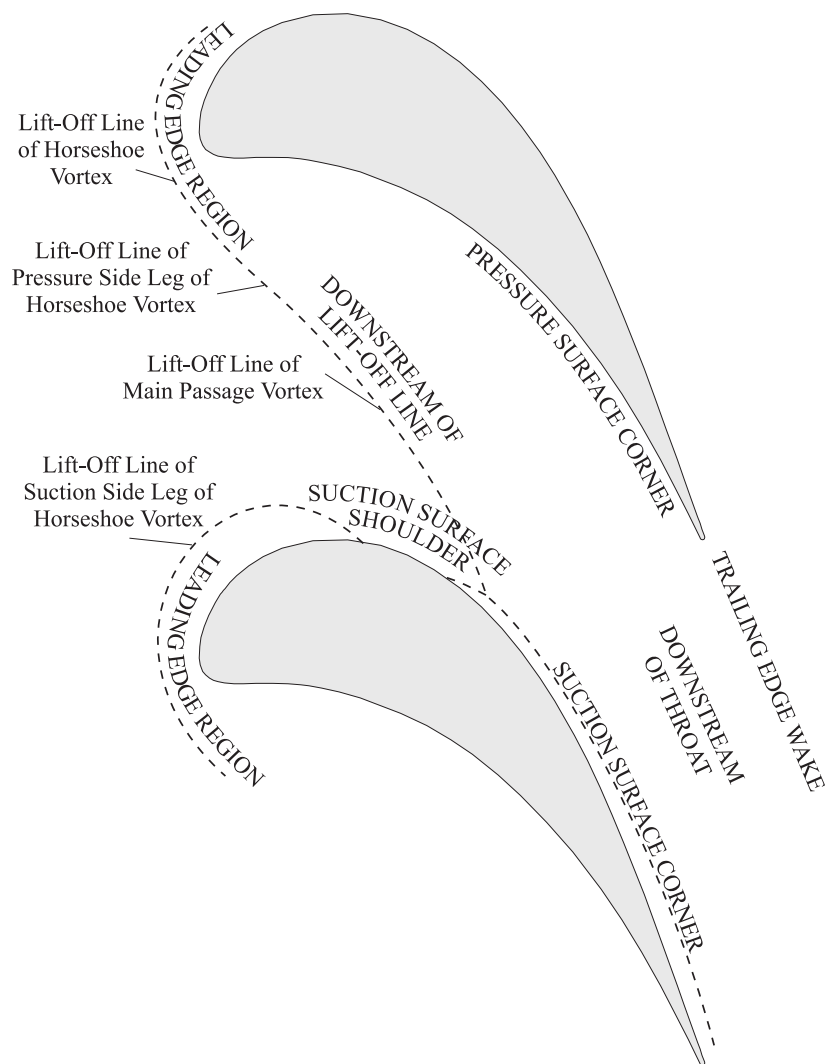


**Figure 2.12:** Regions with increased heat transfer in a blade passage [20]

The studies of Lynch and Thole [23] and Knost and Thole [24] with injection from a slot in a scaled vane cascade propose that mixing of the coolant flow from the slot with the primary flow is more extensive with increasing upstream distance of the slot from the leading edge of the vane. They further deduce that higher mass flow rates between coolant flow and primary flow lead to higher overall cooling effectiveness and a more uniform distribution of the coolant coverage on the endwall. At

higher mass flow rates the coolant flow has more potential to penetrate into the region downstream of the separation line in front of the leading edge. Reducing the slot width at constant mass flow rates elevates the momentum of the coolant flow, resulting in more evenly distributed cooling coverage. This is explained by the higher pressure ratio between the coolant flow supply plenum and the primary flow and is in accordance with the findings by Cardwell [25]. Additionally, Burd [26] hints at the fact that an inclination of the slot in streamwise direction results in higher streamwise momentum of the injected coolant. This can lead to better coolant coverage in regions downstream of the separation line inside the passage.

The phenomena explained in this section refer to findings for stator passage flows. They agree in general for the rotor flow with the formation of vortices at the leading edge and the passage vortex, but flow phenomena inside a rotor passage feature even more three-dimensional characteristics due to rotation. Blair [27] summarises the differences of a rotor passage flow compared to a stator passage flow referring to the heat transfer to the hubside endwall. Firstly, the interaction between the upstream stator and the rotor inlet flowfield makes the transition to a turbulent boundary layer on the rotor hubside endwall occur earlier due to the induced disturbances. Secondly, the secondary flows inside the rotor passage are influenced by the secondary flows exiting from the stator passage. With reference to the works of Joslyn and Dring it is explained that secondary flows induced by the upstream stator tend to move towards the hubside endwall and that effects by tip-leakage vortices can only be reproduced in combination with rotation (compare [28] and [29]).

The examinations in this thesis are conducted in a static system with a symmetric airfoil geometry inside a flow channel. This setup is not suitable to simulate passage flows. Consequently, the forming of secondary flow phenomena in the leading edge region is the focus of the aerodynamic investigations.

# 3 Experimental setup

In advance to the presentation of the experimental results the setups of both the *Large Scale Turbine Rig (LSTR)* and the small flow channel *Kleiner Windkanal (KWK)* are described.

## 3.1 The Large Scale Turbine Rig

The test rig LSTR at the Institute of Gas Turbines and Aerospace Propulsion (GLR) at TU Darmstadt is a 1.5-stage turbine test rig (stator - rotor - stator) with closed-loop air circuits for primary air and diverted secondary air. Low Mach numbers and scaled-up dimensions allow to generate flow conditions at Reynolds numbers representative of those in an engine application. Both air flows can be tempered separately to achieve constant flow temperatures for the primary flow through the turbine and the secondary flow serving as sealing air and simulations of cooling air in the blades and on the stator endwall [30]. Figure 3.1 gives an overview of the complete test rig.
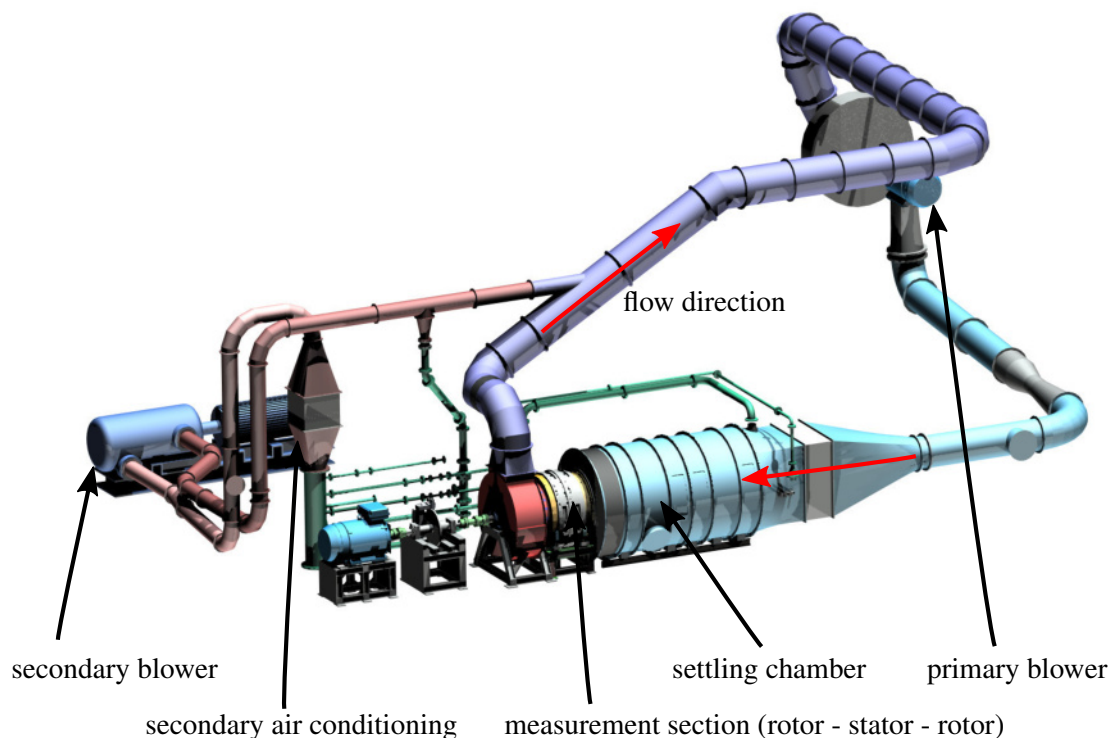


**Figure 3.1:** The Large Scale Turbine test Rig at the institute GLR

The primary flow enters the turbine section of the test rig downstream of swirlers which generate a twist in the flow to simulate flow conditions after passing a combustion chamber. In front of the first nozzle guide vane (NGV1) a RIDN-module (rear inner discharge nozzle) for coolant flow injection through holes is located. Coolant flow for the blades of the NGV1 is supplied from the housing. Between the first stator stage and the rotor itself a cavity for injection of sealing air is located which can be seen in figure 3.2.

The measurements conducted in the present work aim at comparability to the conditions in this particular section downstream of the cavity (Cavity 1 Seal Air in figure 3.2). Similar to the heating plate designed for heat transfer measurements on the stator endwall and implemented by Neubauer [31], the rotor endwall will be equipped with a heating plate as well. In figure
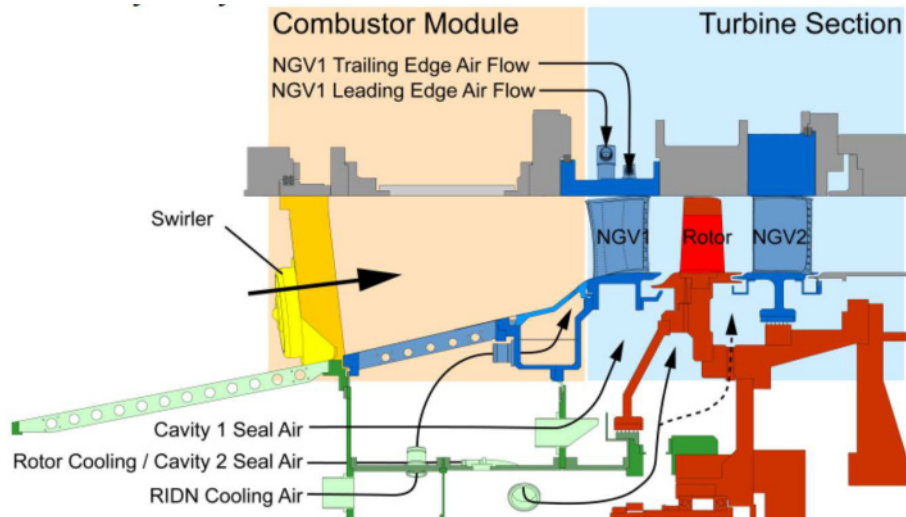
**Figure 3.2:** Measurement sections of the LSTR with indications of primary and secondary air flows [30]

3.3 the cavity at the LSTR is shown as well as the future location of the newly designed heating plate. The heating plate covers the endwall from the exit of the cavity to the trailing edge of the rotor blade within one instrumented rotor passage as indicated by the black component.
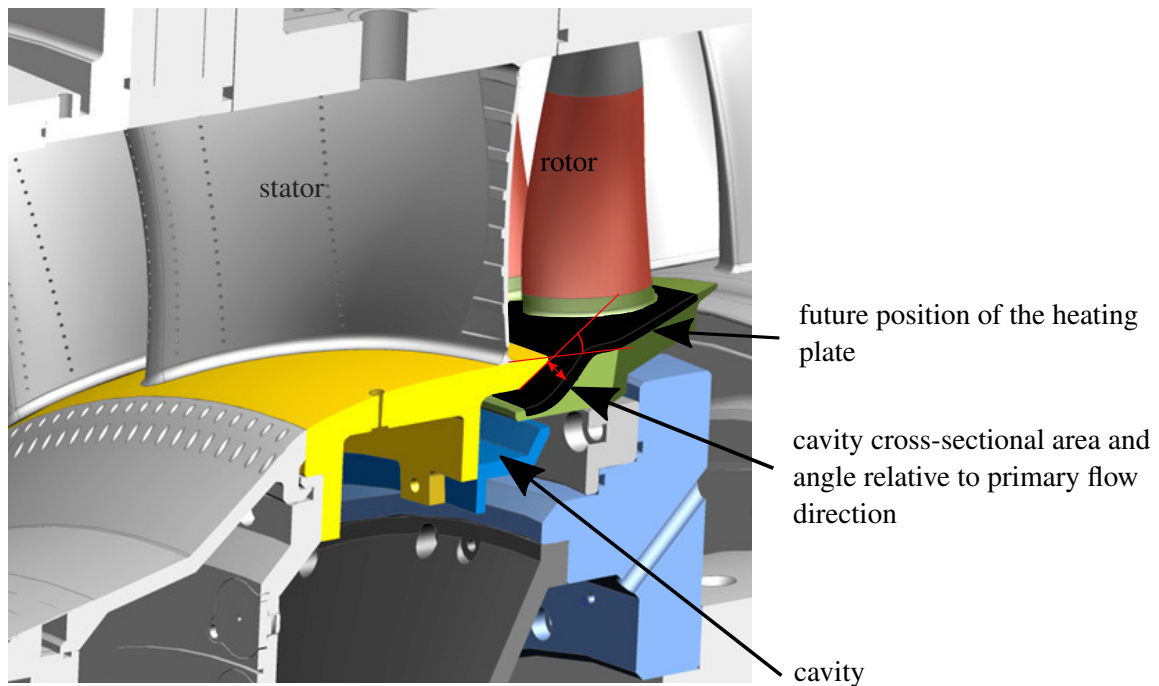


**Figure 3.3:** Sectional view of the cavity at the LSTR and the future position of the heating plate on the endwall

The cavity for sealing air between the first stator stage and the rotor guides the secondary air along multiple deflections before it is injected into the primary flow at an angle of $58.66°$. With a height of $11.17\,\mathrm{mm}$ its total sectional area of the cavity at the outlet is $0.0301\,\mathrm{m^2}$. The cross-section of the primary flow in this measurement section is $0.4211\,\mathrm{m^2}$. These values are used to estimate blowing ratios which are regulated during the measurements at the flow channel. All other relevant information about the operating point of the LSTR are given in table 3.1.

**Table 3.1:** Operating point of the LSTR

| Parameter | Symbol | Value |
|---|---|---|
| rotational speed | $n$ | $1000\,\frac{1}{\text{min}}$ |
| total mass flow | $\dot{m}_{tot}$ | $9.47\,\frac{\text{kg}}{\text{s}}$ |
| RIDN coolant mass flow | $\dot{m}_{RIDN}$ | $0-5\,\%\dot{m}_{tot}$ |
| NGV coolant flows | $\dot{m}_{NGV}$ | $6.85\,\%\dot{m}_{tot}$ |
| rotor cavity mass flow | $\dot{m}_{cav}$ | $2\,\%\dot{m}_{tot}$ |
| cross-section primary flow | $A_{prim}$ | $0.4211\,\text{m}^2$ |
| cross-section cavity | $A_{cav}$ | $0.0301\,\text{m}^2$ |
| primary flow temperature | $T_{prim}$ | $>35\,^{\circ}\text{C}$ |
| secondary flow temperature | $T_{prim}$ | $42-52\,^{\circ}\text{C}$ |

## 3.2 The small flow channel

The test bench used for the investigations in this thesis at the institute GLR features the main components to allow heat transfer measurements based on infrared thermography at boundary conditions comparable to the LSTR. It was initially designed to establish heat transfer measurements with comparability to another test bench at the institute GLR, but due to its modular design adjustments for other measurement applications such as particle image velocimetry can be realised easily. Figure 3.4 shows the test bench and its components. Table 3.2 summarises all relevant geometrical parameters of the flow channel.



| outlet to blower | airfoil | optical access | heating plate | plenum for secondary air supply | injection module with slot | flow straighteners | inlet for primary air |
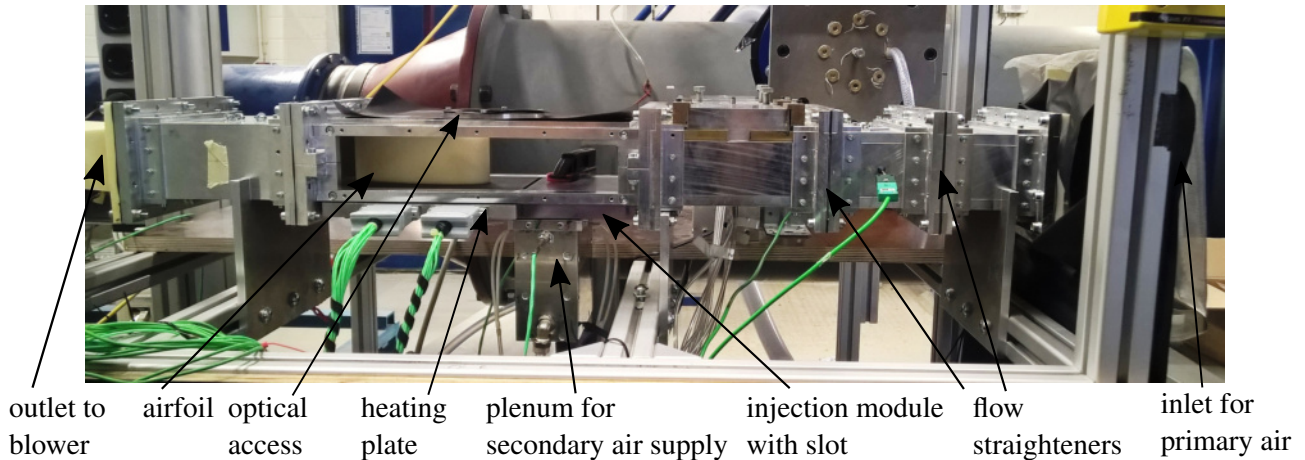
**Figure 3.4:** The small flow channel at the institute GLR

The flow channel has an open-loop air circuit with a blower allowing to operate in suction mode. The primary flow is drawn in from the environment through a specially designed inlet for minimum aerodynamic losses. Downstream of the inlet the primary flow passes flow straighteners to increase the homogeneity of the flow cross-section and two filters to avoid the suction of foreign particles. Afterwards the flow reaches the measurement section consisting of the injection module with the slot for secondary air injection, the heating plate with the airfoil and the optical access above. Directly in front of the heating plate the slot is located as an opening in the injection module. The secondary air is injected into the flow channel through this slot simulating the sealing air at the LSTR. Below the injection module the plenum for the secondary air is located which functions as a settling chamber and contains accesses for thermocouples and differential pressure measurements (compare section 3.2.2). The subsequent part of the measurement section is constituted by the heating plate at the bottom which will be explained in detail in section 3.2.1. The upper side of the channel contains the optical access for the infrared camera which is placed above but is not displayed in figure 3.4. This way, the area of interest for the measurements at hand which

**Table 3.2:** Geometrical parameters of the flow channel

| Parameter | Symbol | Value |
|---|---|---|
| channel cross-section | $A_{prim}$ | $130x50\,\text{mm}^2$ |
| slot width | $S$ | $4\,\text{mm}$ |
| slot cross-section | $A_{sec}$ | $4x100\,\text{mm}^2$ |
| slot injection angle | $\phi$ | $90°$ |
| slot length to width ratio | $\frac{L}{S}$ | 6 |
| airfoil leading edge diameter | $d_{NACA}$ | $30\,\text{mm}$ |
| distance from slot to airfoil leading edge | $x_{LE}$ | $42\,\text{mm}$ |

is the length between the slot and the leading edge of the airfoil can be exposed to the camera. All wall components of the channel are manufactured in aluminium, but can be replaced by identical parts made of acryl glass. Both the primary and the secondary flow subsequently pass the blower and a standard orifice giving the total mass flow. Inlet and outlet are positioned well distanced from one another to avoid influences on the primary air inlet conditions. The temperature of the primary flow is measured with two thermocouples reaching laterally into the flow between the flow straighteners. Additionally, static pressures are recorded at eight positions expanding laterally on the bottom side of the channel after the flow straighteners. Downstream of the flow straighteners a traverse driven by a linear motor can be seen. With the help of this traverse pressure probes can be driven through the cross-section of the flow channel to determine pressure distributions and velocity profiles in the primary flow. Although Schneider [32] found that contaminations in one of the filters may cause inhomogeneities in the velocity profile of the primary flow, Fox [33] successfully conducted heat transfer measurements with this setup. Influences stemming from inhomogeneities in the primary flow profile could not be identified at this time. A detailed investigation of the flow profile and the boundary layer development upstream of the measurement section is not possible in the scope of this work due to the limited time frame.

The cross-section of the channel has a width of 130 mm and a height of 50 mm and does not correspond to the cross-sectional area found at the LSTR. To ensure comparability to measurements at the LSTR the identity of blowing ratios of the secondary air flow is essential to the measurements conducted at this flow channel which will be addressed in section 4.2.

## 3.2.1 Heating plate

The heating plate constitutes the main component within the measurement section. It was designed by Schneider [32] with reference to the basic structure introduced in the theses of Ostrowski [34] and Steinhausen [12]. Its purpose is to allow varying surface temperatures at constant primary and secondary air conditions for the applicability of the regression method explained in section 2.1.1. Heat fluxes are determined with the temperature difference between both sides of an insulating auxiliary wall under the assumption of one-dimensional heat conduction. Surface temperatures are varied by changing the temperatures controlled beneath the auxiliary wall, denoted as set temperatures in the following. The composition of the heating plate and its installation in the flow channel can be seen in the schematic in figure 3.5. Figure 3.6 shows the bottom side of the heating plate mounted in the measurement section of the channel. The installation space for the plenum at the bottom of the injection module is also indicated in figure 3.6.

Six heating foils at the bottom of the heating plate generate the heat flux into the aluminium body above. The analogue power supply is provided by six separate power supply units. The auxiliary wall is manufactured in epoxy resin with a thermal conductivity of approximately $0.195\,\frac{\text{W}}{\text{mK}}$[1]. Its low thermal conductivity is essential to increase the temperature difference through the auxiliary wall and therefore to enhance the accuracy of the calculation of the heat flux. Temperatures are measured by 19 thermocouples which are distributed at two different levels in z-direction below and above the auxiliary wall. Six of the thermocouples below the auxiliary wall are further used to control the set temperature at the upper side of the aluminium body. A maximum of twelve thermocouples above the auxiliary wall can be used as geometric references in the infrared

---

[1]  This value is taken from notes by Fox [33] which refer to information from an expert's interview with an employee of the manufacturer.
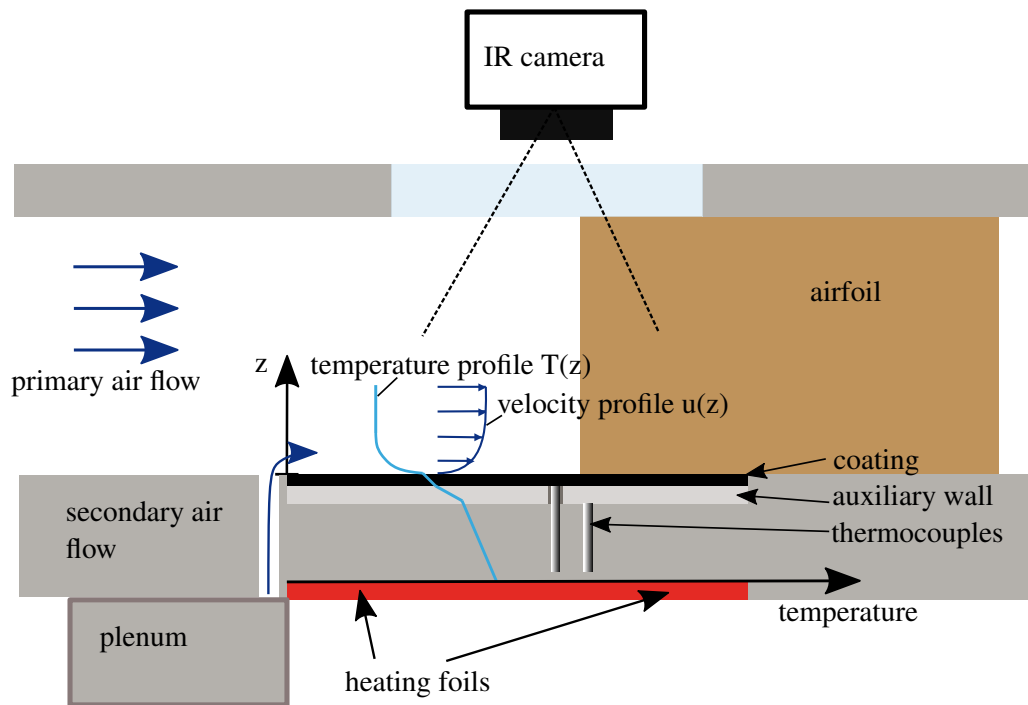
**Figure 3.5:** Heating plate and installation position in the measurement section
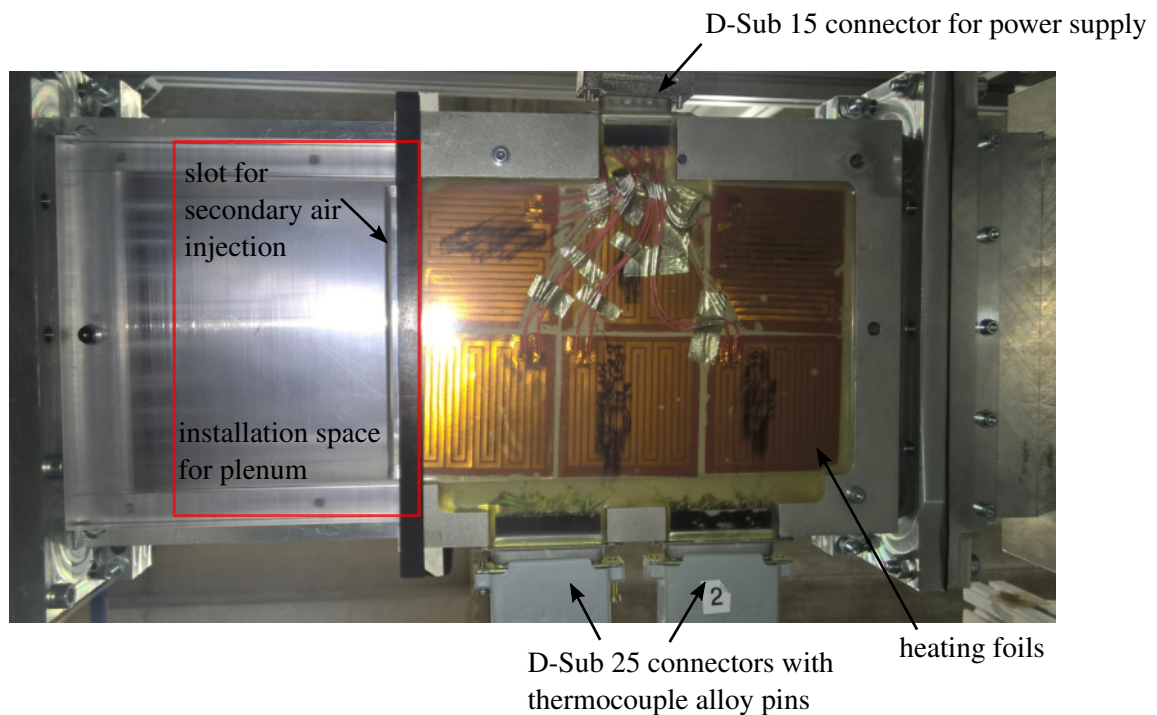


**Figure 3.6:** View of the bottom side of the heating plate mounted in the channel

thermographic recordings. It can be seen later in this section that only five of these thermocouples are accessible in the optical path of the infrared camera. They will be referred to as reference thermocouples in the following. The auxiliary wall is coated with a black paint which features high emissivity and diffuse radiation properties to improve the conditions for infrared thermographic measurements on the upper side. All layers of the heating plate structure were dimensioned with a laser triangulation method when the plate was constructed [33]. The average thickness of these layers and their respective uncertainties as well as the estimated thermal conductivities are gathered in table 3.3.

**Table 3.3:** Specifications of the auxiliary wall and the coating

| Parameter | Symbol | Value | Uncertainty |
|-----------|--------|-------|-------------|
| Epoxy auxiliary wall | | | |
| thickness | $s_{aux}$ | 1.46 mm | $\pm 0.05$ mm |
| thermal conductivity | $\lambda_{aux}$ | 0.195 $\frac{W}{mK}$ | $\pm 50\,\%$ |
| Coating | | | |
| thickness | $s_{coat}$ | 0.12 mm | $\pm 0.05$ mm |
| thermal conductivity | $\lambda_{coat}$ | 0.199 $\frac{W}{mK}$ | $\pm 2\,\%$ |

The area in front of the airfoil leading edge is highlighted in the topview in figure 3.7. On the left, the primary flow is indicated. It overflows the slot for the secondary air injection and runs towards the airfoil. Similar to the conditions at the LSTR considering the axial length on the endwall the running length from the slot position to the leading edge of the airfoil is 42 mm. For reasons of producibility the front edge of the heating plate consists of a 1 mm thick fillet overlapping from the aluminium body below before the auxiliary wall begins. This makes the foremost region after the slot position unreliable with respect to thermal boundary conditions and it is therefore spared in the examination. The dotted line represents the area on the heating plate which is accessible to the camera optics. Due to the small thickness of the coating the reference thermocouples giving temperatures above the auxiliary wall are visible as hot spots in the infrared recordings when the heating plate grows warmer. As mentioned before, only five of these reference thermocouples are located in the accessible area and can be seen in figure 3.7. The physical coordinate system of the heating plate is also indicated in figure 3.7. All further spatially resolved results are projected into this coordinate system (compare sections 4 and 5).

The symmetric airfoil was designed by Fox [33] and is manufactured in a composite of epoxy and acrylate. Reynolds similarity to the airfoil geometry of the rotor at the LSTR is ensured with reference to the leading edge diameter which is 30 mm for the symmetric airfoil.
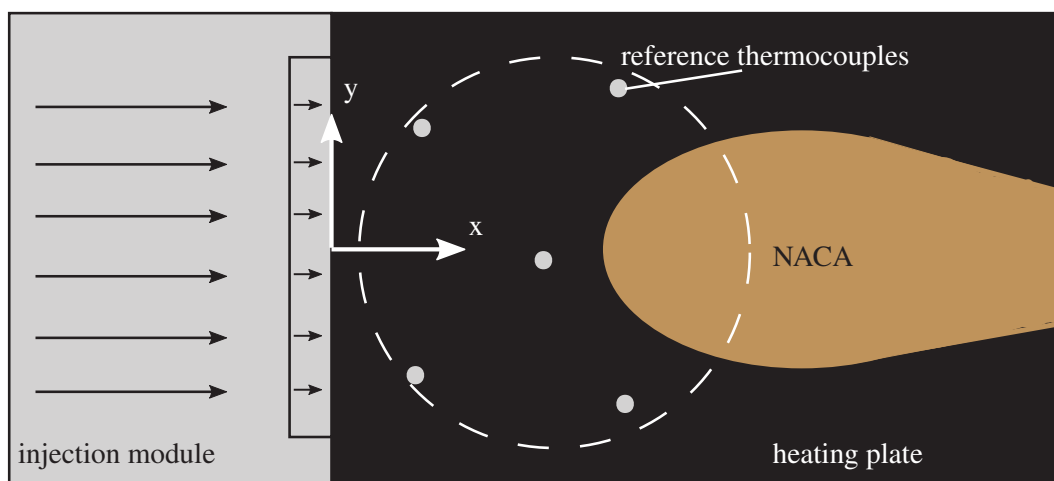


**Figure 3.7:** Topview of the heating plate with reference thermocouples and the position of the airfoil

## 3.2.2 Secondary air supply

The secondary air entering the flow channel thorough the slot simulates the sealing air running through the cavity at the LSTR. It is supplied by the in-house compressed air system. A mass flow meter measures the mass flow of the secondary air[2]. Due to the necessary expansion of the diameter to connect the tubes to the straight running length in front of the flow meter and on account of the long period since the last calibration, the accuracy of the flow meter can only be estimated at $\pm 10\,\%$ of the measured value according to an employee of the producer. An adjustable valve is used to set the mass flow of the secondary air. A strainer is installed at the position where the diameter of the tubes is widened in order to make the secondary flow bulge in the wider diameter. Before entering the plenum the secondary air passes through a cylindrical flow heater. The plenum was designed by Roth [35]. It functions as a settling chamber and is equipped with two strainers which can be seen in figure 3.8.



position of the slot in the injection module

access for thermocouple

static pressure measurement positions
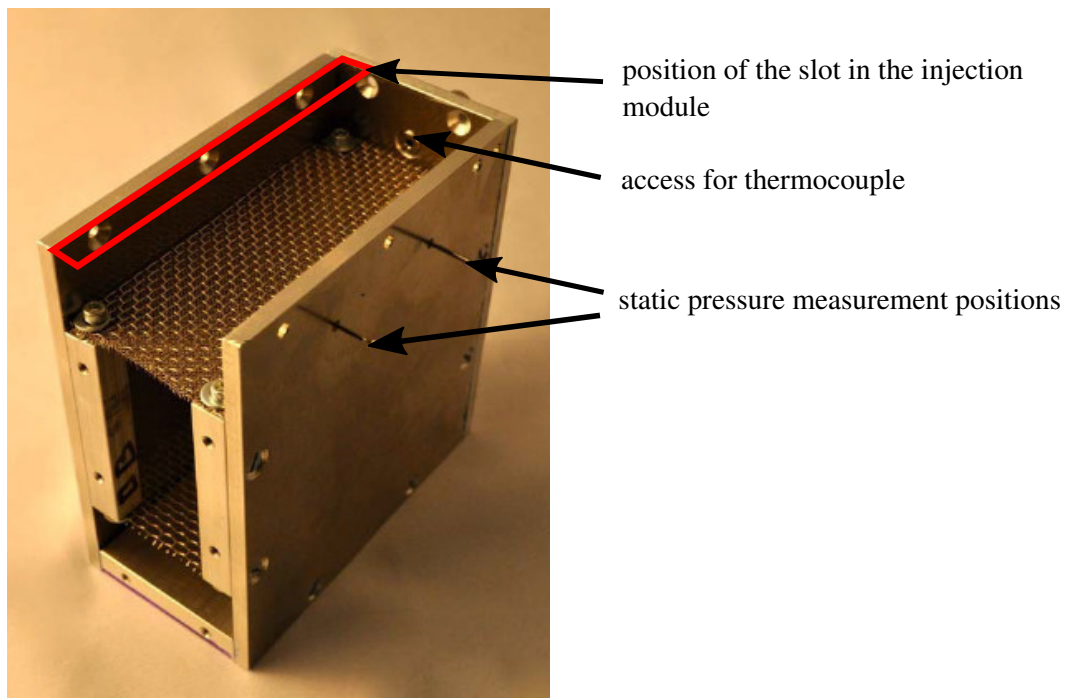
**Figure 3.8:** Plenum for the secondary air with one side opened, adapted from [35]

The connectors for the entry of the secondary air are positioned on opposite sides near the bottom of the plenum. This way, the secondary air enters the injection module above more homogeneously. In figure 3.8 the position of the slot in the injection module is highlighted.

An exemplary measurement of the total pressure distribution at the outlet of an injection module with discrete holes was also conducted by Roth [35]. The homogeneity of the distribution of pressures and velocities in all injection holes could be confirmed. Deviations in the pressure profile at the exit of a single hole due to detachments at the entry of the hole could be related to the findings from other investigations (compare [36]). The fluctuations of the in-house compressed air supply mentioned by Roth [35] can be observed in the measurements at hand as well. As they occur periodically and with amplitudes corresponding to a drop in the secondary air mass flow of $0.2\,\frac{g}{s}$ at all mass flow setpoints, a stationary operation is ensured when this distinct drop is not present and a constant mass flow is reached.

Temperature measurements of the secondary air are taken by two thermocouples in the upper part of the plenum. Their installation space can be seen in figure 3.8. These measurements function as process variables for the temperature control loop that is implemented in an existing *Labview* programme in the course of this work. The flow heater is actuated by a pulse-width modulated signal which switches the main power supply in a high-voltage relay. A first estimation of the regulator parameters for this closed loop controlled system is determined using the step response method and the corresponding parameter values given by Unbehauen [37].

---

[2] The mass flow meter is the model *In-Flow F106AI* by Bronkhorst. It covers the range of the required mass flows for the measurements in this work.

In addition to the temperature acquisition differential pressure measurements are recorded in the plenum so that information on temperature and pressure is available both for the primary air and for the secondary air (compare section 3.2). The tapping points are indicated on one side of the plenum in figure 3.8.

### 3.2.3 Injection module

The secondary air enters the flow channel through the slot implemented in the injection module. It is manufactured in polycarbonate with a high permanent service temperature of $125\,°C$ to $128\,°C$ and low thermal conductivity of approximately $0.2\,\frac{W}{mK}$ according to material data sheets of different industrial producers (compare data sheets for *Makrolon* by Covestro in the appendix). Parameters of the slot geometry are provided in table 3.2 alongside with other geometric parameters of the flow channel for the measurements in this work. The the slot geometry can be seen in figure 3.9.
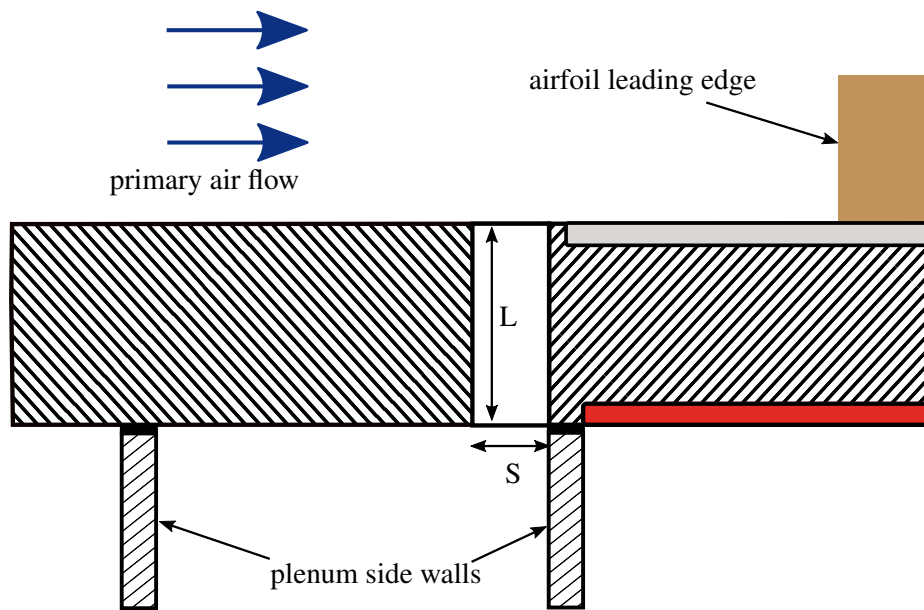


**Figure 3.9:** Sectional view of the injection module and the slot

The modular architecture of the flow channel enables for a quick change of injection modules. In the present work an injection angle of $90°$ is chosen, making the secondary air entering the flow channel perpendicularly to the primary air flow. The slot width $S$ is orientated at the slot width of other injection modules available at the institute. It features a length to width ratio of $\frac{L}{S} = 6$, taking into account the aforementioned findings of Roth [35] and auf dem Kampe [36] concerning detachments inside injection holes. These detachments are supposed to be avoided by the greater length to width ratio, the perpendicular slot direction and by locating the slot at one end of the injection module. This way, deflections at the entry into the slot are diminished and the running length inside the slot enables the flow to reattach and exit the slot more homogeneously. On top of that, all other available injection modules raise troubles when it comes to positioning a sealing between the plenum and the injection module and the heating plate, respectively. This issue is solved with the injection module used for the measurements at hand. Another identical injection module with a slot width of $7.5\,mm$ is constructed as well in the course of this work, but measurements are only performed with the smaller slot width due to the limited time frame.

### 3.2.4 Infrared camera system

Thermographic measurements on the upper side of the heating plate are recorded with a *FLIR X6540sc* infrared camera. Its spectral range reaches from $1.5\,\mu m$ to $5.5\,\mu m$ in the respective midwave infrared range. The maximum full frame rate is $126\,Hz$ which is sufficient for the future application at the LSTR where the recording of one frame per revolution requires a frame rate of $16.67\,Hz$ at a speed of $1000\,\frac{1}{min}$. A variable integration time setting between $160\,ns$ and $20000\,\mu m$ in combination with a multi-integration time function makes it possible to record the same scene with different integration times and

a lowest possible time difference. The camera is mounted on a tripod above the flow channel and the optics are directed to the infrared-transparent glass used as an optical access. It features a transmission coefficient of approximately 70 % in the respective infrared wavelength region (compare data sheet *Vitron CVD Zinc Sulfide* in the appendix). An objective with a focal length of 25 mm is installed at the camera. The field of view is arranged in such way that the optical access above the measurement section is fully enclosed while the positions of five of the reference thermocouples upstream of the airfoil need to be captured as well. The focus of the camera is adapted manually to the reference thermocouples once in advance to the measurements.

With the known physical positions of the reference thermocouples the resolution of the thermographic recordings can be estimated at $0.233 \frac{\text{mm}}{\text{pixel}}$ neglecting the viewing angle. The size of a single reference thermocouple in the recordings is about 10 pixels. Their respective position in the digital camera output array is determined with an algorithm called *imfindcircles* during the evaluation routine in Matlab [38]. As the camera signal-temperature value pairs at these locations are the inputs for the pixelwise determination of the calibration coefficients, it is necessary to avoid any displacement of the camera between the recordings at varying set temperatures.

### 3.2.5 PIV system

Two cameras are used for the aerodynamic measurements with stereo-PIV recordings. The manufacturer *LaVision* also provides the corresponding measurement acquisition and processing software *DaVIS*. Both cameras feature a dynamic range of 14 bit and a resolution of $1600x1200$ pixels defined by the array size of the CCD-chip. They are equipped with 50 mm 1:1.4 objectives and Scheimpflug adapters designed by Brandstetter [39]. As the position of the image plane relative to the optics can be changed inside the Scheimpflug adapter as well, the effective focal length does not necessarily correspond to the fixed focal length of the objective. This way, it is possible to cover wider ranges of object distances with one objective while the focus can be adapted to the desired scene.

Optical accesses for the cameras to the flow channel are realised by exchanging the aluminium side walls and the upper wall in the measurement section with acryl glass components. For the aerodynamic measurements a coated aluminium plate is installed for exchange of the heating plate used in the heat transfer measurements. This way, similar properties of the endwall surface are achieved and reflections are reduced compared to the usage of acryl glass components. The installation positions of the cameras can be seen in figure 3.10. Their angle relative to the light sheet defined by the position of the target is approximately 48°. The vertically adjustable mounting for the laser sheet optics is also indicated in this figure.
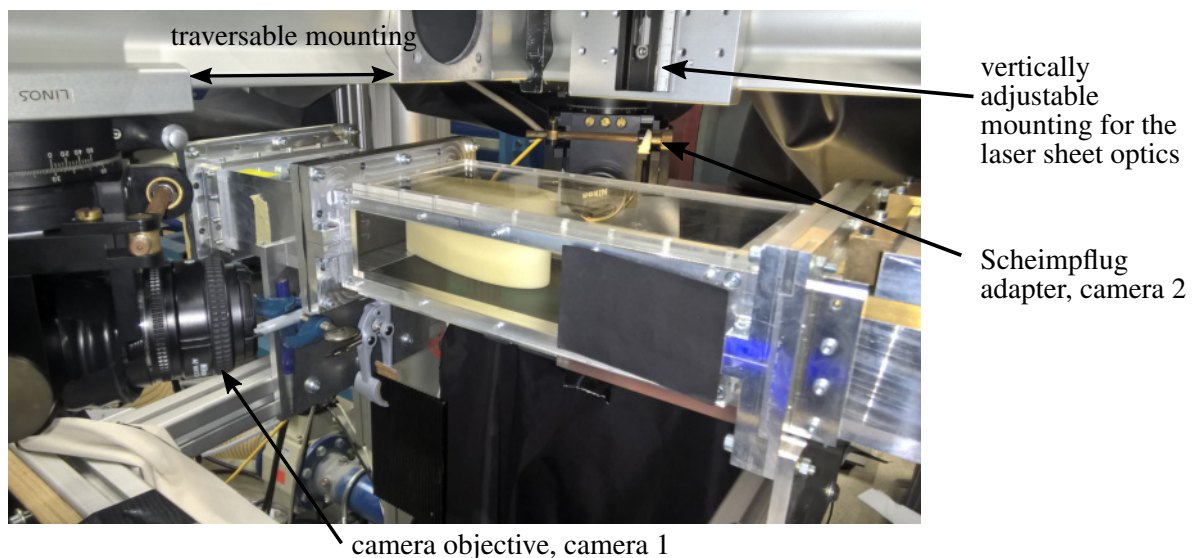


**Figure 3.10:** PIV cameras positioned on both sides of the flow channel with the help of a traversable mounting

Another traversable mounting for both cameras and the laser sheet optics makes it possible to move all components necessary for the recordings across the measurement section. Positioning the laser sheet optics closer to the flow channel makes it possible to further adjust the thickness of the laser sheet. The calibration of the cameras and their focus do not need to be

redone or rearranged because the relative distance from the cameras to the light sheet does not change when traversed laterally across the flow channel. Refraction characteristics remain unchanged and minor inhomogeneities in the acryl glass walls do not disturb the optical path as these walls are out of focus.

The front side of the three-dimensional calibration target is aligned with the centerline of the flow channel for calibration purposes. As the calibration is performed after the measurements it is possible to orient the target to the laser sheet which is more reproducible due to the small thickness of the laser sheet. This way, it is ensured that the whole side of the target is in the symmetry plane and directed towards the leading edge of the airfoil. A single calibration performed in the streamwise symmetry plane of the flow channel is consequently used for measurement recordings in the symmetry plane and at lateral positions shifted in the y-direction of the heating plate coordinate system. Figure 3.11 illustrates the installation position of the calibration target inside the flow channel.
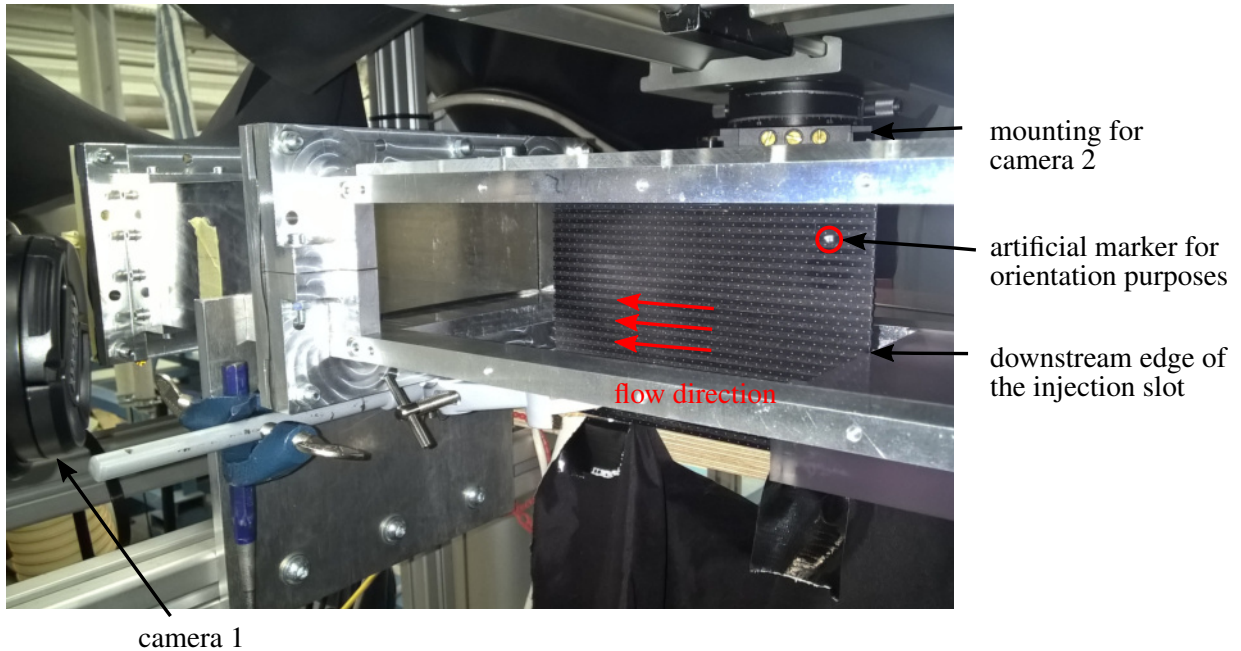


**Figure 3.11:** PIV calibration target positioned in the flow channel with the front plane aligned to the leading edge

Connecting points for the supply with seeding particles from separate seeding generators are constructed for both the primary flow and the secondary flow. The supply for the primary flow is made of tubes connected to the output of one of the seeding generators. At the end of the tubes a cone is attached to simulate an effect similar to a diffusor which broadens the flow containing the seeding. It is positioned half a meter in front of the inlet of the flow channel and its vertical position is adjusted after a visual inspection of the seeding particle density in the observed region in the measurement section. As stated in section 3.2 obstacles in front of the inlet do not seem to interfere with the heat transfer on the heating plate in the measurement section. It is therefore assumed that boundary layer conditions comparable to those during the heat transfer measurements can be achieved when the seeding supply is placed in this position. The seeding generator for the secondary flow is depicted in figure 3.12. It is connected to the in-house compressed air supply downstream of the mass flow meter.

The flow heater is not installed in the PIV setup so that the seeded secondary air is directly led to the plenum. This approach neglects the equality of density ratios between the heat transfer measurements and the aerodynamic measurements, but blowing rates can be controlled at the same levels. Seeding generators require a minimal inlet pressure in order to switch on the valves opening the Laskin nozzles. The minimal seeding amount generated by the seeding generator at the lowest possible inlet pressure still is too high for a proper detection of particles. Hence, the seeding generator is bypassed to create an additional control for the particle density independently from the mass flow.

control valves for
seeding particle
amount

bypass

outlet to plenum
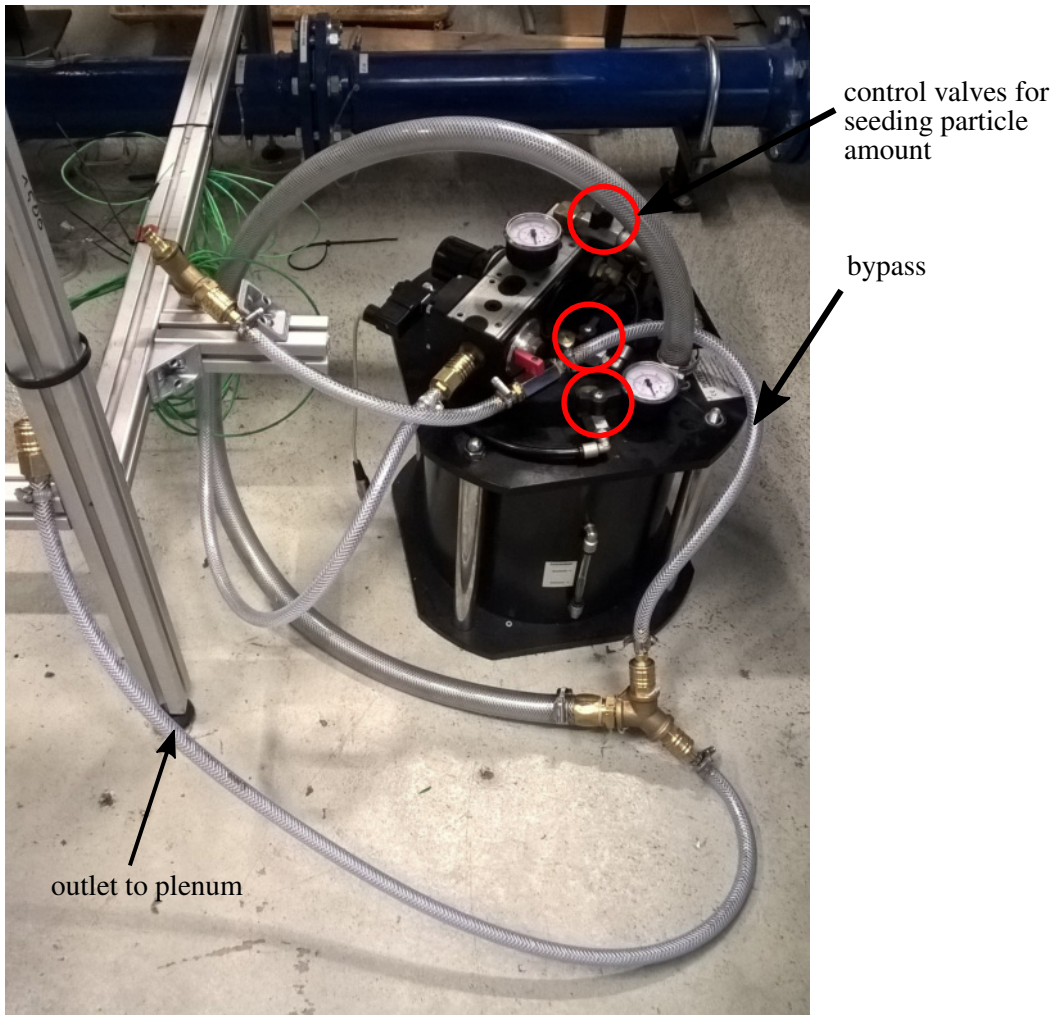
**Figure 3.12:** Seeding generator for the secondary flow equipped with a bypass

# 4 Heat transfer measurements

In the following sections results of the heat transfer measurements at the flow channel are presented. The selection of proper operating points is discussed and the variation of both integration times and blowing rates is explained in detail.

## 4.1 Camera settings and integration times

The choice of integration times for future measurements at the rotor of the LSTR is dependent on the rotational speed. At a constant rotational speed and a fixed distance between the camera optics and the endwall, displacements in the camera recordings increase linearly with the integration time. As these exact geometrical dimensions of the installation situation at the LSTR cannot be imitated at the flow channel information on the spatial resolution is taken from earlier works dealing with thermographic measurements on the stator endwall. From the recordings by Wiemer [13] a spatial resolution *Res* of approximately $0.24 \frac{\text{mm}}{\text{pixel}}$ can be derived when the curvature of the endwall is neglected. The average pixel displacement $\delta px$ for a comparable recording position at the rotor is therefore estimated with the mean radius of the endwall between the hub side edge of the cavity and the trailing edge of the rotor vane being $r_{mean,rotorendwall} = 423\,\text{mm}$. The rotational speed is adopted from the design point at $n = 1000 \frac{1}{\text{min}}$ and the pixel displacement is estimated for an integration time of $12\,\mu s$.

$$\delta px(t_{int} = 12\,\mu s) = \frac{2\pi \frac{n}{60} r_{mean,rotorendwall}}{Res} \cdot 12\,\mu s \approx 3\,\text{pixel} \tag{4.1}$$

Gazzini [40] proposes to restrict the integration time for a sharp image to the uncertainty of the rotor displacement occurring within a recording time for 1000 frames. The equivalent pixel displacement is 3 pixels and the associated integration time in his experiments is $10\,\mu s$. Their subsequent post-processing method of merging images taken at different integration times is conducted successfully with this pixel displacement. Thus, for the course of the present work a pixel displacement of 1-5 pixels is agreed upon to sufficiently restrict the future measurement conditions at the rotor of the LSTR because a comparable postprocessing method is planned to be implemented in succession to this work. Besides, a resolution comparable to the previous measurements on the stator endwall can be realised in those on the rotor endwall as well.

Preliminary measurements with integration times of $5\,\mu s$, $50\,\mu s$, $100\,\mu s$ and $900\,\mu s$ are done at various wall temperatures on the heating plate. Air flows are not present during these measurements in order to exclude the temperature-dependent transmission behaviour in the optical path discussed by Ochs [14] and implemented in the data processing structure by Steinhausen [12]. This way the set temperature, controlled underneath the auxiliary wall of epoxy resin, is supposed to be representative of the homogeneous surface temperature as only natural convection drives the heat flux into the resting air inside the flow channel.

An integration time of $900\,\mu s$ was used in the former works by Wiemer [13] and Fox [33]. It is further recommended in the camera software in connection with the sensitivity of the camera detector for an observed temperature range of $-5\,°C$ to $85\,°C$. It is therefore referred to as a reference by which to assess the influence of lowering the integration time in the following. Figure 4.1 shows the camera signals as a function of integration times for a set temperature of $60\,°C$ beneath the auxiliary wall. The camera signals are averaged within a uniformly heated area on the heating plate. It can be seen that the camera signals increase linearly with the integration time when the observed scene remains unchanged. This linear behaviour is also confirmed in the work of Gazzini [40]. Results for the reference at $900\,\mu s$ are not displayed but are in agreement with the linear fit through the three lower integration times.

An integration time of $12\,\mu s$ is correspondent to a pixel displacement of 3 pixels according to the approach in equation 4.1. This displacement is considered an acceptable value in order to produce sharp images. Following arrows 1 and 2 in figure 4.1 the associated camera signal for this integration time would be approximately 700 digital counts (DC). The transmission coefficient of the glass used as the optical access at the LSTR is about 25 % higher than the transmission coefficient at the flow channel (compare section 3.2.4), reaching 95 % in the respective wavelength area. Consequently, camera signals are

Linear regression of camera signal against integration time at 60 °C
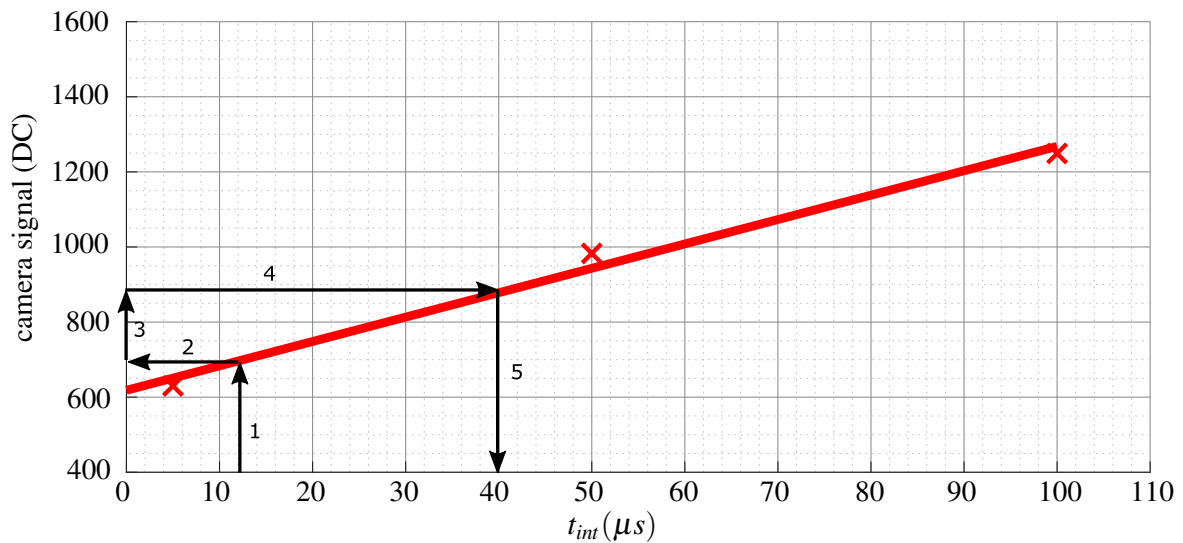
**Figure 4.1:** Determination of integration time for camera signals equivalent to the level at the LSTR

expected to rise by 25 % compared to the values obtained with the glass installed at the flow channel. Arrows 3 and 4 in figure 4.1 indicate these expected higher values. As a conclusion an integration time of 12 $\mu$s at the LSTR can be imitated with corresponding camera signals in the present measurements with an integration time of 40 $\mu$s (compare arrow 5 in figure 4.1). Due to the fact that the set temperatures in the heating plate in future applications at the LSTR can be higher than in the present work an integration time of 50 $\mu$s is eventually chosen as the one most comparable to measurements at the rotor of the LSTR. An intermediate integration time of 100 $\mu$s is furthermore used to depict potential trends when lowering the integration time from 900 $\mu$s. 1000 frames are recorded at each integration time and at each set temperature level which are defined in section 4.2. They are subsequently averaged and processed with the aforementioned evaluation routine *HTCVal1.7*.

Taking images from an identical scene at multiple integration times is referred to as *Multi-IT* or *Superframing*. The infrared camera *FLIR X6540sc* supports this procedure. It can be used to merge recordings of a scene which features high temperature difference. Short integration times do not evoke saturation in regions where hot surface are observed while images taken with a long integration time capture parts of the scene with comparably low surface temperatures. However, the measurements at hand require images of the same scene taken at different integration times, but with the shortest possible time difference which is another advantage of *Multi-IT*. Images at different integration times are taken consecutively which causes a drop in the total frame rate between two images with the same integration time [11, p. 267]. In the present application a frame rate of 100 Hz is adjusted in the camera software *FLIR ResearchIR* resulting in a total frame rate of 33.3 Hz for each of the three integration times. The applied integration times can be found in the camera software in field 1 highlighted in figure 4.2. All recordings taken at a specific integration time are exported to *.tif* files with a depth of 16 bit containing the respective camera signals. This is done by manually selecting the desired preset integration times (figure 4.2, no. 2) and choosing the camera signals as digital counts to be displayed (figure 4.2, no. 3).
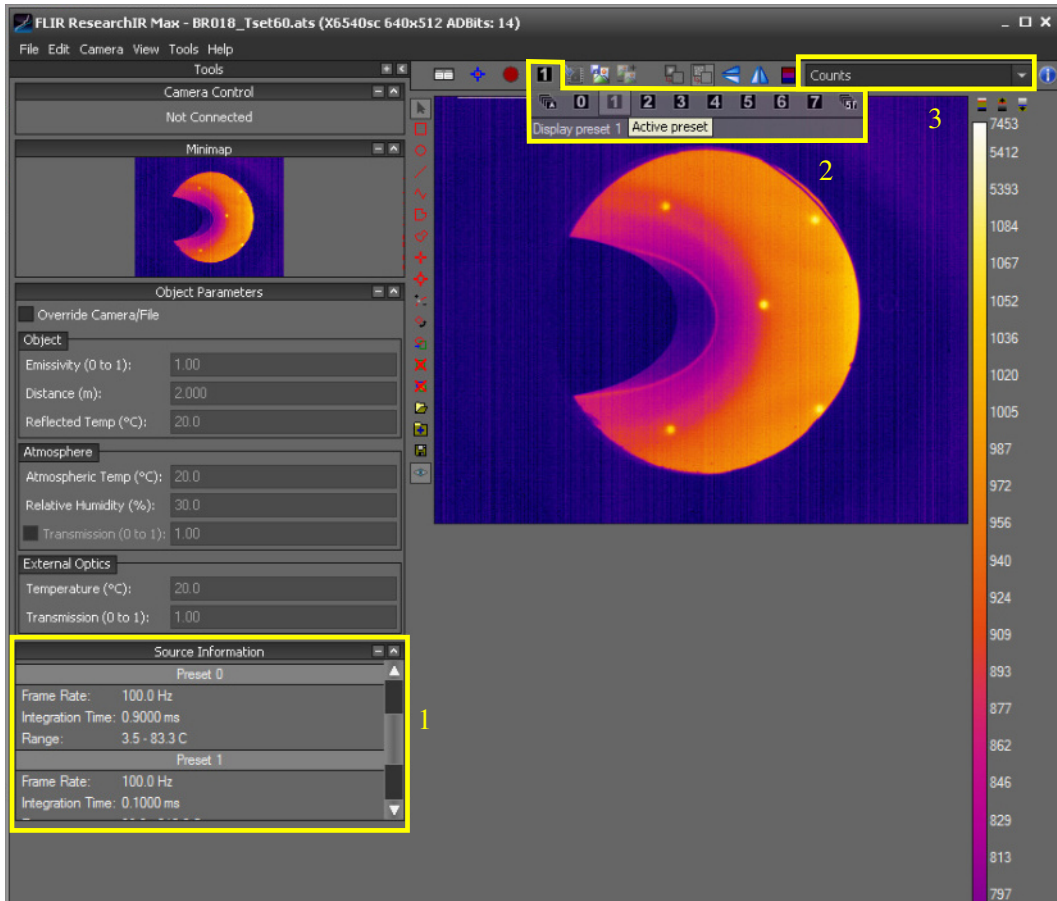
**Figure 4.2:** Camera software *FLIR ResearchIR* with preset integration times highlighted

## 4.2 Operating points

The operating points of the flow channel for the measurements are defined with regard to the operating conditions at the LSTR. Table 3.1 summarises the operating points. The primary mass flow is oriented to the Reynolds similarity of the airfoil used in these experiments and is controlled at $0.123 \frac{kg}{s}$. An average primary flow velocity of $16.2 \frac{m}{s}$ is regulated, resulting in a Reynolds number of $Re_D = 31300$ with reference to the leading edge diameter.[1]

Variations of the blowing rate are chosen according to the cavity mass flow of 2 % at the design point of the LSTR. The pairs of corresponding blowing rates and mass flow ratios at the LSTR are given in table 4.1. Blowing rates are calculated by multiplying the known mass flow ratios with the inverse ratio of the respective cross-sections $A_{prim}$ for the primary and $A_{sec}$ for the secondary flow at their entrance to the measurement section as expressed in equation 4.2.

$$BR = \frac{\dot{m}_{sec}}{\dot{m}_{prim}} \frac{A_{prim}}{A_{sec}} \tag{4.2}$$

The reference case without secondary air injection, referred to as $BR = 0$, is examined while the slot is masked with adhesive tape. It is later used to point out the general influence of the secondary air injection on the adiabatic characteristics.

---

[1] This velocity is $20 - 25\,\%$ lower than the velocity proposed in Fox's work [33] to match the Reynolds similarity at the operating point of the LSTR. After the heat transfer measurements at hand were performed the results from PIV recordings suggested a bias in the mass flow measured by the standard orifice. The corrected average mass flow of $0.123 \frac{kg}{s}$ is therefore calculated with the velocity profile obtained from the PIV recordings in a case without secondary air injection $8\,\text{mm}$ upstream of the measurement section.

The non-equally spaced steps of mass flow ratios between 0 % and 2.71 % are owed to the fact that in advance to the final decision on the operating points, measurements have been performed with a blowing rate of 0.24. In total, the choice of blowing rates spans correspondent mass flow ratios both below and above the design point of 2 % at the LSTR. The density ratio of secondary flow density to primary flow density ranges around 0.9 and is smaller than 1 for all operating points examined given the elevated secondary air temperature.

Primary flow total temperatures varied in the range of 14.5 °C to 17.2 °C between the measurements at different blowing rates due to changes in the ambient temperature from day to day. The secondary flow total temperature is held at 55 °C for all measurements to provide a temperature difference between the primary flow and the secondary flow. 10 equally distanced heating plate set temperatures between 30 °C and 75 °C define the temperature levels at which thermographic measurements on the coated surface of the heating plate are conducted. The highest temperature level is oriented to the glass transition temperature of the epoxy resin the auxiliary wall is made of.[2] Although Steinhausen [12] suggests measurements at 14 temperature levels as inputs for the regression method a more important source of errors is identified in the choice of the lowest temperature level.

As the primary flow cannot be tempered in the experimental setup and the secondary flow temperature is well above the ambient temperature the heating plate experiences heating by the secondary flow. This leads to a minimum temperature of approximately 30 °C at the reference thermocouples in case the heating plate is not powered. This issue will be addressed in section 4.4.2 again.

**Table 4.1:** Operating points for the heat transfer measurements

| Mass flow rate at the LSTR $MFR_{LSTR}$ | Blowing rate $BR$ | Secondary air temperature $T_{sec}$ | Heating plate temperature levels | Integration time of the camera $t_{int}$ |
|---|---|---|---|---|
| 0 % | 0 | 55 °C | $30 - 75$ °C, step 5 °C | $900\,\mu s, 100\,\mu s, 50\,\mu s$ |
| 0.76 % | 0.11 | 55 °C | $30 - 75$ °C, step 5 °C | $900\,\mu s, 100\,\mu s, 50\,\mu s$ |
| 1.73 % | 0.24 | 55 °C | $30 - 75$ °C, step 5 °C | $900\,\mu s, 100\,\mu s, 50\,\mu s$ |
| 2.12 % | 0.30 | 55 °C | $30 - 75$ °C, step 5 °C | $900\,\mu s, 100\,\mu s, 50\,\mu s$ |
| 2.71 % | 0.38 | 55 °C | $30 - 75$ °C, step 5 °C | $900\,\mu s, 100\,\mu s, 50\,\mu s$ |

The secondary air temperature from table 4.1 represents the total temperature in the plenum. In contrast, the primary flow exhibits a much higher flow velocity so that temperature measurements rather reflect the recovery temperature than the total temperature. Equation 4.4 shows, however, that at the operating point the recovery temperature $T_{prim,rec}$ does not differ from the total temperature $T_{prim,tot}$ more than 0.02 °C which is considered negligible. For the calculation of the Mach number the static primary flow temperature is derived from an exemplary total temperature of 15 °C. The specific gas constant $\hat{R}$ equals $287.1\,\frac{J}{kgK}$ and the isentropic exponent $\gamma$ is 1.4. The recovery factor $\hat{f}$ is assumed equal to 0.85 for a laminar flow around the thermocouple with a diameter of 1 mm [41]. All adiabatic results of the present work are therefore referred to the measured air temperatures as total temperatures without further correction.

$$T_{prim,stat} = T_{prim,tot} - \frac{u_{prim}^2}{2c_p} = 288.15\,\text{K} - \frac{16.2\,\frac{m}{s}}{2 \cdot 1006\,\frac{J}{kgK}} = 288.14\,\text{K} \tag{4.3}$$

$$T_{prim,tot} - T_{prim,rec} = T_{prim,tot}\left(1 - \frac{1 + \hat{f}\frac{\gamma-1}{2}Ma^2}{1 + \frac{\gamma-1}{2}Ma^2}\right) = 0.02\,°\text{C} \tag{4.4}$$

---

[2]    Compare with the data sheet of epoxy resin *Polytec EP 601* in the appendix.

## 4.3 Variation of the integration time

In the following section results for the adiabatic heat transfer coefficient $HTC$ and for the adiabatic cooling effectiveness $\eta_{ad}$ are presented for three different integration times. Adiabatic heat transfer coefficients are mainly presented in terms of Stanton numbers $St$ according to equation 2.7. They are referred to the primary flow velocity $u_{prim} = 16.2\,\frac{m}{s}$, the density and heat capacity at representative conditions at the inlet of the flow channel being $T = 288.15\,K$ and $p = 1000\,mbar$. To clarify the visualization of the data in the physical coordinate system of the heating plate in front of the leading edge a simplified geometry of the measurement section is presented in figure 4.3. The data plotted on the heating plate surface show a distribution of adiabatic heat transfer coefficients which will be elucidated in the following sections.
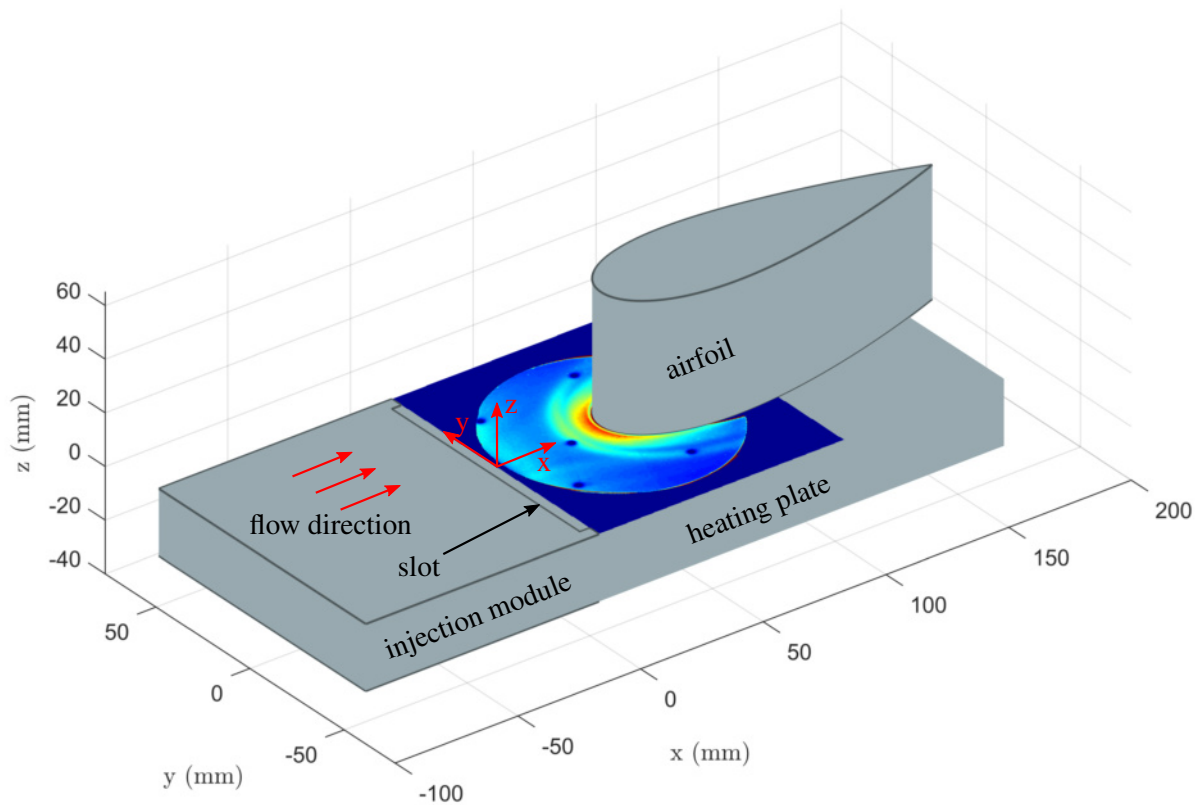


**Figure 4.3:** Overview of the measurement section and and exemplary distribution of heat transfer coefficients in the physical coordinate system of the heating plate

### 4.3.1 Results for the heat transfer coefficient

Figures 4.4(a) through 4.4(c) visualise the adiabatic heat transfer coefficient in the physical coordinate system of the heating plate introduced in section 3.2.1. An intermediate blowing rate of $BR = 0.24$ is chosen for the visualisation because it features characteristic patterns in the heat transfer distribution also found in the reference case. The coordinates are made dimensionless with the slot width $S = 4\,mm$. Accordingly, the flow direction points towards positive running lengths $X/S$.
The field of view of the camera is originally larger, but for reasons of practicability all results are confined to the displayed area. Results at running lengths smaller than $X/S = 1$ are not visible in the field of view, but are not considered representative due to the thin aluminium fillet at the front edge of the heating plate. Two lines at $X/S = 0$ and $X/S = -1$ indicate the location of the slot upstream of the heating plate. The contour of the airfoil is cut out in the upper part of the plots. The dark spot at

$X/S = 7$ gives the position of the reference thermocouple 5. Results at the locations of the reference thermocouples are not representative because these thermocouples penetrate the auxiliary wall.
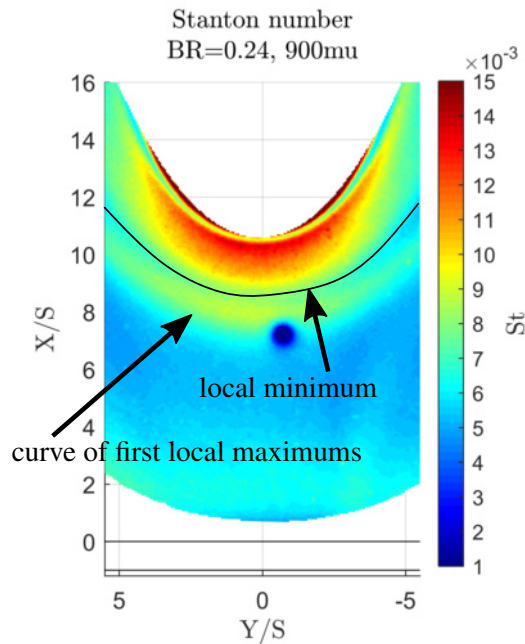


(a) Stanton number at $BR = 0.24$ and $t_{int} = 900\mu s$
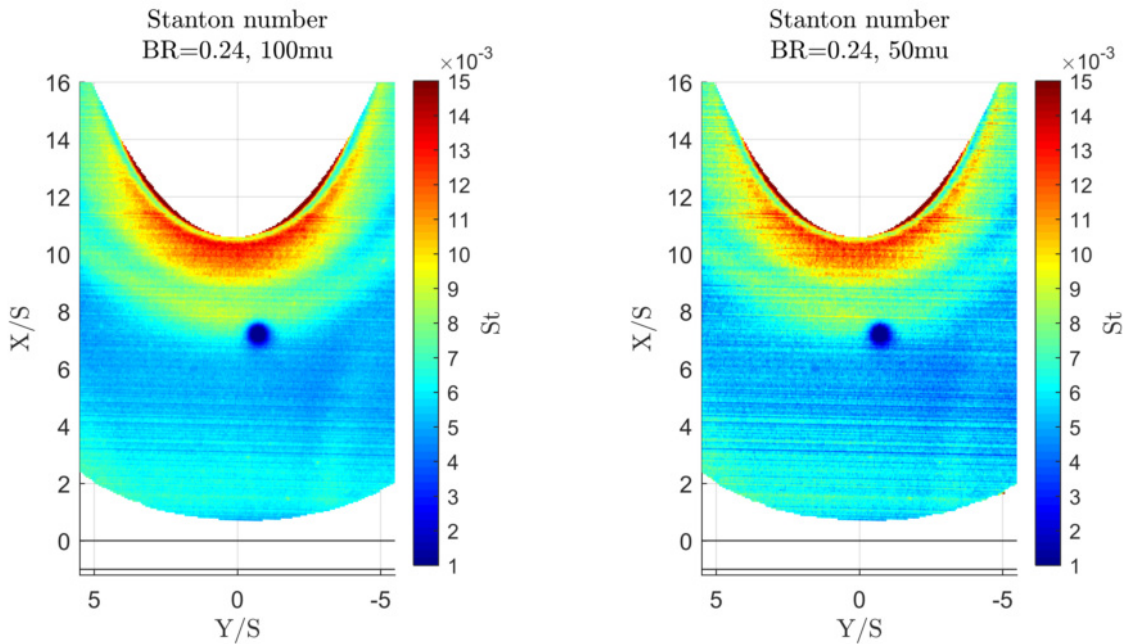


(b) Stanton number at $BR = 0.24$ and $t_{int} = 100\mu s$ (c) Stanton number at $BR = 0.24$ and $t_{int} = 50\mu s$

**Figure 4.4:** Adiabatic Stanton numbers for a blowing rate of $0.24$ at three different integration times

Several regions of distinct heat transfer characteristics can be identified in the data whose causes will be elucidated in section 5:

- Up to a running length of $X/S = 4$ the Stanton numbers decrease before reaching a nearly constant level of $5 - 5.5$.

- An increase of Stanton numbers is observable from $X/S = 6.5$ on, leading to a local maximum. The maximums are located along a curvature around the airfoil.

- After a slight decrease to a local minimum the Stanton numbers rise again continuously until the leading edge is reached. These areas of high heat transfer in front of the leading edge are in accordance with the findings by Friedrichs [20]. The characteristic structures of low and high heat transfer are attributed to the interaction of the horseshoe vortex with the primary flow. Its presence near the endwall affects the local flow velocities and convective heat transfer underneath while its rotation deflects flow from above the vortex onto the endwall, strongly increasing heat transfer coefficients in front of the leading edge.

- The curvature of the first local maximums of the Stanton numbers along $X/S$ is broader than the curvature of the airfoil contour. This is particularly visible in the region between the first band of high heat transfer and the second region of high heat transfer farther downstream at lateral positions $Y/S \approx \pm 5$. At these positions the intermediate region with locally decreasing heat transfer coefficients widens before giving way to the second region of augmented heat transfer.

Regarding the data from figure 4.4(a) through 4.4(c) for reduced integration times, the following changes can be stated:

- Fixed pattern noise is recognisable as discrete lines in the images. These are directed along the coordinate $Y/S$ which corresponds mainly to the short edge of the focal plane array (FPA) of the infrared camera (512 pixels).

- Single lines in the fixed pattern noise lead to high-frequency changes in heat transfer coefficients which are not expected in a physical sense. This effect seems to amplify from $100\,\mu s$ to $50\,\mu s$.

- The contours of certain regions like the aforementioned assumed separation line are smeared along the $Y/S$ coordinate.

In order to improve comparability between the results for different integration times data are plotted along different lateral locations $Y/S$. In advance, they are averaged within a band of $1\,mm$, reaching $0.5\,mm$ to either side of the indicated position. The location $Y/S = 0$ is subsequently referred to as the stagnation line or the symmetry line, implying a symmetrical flow field with the stagnation point situated at this y-coordinate. Figure 4.5 combines the results from figures 4.4(a) to 4.4(c) in one-dimensional plots of averaged Stanton numbers as a function of the running length $X/S$. Data are plotted along the symmetry line starting at $X/S = 1$ up to the respective location of the airfoil contour.
The spatial oscillations caused by the fixed pattern noise increase in amplitude for decreasing integration times. In the reference data for $900\,\mu s$ the oscillations do not have a significant influence on the course of the data values. Their progress along $X/S$ is steady and minor oscillations in the data are mainly accounted for by the interpolation scheme when the data are projected into the physical coordinate system.
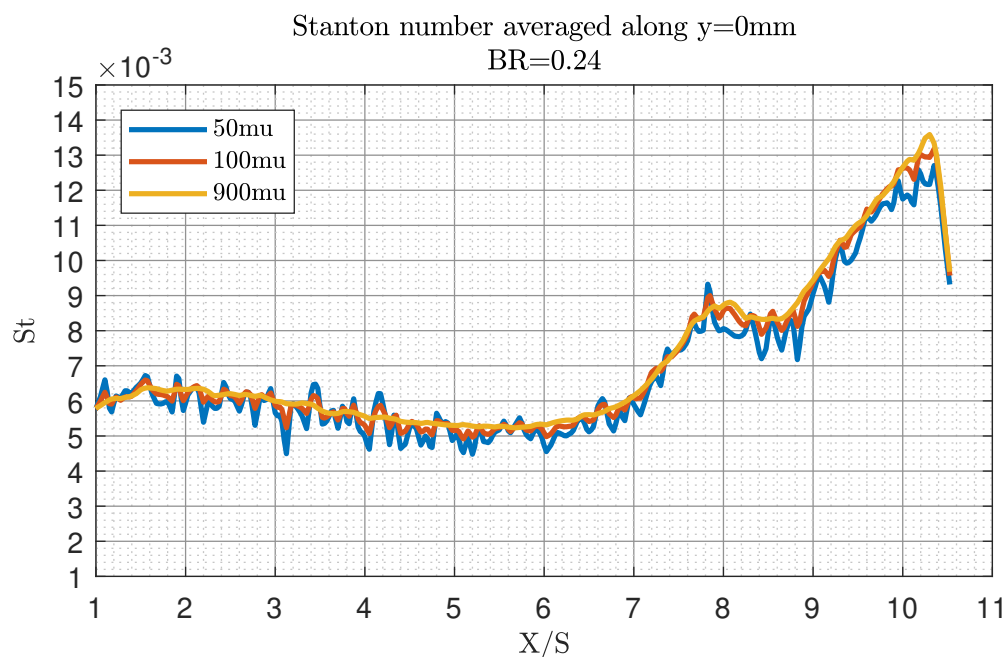


**Figure 4.5:** Course of the Stanton number along $X/S$ at $Y/S = 0$ for $BR = 0.24$ at three integration times

The local peak of the heat transfer coefficients at $X/S \approx 8$ is visible for all three integration times just as the steady increase up to the leading edge from this point on. In total Stanton numbers for an integration time of $50\,\mu s$ remain slightly lower on average than the reference with $900\,\mu s$.

Calibration coefficients are determined at the specific locations of the reference thermocouples and are subsequently distributed across the FPA. Due to this fact pixelwise deviations in the pixel response behaviour cannot be corrected with the calibration method. A one-point non-uniformity correction (*NUC*) revises pixelwise differences in the offset of the pixel response to the incident radiation. It is easily applied to the images recorded in the present work by taking 1000 additional images when the cap covers the optics of the camera while it is running at operating temperature. They are subsequently averaged and the pixelwise amplitude of the oscillations in the average image are subtracted from the measurement recordings. Although a two-point non-uniformity would additionally straighten out the linearity of the pixel response, the one-point NUC is able to reduce the fixed-pattern noise at low integration times.

Figure 4.6 exemplifies the enhancement of the *Signal-to-noise ratio SNR* in the raw camera data. The *SNR* in this case is defined as the ratio of the average signal $U_{mean}$ to the standard deviation of the noise $\sigma_U$. This approach is commonly used to express the signal-to-noise ratio in digital imaging [42, 5:49].

$$SNR = \frac{U_{mean}}{\sigma_U} \tag{4.5}$$

The effect of correcting the fixed pattern noise in the recordings at $50\,\mu s$ integration time can be seen in figure 4.6. The SNR of uncorrected and corrected camera raw signals is compared along the running length $X/S$. Values from corrected images are presented with dotted lines. An increase in the SNR for the corrected images is especially detectable in regions upstream of the separation line mentioned above. In this region wall temperatures and camera signals are generally higher due to the presence of the warmer secondary flow. Random noise influences remain dominant at low signal levels and the non-uniformity correction does not improve the SNR to the same extent. This can be recognised in the region for running lengths $X/S$ greater than 6 where the separation line is expected to form and lower wall temperatures are dominant due to the detached warm secondary flow. The aerodynamic interpretation of these phenomena is continued in sections 4.3.2 and 5.
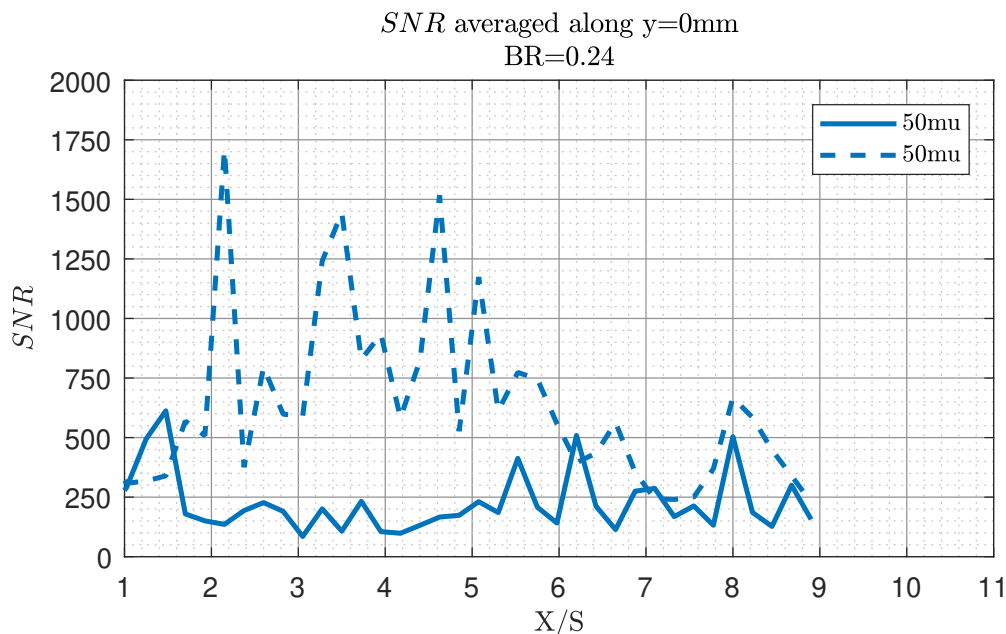


**Figure 4.6:** Augmentation of SNR achieved with one-point NUC in the recordings with $50\,\mu s$ integration time

Figures 4.7(a) and 4.7(b) show results of Stanton numbers for the two lower integration times and at the same blowing rate as displayed before with a one-point NUC applied to the raw camera images. It is obvious that the fixed pattern noise directed along columns of the FPA can be diminished with this approach.
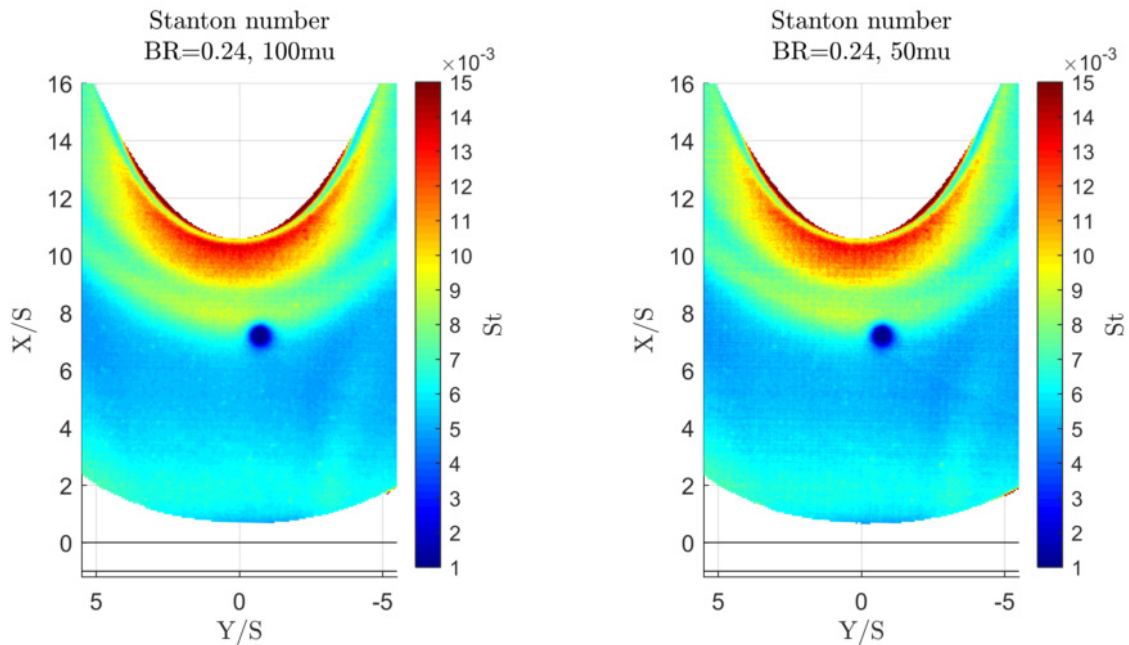


(a) Results from 4.4(b), corrected with NUC  (b) Results from 4.4(c), corrected with NUC

**Figure 4.7:** Adiabatic heat transfer coefficient HTC for a blowing rate of $0.24$ at the two lower integration times with a one-point NUC applied to the raw images
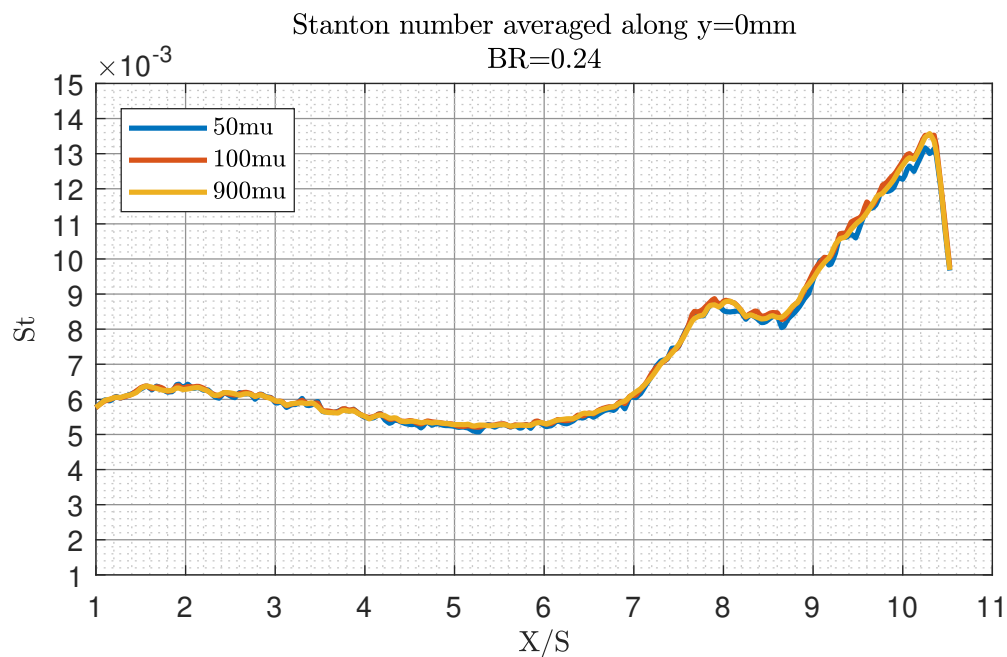


**Figure 4.8:** Course of the Stanton number along $X/S$ at $Y/S = 0$ for $BR = 0.24$ at three integration times with NUC applied to the camera raw images

Both the smearing of contours along $Y/S$ and the high-frequency changes in heat transfer coefficients are reduced and the images seem smoother. This is confirmed by the course of the Stanton numbers from the corrected data plotted along $X/S$ in figure 4.8. Compared to the results given in figure 4.5 spatial oscillations can hardly be detected at the two lower integration times. On top of that the total values of Stanton numbers for $50\,\mu s$ seem to approximate the reference data better and slightly lower values are merely visible for running lengths greater than 8.

## Effect of reduced integration time on the uncertainty contribution to $HTC$

Effects on the uncertainty in the calculation of adiabatic heat transfer coefficients imposed by reduced integration times are shown in figures 4.9 and 4.10. The uncertainty in $HTC$ stemming from a reduction of the integration time is described by the proportion of the uncertainty of the surface temperatures. These temperatures are directly linked to the camera signals through the calibration procedure. The uncertainty in the temperature readings of the thermocouples located in the heating plate cannot be determined accurately within the scope of this work. Hence, all uncertainties associated with temperature readings are set to a very low level of $0.8\,°C$ in the evaluation routine $HTCVal1.7$ which corresponds to the uncertainty of a PT100 reference thermometer available at the institute. This way, the exclusive influence of different integration times and different camera signal intensities on the results for the adiabatic characteristics can be isolated.
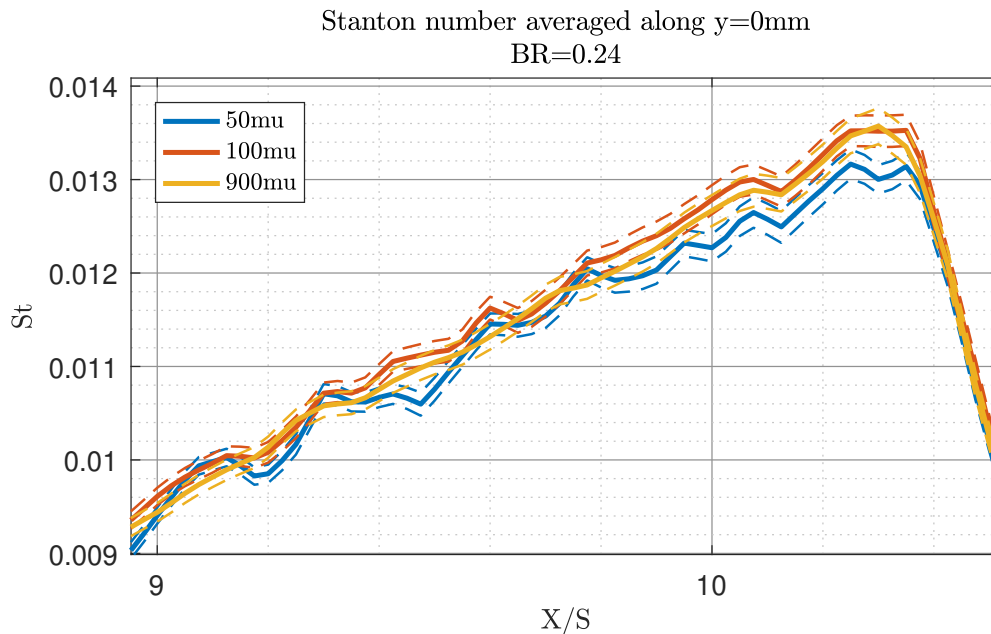


**Figure 4.9:** Stanton numbers averaged at the stagnation line $Y/S = 0$ with error bars from the contribution of surface temperatures at different integration times

As the total uncertainty of the adiabatic characteristics is dominated by the high uncertainty in the material properties and the geometry of the auxiliary wall and the coating (compare table 3.3), nominal uncertainties of $HTC$ and $\eta_{ad}$ are not presented in this context. An uncertainty analysis routine implemented by Steinhausen [12] and by Wiemer [13] is used to extract the relative contributions from various input parameters by means of successive perturbation of the input parameters.

In figure 4.9 the courses of Stanton numbers from above are shown in an enlarged section downstream of $X/S = 9$ with dotted lines indicating error bars. These error bars represent the proportion of the uncertainty of Stanton numbers that is caused by the uncertainty of surface temperatures. Results obtained at $50\,\mu s$ are in accordance with the reference data taken at $900\,\mu s$ mainly within the range of two times the measurement uncertainty stemming from the surface temperature alone. The displayed section is representative of the highest overall deviations between the results at $50\,\mu s$ and at $900\,\mu s$ as they are found in regions with predominantly low surface temperatures and high values of heat transfer coefficients.

Figure 4.10 shows the relative contribution of the surface temperature to the uncertainty in $HTC$ for different integration times. The fractional contribution $\frac{\delta T_w}{\delta HTC}$ is normalized with the same fraction obtained with the reference at $900\,\mu s$. As the aforementioned uncertainties from table 3.3 do not suggest to compare nominal errors in the presented results, the relative contributions normalized with the reference at $900\,\mu s$ serve to extrapolate the influence of reduced integration times to future

applications at the LSTR. It is obvious that the reduction of the integration time to $50\,\mu s$ only has minor influences on the uncertainty in $HTC$. On average the proportion of the uncertainty in $HTC$ resulting from the surface temperature readings and consequently from the camera signal increases by $5-10\,\%$ compared to the reference. Single peaks which reach up to nearly $30\,\%$ are observed in the vicinity of the local maxima in the course of the $HTC$. The development of this error contribution also implies that recordings taken at $100\,\mu s$ transmit less of the oscillations caused by the fixed pattern noise than recordings taken at $50\,\mu s$.
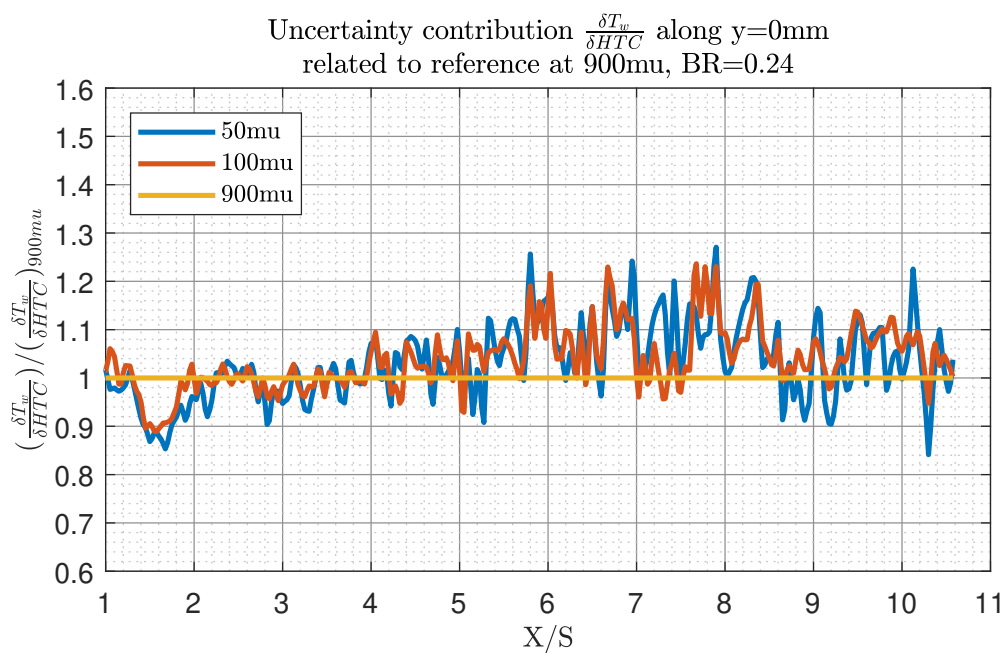


**Figure 4.10:** Development of the fractional contribution of surface temperatures to the uncertainty in $HTC$ as a function of integration times

The following figures 4.11(b) and 4.11(a) show the distribution of this relative contribution to the uncertainty in $HTC$ for the blowing rates $BR = 0.11$ and $BR = 0.24$. Allocations at the lower blowing rate suggest an increase of the relative contribution especially in regions with high gradients of the heat transfer coefficient and therefore high deviations of surface temperatures in a confined area. Peak values reach up to an exaltation of $60\,\%$ upstream of the band of local maximums in heat transfer. However, the values obtained at $BR = 0.24$ are more homogeneous across the whole observed area in front of the airfoil.

Wiemer stated that the surface temperatures contribute to the total uncertainty in $HTC$ by about as much as $20\,\%$ in the adiabatic results for the particular setup [13]. Taking the deviations in the data from figure 4.10 into account an increase up to a relative contribution of $26\,\%$ can be expected in an identical setup with an integration time being reduced to $50\,\mu s$.
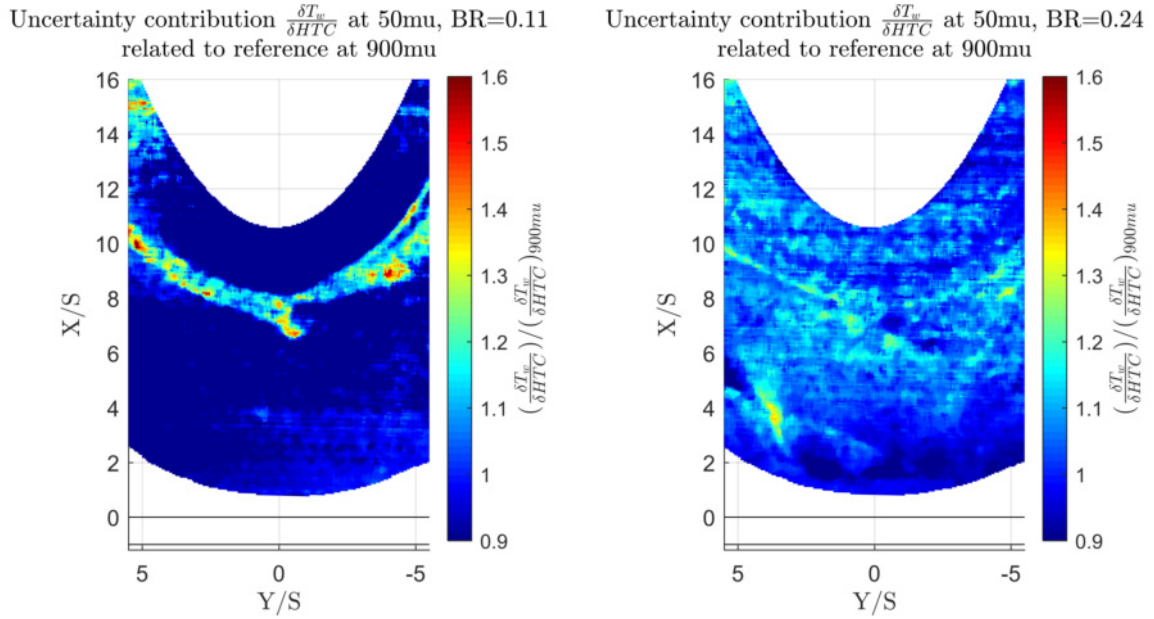
(a) Distribution of uncertainty proportion from surface temperatures at $BR = 0.24$

(b) Distribution of uncertainty proportion from surface temperatures at $BR = 0.11$

**Figure 4.11:** Relative contribution of the surface temperatures to the uncertainty of $HTC$ at $50\,\mu s$ related to $900\,\mu s$ shown for the two blowing rates $BR = 0.11$ and $BR = 0.24$

## 4.3.2 Results for the cooling effectiveness

In extension to the results of the heat transfer coefficients the findings for the adiabatic cooling effectiveness are outlined in the following. Surface data without a previous non-uniformity correction applied to the raw camera images feature the same disadvantageous noise patterns which are described in section 4.3.1. Impacts of lowered integration times on the visualized data are basically the same as explained for the surface data of heat transfer coefficients. Due to this fact results from corrected raw images only are shown in the following. The figures 4.23(b) through 4.23(b) depict results of the adiabatic effectiveness $\eta_{ad}$ projected into the physical coordinate system of the heating plate. Like the results in section 4.3.1 they belong to measurements at a blowing rate of $BR = 0.24$. Distinct regions of adiabatic quantities can be spotted in the images:

- Cooling effectiveness levels decline monotonically along the running length $X/S$ approximating zero in front of the airfoil leading edge.

- A distinct drop can be seen at $X/S \approx 9$ where cooling effectiveness levels seem to decrease with a higher gradient along $X/S$.

- Unlike the findings from section 4.3.1 the cooling effectiveness distribution does not exhibit an intermediate region between two maximums in front of the leading edge.

In the reference case without secondary air injection an interpretation of cooling effectiveness cannot be given. The adiabatic wall temperature in this case is expected to equal the primary flow temperature as no cooling flow is present. Figure 4.13 displays the course of the adiabatic wall temperature along $Y/S = 0$ in the reference case for three integration times. The primary flow temperature in this measurement is determined as $15.5\,^{\circ}$C upstream of the measurement section.

Adiabatic wall temperatures are within a range of $\pm 1\,^{\circ}$C of the measured primary flow temperature for all integration times. Deviations from the reference integration time grow with reduced integration times, but the greatest discrepancy is found between $X/S = 5$ and $X/S = 6$ where data obtained at $50\,\mu s$ differ as much as $1.5\,^{\circ}$C from the reference data. This value is only $0.5\,^{\circ}$C higher than the maximum deviation in the reference data from the primary flow temperature itself. The results
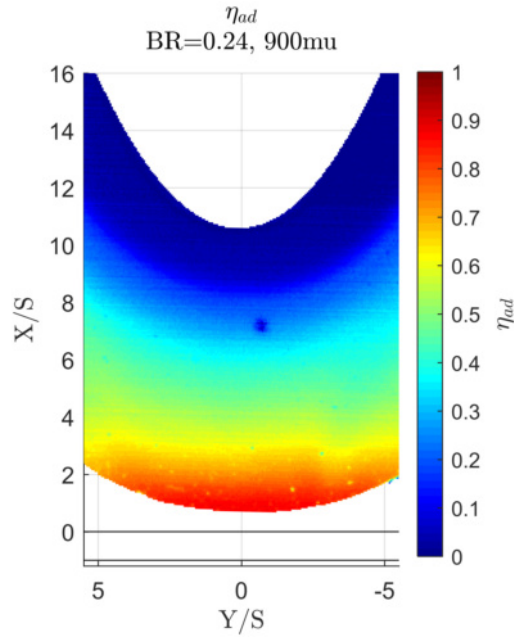
(a) $\eta_{ad}$ at $BR = 0.24$ and $t_{int} = 900\mu s$
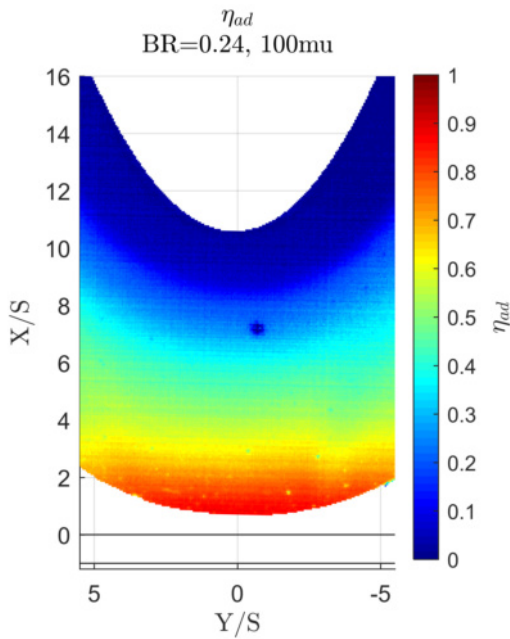


(b) $\eta_{ad}$ at $BR = 0.24$ and $t_{int} = 100\mu s$
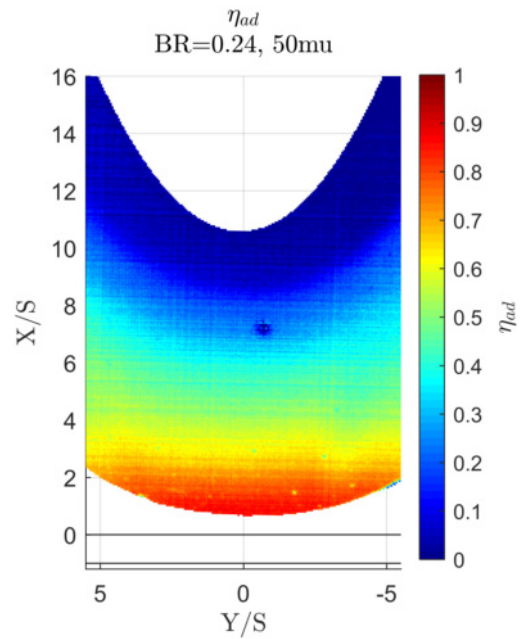


(c) $\eta_{ad}$ at $BR = 0.24$ and $t_{int} = 50\mu s$

**Figure 4.12:** Adiabatic cooling effectiveness $\eta_{ad}$ for a blowing rate of $0.24$ at three different integration times

prove that the applied method to calculate the adiabatic quantities works well and that even at low primary flow temperatures data from reduced integration times deliver final adiabatic parameters with an acceptable uncertainty.
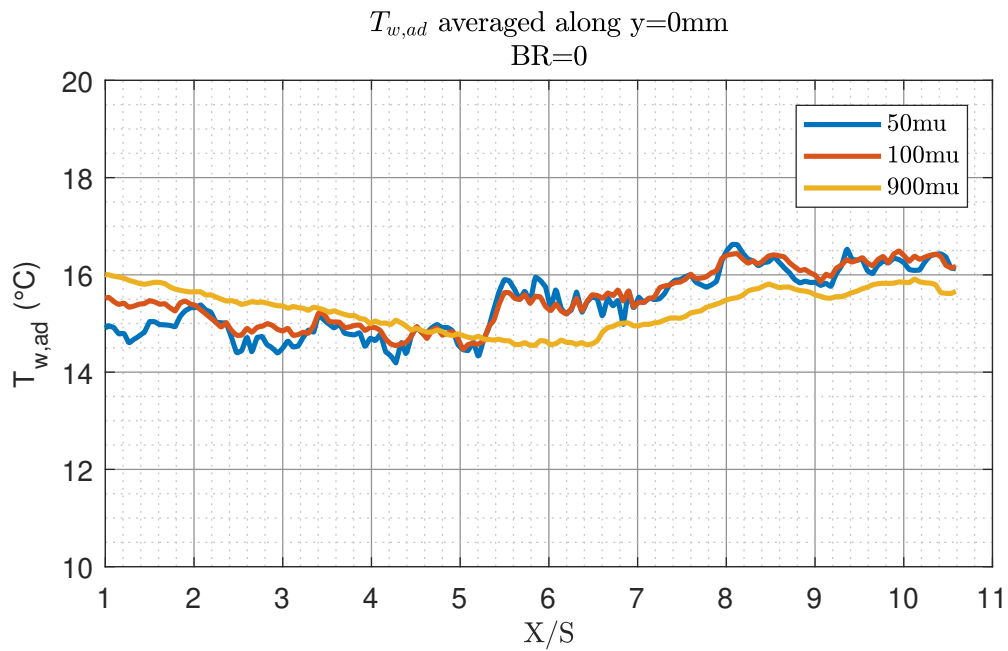
**Figure 4.13:** Adiabatic wall temperature along the stagnation line in the reference case

## Effects of a medianfilter

The courses of the averaged cooling effectiveness at the position $Y/S = 0$ for the varied integration times are given in figure 4.14.
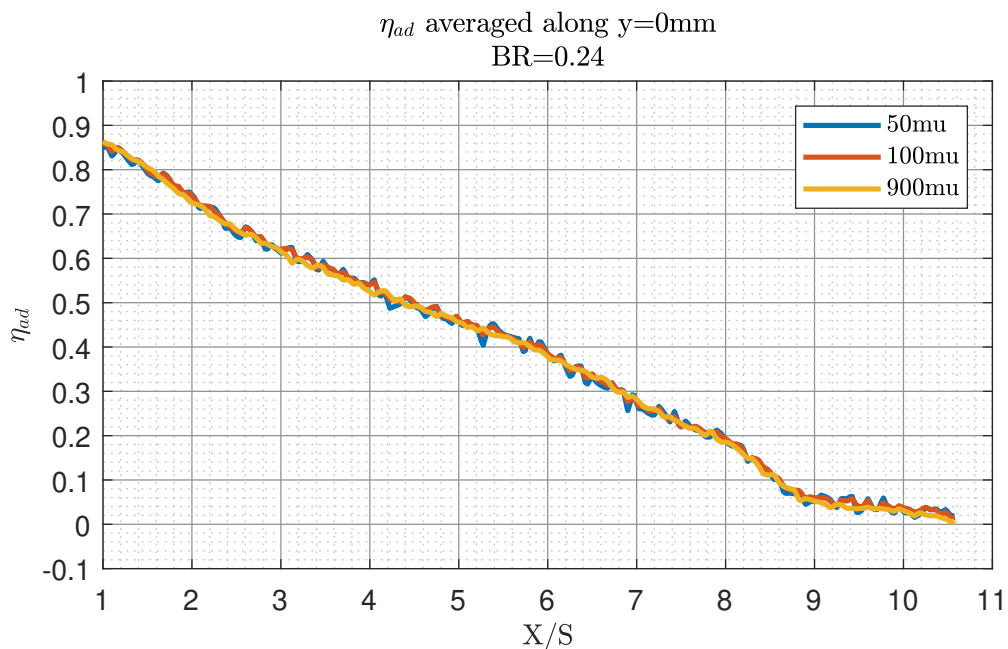


**Figure 4.14:** $\eta_{ad}$ at $BR = 0.24$

It can be seen that just as the results for the Stanton numbers presented before the courses of the cooling effectiveness exhibit minor spatial oscillations which are not explicable with physical flow phenomena. From running lengths of $X/S = 4$ to $X/S = 7$ some amplitudes of these oscillations reach up to 4 or 5 % in total value. A practical approach to remove these oscillations is found in applying low-pass-filters to the final results. Figure 4.15 shows the same results from figure 4.14
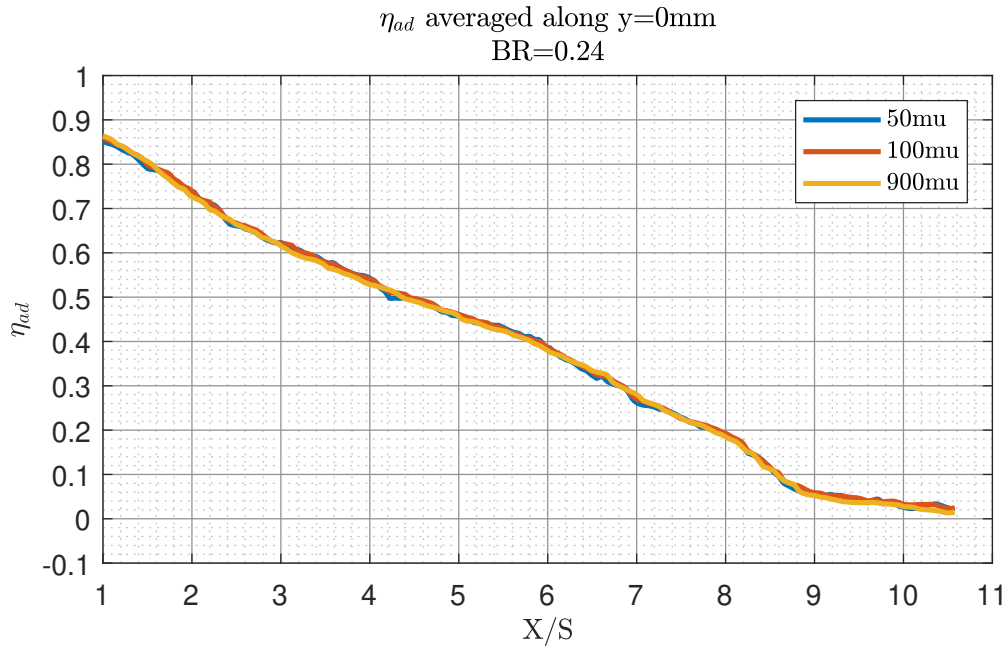
**Figure 4.15:** $\eta_{ad}$ at $BR = 0.24$ with 5x5 medianfilter

altered by a medianfilter with a size of 5x5 pixels. This way, the results obtained from the reference data at $900\,\mu s$ can be reconstructed more precisely, reducing the influence of integration times on the final results more effectively.

### Effect of reduced integration time on the uncertainty contribution to $\eta_{ad}$

Figure 4.16 exemplifies the effect of the reduction of integration times on the relative contribution to the uncertainty in $\eta_{ad}$ like it is displayed for the heat transfer coefficient in figure 4.10. An increase in the relative contribution to uncertainties in $\eta_{ad}$ at lower integration times can be detected for running lengths greater than $X/S = 6$.

This region corresponds to the section of increased relative contributions to the uncertainty in $HTC$ shown in figure 4.10. The amplification of the relative contribution to the uncertainty in $\eta_{ad}$ for lower integration times is generally higher than observed for the corresponding uncertainty in $HTC$ (compare figure 4.10). On average, an increase of $20\,\%$ is recognizable from the course of the data for $50\,\mu s$ while single peaks lead to an augmentation of almost $40\,\%$.

Apparently, the calculation of the adiabatic characteristics has a higher sensitivity to local wall temperatures (and to camera raw signals accordingly) in this region of predominantly low wall temperatures than in regions with higher wall temperatures. This can be explained with the location of the nodes for the regression method used for this calculation which is introduced in section 2.1.1.

As already stated by Steinhausen [12] the choice of set temperatures in conjunction with the concept of hot secondary flow might improve the sensitivity of the regression method compared to the experimental setup used by Steinhausen. Figures 4.17(a) and 4.17(b) show the regression lines at two different locations on the heating plate calculated from data acquired at $50\,\mu s$. On the left side the regression of heat transfer coefficients $\alpha$ over the dimensionless wall temperature $\Theta$ is shown and the right part displays the regression expressed as a fit of the heat flux $\dot{q}$ over the surface temperature $T_w$. Markers give the respective data pairs at different set temperatures of the heating plate. In figure 4.17(a) the $HTC$ is determined by the intersection of the linear regression line with the ordinate whereas the intersection point with the abscissa defines $\frac{1}{\eta_{ad}}$ (compare section 2.1.1). Accordingly, in figure 4.17(b) the intersection with the abscissa gives the adiabatic wall temperature. The position $X/S = 3.3$, $Y/S = 0.425$ represents a location on the heating plate with high cooling effectiveness levels while the position $X/S = 9.5$, $Y/S = 0.425$ is representative of region with low cooling effectiveness levels. Shorter running lengths $X/S$ feature higher cooling effectiveness levels than longer running lengths because surfaces temperatures approximate the elevated secondary flow temperature in the vicinity of the secondary air injection. It is advantageous to locate the nodes as pairs of the dimensionless wall temperature $\Theta$ and the temperature-dependent heat transfer coefficient $\alpha$ in such manner that the distance from the nearest node to the abscissa and to the ordinate is as small as possible. Placing nodes on both sides
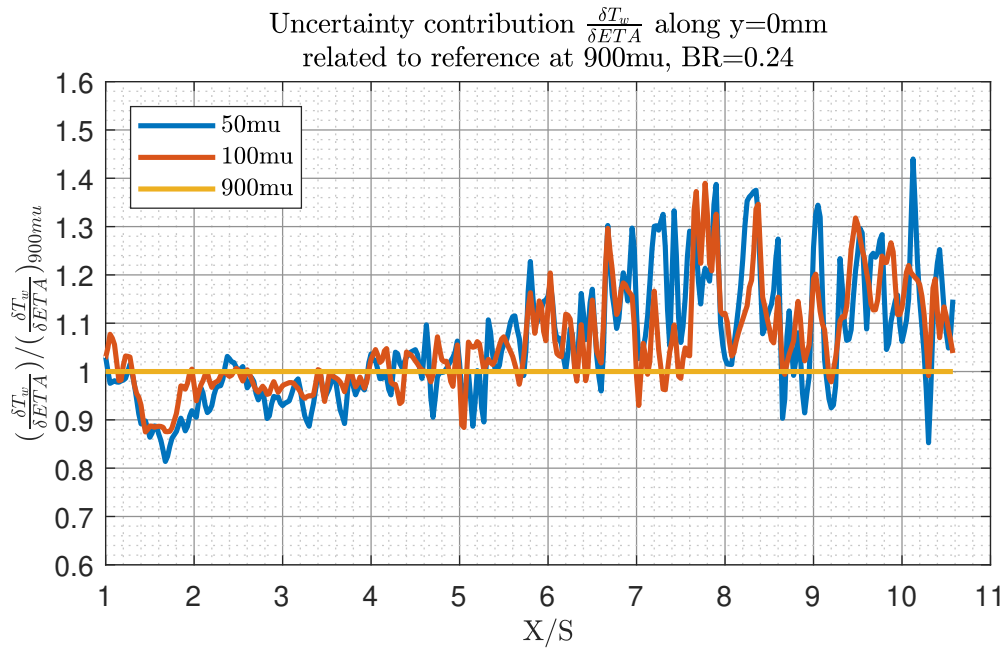
**Figure 4.16:** Development of the fractional contribution of surface temperatures to the uncertainty in $\eta_{ad}$ as a function of integration times

of the axes makes it possible to interpolate the adiabatic results instead of extrapolating with higher errors and especially higher sensitivities to the input parameters. For the location $X/S = 3.3$, $Y/S = 0.425$ the nodes are placed on both sides of the abscissa indicating that heat fluxes from the wall into the flow and vice versa are present at different set temperatures. This effect is desirable as it makes the regression more stable with reference to the cooling effectiveness. Low surface temperatures and low cooling effectiveness levels are mainly found where primary air is washed down onto the endwall so that in these regions the absolute value of the heat flux is notably higher as well. It can be seen in figures 4.17(a) and 4.17(b) that the pairs of $\Theta$ and $\alpha$ have a longer distance to the abscissa at the location on the heating plate with a low cooling effectiveness level.

As a consequence, uncertainties in the determination of the cooling effectiveness are supposedly higher in regions with predominantly low surface temperatures than in regions with predominantly high surface temperatures. Deviations in the respective input data to the regression such as the surface temperatures and the heat fluxes therefore have a substantial impact on the extrapolated value of the cooling effectiveness. This is assumed to explain the elevated contributions of surface temperatures to the uncertainty in cooling effectiveness. In section 4.4.2 this issue is addressed again in context with defective results of the cooling effectiveness in this area. On the contrary, the differences in the distance to the ordinate are much smaller between respective regions with low and high surface temperatures suggesting that the determination of $HTC$ is more accurate than the determination of $\eta_{ad}$ regardless of the location on the heating plate.

(a) Regression $\alpha$ over $\Theta$       (b) Regression $\dot{q}$ over $T_w$

**Figure 4.17:** Depiction of regression lines at two different positions in the heating plate coordinate system with distinct differences in cooling effectiveness

## 4.4 Variation of the blowing rate

In the following section adiabatic results are presented for varied blowing rates. Data are mainly taken from measurements with an integration time of $900\,\mu s$. The corresponding results for lower integration times are in accordance with these references as explained in the previous sections.

### 4.4.1 Results for the heat transfer coefficient

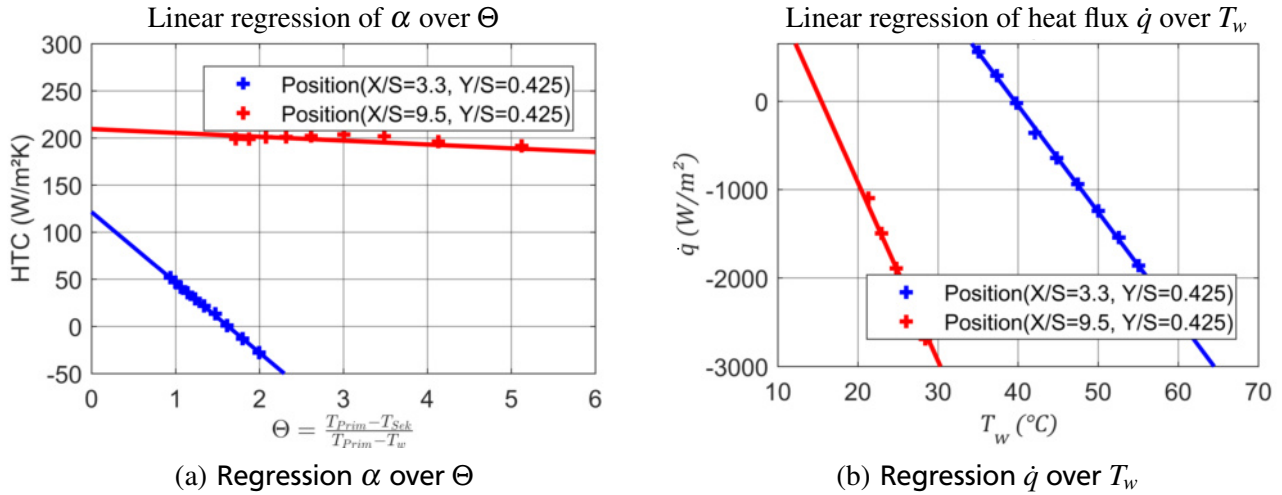Results for the adiabatic heat transfer coefficient $HTC$ are displayed in the same two-dimensional surface plots as introduced in section 4.3.1. They are given in the non-dimensional expression of Stanton numbers $St$. Additionally, they are presented in terms of their effect on heat transfer augmentation related to the reference case without secondary air injection in one-dimensional plots along different lateral locations $Y/S$. Distributions of $St$ in the physical coordinate system of the heating plate are calculated for the five different blowing rates summarised in table 4.1.

#### Distribution of Stanton numbers

The surface plots in figures 4.18(a) to 4.18(c) depict two-dimensional distributions for three of the blowing rates: $BR = 0$ as the reference without secondary air injection, $BR = 0.24$ as an intermediate blowing rate comparable to a moderate mass flow ratio of $1.73\,\%$ at the LSTR and $BR = 0.38$ as the highest blowing rate investigated in the present work, equivalent to a mass flow ratio of $2.71\,\%$ at the LSTR.

The distribution of heat transfer coefficients for the intermediate blowing rate $BR = 0.24$ has been described in section 4.3.1. In the image of the reference data without secondary air injection all characteristic flow phenomena that are visible for a blowing rate of $BR = 0.24$ can be seen as well. Stanton numbers assume nearly constant values between $X/S = 2$ and $X/S \approx 8$ before rising to a local maximum and decreasing in a narrow region. Downstream of this decrease Stanton numbers rise again up to the leading edge of the airfoil. This region of spatially reduced heat transfer appears shorter along $X/S$ for $BR = 0$ than for $BR = 0.24$. Evidently the band of local maximums moves upstream when the blowing rate is raised from $BR = 0$ to $BR = 0.24$. The upstream starting point of this band can be located at $X/S \approx 7$ at the symmetry line $Y/S = 0$ for a blowing rate of $BR = 0.24$ it does not appear until $X/S$ is slightly higher than 8 for the reference without slot injection. It can also be seen that the curvature of the trajectory with local maximums flattens from the reference to the case with $BR = 0.24$.
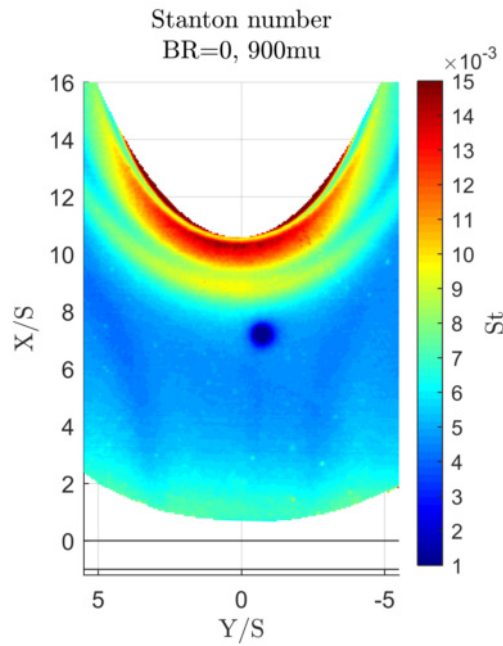
(a) Stanton number at $BR = 0$
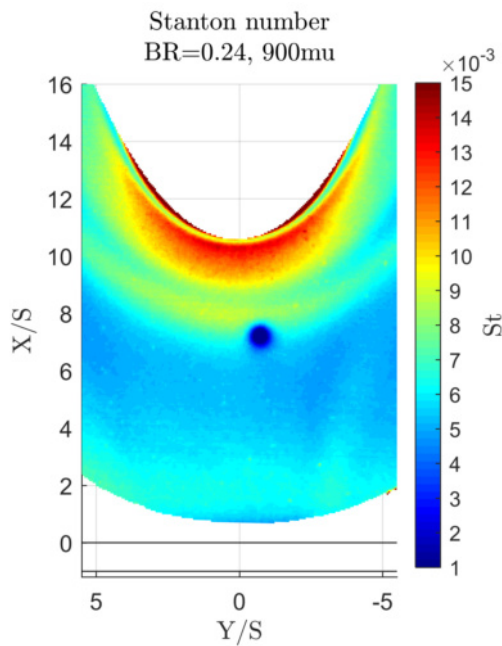


(b) Stanton number at $BR = 0.24$
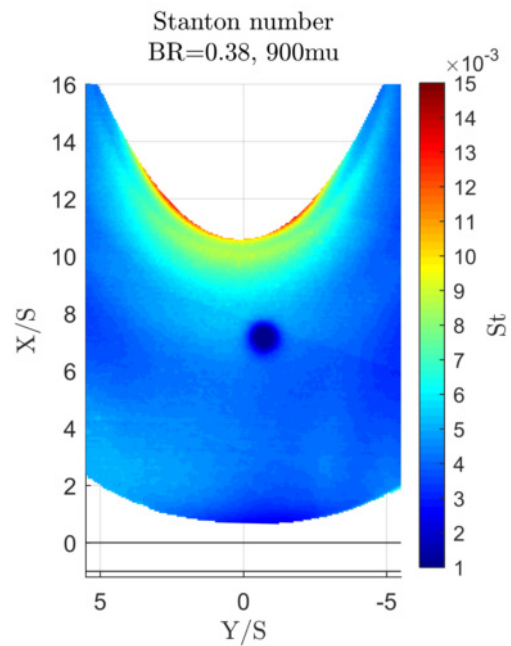


(c) Stanton number at $BR = 0.38$

**Figure 4.18:** Distribution of Stanton number referred to adiabatic heat transfer coefficient for three different blowing rates

This is obvious at the lateral limitations in this illustration: The curvature intersects the coordinate $Y/S = \pm 5.5$ at about $X/S = 10$ at a blowing rate $BR = 0.24$. It moves two slot widths upstream compared to the reference case whereas in the symmetry line the upstream displacement constitutes approximately one slot width. In total, Stanton numbers are higher at running lengths upstream of the horseshoe vortex for the blowing rate $BR = 0.24$ compared to the reference.

The highest blowing rate $BR = 0.38$ differs dramatically from the lower blowing rates as regards the distribution of heat transfer coefficients. Not only are the levels of Stanton numbers lowered in the entire region observed, reaching maximum values of 6.5 right in front of the leading edge, but also the distinctive structures in Stanton number distributions attributed to

the horseshoe vortex at other blowing rates are not visible. A region of elevated heat transfer is detectable around the leading edge which is permeated by a thin curve of local minimums directly before another rise in heat transfer coefficients in front of the leading edge tip. As will be shown later this might be an effect of the small corner vortex forming on the airfoil surface. On both sides of the leading edge vague indications of a branches propagating from this region are recognisable.

## Stanton numbers along the symmetry line $Y/S = 0$

Averaged results for the Stanton number along varied lateral locations $Y/S$ are shown in figures 4.19, 4.21 and 4.22. Like the results presented in previous sections, data are averaged within a lateral span of 1 mm around these locations. Additional results for the two intermediate blowing rates of $BR = 0.11$ and $BR = 0.30$ are incorporated in these plots as well. Along the stagnation line $Y/S = 0$ Stanton numbers for the blowing rate $BR = 0.11$ are the lowest until a running length of $X/S \approx 7.7$ where values rise above the level obtained for $BR = 0.38$. Beyond that, these two blowing rates exhibit almost constant heat transfer coefficients from $X/S = 2$ up to $X/S = 7$ unlike the other blowing rates. The blowing rates $BR = 0.30$ and $BR = 0.24$ show a smooth increase in Stanton numbers until $X/S \approx 2$ before declining to values about 10 % higher than the reference case.
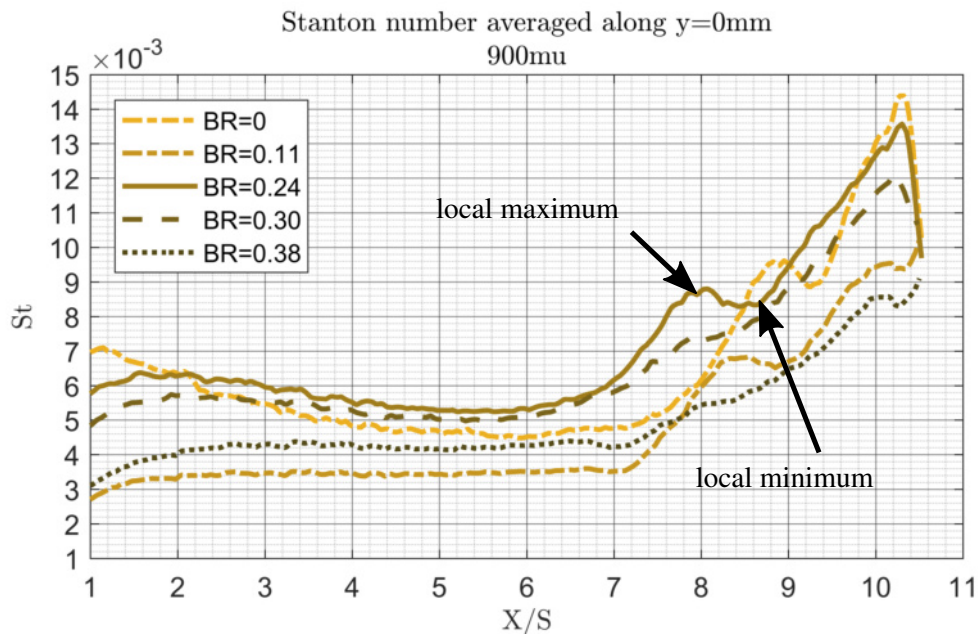


**Figure 4.19:** Stanton numbers for different blowing rates along the stagnation line $Y/S = 0$

In the reference case without secondary air injection the course of Stanton numbers compares well with the expected course above a flat plate and a thermal boundary layer beginning at $X/S = 0$. However, Stanton numbers show a local maximum at short running lengths around $X/S \approx 1$. Although the slot is carefully sealed with adhesive tape it cannot be entirely avoided that the surface of the tape is bended by the pressure gradient between the flow channel and the subjacent slot and plenum or that the edge of the adhesive tape leads to detachments of the boundary layer.
The course of the Stanton number for the reference case is qualitatively similar to the one found by Bittlinger et al. [43]. In the cited work, heat transfer coefficients are measured for a configuration with a tangential slot for the secondary air injection and the primary flow passing above. Amongst others a velocity ratio of 1 between the primary flow and the secondary flow is investigated. Like in the reference case of the present work, Stanton numbers feature a local maximum at short running lengths which is attributed to the new boundary layer formed by the tangentially injected secondary flow. The maximum of heat transfer coefficients in this setup moves away from the tangential slot when the secondary flow is not present because the primary flow runs over a backward facing step and attaches to the endwall farther downstream [43].

However, Stanton numbers in the reference case exhibit a short region of constant values between $X/S = 5$ and $X/S = 7$. Taking into account the findings by Milidonis et al. [44] for a case without secondary air injection compliance can be found

that Stanton numbers do not begin to rise towards the leading edge tip until a running length situated one leading edge radius upstream of a symmetric airfoil contour.

It is clearly visible that the local maximums of Stanton numbers shift upstream from $X/S = 9$ at $BR = 0$ to $X/S = 8.8$ at $BR = 0.11$ and to $X/S = 8$ at $BR = 0.24$. For the cases $BR = 0.30$ and $BR = 0.38$ this local maximum cannot be identified as clearly any more. The aforementioned local minimums of reduced heat transfer between the first local maximum and the consecutive rise is also notable for the two lowest blowing rates and for the reference without secondary air injection. Both the first local maximum and the maximum directly in front of the leading edge tip in the reference case feature higher Stanton numbers than any of the cases with secondary air injection. Values of the Stanton number at the maximum in front of the leading edge increase to as much as $150\%$ of the values attained at the blowing rates $BR = 0.11$ and $BR = 0.38$.

## Heat transfer augmentation along the symmetry line

An illustration of the heat transfer augmentation along the symmetry line is given in figure 4.20. The augmentation is expressed as the ratio of Stanton numbers at different blowing rates to the Stanton number $St_0$ in the reference case without secondary air injection. Ratios below 1 indicate smaller adiabatic heat transfer coefficients than in the reference case. At the blowing rates $BR = 0.24$ elevations up to $45\%$ are reached at running lengths near the location of the local maximum $X/S = 7.6$. Between $X/S = 2$ and said high elevation heat transfer is increased by about $15 - 20\%$ on a constant level. The elevation between $X/S = 9$ and $X/S = 10$ results from the earlier rise of Stanton numbers towards the leading edge tip due to the upstream shift of the band of local maximums. Generally, heat transfer at a blowing rate of $BR = 0.30$ exhibits the same development along the flow direction like at $BR = 0.24$, but in total Stanton numbers are slightly lower. Downstream of $X/S = 9$, heat transfer augmentation does not exceed $5\%$ relative to the reference case.

At the lowest blowing rate $BR = 0.11$ heat transfer does not rise above the level attained without secondary air injection. The same conclusion can be drawn from the course at the highest blowing rate $BR = 0.38$ where the maximum heat transfer does not exceed $95\%$ of the reference case at $X/S = 6$. Downstream of $X/S \approx 7.8$ the level of heat transfer augmentation at $BR = 0.11$ exceeds that at $BR = 0.38$.
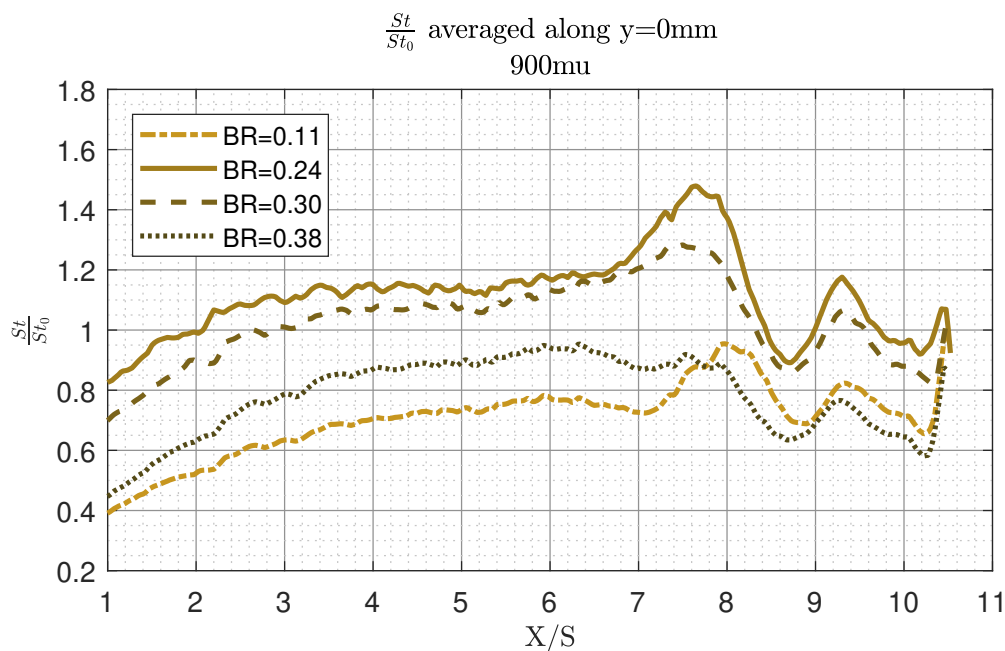


**Figure 4.20:** Heat transfer augmentation relative to the reference case $BR = 0$

Figures 4.21 and 4.22 show Stanton numbers along the lateral positions $Y/S = 1.5$ and $Y/S = 3$, respectively. Note that in figure 4.22 the x-axis reaches from 1 to 12 as the airfoil contour begins farther downstream for growing lateral distances from the symmetry line.
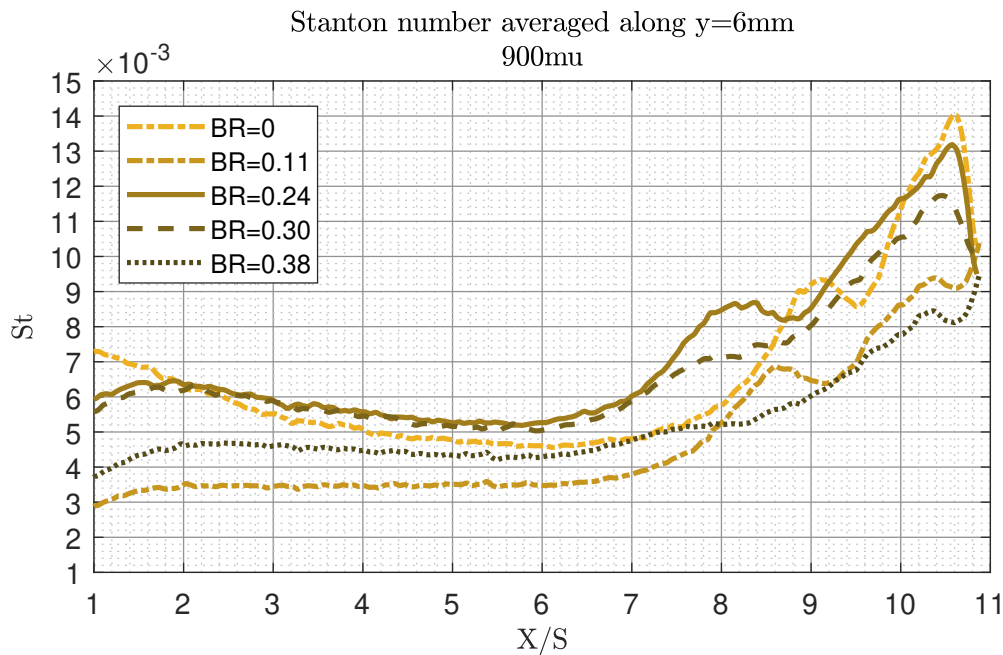


**Figure 4.21:** Stanton numbers for different blowing rates along $Y/S = 1.5$

The first local maximums and minimums are still only visible at the blowing rates $BR = 0$, $BR = 0.11$ and $BR = 0.24$. They shift downstream as is expected by the curvature around the airfoil tip in the two-dimensional surface plots shown earlier. Amplitudes of the Stanton numbers are diminished in comparison to the course along the symmetry line which can be attributed to the enhanced mixing of primary and secondary flow due to the longer running lengths and because a three-dimensional flow is present in front of the leading edge. This way, stream tubes from near the symmetry line are deflected due to the pressure gradient and are washed down onto the endwall at these lateral positions increasing the effective running length for primary and secondary flow to exchange heat. In section 5.2.1 it is also argued with reference to the work by Praisner [22] that the horseshoe vortex around the leading edge moves away from the endwall with growing lateral distance from the airfoil. This diminishes its impact on local heat transfer to the endwall. The relative decrease in Stanton number maximums around the leading edge arc with growing distance from the symmetry plane is confirmed by Milidonis as well [44].

At shorter running lengths $X/S < 5$ changes of Stanton numbers are hardly noticeable for any of the blowing rates at lateral positions. Stanton numbers for $BR = 0.30$ approximate those at $BR = 0.24$ for these shorter running lengths which can already be seen in the courses at $Y/S = 1.5$. However, results for the blowing rate $BR = 0.38$ do show significant changes compared to the symmetry line. Along $Y/S = 3$ Stanton numbers for this case rise in the region between $X/S = 1$ to $X/S = 4$ with increasing distance from the symmetry line. From $X/S = 1$ to $X/S = 2.5$ gains of $20 - 30\,\%$ relative to the values along the symmetry line are detectable at the lateral position $Y/S = 3$. One possible explanation might be an inhomogeneous injection across the cross-section of the slot which leads to inhomogeneous developments of the boundary layer downstream of the slot. Another explanation is found in the blockage of the primary flow which is caused by the slot injection. The primary flow is consequently guided around the injected secondary air and redirected towards the symmetry plane downstream of the slot.

**Figure 4.22:** Stanton numbers for different blowing rates along $Y/S = 3$
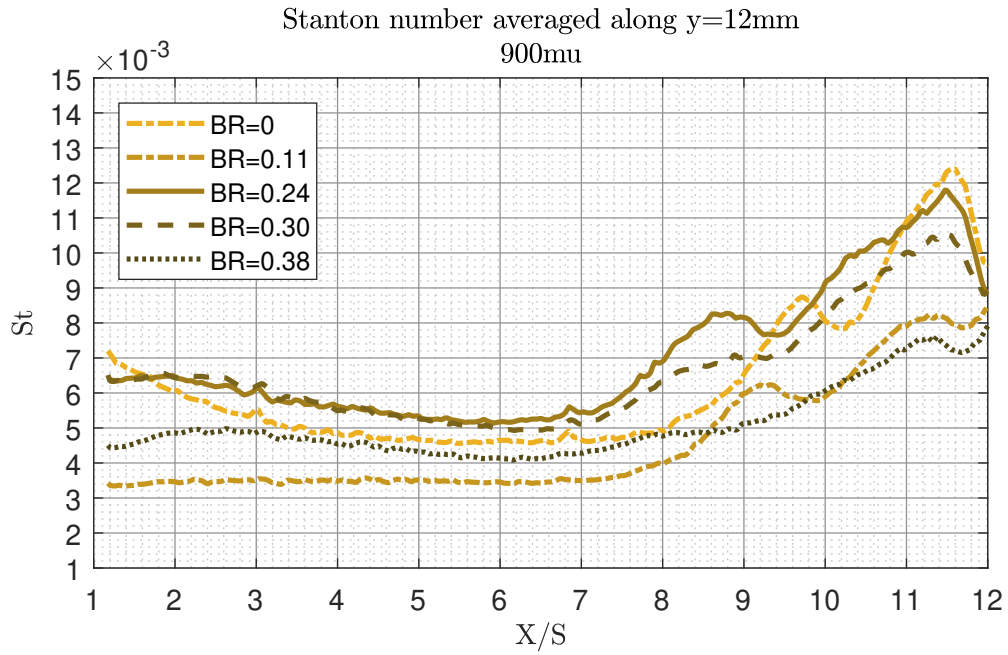
## 4.4.2 Results for the cooling effectiveness

The following section contains results for the adiabatic cooling effectiveness $\eta_{ad}$ at varied blowing rates. Results will also be discussed with reference to the regression method used to derive the adiabatic cooling effectiveness.

### Distribution of cooling effectiveness

For the case without secondary air injection, the cooling effectiveness cannot be expressed in the dimensionless formulation of $\eta_{ad}$. Therefore, the adiabatic wall temperature is depicted in figure 4.23(a) alongside with the film cooling effectiveness for blowing rates of $BR = 0.24$ in figure 4.23(b) and $BR = 0.38$ in figure 4.23(c).

The expected adiabatic wall temperature for the case without secondary air injection is the primary air temperature. It varies between $15.25\,°C$ and $15.75\,°C$ during the heat transfer measurements. This inconsistency cannot be avoided as the primary air is drawn in from the environment (compare section 3.2).

Adiabatic wall temperatures shown in the distribution in figure 4.23(a) mainly range within $-0.25\,°C$ below the minimum value and $+0.25\,°C$ above the maximum value of the primary air temperature span. Higher adiabatic wall temperatures at short running lengths up to $X/S = 2$ are expected to be the consequence of the aluminium fillet inside the heating plate. At these positions, the assumption of one-dimensional heat conduction might not be ensured. The distribution of cooling effectiveness for a blowing rate of $BR = 0.24$ has already been presented in section 4.3.2. Striking differences in the distribution at $BR = 0.38$ cannot be deduced from the surface plots. Only a small dent in the contour of $\eta_{ad}$ can be seen near the symmetry line. This might be a consequence of the blockage of the primary flow caused by the injected secondary air. Primary air is deflected around the secondary air and redirected towards the symmetry plane shortly downstream of the slot, resulting in higher Stanton numbers at lateral positions compared to results along the symmetry line. The flow around the injected secondary air might therefore lead to an enhanced mixing, consequently raising cooling effectiveness levels in this region and leaving a dent in the symmetry plane. This issue is addressed in section 5 where results from the aerodynamic investigations are interpreted.
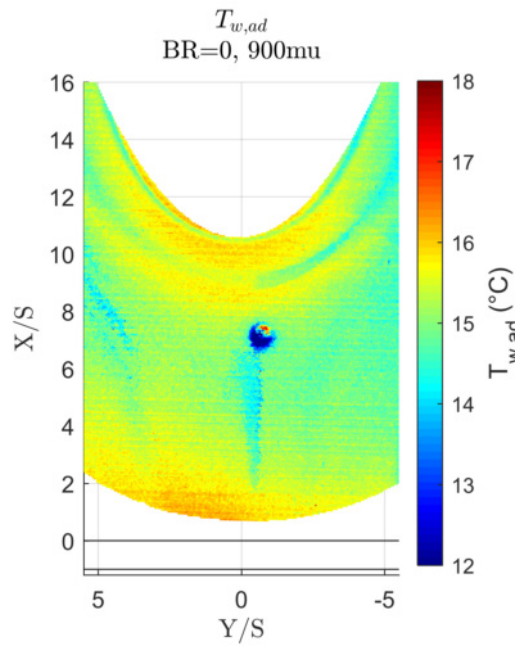
(a) Adiabatic wall temperature $T_{w,ad}$ at $BR = 0$
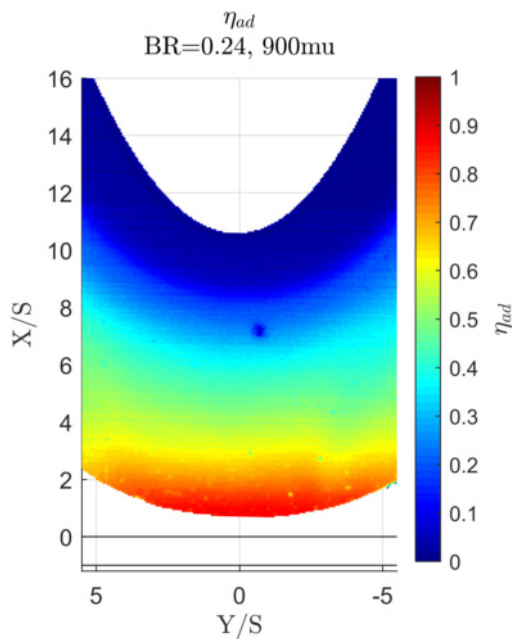


(b) Cooling effectiveness $\eta_{ad}$ at $BR = 0.24$
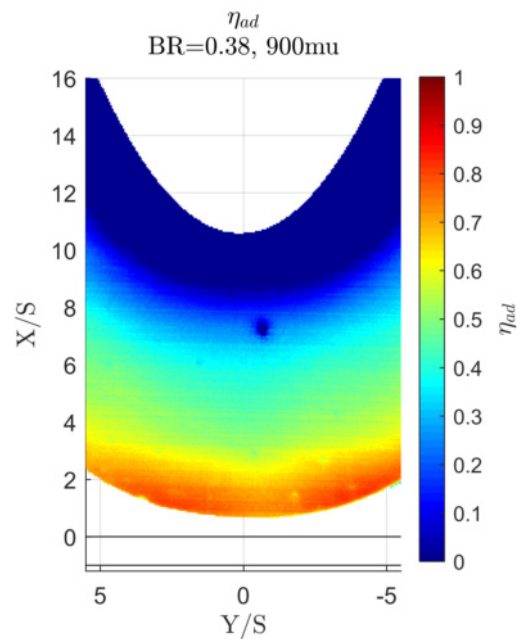


(c) Cooling effectiveness $\eta_{ad}$ at $BR = 0.38$

**Figure 4.23:** Distribution of cooling effectiveness for three different blowing rates

## Cooling effectiveness levels along the symmetry line $Y/S = 0$

Figure 4.24 depicts the courses of the adiabatic cooling effectiveness for the varied blowing rates along the symmetry line $Y/S = 0$. For all cases cooling effectiveness levels decrease steadily from the injection position to the leading edge. This basic course is well-established in literature for a single slot injection (compare to the study by Bittlinger et al. [43] for a tangential slot injection without airfoil). It is furthermore confirmed by the data along a line upstream of the stagnation point and aligned with the initial primary flow velocity in a vane cascade in the work of Lynch and Thole [23]. Bittlinger et al. attribute the fact that cooling effectiveness levels are below 1 directly downstream of the slot to local separations, even for

the case of a tangential injection [43]. Note that right after the slot at $X/S = 1$ cooling effectiveness for $BR = 0.11$ obtains levels as high as those for the blowing rates $BR = 0.24$ and $BR = 0.30$. As the mass flow from the slot and its momentum are low in comparison to the higher blowing rates, the injected secondary air does not penetrate into the primary flow, but might be mixed or swept away in streamwise direction right after the exit. Its cooling effect on the endwall therefore only ranges within the same levels at short running lengths. An increase in cooling effectiveness levels with higher slot mass flows is also found by Lynch and Thole [23] when comparing respective blowing rates of $BR = 0.19$ and $BR = 0.36$. After a running length of $X/S = 4$ cooling effectiveness is reduced to values which are $20\%$ lower than for the blowing rates $BR = 0.24$ and $BR = 0.30$. A distinctive drop in the results for $BR = 0.38$ can be seen where cooling effectiveness levels decrease from $25\%$ at $X/S = 7.5$ to $5\%$ at $X/S = 8.5$. Only within the region $X/S = 6$ to $X/S = 7.4$ does the cooling effectiveness at $BR = 0.38$ reach the same level like at the blowing rates $BR = 0.24$ and $BR = 0.30$. A drop with the comparable gradient is recognizable for $BR = 0.24$ as well as for $BR = 0.30$ from $18\%$ at $X/S = 8$ to $10\%$ at $X/S = 8.5$.

At the blowing rates $BR = 0.11$ and $BR = 0.24$ the location of this distinct drop corresponds to the location of the first local maximum of Stanton numbers from figure 4.19, which are $X/S = 8.8$ and $X/S = 8$, respectively. It is assumed that this is caused by the horseshoe vortex scraping the near-wall flow from the endwall and consequently removing residuals of a cooling film. An aerodynamic assessment of these flow characteristics follows in section 5.
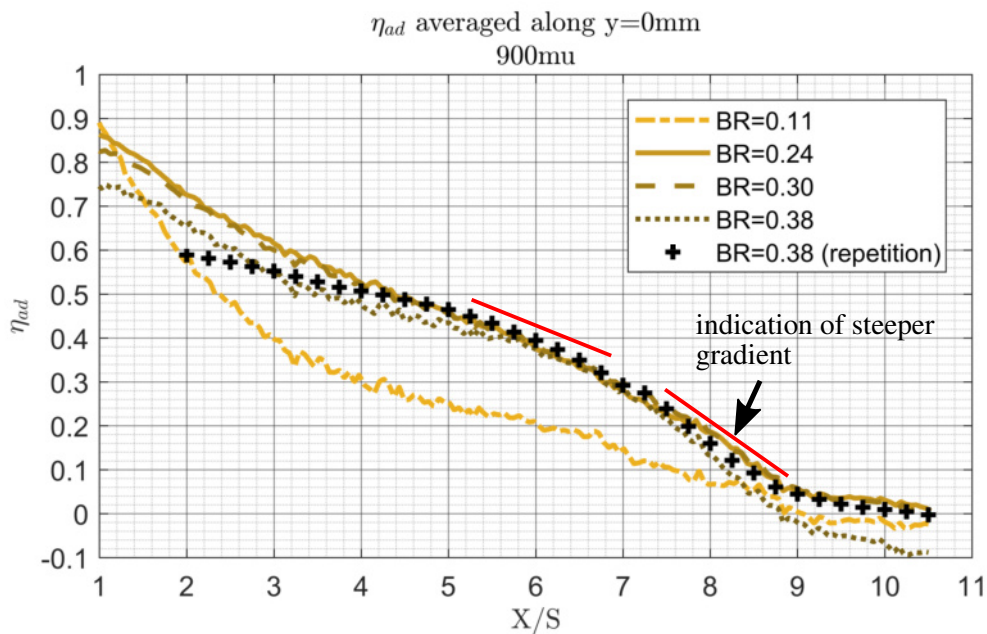


**Figure 4.24:** Adiabatic cooling effectiveness $\eta_{ad}$ for different blowing rates along the stagnation line $Y/S = 0$

Noticeable negative values for the cooling effectiveness are present at blowing rates $BR = 0.11$ and $BR = 0.38$ in the region downstream of the horseshoe vortex. The cause of these unphysical values is not easy to spot. In general, the adiabatic wall temperature is lower than the measured primary flow temperature in the respective regions. Elevations of the primary flow temperature or major reductions of the secondary flow temperature between the measurement position and the heating plate cannot be the root cause as the regression of the heat flux against wall temperatures according to the method in figure 4.17(b) shows that even with this calculation the adiabatic wall temperature assumes values lower than the primary flow temperature.[3] The regression for an exemplary location at $X/S = 10$, $Y/S = 0$ with a cooling effectiveness of $-7\%$ is given in figure 4.25.

Negative heat fluxes indicate that heat is being transferred from the heating plate into the flow. While the average primary flow temperature during this measurement is $16.91\,^\circ$C the adiabatic wall temperature is calculated as $14.05\,^\circ$C from the linear fit at this location. Higher wall temperatures at the individual set temperatures steps would shift the linear curve to the right, resulting in intersection with the abscissa at higher values for the adiabatic wall temperature. One possible explanation for defective values of the wall temperatures in this region might be the span of the calibration curves derived from the in-situ calibration. The lowest set temperature, controlled underneath the insulating auxiliary wall, is $30\,^\circ$C (compare table 4.1). However, none

---

[3]    The other calculation results from the regression of the heat transfer coefficient $\alpha$ against the dimensionless wall temperature $\Theta = \frac{T_{prim} - T_{sec}}{T_{prim} - T_w}$, compare equation 2.5. This calculation would incorporate the secondary flow temperature as well.

**Figure 4.25:** Regression of heat flux $\dot{q}$ against wall temperatures $T_w$ at a position with negative cooling effectiveness value

of the five reference thermocouples delivering the pairs of temperature and camera signal is exposed to temperatures below this initial set temperature. Reference thermocouple 5 is, for example, situated slightly ups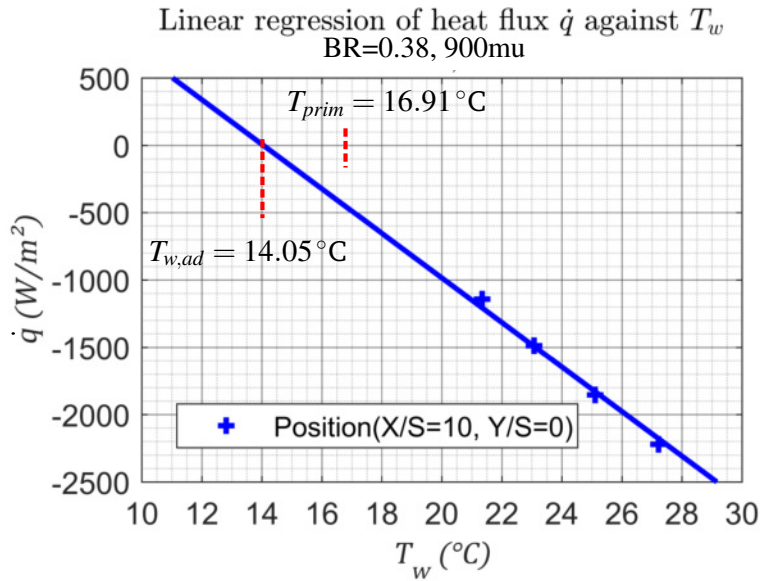tream of the region where negative cooling effectiveness levels occur as can be seen in figure 4.23(c). The calibration coefficients are scattered across the array of pixels with a weighting scheme considering the respective distances to the reference thermocouples (compare section 2.2.2 and [13]), but reference thermocouple 5 is, unfortunately, not positioned in a region where cold primary flow is directed onto the wall at any blowing rate. As the five lowest steps of set temperatures result in wall temperatures below $30\,°C$, the corresponding camera signals obtained at these temperature steps are outside the calibration range. Consequently, the linear regression curve is liable to intersect the abscissa at values below the primary flow temperature and cooling effectiveness levels are not as reliable as in regions where higher wall temperatures are predominant.This error is also owed to the fact that the primary flow cannot be heated and its temperature remains below the minimum set temperature. As a dependency of the transmissivity in the optical path on the temperature exists, calibration data can only be collected in-situ. Gathering the data in the absence of the hot secondary flow neglects this dependency.

The measurements at a blowing rate of $BR = 0.38$ are repeated and results of the cooling effectiveness are displayed in figure 4.24 as well. It can be seen that accordance with data from the initial measurements is achieved downstream of running lengths $X/S = 3$. Especially the limitation of cooling effectiveness levels between $X/S = 5$ and $X/S = 7$ like it is seen in results at $BR = 0.24$ and $BR = 0.30$ as well is confirmed again. Downstream of $X/S \approx 8$ results from repeated measurements show a flattened decline in cooling effectiveness levels, eventually approaching zero in the vicinity of the leading edge unlike in the first measurements. At short running lengths upstream of $X/S = 3$ compliance with the initial measurements is not found which can be caused by the unstable nature of detachments and vortex structures directly downstream of the injection position as will be discussed in section 5.2.2.

In these newly conducted measurements the primary flow temperature is elevated to $24.5\,°C$ as ambient temperatures have risen since the initial heat transfer measurements. The smallest temperature difference between the primary air temperature dominating the surface temperatures at low cooling effectiveness levels and the lower limit of the calibration range is therefore decreased. In the first measurements the difference between the primary flow temperature at $16.91\,°C$ and the lowest temperature within the calibration range of the thermocouple 5 at approximately $30\,°C$, for example, is more than $13\,°C$. In the repeated measurements, however, the primary flow temperature approaches the lowest temperature within the calibration range to a difference of $6.5\,°C$, approximately dividing the former temperature difference and the respective distance to the calibration range in half. This way, the surface temperatures in the repeated measurements do not have to be extrapolated from the calibration range as far as in the initial measurements, a fact that can be avoided in applications at the LSTR with a heated primary flow.

At the lateral positions $Y/S = 1.5$ and $Y/S = 3$ cooling effectiveness levels show a similar decline like along the symmetry line which is depicted in figures 4.26 and 4.27. Up to a running length of $X/S = 7$ cooling effectiveness levels at blowing rates $BR = 0.30$ and $BR = 0.38$ approximate those attained at $BR = 0.24$ for growing lateral positions. For the lowest blowing rate $BR = 0.11$ the cooling performance remains below those of any other blowing rate. Again, note that the x-axis spans from $X/S = 1$ to $X/S = 12$ at the lateral position $Y/S = 3$ unlike in the other figures.
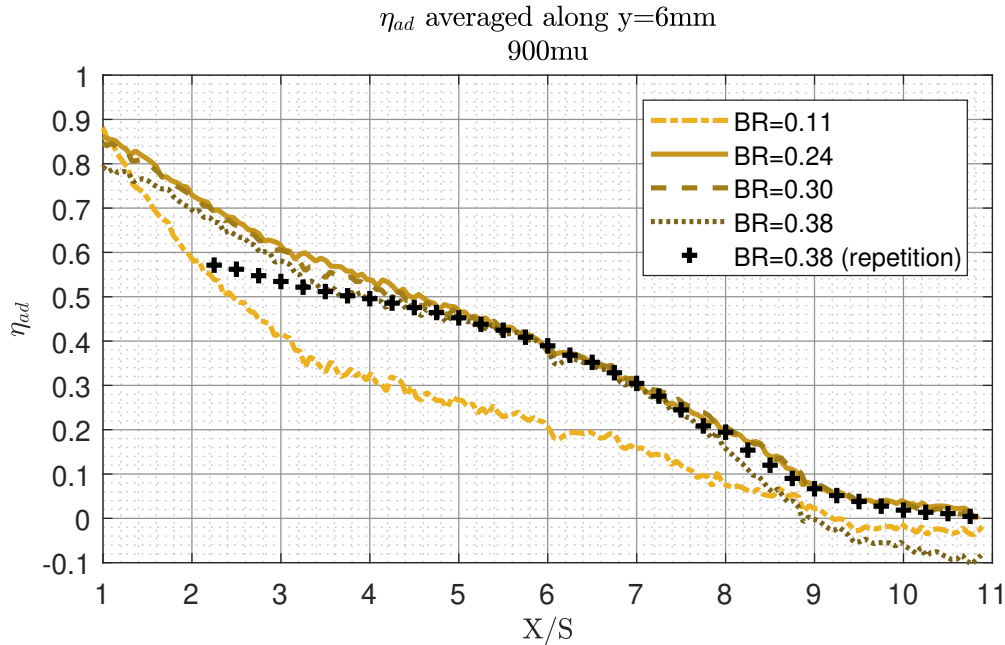


**Figure 4.26:** Adiabatic cooling effectiveness $\eta_{ad}$ for different blowing rates along $Y/S = 1.5$
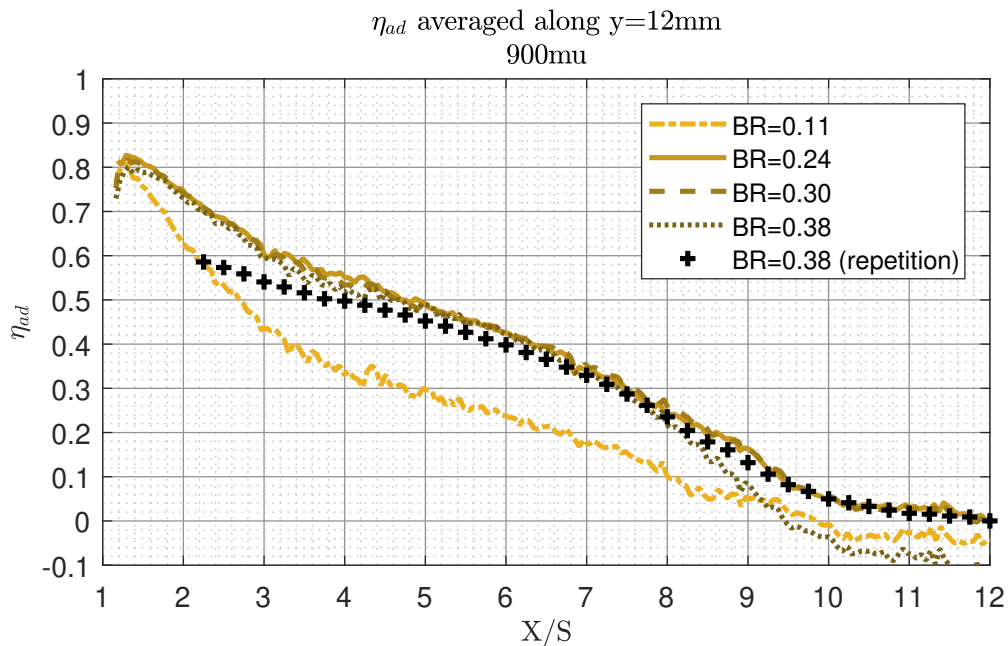


**Figure 4.27:** Adiabatic cooling effectiveness $\eta_{ad}$ for different blowing rates along $Y/S = 3$

Consequently, it seems like the highest efficiency in cooling effectiveness is reached with a blowing rate of $BR = 0.24$ among the steps of blowing rates investigated in this work. Cooling effectiveness levels for the next higher blowing rate do not

feature a better cooling performance and even decrease in the major part of the measurement section for a blowing rate of $BR = 0.38$. The greater secondary mass flow injected through the rotor cavity does not give a benefit in cooling effectiveness and would contribute as an additional loss in a turbine engine application. The repeated measurements at the highest blowing rate exhibit the same tendency to approach results obtained at $BR = 0.24$ in front of the leading edge tip like it is seen along the symmetry line.

# 5 Aerodynamic measurements

In this chapter the results from PIV recordings at the flow channel are presented. The operating points of these measurements are identical with those from the heat transfer measurements to allow for a combination of the adiabatic results presented in the previous sections with the aerodynamic results.

## 5.1 Operating points and PIV parameters

The operating points of the aerodynamic measurements are held identical to those of the heat transfer measurements except from the heating of the injected secondary air. The temperature control cannot be secured and stabilised when the seeding generator is connected to the output of the flow heater. Additional heat-resistant tubes for the connection of the flow heater and the seeding generator are not available. Blowing rates and Reynolds similarity are held identical to the parameters of the heat transfer measurements, but the density ratio of secondary and primary flow is held near unity for the aerodynamic measurements, accordingly. At each of the lateral positions 1000 double frames are acquired with a frequency of 14 Hz for every blowing rate examined. The post-processing parameters given in section 5.1.3 are applied to all frames and the resulting vector fields are averaged.

Operating points of the heat transfer measurements have been summarised in table 4.1. Table 5.1 integrates the operating points controlled in the aerodynamic measurements. Additionally, information on the varied lateral positions is incorporated in this table.

**Table 5.1:** Operating points for the aerodynamic measurements

| Equivalent mass flow rate at the LSTR $MFR_{LSTR}$ | Blowing rate $BR$ | Lateral positions $y$ of the light sheet |
|---|---|---|
| 0 % | 0 | $0 - 12$ mm, step 3 mm |
| 0.76 % | 0.11 | $0 - 12$ mm, step 3 mm |
| 1.73 % | 0.24 | $0 - 12$ mm, step 3 mm |
| 2.12 % | 0.30 | $0 - 12$ mm, step 3 mm |
| 2.71 % | 0.38 | $0 - 12$ mm, step 3 mm |

### 5.1.1 Measurement region

The aerodynamic measurements of the flow field in front of the airfoil in the flow channel have been performed with particle image velocimetry (PIV). As it is shown in section 3.2.5 two cameras are placed on either side of the flow channel which makes it possible to reconstruct three-dimensional velocity vectors from stereo-PIV data. The region observed by the two cameras is situated upstream of the airfoil and spans from shortly upstream of the injection slot to the leading edge tip. Its physical dimensions are approximately $52x35$ mm$^2$ in the x-z-plane, but the section in which data are evaluated and visualised is confined to approximately 40 % of the height of the flow channel by a geometric mask. This considers a sufficient particle density in the masked region and reduces time for the evaluation. In figure 5.1(a) this trimmed area with a size of $50x19$ mm$^2$ is depicted.

The light sheet illuminating the particles in the flow is traversed to one side of the flow channel in order to obtain measurement data at different displacements from the symmetry line as it has been presented in the previous sections. At these lateral positions the observable region in the plane of the light sheet is partially blocked by the airfoil for camera 2 and the distinguished horseshoe vortex observed in front of the leading edge is not visible for both cameras. This is the case for

measurements at $y \geq 9\,\text{mm}$ ($Y/S \geq 2.25$). Consequently, at these lateral positions data are only available as two-dimensional vectors of the flow field. Figure 5.1(a) illustrates the plane along the symmetry line with exemplary vectors from the flow field. The dimensions of the complete evaluation plane of the PIV results are shown. Additionally, the blue plane indicates the area which is used in further illustrations to connect aerodynamic results to results of heat transfer measurements. Figure 5.1(b) shows the planes at the two lateral positions $Y/S = 1.5$ and $Y/S = 3$, respectively. A distribution of Stanton numbers from the thermal measurements is plotted on the surface of the heating plate to put the images in context with figure 4.3.
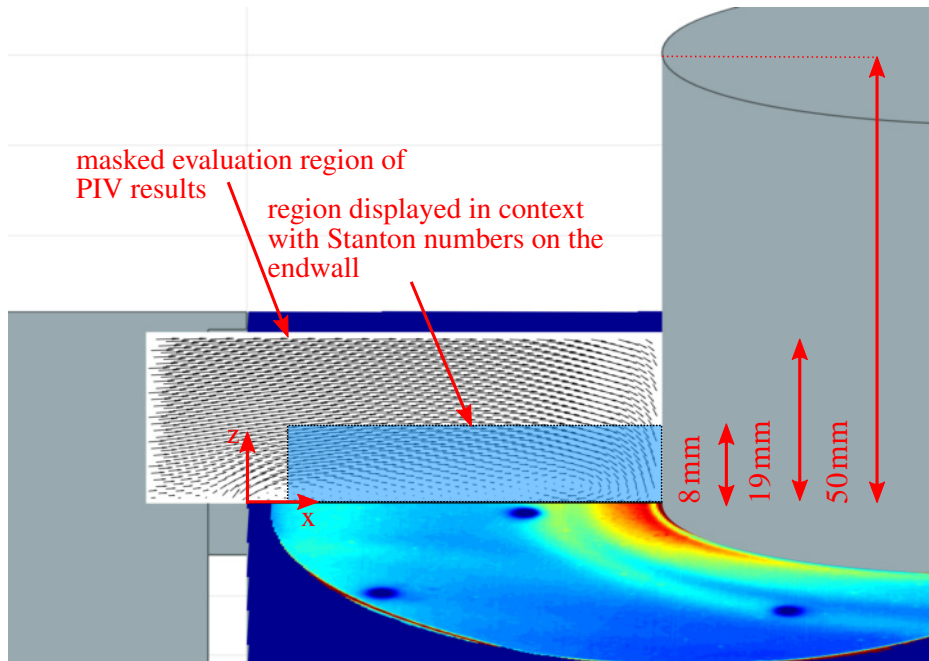


(a) Velocity vectors in the symmetry plane $Y/S = 0$
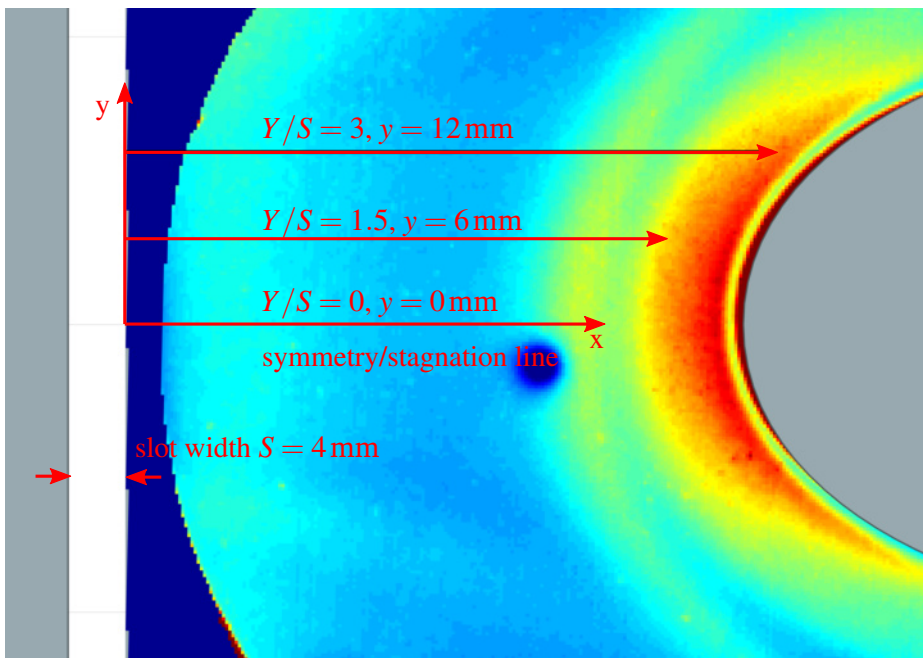


(b) Locations of the evaluation planes at $Y/S = 1.5$ and $Y/S = 3$

**Figure 5.1:** Dimensions and locations of the evaluation planes of PIV results

Aerodynamic results are available as three- or two-dimensional velocity vectors at corresponding positions in the PIV coordinate system. They are transformed into the physical coordinate system of the heating plate which has been named throughout

the previous sections. The location of the origin specified on the calibration target is measured manually from the upstream edge of the injection slot.

## 5.1.2 Spatial resolution and time delay

The spatial resolution of the PIV data is dependent on the size of the interrogation area used for the correlation. In the present case an interrogation area size of $64x64\,\text{pixel}^2$ in combination with a time delay of $15\,\mu s$ has proven suitable for the stereo PIV recordings. This is controlled with the help of the shift of single particles in a double-frame recording. Whereas in the region of the undisturbed primary flow field a displacement of approximately 8 pixels is detectable, the displacement is reduced to $4-5$ pixels near the wall (with secondary air injection). A thumb rule of a maximum displacement of one quarter of the interrogation area is therefore met with this time delay. Besides, a further reduction of the time delay is not appropriate as it deteriorates the possible velocity resolution and the risk of *peak locking* in the near-wall regions becomes higher. This effect denotes the improper reconstruction of velocities due to particle displacements which are too small and remain below one pixel [16, p. 167]. The effective spatial resolution of the stereo PIV recordings is given by the equivalent physical dimensions of one interrogation area. This resolution can be altered during the calculation of the vector components in the software (compare section 5.1.3).

$$Res_{PIV} = \frac{35\,\text{mm}}{1200\,pixel} \cdot 64\,\text{pixel} = 1.86\,\text{mm} \tag{5.1}$$

The particle density is adjusted to approximately $0.02\,\frac{\text{particles}}{\text{pixel}^2}$ by controlling the bypass of the seeding generator for the secondary flow. This way, the quality of distinct peaks in the correlation map can be altered as the assignment of the particles is improved. It is inspected visually in the PIV software at several locations in the near-wall region.

Figure 5.2(a) shows an unedited stereo PIV recording of camera 1 at a blowing rate of $BR = 0.24$ in the symmetry plane $y = 0\,\text{mm}$.
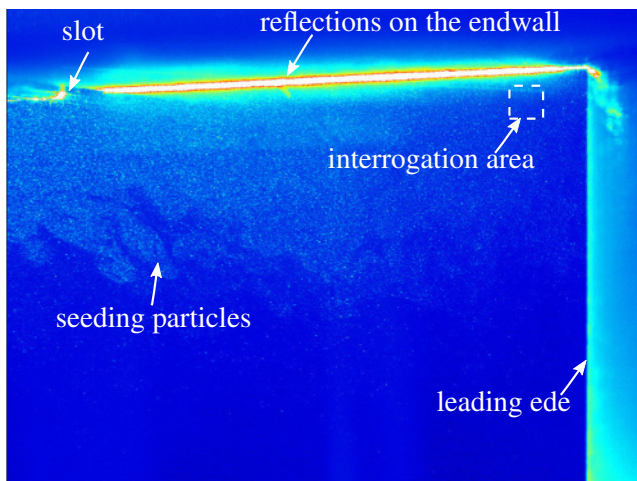


(a) Unedited PIV recording with interroation area marked

(b) 3D correlation map for the interrogation area marked on the left

**Figure 5.2:** PIV recording and corresponding correlation map for an exemplary interrogation area

Note that the camera is mounted upside down so that the secondary flow enters from the slot in the upper left part of the image. The reflections of the light sheet on the endwall can be seen clearly. They are amplified by the accumulation of seeding oil which also leaves characteristic streaks on the leading edge tip. Directly above the endwall these reflections prevent a proper detection of seeding particles in the flow as the illuminated background dominates the scattered light intensity. Residuals of

seeding oil are removed between the measurements at different blowing rates to keep the optical path clean.

Figure 5.2(b) illustrates the three-dimensional correlation map, giving the displacement of the correlation peak in terms of pixels on the bottom plane and the correlation value on the vertical axis. This is an example of a distinct and satisfactory correlation peak inside an interrogation area near the endwall which is also marked in figure 5.2(a). The correlation peak is situated at a particle displacement of $4-5$ pixel.

### 5.1.3 Parameter settings for the correlation

For each measurement recording an image of the background in the same scene without seeding particles is taken. It is subtracted from the measurement recordings before the correlation in order to remove reflections. On top of that, the use of a geometric mask reduces the time for the calculations as the number of interrogation areas is diminished. This mask defines the dimensions of the complete evaluation plane shown in figure 5.1(a).

The aforementioned resolution can be reduced to an eighth of the value by iteratively reducing the interrogation area size to a final value of $16x16$ pixel$^2$ and $50\%$ overlap. With this method particles are pursued in overlapping interrogation areas of decreased size and varied weighting. The weighting of these interrogation areas mainly affects the quality of correlations in the boundary region of the interrogation areas. They correspond to form functions which consider particles in these boundary regions with a lower weighting which generally reduces influences from random noise [45]. An adaptive interrogation area size and shape is especially helpful when the smallest area sizes are used as they might not contain enough information on particle displacements in their boundary regions.

As stated in section 2.3.3 the calibration process constructs a coordinate system from the position of the reference points on the calibration target. This system of equations is over-determined due to the high amount of reference points compared to the 12 degrees of freedom which determine the positions of two cameras. The RMS of the calibration process is expressed in terms of pixel sizes and represents the quality of the calibration. Values below 1 pixel indicate a very good quality of the reconstruction. The same applies to the reconstruction of a three-dimensional displacement vector in stereo-PIV from four parameters by the two cameras. A threshold for the goodness of this 3D vector validation can also be entered in the post-processing of the software *DaVIS*. In order to reduce the number of vectors which result from bad correlations a minimum limitation of the correlation peak value, denoted as *Q-Peak*, is set to $4$. This way, only regions with distinct correlation peaks are committed to the final results of the vector field from each of the 1000 frames. Table 5.2 summarises the settings for the vector calculation in the processing software for both the stereo PIV recordings at lateral positions up to $y = 6$ mm and for the planar PIV recordings.

**Table 5.2:** Parameter settings for the vector calculation in *DaVIS*

| Parameter | Value | |
|---|---|---|
| | stereo PIV | planar PIV ($y = 9 - 12mm$) |
| RMS of the calibration | 0.85 pixel | 0.84 pixel |
| Interrogation area size, start | $64x64$ pixel$^2$ | $128x128$ pixel$^2$ |
| Weighting | none | none |
| Iterations | 1 | 1 |
| Interrogation area size, final | $16x16$ pixel$^2$ | $24x24$ pixel$^2$ |
| Weighting | none, circle | none, circle |
| Iterations | 2 | 3 |
| Overlap | $50\%$ | $50\%$ |
| 3D vector validation | 1 pixel | - |
| Q-Peak | 4 | 4 |

## 5.2 Aerodynamic results

This section serves to put the aerodynamic results in context with the heat transfer measurements from section 4. A connection between the aerodynamic phenomena in front of the leading edge and the distribution of adiabatic heat transfer coefficients as well as cooling effectiveness is made. Mainly, flow field results are presented as time-averaged data from 1000 single PIV recordings to allow for a statistical assessment of some of the phenomena. Results for other lateral positions than the displayed can be found in the appendix.

### 5.2.1 Reference case without secondary air injection

The reference case without secondary air injection points out the influence of varying blowing rates on the aerodynamic characteristics of the flow in front of the airfoil which are addressed later in this section. The formation of a multiple vortex system in front of the leading edge is proposed by many researchers like Goldstein and Spores [46], Devenport and Simpson [47] or, more recently, Praisner [48]. Praisner visualises a vortex system consisting of the horseshoe vortex (HV), an adjacent secondary vortex (SV) with an opposite rotational sense and another vortex with the same rotational sense like the horseshoe vortex, denoted as tertiary vortex (TV), which are both located upstream of the horseshoe vortex. A fourth vortex is situated near the junction of the airfoil and the endwall. It is named corner vortex (CV) and its size is much smaller compared to the other vortices, but an upscaled water flow channel enables the spatially resolved detection of this vortex as a steady flow characteristic. This vortex is assumed to form from a separation of the boundary layer of downwashed fluid on the airfoil leading edge [48]. Figure 5.3 shows a schematic of the proposed vortex system in the symmetry plane in front of the leading edge.
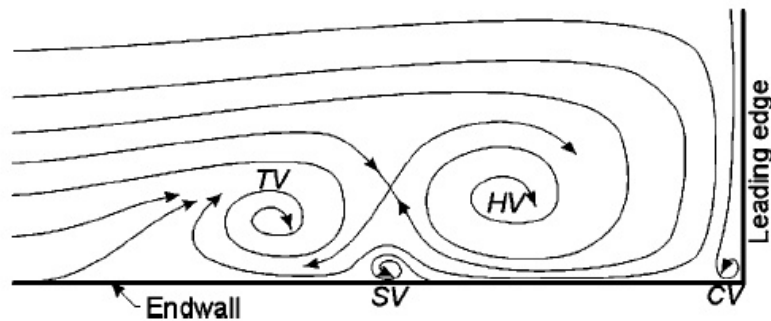


**Figure 5.3:** Schematic of the vortex system in the symmetry plane in front ot the leading edge as proposed by Praisner [22]

Praisner also elucidates the transition of the vortex system between different flow modes which directly affects the heat transfer on the endwall. The details of this transition are confirmed in the work of Thrift et al. [49] as well. It is displayed in figure 5.4 and can be summarised as follows: Firstly, a reverse flow beneath the horseshoe vortex passes above the secondary vortex which is located near the endwall (a). This pattern is described by Thrift et al. as the predominant state over the better part of the time. Secondly, the reverse flow merges with the secondary vortex while a portion of the flow above the tertiary vortex is directed perpendicularly to the endwall between the secondary and the tertiary vortex (b). Thirdly, the secondary vortex, grown in strength and size, erupts and moves away from the endwall (c). In this pattern, an inrush of flow from above the tertiary vortex is directed to the endwall where the secondary vortex used to persist. Finally, the secondary vortex moves above the horseshoe vortex and this quasi-periodic flow pattern repeats (d) [22]. During this process the horseshoe vortex core is observed to move about $\pm 0.04\,D$ in a streamwise direction. The implications for the heat transfer on the endwall will be addressed later in this section.

### Vortex location

The time-averaged results by Praisner [48] in figure 5.5 feature streamlines of the vector field in front of the leading edge. Reynolds numbers with respect to the leading edge diameter range around $Re_D \approx 24000$. The respective distances from
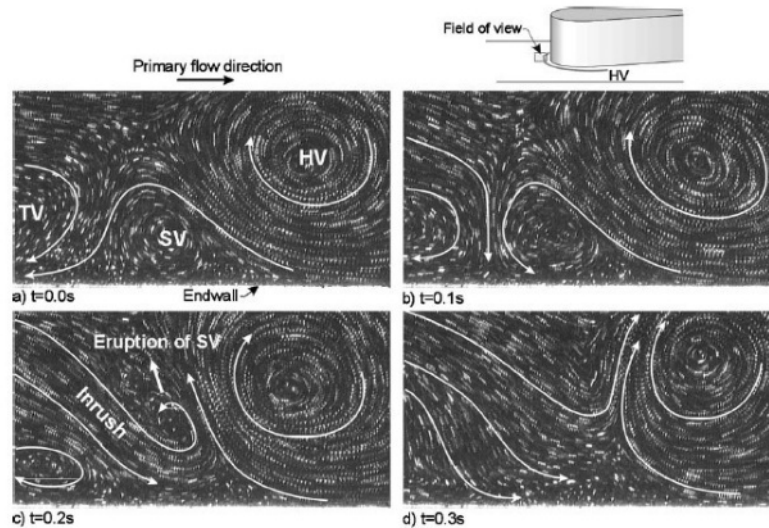
**Figure 5.4:** Transition of the vortex system in front of the leading edge between different flow modes, eruption of the SV [22]

the leading edge $x$ and from the endwall $z$ are scaled with the tip diameter $D$. The background colour in this illustration discriminates different rotational senses. Note that the upward direction is denoted as the y-direction unlike the z-direction in the coordinate system defined for the measurements in the present work.
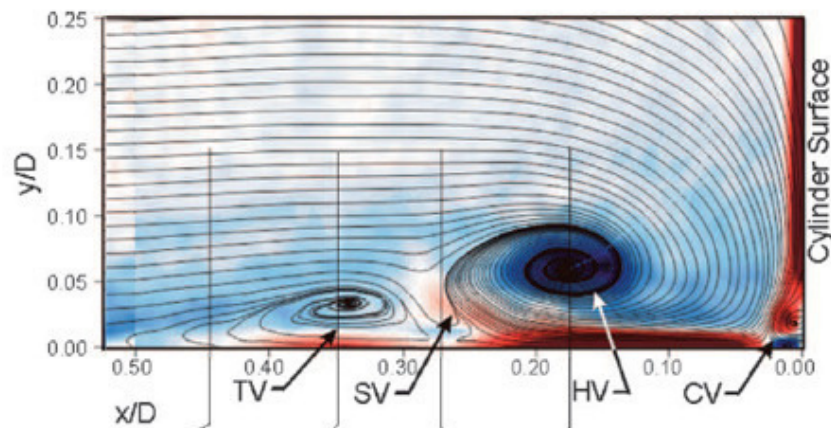


**Figure 5.5:** Time-averaged high-density PIV recordings by Praisner [48] (y-axis added)

It can be seen that Praisner identifies the large horseshoe vortex at a location of $x/D = 0.18$ upstream of the leading edge and $y/D = 0.06$ above the endwall. Primary flow from above the vortex structure is deflected and washed down onto the endwall between the horseshoe vortex and the leading edge. The newly formed boundary layer on the leading edge surface subsequently rolls up into the corner vortex. Upstream of the horseshoe vortex the secondary vortex is spotted from its opposite rotational sense, resulting in streamlines which bend towards the horseshoe vortex in a confined region around $x/D \approx 0.25$. The tertiary vortex can be found adjacent to the secondary vortex farther upstream. Praisner hints at the fact that its presence is not evident from the vorticity distribution alone, but the streamlines strongly suggest that it is centered around $x/D \approx 0.35$. The separation point of the endwall boundary layer is located between $x/D = 0.55$ and $x/D = 0.45$ based on a turning point in the streamwise velocity profile along $y$ [48].

Results of the PIV recordings in the reference case without secondary air injection conducted in the present work are given in figure 5.6. The distances from the leading edge which is indicated by a gray block on the right and the location above the

endwall are given on the x-axis and on the z-axis, respectively. Dimensions are scaled with the diameter of the leading edge tip being 30 mm. The streamlines in the x-z-plane are calculated from the averaged vector field.
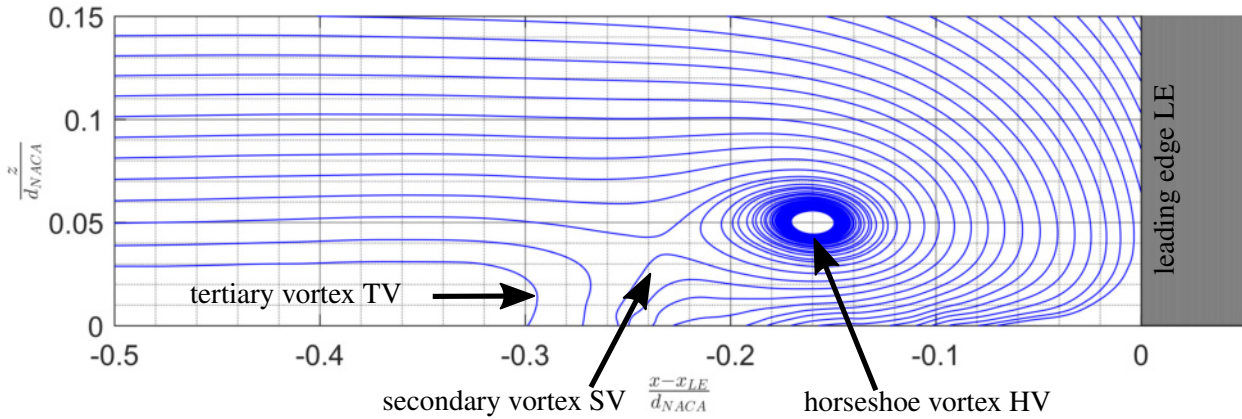


**Figure 5.6:** Location of the horseshoe vortex in the symmetry plane for the reference case without secondary air injection

A distinct region where streamlines roll up clockwise to form the horseshoe vortex is observable between $0.2\,\mathrm{d_{NACA}}$ and $0.12\,\mathrm{d_{NACA}}$ upstream of the leading edge. The center of the HV can be located at $x - x_{LE} = 0.16\,\mathrm{d_{NACA}}$ and $z = 0.05\,\mathrm{d_{NACA}}$ estimated from the streamline topology. This position compares well with the findings by Praisner [48]. It is also in good accordance with the results along the stagnation plane by Thrift and Thole [50] who carried out flow visualisations in a vane cascade at slightly higher Reynolds numbers of $Re_D \approx 50000$. The fact that both Praisner [48] and Thrift and Thole [50] observe identical flow patterns at Reynolds numbers below and above the Reynolds number configuration in this work supports the reliability of the present results.

One implication of the aforementioned reflections near the endwall is that only few particles are identified in this area or that particles are not matched correctly in double-frame recordings. As the reflections exemplified in figure 5.2(a) exhibit high intensity levels a subtraction of background images without seeding might also remove the particles from the images. Streamlines are not as dense near the endwall and upstream of the location of the horseshoe vortex as in the rest of the observed region.



**Figure 5.7:** Location of the vortex system in the symmetry plane in an instantaneous PIV recording

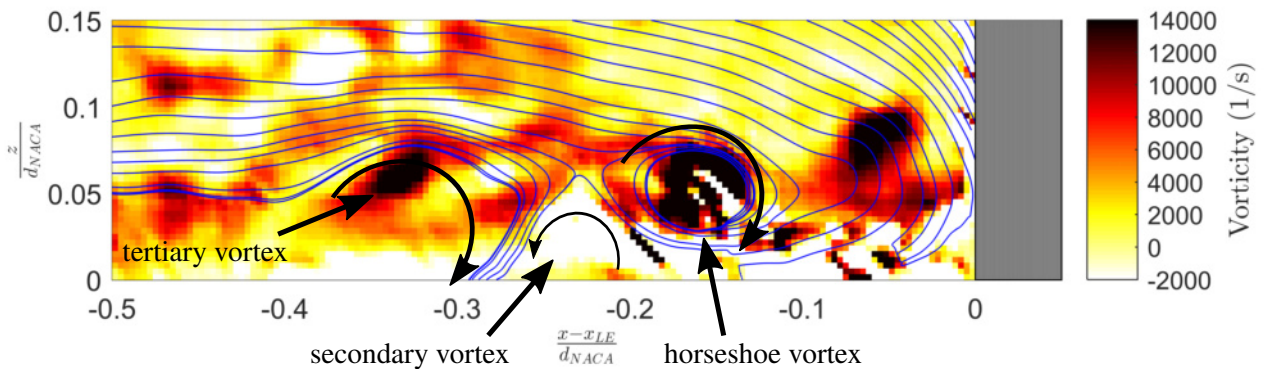A corner vortex near the leading edge is not present in the time-averaged results. Both the secondary vortex and the tertiary vortex are not identifiable from the streamlines as explicitly as in the results by Praisner [48] in figure 5.5. Their respective rotational sense can be derived from the direction of the streamlines upstream of the horseshoe vortex in figure 5.6. The lack of a sufficient amount of particles in the near-wall region is expected to cause this improper visualisation of the secondary and the tertiary vortex in time-averaged results. In many instantaneous PIV recordings the vortex structures are visible more clearly although regions with few data available in the vector field still exist. Both in the time-averaged results and in the instantaneous recording the streamline topology around the secondary vortex strongly resembles the flow mode described by Thrift et al. [49] as the most stable one where the reverse flow beneath the horseshoe vortex passes over the secondary vortex.
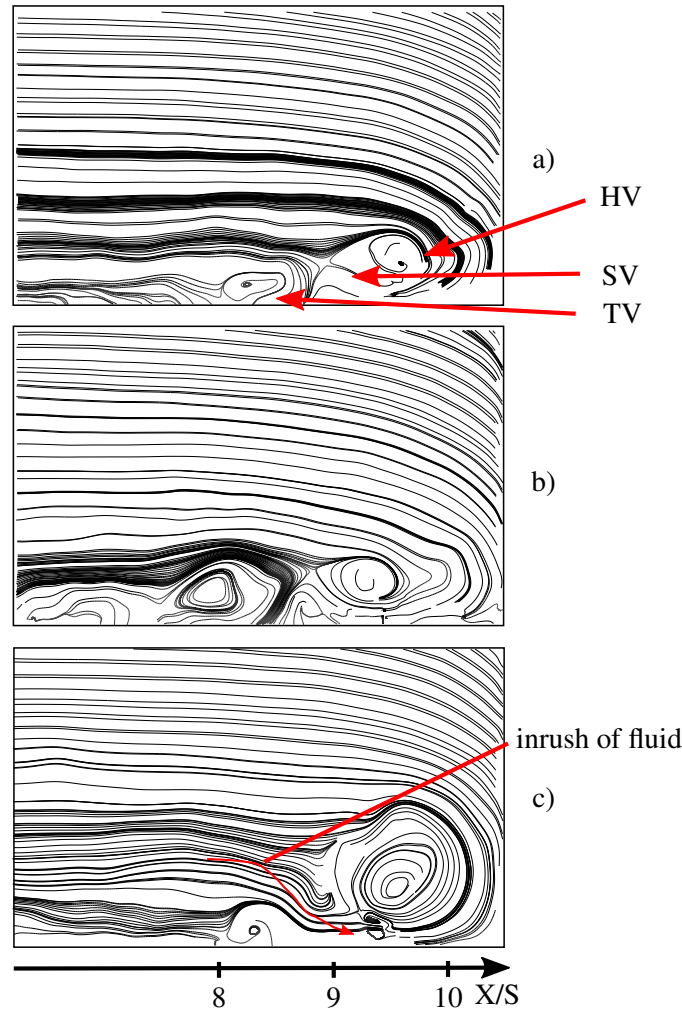


**Figure 5.8:** Instantaneous PIV recordings from the reference case capturing the transition between flow modes in the vortex structure

Streamwise movements of the horseshoe vortex core are detectable between as far as $x - x_{LE} = -0.11\,\mathrm{d}_{NACA}$ and $x - x_{LE} = -0.19\,\mathrm{d}_{NACA}$, but the distinctive movement of the secondary vortex above the horseshoe vortex is not obvious from subsequent PIV recordings of this work. This greater frame of streamwise displacement of the horseshoe vortex core compared to those reported by Praisner [22] and Thrift et al. [49] implies that other instabilities might be present and impact the formation of the characteristic vortex system. A disturbance by the adhesive tape as mentioned in section 4.4.1 cannot be entirely negated as the boundary layer has not been surveyed.

However, as will be shown later the existence of both the secondary and the tertiary vortex with their characteristic flow patterns is suggested in this setup from the comparison of time-averaged aerodynamic data and heat transfer data. Figure 5.7 shows the same scope like figure 5.6 with streamlines and overlaid vorticity $\omega_y$ in the x-z-plane from a single PIV recording. The definition of the vorticity and its component in the x-z-plane are given in equation 5.2. Both the secondary and the tertiary vortex are more evident than in the time-averaged results. Especially the secondary vortex can be derived from the streamlines and from the concentrated positive vorticity indicating a clockwise rotational sense.

$$\vec{\omega} = \nabla \times \vec{u} \qquad \omega_y = \frac{\delta u_x}{\delta z} - \frac{\delta u_z}{\delta x} \qquad\qquad\qquad (5.2)$$

The streamlines at a streamwise position approximately $0.35\,d_{NACA}$ upstream of the leading edge where the tertiary vortex is assumed show a circular course enclosing spots of high vorticity as it is the case for the horseshoe vortex as well.

On the contrary, the corner vortex which is located directly in front of the leading edge in the results by Praisner [48] cannot be seen in any of the instantaneous PIV recordings. It is assumed that the spatial resolution is not fine enough to resolve this structure whose size is estimated by Praisner with 25 % of the diameter of the horseshoe vortex [48]. The low density of seeding particles and the light scattered by reflections and the smearing of seeding oil on the leading edge surface might also prevent a proper visualisation of this vortex.

A series of instantaneous PIV recordings from the reference case with a relative time difference of $0.0714\,\mathrm{s}$ is shown in figure 5.8. The transition described by Praisner [22] and by Thrift et al. [49] can be seen in the three subsequent images. It compares well with the illustration in figure 5.4. At first, the horseshoe vortex feeds the secondary vortex and the streamlines indicate a stagnation point on the endwall between the tertiary and the secondary vortex (a). Then, the tertiary vortex is intensified (b) before the secondary vortex finally collapses and fluid from above the tertiary vortex runs beneath the horseshoe vortex (c). The location of the inrush of fluid from this exemplary extraction matches well with the average location of the local maximum of heat transfer coefficients as will be shown in the next section.

## Influence on the endwall heat transfer

Implications of the aerodynamic measurements on the endwall heat transfer are presented in figure 5.9. The upper part of the figure shows the course of the Stanton number along $Y/S = 0$. The bottom part depicts the same streamwise scope with streamlines and vorticity distributions from time-averaged data. A gray block on the right side represents the leading edge. Dimensions are scaled with the slot width $S$ again as known from the presentation of the heat transfer measurements in section 4. The height of the displayed area reaches up to $8\,\mathrm{mm}$ above the endwall.

Starting from shortly downstream of the slot injection regions of high vorticity values are visible in the aerodynamic results. These regions are restricted to a height of about $0.2\,Z/S$ and are in accordance with the theoretical distribution of swirling strengths in the near-wall region. Large vorticity values occur in this region because the horizontal velocity component $u_x$ varies strongly while the vertical component $u_z$ only features small gradients. However, reflections on the endwall strongly influence the amount of seeding particles being tracked in this region as stated before. Data are therefore not considered representative of the actual flow conditions within this confined distance from the endwall and up to approximately $X/S = 6$. Farther downstream, Stanton numbers remain almost constant and do not rise up to a running length of $X/S \approx 7$ as it is described in section 4.4.1. This position coincides with the location of the boundary layer separation point suggested by Eckerle and Langston [51] who expect it approximately half a diameter upstream of a cylinder in a flow field. They observe a rise in the static pressure at the endwall from this point on in front of the cylinder.

The characteristic course of Stanton numbers in front of the leading edge tip can be combined with the results from aerodynamic investigations. The first band of local maximums wrapped around the leading edge coincides with the notional location of the secondary vortex. Praisner attributes it to the inrush of fluid from above onto the endwall. A short temporal delay between the transition to this particular flow pattern and the increase in heat transfer to the endwall supports this interpretation [22]. The following local minimum in Stanton numbers is, in accordance with the time-averaged results by Praisner [48], situated within the region of a reverse flow beneath the horseshoe vortex. In his work, Praisner localises this local minimum of heat transfer coefficients near the separation point of the reverse flow boundary layer, identified by a point of vanishing wall shear stress [48].

Finally, the rising heat transfer coefficients towards the leading edge tip are explained with the high amount of fluid being washed down from the primary flow which is evident from the streamline topology in figure 5.9. Another drop in Stanton numbers right before the leading edge can also be seen in the results by Praisner [48], coinciding with the location of the stagnation point of the boundary layer on the leading edge surface directly above the endwall. However, it is neither observed by Thrift et al. [49] who do not observe the corner vortex nor by Milidonis [44].

In a plane perpendicular to the streamwise direction and $0.5\,D$ downstream of the leading edge, Praisner [48] observes that
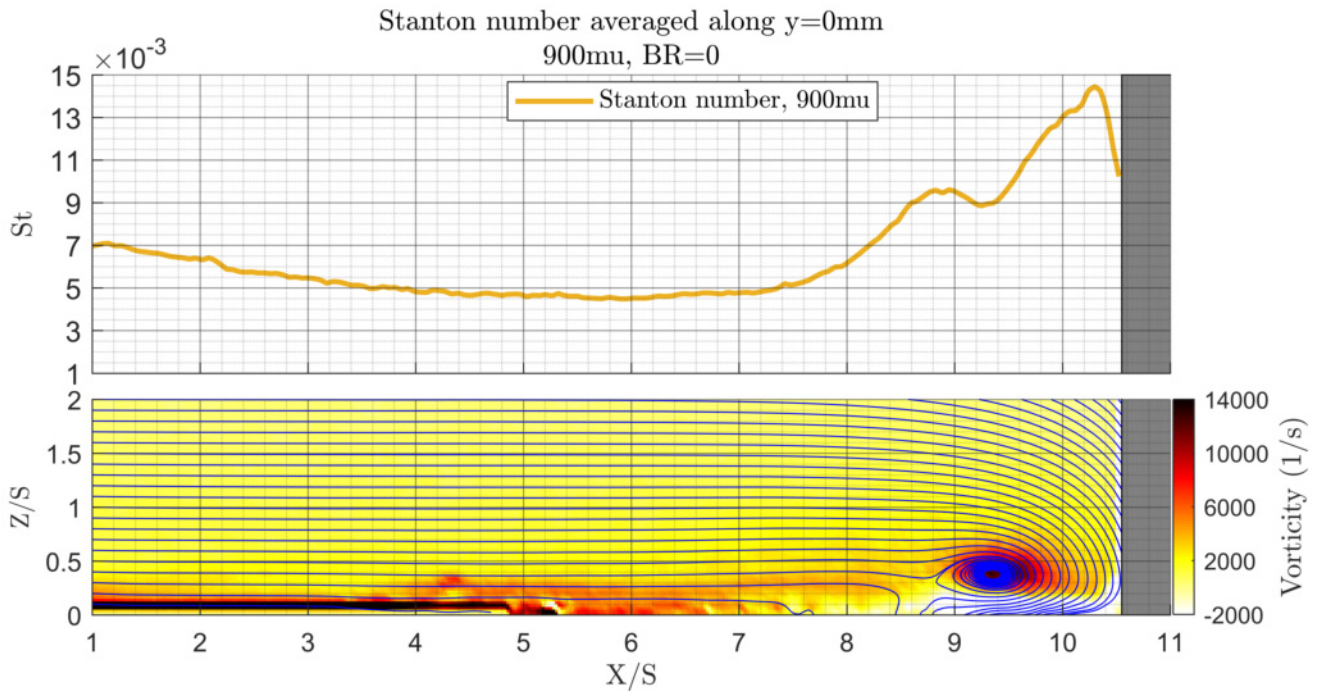
**Figure 5.9:** Stanton number along the symmetry line for the reference case without secondary air injection, combined with streamlines from the aerodynamic measurements below

the horseshoe vortex branches propagate while moving away from the endwall. Although this effect cannot be observed in the limited laterally displaced planes in this work the surface data of Stanton number distributions such as in figure 4.18(a) show that the region of impact on the endwall heat transfer becomes smaller with growing lateral displacement from the symmetry plane. The narrowing band of local maximums in heat transfer coefficients mentioned in section 4.3.1 matches this description of the horseshoe vortex moving away from the endwall with higher downstream distance.

Temporal deviations of adiabatic heat transfer coefficients are derived from 1000 images with the camera output signal. Once the adiabatic heat transfer coefficients are calculated from averaged data in the evaluation procedure *HTCVal1.7* a functional relation between the averaged camera signal at a fixed set temperature of the heated endwall and the adiabatic quantities is created. A polynomial fit of degree four is used which reflects the $T^4$-relation expressed in *Boltzmann's Law* (compare equation 2.11). It is illustrated in figure 5.10 with the ensemble of camera signal-*HTC* pairs used for the mathematical fit in the reference case. The ensemble is taken from a representative region along the streamwise direction with a vast span of heat transfer coefficients. The functional relation is then applied to 1000 raw images of the same scene taken at the same set temperature as the averaged data used to derive this dependence. This way, a qualitative evaluation of adiabatic heat transfer coefficients for 1000 single images is achieved.

Figure 5.11 puts the temporal fluctuations of heat transfer coefficients in context with the temporal fluctuations observed in the aerodynamic measurements of velocities. The standard deviation of Stanton numbers is scaled with the maximum value obtained along the symmetry line whereas the standard deviation of the absolute velocity (including the component normal to the x-z-plane) is normalized with the average inlet velocity in the flow channel.

A distinct concentration of high velocity fluctuations can be seen near the endwall at running lengths between $X/S = 7.5 - 9$. It covers the locations of the tertiary and the secondary vortex. The region of high fluctuations includes the area where the inrush of fluid from above the vortex system is observed with a quasi-periodic behaviour by Praisner [22] and Thrift et al. [49]. Both the elevated heat transfer and the increased velocity fluctuations coinciding with the assumed position of this event suggest that they are existent and strongly influence the heat transfer to the endwall. The temporal deviations of Stanton numbers reach their maximum at a running length $X/S = 9$ which is in good accordance with the area where the inrush of fluid onto the endwall takes place.

Another area of relatively high fluctuations is congruent with the core of the horseshoe vortex and extends in streamwise
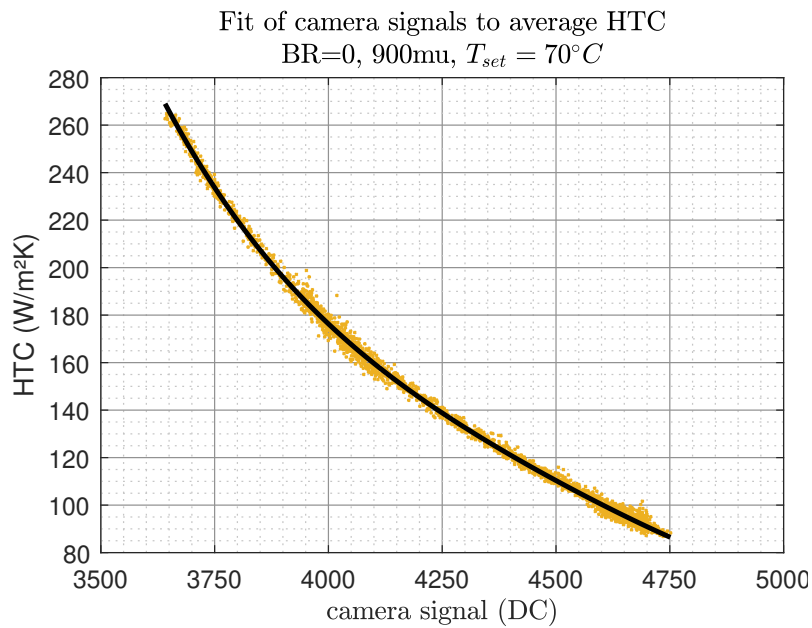
**Figure 5.10:** Polynomial fit of degree 4 between averaged camera signals and adiabatic heat transfer coefficients
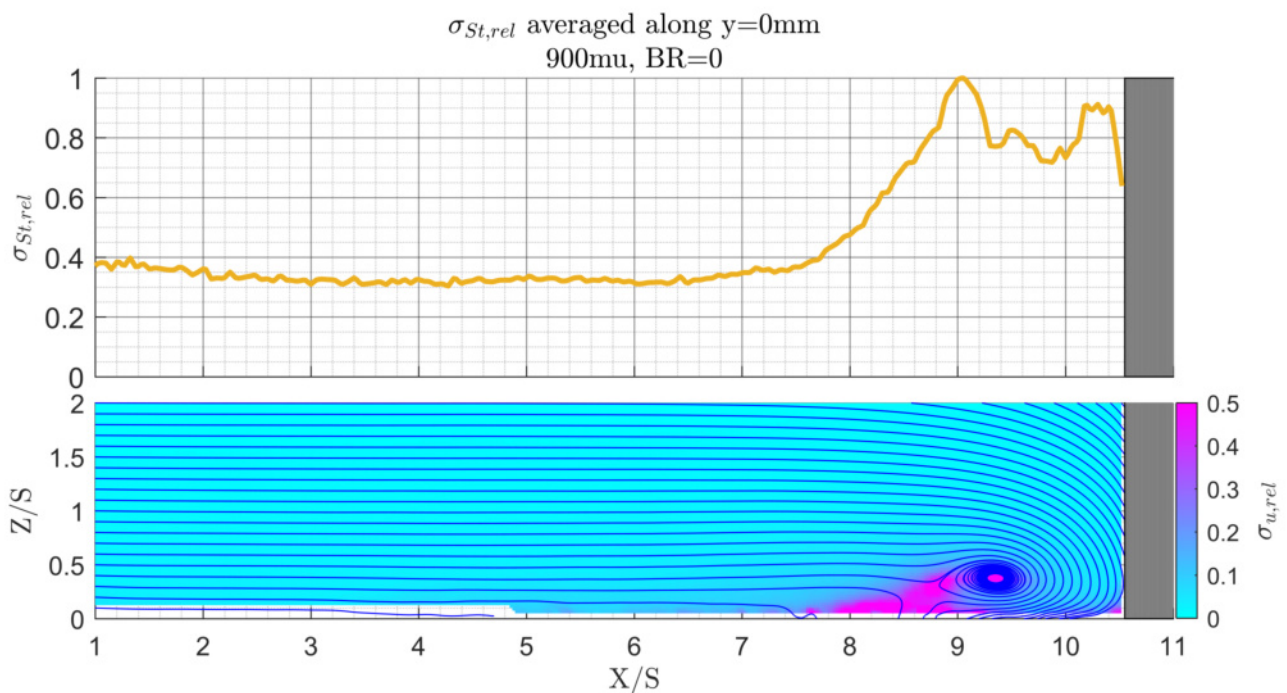


**Figure 5.11:** Normalized standard deviation of Stanton numbers and normalized standard deviation of absolute velocity in the symmetry plane

direction, implying temporal movements along this direction. The fact that Stanton numbers show no striking temporal deviations for running lengths shorter than $X/S = 7$ supports the assumption that high vorticity values like those in figure 5.9 in said region are not representative for the flow configuration.

## 5.2.2 Secondary air injection and variation of blowing rates

The following sections contain results from heat transfer measurements and from aerodynamic measurements for all cases with secondary air injection. They are compared to the findings in the reference case introduced in the previous section.

### Vortex location

The location of the horseshoe vortex as a stable flow phenomena in temporally averaged results varies strongly with the blowing rate of secondary air injection. This effect has already been expected from the shift of heat transfer maximums and will be addresses in the next section.
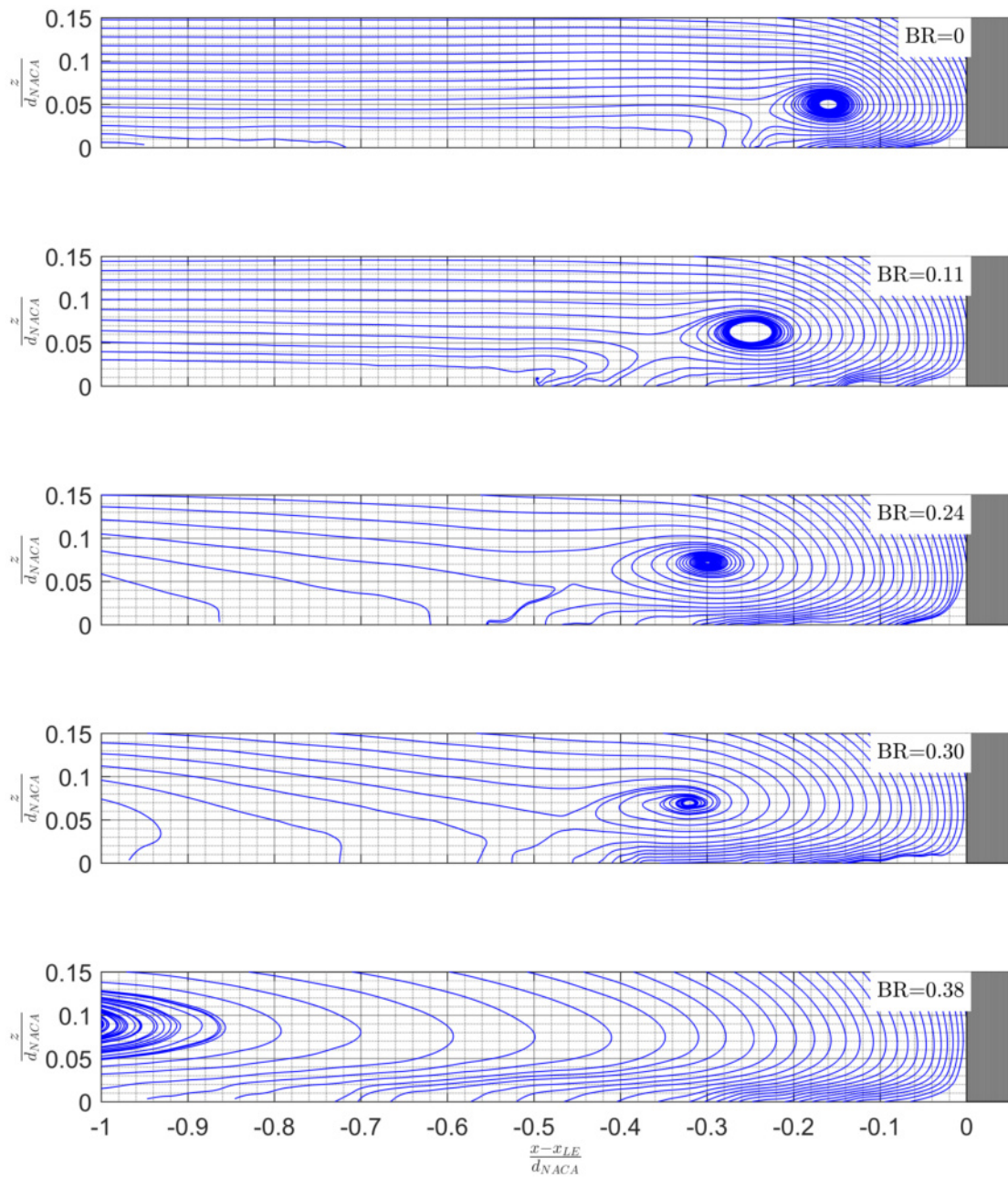


**Figure 5.12:** Streamline topologies indicating the location of the vortex system at different blowing rates

Figure 5.12 juxtaposes streamline topologies from time-averaged PIV results in the symmetry plane for different blowing rates. The streamwise distance is shown starting at $1\,\mathrm{d_{NACA}}$ upstream of the leading edge in order to capture the location of the tertiary vortex as well for higher blowing rates. The movement of the horseshoe vortex dependent on the blowing rate can be summarised as follows: At all blowing rates examined except from the highest one a distinct structure of the horseshoe vortex is existent like it has been presented for the case without secondary air injection. The horseshoe vortex moves towards shorter running lengths with rising secondary air injection. While the core of the horseshoe vortex is located $0.16\,\mathrm{d_{NACA}}$ upstream of the leading edge in the reference case, it can be estimated at $0.25\,\mathrm{d_{NACA}}$ at a blowing rate of $0.11$ and at $0.3\,\mathrm{d_{NACA}}$ upstream of the leading edge at a blowing rate of $0.24$. At a blowing rate of $0.30$ it is found $0.32\,\mathrm{d_{NACA}}$ in front of the leading edge which is equivalent to a shift of $0.14\,\mathrm{d_{NACA}}$ or $4.2\,\mathrm{mm}$ compared to the reference case. Anti-clockwise curvatures of the streamlines upstream of the horseshoe vortex which are indicative of the existence of a secondary vortex (compare section 5.2.1) move even farther upstream. The same applies to the structures attributed to the tertiary vortex whose most downstream streamline indication moves from $0.25\,\mathrm{d_{NACA}}$ in the reference case to more than $0.5\,\mathrm{d_{NACA}}$ away from the leading edge at $BR = 0.30$. A similar movement applies to the upward location in z-direction of the horseshoe vortex. Between the reference case and the blowing rate $BR = 0.30$ the vortex core moves from $0.05\,\mathrm{d_{NACA}}$ above the endwall to approximately $0.07\,\mathrm{d_{NACA}}$. These results suggest that the vortex structures elucidated for the reference case and compared with descriptions from literature are also existent in configurations with secondary air injection. Their occurrence varies, but their qualitative impact on the endwall heat transfer might be the same. However, the inspection of several instantaneous PIV recordings implies that especially the tertiary vortex structure is not as stable as in the reference case.

The extension of the reverse flow beneath the horseshoe vortex grows in streamwise direction with higher blowing rates. This can be seen in the streamlines downstream of the horseshoe vortex which run parallel to the endwall and penetrate farther into the upstream region where the aforementioned fluid inrush takes place. At the highest blowing rate $BR = 0.38$ a distinguished vortex structure cannot be observed any more. Nearly all streamlines originate from farther above and a reverse flow can be detected up to a height of $z = 0.05\,\mathrm{d_{NACA}}$ at the running length $0.7\,\mathrm{d_{NACA}}$ upstream of the leading edge. Whereas the streamlines in the reference case and at the lowest blowing rate $BR = 0.11$ proceed almost horizontally above $z = 0.1\,\mathrm{d_{NACA}}$ they feature a steep inclination towards the endwall at the highest blowing rate. This is expected to be caused by the deflection due to the injected secondary air.

Figure 5.13 summarises the effect of blowing rates on the position of the horseshoe vortex. Using the $\lambda_2$-criterion a vortex can be identified by the distribution of negative second eigenvalues of a matrix generated from the derivatives of the flow field velocity components [52]. This method is based on the assumption that a local minimum of the static pressure is a necessary precondition for the existence of a vortex core. The actual eigenvalue does not have a physical significance, but it serves to locate vortices in a flow field from the velocity distribution alone.[1] Two contour lines at $\lambda_2 = -5$ and $\lambda_2 = -10$ are plotted in the flow field in front of the leading edge for the different blowing rates. This way, the movement of the horseshoe vortex core can be retraced by the movement of the contour lines enclosing this vortex core. Both the secondary vortex and the tertiary vortex cannot be captured with the chosen contour limits.
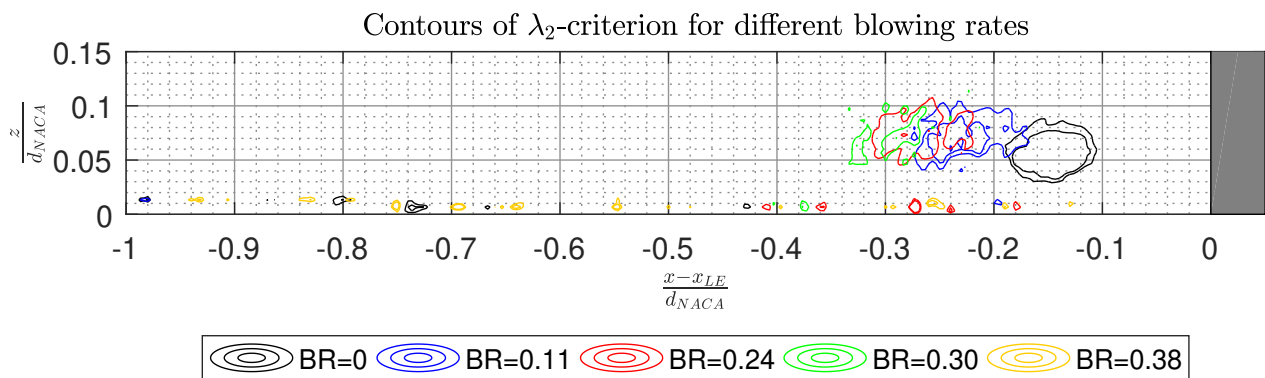


**Figure 5.13:** Identification of the horseshoe vortex core from contours at $\lambda_2 = -5$ and $\lambda_2 = -10$ of the $\lambda_2$-criterion

The upstream displacement and the upward movement of the horseshoe vortex with growing blowing rates can be seen in the shift of the closed contours in figure 5.13 as well. As only two contours are given the exact position of the vortex core cannot be determined from this depiction, but for all blowing rates the position of the vortex core derived from the interrogation of the

---

[1] For further information on the construction of the necessary matrices from velocity components consult [52] and [5]

streamline topology are included in the contours from the $\lambda_2$-criterion. Especially at the highest blowing rate the $\lambda_2$-criterion supports the fact that the vortex structures observed throughout the other blowing rates are not existent.

## Velocity profiles

The increase in secondary air mass flow with higher blowing rates also elevates the momentum ratio as the velocity of the secondary flow at the exit from the slot rises. This results in a stronger perpendicular penetration of the secondary flow into the primary flow, causing a region of low-pressure comparable to a dead-water zone downstream of the slot. Regarding the blowing rates $BR = 0.11$ and $BR = 0.38$ this development can be exemplified: At the lowest blowing rate the momentum transferred with the secondary flow and perpendicular to the streamwise direction is not sufficient to deflect the primary flow from its predominant horizontal direction. At the highest blowing rate, however, the secondary air mass flow is high enough to create a blockage for the approaching primary flow. The region of assumedly low pressure in conjunction with the stagnation in front of the leading edge causes the mixture of primary flow and secondary flow to come down to the endwall and form a massive reverse flow.

An exemplary selection of velocity profiles of the x-component $u_x$ of the absolute velocity in the symmetry plane at different running lengths is given in figure 5.14. Profiles for the lateral position $Y/S = 3$ are shown in figure 5.15. Flow field data are extrapolated to half the channel height to obtain the velocity profiles shown.
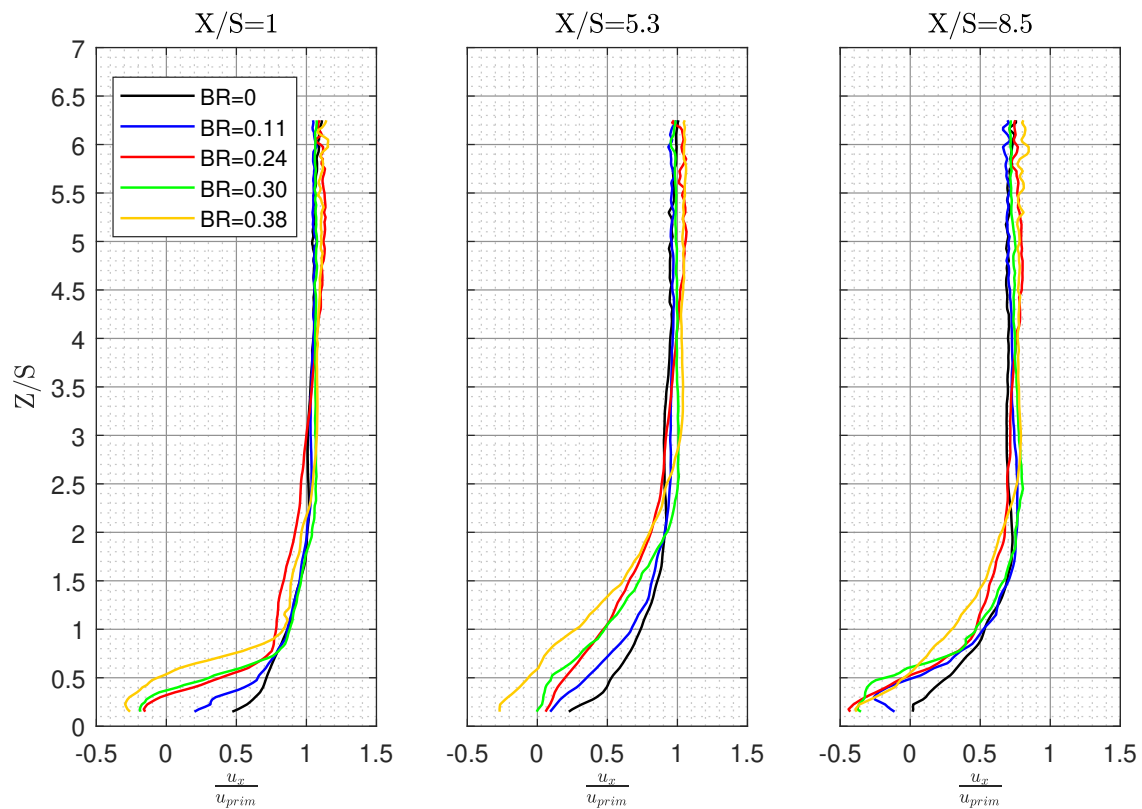


**Figure 5.14:** Profiles of the streamwise velocity component at varied running lengths

The running lengths represent a position one slot width downstream of the secondary air injection where a region of low pressure and reverse flow is assumed ($X/S = 1$), a position corresponding to the coordinate $\frac{x-x_{LE}}{d_{NACA}} = -0.7$ in figure 5.12 and the position where the local minimum in heat transfer is obtained at the blowing rate $BR = 0.24$ ($X/S = 8.5$). The latter position is chosen to point out the different locations of the reverse flow beneath the horseshoe vortex dependent on the blowing rate. At $X/S = 5.3$ it is also visible in the vector fields from the PIV recordings that the flow reattaches and two regions of reverse flow are separated. Velocities are scaled with the average streamwise primary flow velocity shortly upstream of the slot, $u_{prim} = 16.2 \frac{m}{s}$ obtained from the reference case without secondary air injection. Note that the upward z-direction is scaled with the slot width. Besides, data are spared out in the region near the endwall due to the reflections explained above.

Shortly downstream of the slot injection the velocity profiles for the blowing rates $BR = 0.11$ and $BR = 0.30$ feature the least deviation from the reference case without secondary air injection above $Z/S \approx 0.7$. At heights greater than $Z/S = 4$ velocities at the blowing rates $BR = 0.24$ and $BR = 0.38$ exceed those from the reference case by as much as $10\%$ at all running lengths. An acceleration of the primary flow due to the blocking of the lower part of the channel by the secondary air can explain this course of the profiles towards the channel centre. Obviously, at all blowing rates the streamwise velocity component is reduced in regions near the endwall compared to the reference case. This is observable at all running lengths investigated. As the vortex structures do not occur before $X/S = 5.3$ at any blowing rate the heights where the velocity profiles approximate the one from the reference case grow from $X/S = 1$ to $X/S = 5.3$. The secondary air injection supposedly decelerates the flow in streamwise direction in these lower regions, resulting in a flattened velocity boundary layer. Additionally, it can cause the aforementioned acceleration at higher blowing rates as the primary flow is deflected and its effective cross-section is reduced. This effect is definitely weakened by dissipation processes as the injection angle is perpendicular to the streamwise direction. Taking the blowing rate $BR = 0.24$, for example, the velocity gradient in the upward z-direction is lower compared to the reference case, but positive streamwise velocity components are present which allows for a detachment and a roll-up of the boundary layer into the horseshoe vortex.

A reverse flow in the near-wall region is observable at the running length $X/S = 1$ for the three highest blowing rates which feature negative velocities. This supports the assumption of a dead-water zone downstream of the slot injection caused by the perpendicular injection with elevated momentum ratio at higher blowing rates. For the highest blowing rate $BR = 0.38$ the reverse flow is furthermore evident at all running lengths. At the running length $X/S = 8.5$ velocity profiles from all blowing rates except from the reference case feature negative velocities in the near-wall region. This coordinate is equivalent to $x - x_{LE} = -0.27 \, \mathrm{d_{NACA}}$ in figure 5.12 where the impact of the horseshoe vortex and the reverse flow beneath is only captured for the cases with secondary air injection. In the reference case this coordinate corresponds to a position where streamlines from both the secondary and the tertiary vortex are directed towards the endwall and hardly any reverse flow is present.
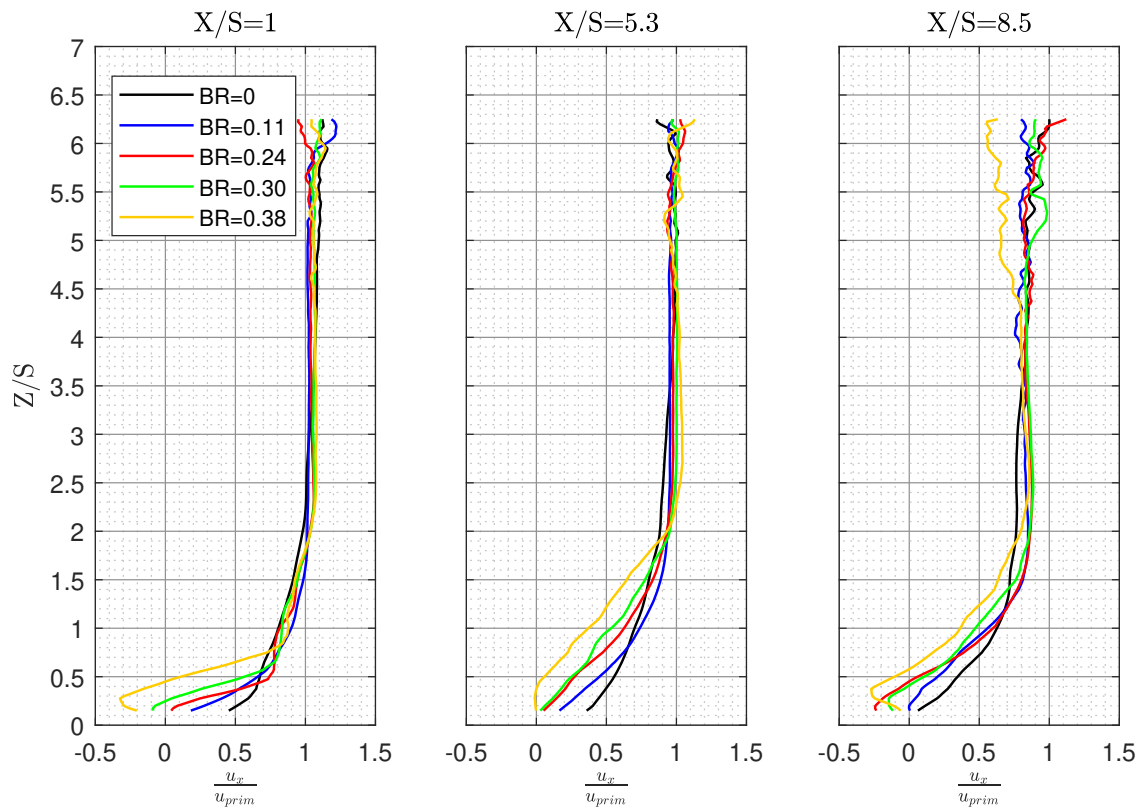


**Figure 5.15:** Profiles of the streamwise velocity component at varied running lengths and $Y/S = 3$

The velocity profiles at $Y/S = 3$ in figure 5.15 show similar developments along the streamwise direction like those in the symmetry plane. Still, the reference case features the highest velocity in x-direction at small heights $Z/S$ as no secondary air injection is present which decelerates the primary flow. It can be seen that at the highest blowing rate no reverse flow is detectable at a running length of $X/S = 5.3$ at the lateral position $Y/S = 3$. The same applies to the blowing rate $BR = 0.24$ at $X/S = 1$ shortly downstream of the slot where $u_x$ is near zero. It is expected that especially for the blowing rate $BR = 0.38$ the velocity component perpendicular to the x-z-plane rises in comparison to the results in the symmetry plane. This is

supported by the three-dimensional flow field at the lateral position $Y/S = 1.5$. These results are given in figure 5.16 showing the streamlines of the velocity components in the x-z-plane for the visualisation of the vortex structures at the intermediate blowing rate $BR = 0.24$ and at the highest blowing rate $BR = 0.38$. The y-component $u_y$ of the absolute velocity is added in the background. It is scaled with the average streamwise primary flow velocity $u_{prim}$. Be aware that the field of view which is captured by both cameras is restricted by the viewing angle. Three-dimensional flow field data are therefore not available up to the respective beginning of the airfoil contour indicated on the right side.
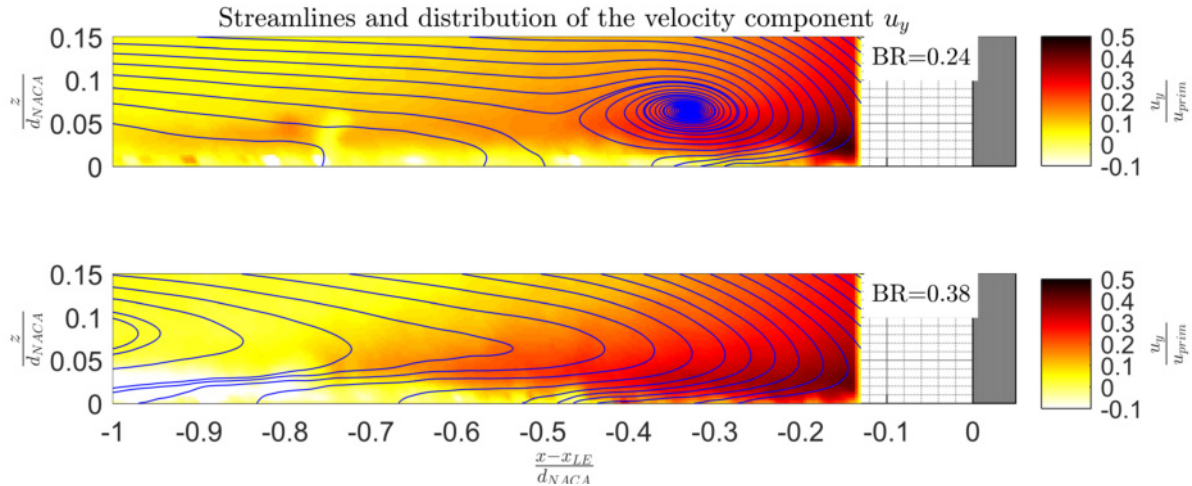


**Figure 5.16:** Streamlines and velocity component in the y-direction in the plane $Y/S = 1.5$

Velocity components in the positive y-direction increase with smaller distance to the leading edge tip at both blowing rates. This is accounted for by the lateral pressure gradient and the deflection by the airfoil. Fluid which is washed down by the horseshoe vortex features even higher velocity components in the y-direction as it approaches the endwall. Within the region of the reverse flow beneath the horseshoe vortex $u_y$ is significantly lower indicating that the vortex structure redirects the reverse flow in the streamwise direction. A notable observation is made at the highest blowing rate where the velocity component normal to the x-z-plane near the endwall switches its direction along the running length. Approaching the airfoil contour positive velocity components are present whereas negative values indicating a flow direction towards the symmetry plane are observable between shortly after the slot injection and a coordinate approximately $x - x_{LE} = -0.8\,d_{NACA}$. At the blowing rate $BR = 0.24$ and at smaller blowing rates this turn in the direction of the normal velocity component is not existent. Additionally, results at $Y/S = 0.75$ and at $Y/S = 0$ that are not displayed here in detail suggest that these velocity components grow with bigger lateral displacement from the symmetry plane.

This might be a results of the blockage of the primary flow caused by the perpendicular injection from the slot. As mentioned in section 4.4.1 this redirection towards the symmetry plane downstream of the slot is likely to explain the higher heat transfer coefficients for the highest blowing rate at the lateral positions up to a running length of $X/S = 3$ (compare figure 4.22). The redirection of the flow from lateral positions towards the symmetry plane is furthermore a consequence of the geometry of the channel. Without the channel walls as boundaries and assuming a continuous slot upstream of the measurement section this deflection would not occur.

## Influence on the endwall heat transfer

Figure 5.17 illustrates the course of Stanton numbers as well as the adiabatic cooling effectiveness $\eta_{ad}$ and the streamline topology for the blowing rate $BR = 0.11$.

The constant course of Stanton numbers reaching $St = 0.0035$ up to $X/S = 7.2$ can be explained in conjunction with the velocity profiles presented in figure 5.14. At $X/S = 1$ the streamwise velocity component is approximately $25\%$ lower compared to the reference case and at $X/S = 5.3$ it is still about $10 - 15\%$ lower. These reduced velocities lead to lower convective heat transfer on the endwall. Furthermore, primary flow is not directed towards the endwall as it is the case for higher blowing rates which will be shown later. The small amount of cooling air from the slot seems to mingle with the
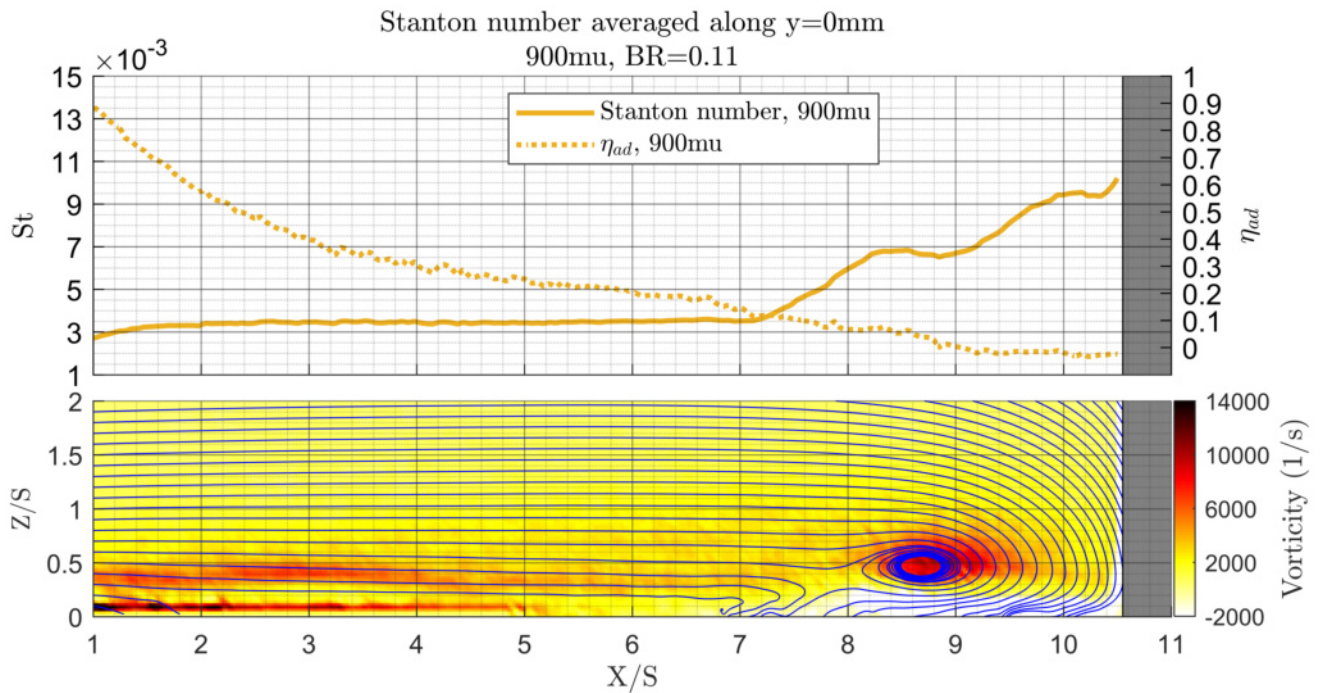
**Figure 5.17:** Stanton number along the symmetry line for the blowing rate $BR = 0.11$ combined with streamlines from the aerodynamic measurements below

primary flow quickly, reducing the temperature difference between the primary flow and the endwall. Moreover, the amount of cooling air is small resulting in lower overall cooling effectiveness levels than those obtained at higher blowing rates. Stanton numbers do not rise before $X/S \approx 7.2$ which corresponds to the location of the tertiary vortex. It cannot be deduced if this rise in heat transfer coefficients is caused by a boundary separation point like it is assumed in the reference case or if the downwash of fluid by the tertiary vortex is responsible. The characteristic maximum in Stanton numbers is located slightly downstream of the position of the secondary vortex while the local minimum coincides with the beginning of the reverse flow beneath the horseshoe vortex. From $X/S = 6.8$ on cooling effectiveness levels decrease with a higher gradient than between $X/S = 4$ and $X/S = 6.8$. Taking the vortex structures beginning at $X/S \approx 7$ into account the reduction of cooling effectiveness levels can be interpreted as follows: Cooling effectiveness decreases continuously along the running length due to heat exchange and mixing of the secondary and the primary flow. The propagation of the secondary air in the primary flow can also be deduced from the distribution of elevated vorticity between heights of $Z/S = 0.3$ to $Z/S = 0.5$. The horseshoe vortex transports fluid from above to the endwall and induces a reverse flow. This way, the residual cooling air on the endwall is washed away and replaced by fluid from farther above which has already exchanged heat with the cooling air downstream. Therefore, the drops in cooling effectiveness levels are not extremely high (approximately $-10\,\%$ at the location of the tertiary vortex), but it is entirely removed downstream of $X/S \approx 9$ where cooling effectiveness levels reach 0.
The temporal deviations of the Stanton numbers and the absolute velocity are displayed in figure 5.18.

Compared to the reference case the fluctuations of the velocity span the same characteristic region upstream of the horseshoe vortex and the core of the horseshoe vortex itself. However, the area of elevated temporal deviation in velocities covers a greater space which corresponds to the bigger vortex structures in comparison to those found in the reference case. In total, the fluctuations show higher amplitudes than in the reference case as can be seen from the colour scale. Temporal changes of heat transfer coefficients also rise significantly from $X/S = 6$ on. A maximum is attained right at the junction of the leading edge and the endwall. Potential alterations to a corner vortex in this region cannot be described because this structure is not resolved in the aerodynamic results. These statistical evaluations support the assumption that the same vortex structures are present at this blowing rate, but their occurrence is less stable than in the reference case.

Results for the next higher blowing rate are displayed in figure 5.19. In this depiction the tertiary vortex is not as evident as in figure 5.12 due to the different number of visualised streamlines.
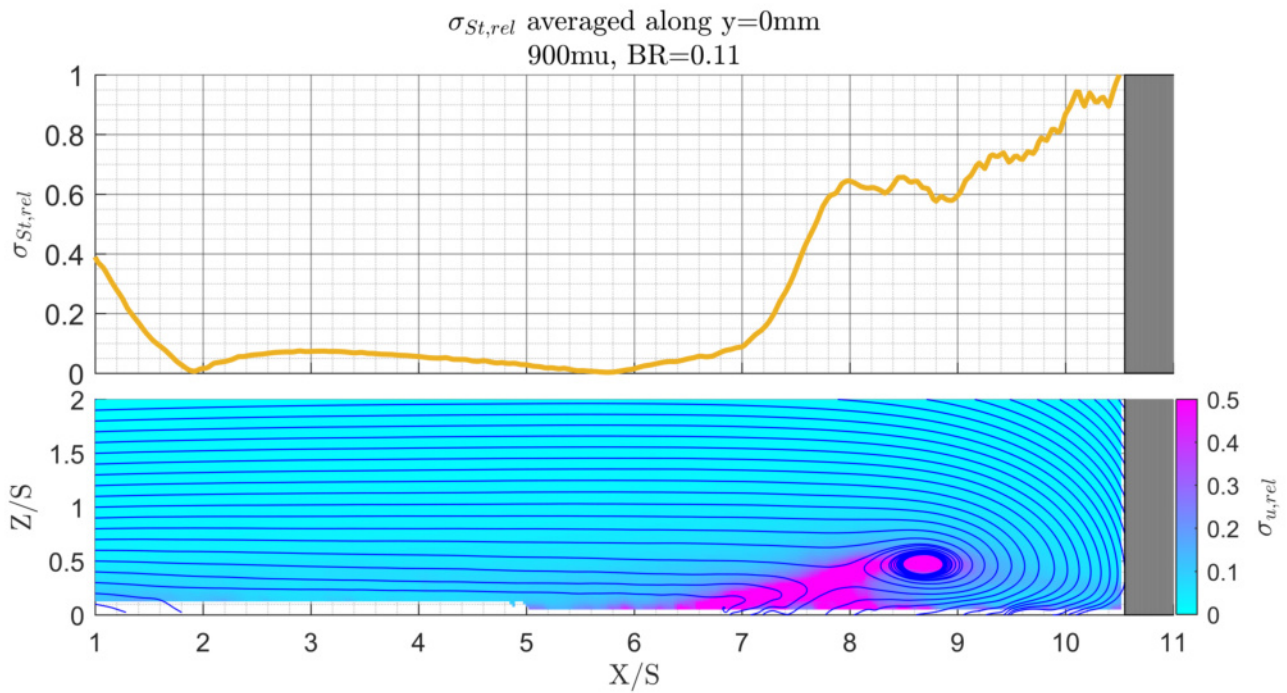
**Figure 5.18:** Normalized standard deviation of Stanton numbers and normalized standard deviation of absolute velocity in the symmetry plane line at the blowing rate $BR = 0.11$
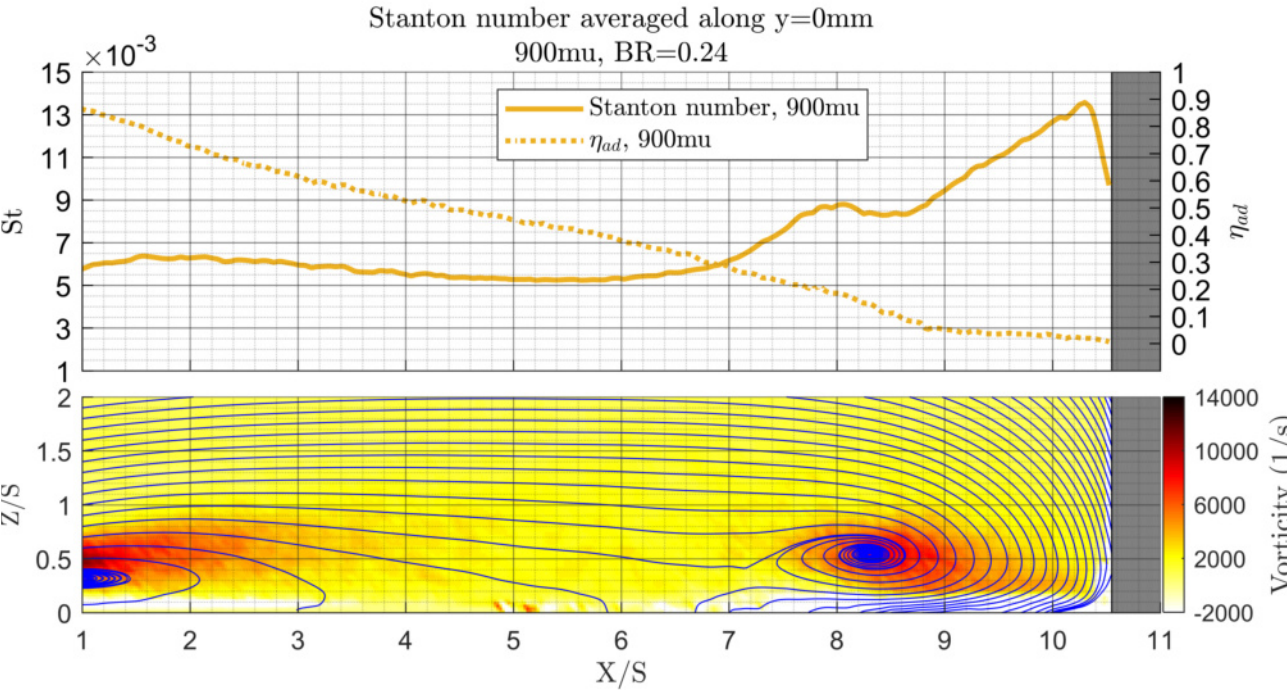


**Figure 5.19:** Stanton number along the symmetry line for the blowing rate $BR = 0.24$ combined with streamlines from the aerodynamic measurements below

Stanton numbers are increased in comparison to those at the blowing rate $BR = 0.11$, reaching values of $St = 0.0065$ at $X/S = 2$. The elevation is caused by the fluid which is directed onto the endwall rather than running parallel to the wall like

at the blowing rate $BR = 0.11$. The streamline topology in the lower part of figure 5.19 also shows how the primary flow is deflected upwards by the injected secondary air shortly downstream of the slot. Additionally, another vortex is visible from the distribution of vorticity and the streamline topology. It extends from $X/S = 1$ to $X/S \approx 3$ in this illustration. It rolls up under the influence of the perpendicular injection from the slot and results in a low-pressure area where a reverse flow can be detected in the near-wall region like it is shown in figure 5.14.

Stanton numbers begin to rise significantly at $X/S \approx 6$, a shorter running length than for the blowing rate $BR = 0.11$. Again, this position coincides with streamlines indicating a tertiary vortex. The local maximum at $X/S = 8$ is situated at the point where the reverse flow beneath the horseshoe vortex rolls up into the secondary vortex. As already stated for the reference case in section 5.2.1 a periodic inrush of fluid generated by the unstable nature of the vortex structure might impact at this point as well. A series of instantaneous PIV recordings from measurements at the blowing rate $BR = 0.24$ is exemplified in figure 5.20. The illustration corresponds to figure 5.8 where the transition between flow modes in the vortex structures is shown.
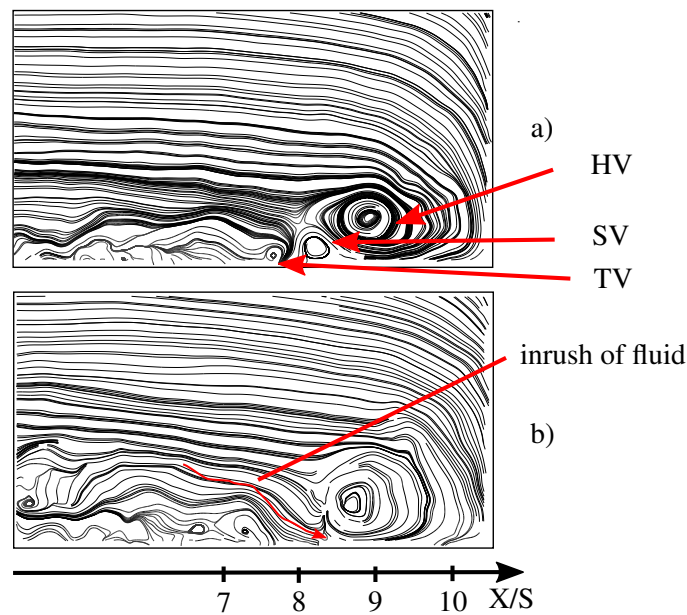


**Figure 5.20:** Instantaneous PIV recordings from measurements at the blowing rate $BR = 0.24$ capturing the inrush of fluid below the horseshoe vortex

At the first time step the horseshoe vortex, the secondary vortex and the tertiary vortex are visible in the flow field (a). Similar to the predominant flow mode in the reference case the horseshoe vortex supplies the reverse flow to the secondary vortex. Streamlines of the secondary vortex run beneath the tertiary vortex. The next time step shows the same transition like in the reference case, namely the collapse of the secondary vortex and the flow towards the endwall at its former position (b). Comparing these snap-shots to the average results in figure 5.19 it can be seen that the position of the inrush of fluid coincides with the local maximum of Stanton numbers The location of the horseshoe vortex core is determined at $X/S \approx 9$ instead of $X/S = 8.2$ like in the averaged results which gives an estimate of the streamwise range where the horseshoe vortex performs oscillating movements. These images confirm that the transition between different flow modes of the vortex structure also occurs in the presence of secondary air injection and impacts the endwall heat transfer accordingly.

Higher values of Stanton numbers towards the leading edge tip are mainly driven by the grown size of the vortex structure and the displacement farther upstream. This forces more fluid to wash down onto the endwall and accelerating upstream into the reverse flow. At $X/S = 9$ the absolute streamwise velocity component below the horseshoe vortex is found to be 20% higher than for the blowing rate $BR = 0.11$, increasing convective heat transfer in this region.

Cooling effectiveness levels are higher than for the blowing rate $BR = 0.11$ along the entire running length which can be explained with the accelerated mixing process of secondary and primary air due to the higher momentum and the higher secondary mass flow. The drop in cooling effectiveness levels mentioned in section 4.4.2 and explained above for the blowing rate $BR = 0.11$ is also evident in figure 5.19. Cooling effectiveness at $BR = 0.24$ decreases steadily up to a running length of $X/S = 8$ where the decrease suddenly strengthens. This particular point is located beneath the horseshoe vortex suggesting the same mechanism of residual cooling air being washed away from the endwall like at the blowing rate $BR = 0.11$. From $X/S = 9$ on cooling effectiveness levels decrease with a lower gradient an decline to zero right in front of the leading edge

tip.

Figure 5.21 adds the depiction of temporal deviations in heat transfer coefficients and velocities to the understanding of the flow configuration.
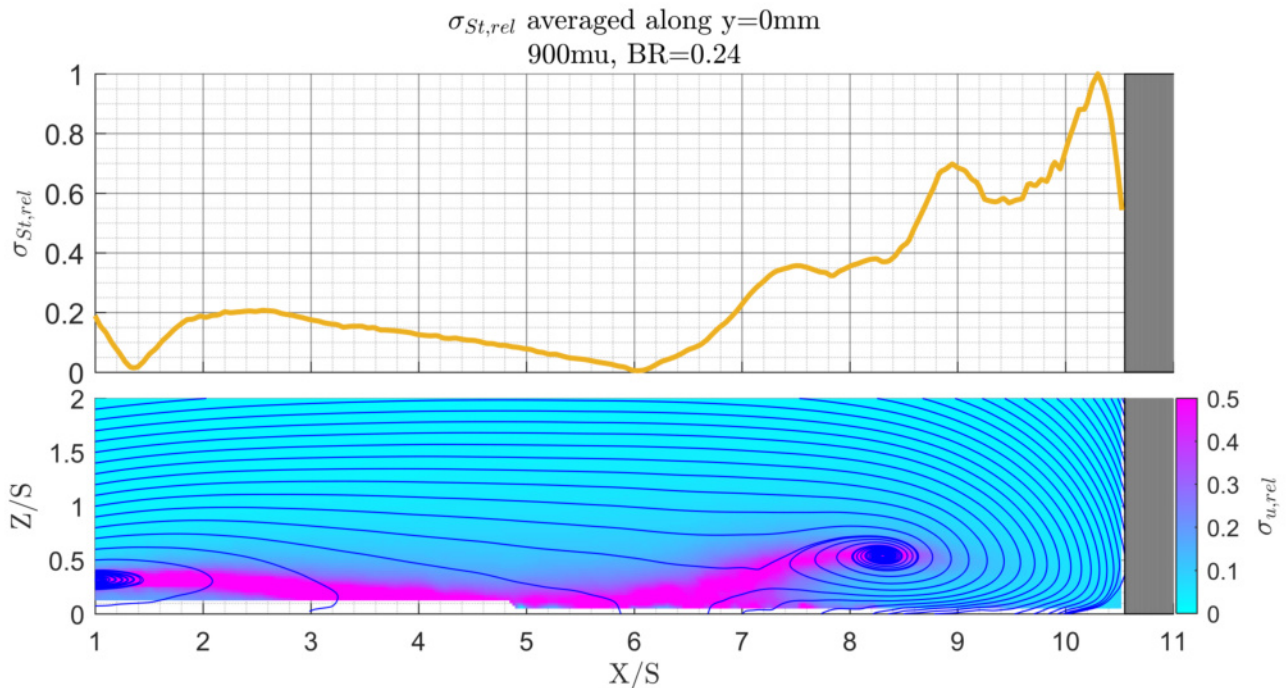


**Figure 5.21:** Normalized standard deviation of Stanton numbers and normalized standard deviation of absolute velocity in the symmetry plane at the blowing rate $BR = 0.24$

Apart from the region of high deviations where the secondary and tertiary vortices are expected the velocity fluctuations occur along the whole running length and up to $Z/S = 0.4$. The interrogation of temporally resolved PIV recordings shows that unstable detachments and vortex developments take place in the region downstream of the slot injection. However, the reverse flow above the endwall in the averaged results seems to be a stable flow characteristic as the temporal fluctuations of heat transfer coefficients within this area are comparably low. The highest fluctuations in heat transfer coefficients are found near the leading edge tip followed by locations downstream of the horseshoe vortex as well as in the vicinity of the secondary vortex.

The variation of blowing rates between $BR = 0.24$ and $BR = 0.30$ shows similar aerodynamic results as it is expected from the courses of Stanton numbers presented in figure 4.19 and the nearly congruent cooling effectiveness levels given in figure 4.24.

The streamline topology in figure 5.22 mainly differs in the streamwise extension of the vortex generated by the slot injection which is plausible due to the higher secondary mass flow. It is evident that the horseshoe vortex is weakened and features lower vorticity values than at the blowing rate $BR = 0.24$. This effect directly impacts the endwall heat transfer and the first local maximum at the position of the fluid inrush near the secondary vortex is lower, resulting in Stanton numbers of $St \approx 0.007$ compared to $St \approx 0.009$ at $BR = 0.24$. What is more, this faint local maximum is situated at the position of the horseshoe vortex core at $X/S = 8$ and a subsequent local minimum is hardly detectable. Like at the blowing rate $BR = 0.24$ a sudden drop in cooling effectiveness levels is present at $X/S = 8$ before the gradient weakens again at $X/S = 9$.

Figure 5.23 contains the temporal deviations of heat transfer coefficients and absolute velocities for the blowing rate $BR = 0.30$. These results are very similar to those at a blowing rate of $BR = 0.24$, but it can be seen that the aforementioned increase in fluctuations of the heat transfer coefficients at the respective location of the secondary vortex is no longer a local maximum. $\sigma_{St,rel}$ rises from $X/S = 6$ on and passes into a plateau of elevated fluctuations in Stanton numbers before increasing to a maximum downstream of the horseshoe vortex. It is deduced that the typical vortex structures in front of the leading edge are beginning to dissolve in the time-averaged results at this blowing rate. This interpretation matches the lower vorticity values found at this blowing rate. At shorter running lengths from the slot injection the increased temporal deviation
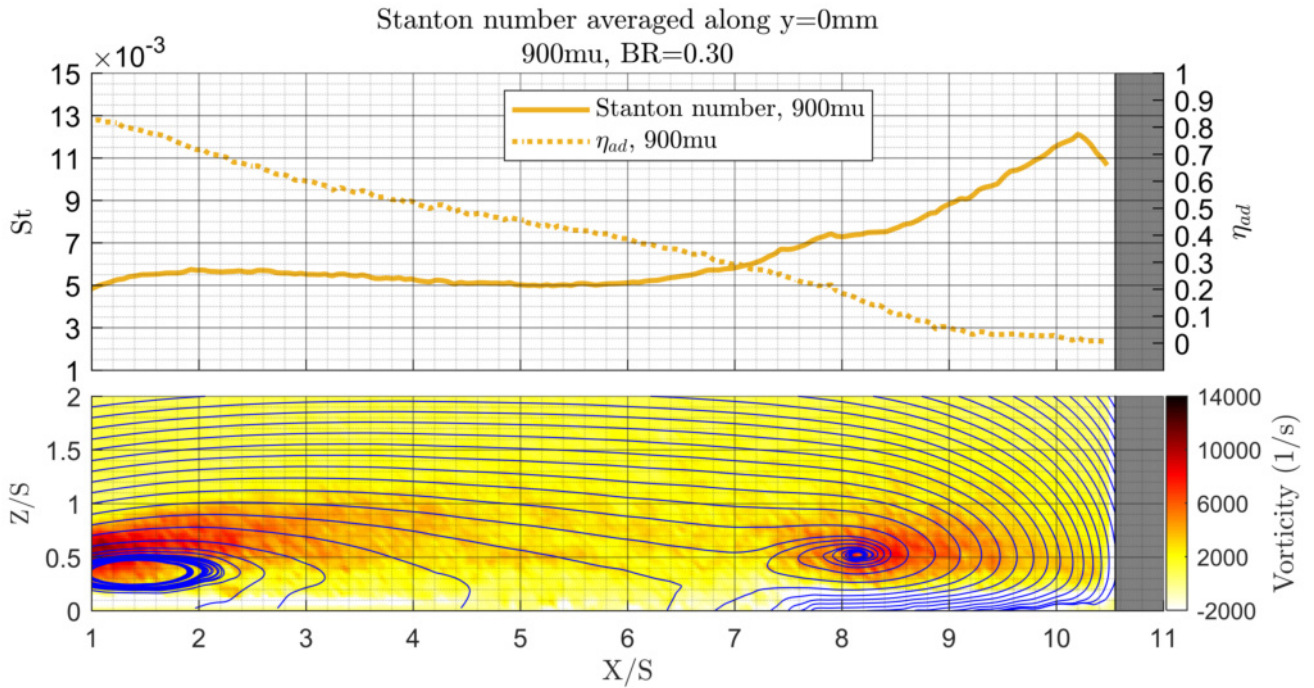
**Figure 5.22:** Stanton number along the stagnation line for the blowing rate $BR = 0.30$ combined with streamlines from the aerodynamic measurements below

of the absolute velocity spreads towards greater heights $Z/S$ compared to the blowing rate $BR = 0.24$. This indicates that the vortices induced by detachments in this area of low pressure and reverse flow in the time-averaged results exhibit a less stable nature with rising secondary mass flow.

At the highest blowing rate an entirely different streamline topology can be recognised. It is displayed in figure 5.24. Like in the reference case, streamlines are not directed towards the endwall and the reverse flow which is present along the better part of the observed running length results in a parallel flow in the near-wall region. Resulting Stanton numbers are similar to those obtained in the reference case without secondary air injection, featuring a maximum elevation of merely 0.001 up to $X/S = 7$. The indications of a counter-clockwise vorticity distribution near the endwall is plausible as the boundary layer now forms from a flow into the opposite direction. As stated before, the characteristic vortex structures described for the other blowing rates are not observable at this blowing rate. The higher amount of cooling secondary air forces the region of reverse flow to expand over the entire running length up to the leading edge tip. It is obvious from figure 5.24 that no streamlines can be captured which are directed onto the endwall and indicate separate vortices like it is found at the other blowing rates and in the reference case. Consequently, the horseshoe vortex as the dominant structure cannot form because of the missing boundary layer approaching the airfoil in streamwise direction. The distinctive local maximum and the local minimum associated with the vortex structures are not detectable, either. A small minimum in Stanton numbers at $X/S = 10.5$ is visible as it is the case for the blowing rate $BR = 0.11$. It cannot be discussed in detail if it is caused by an amplification of the corner vortex due to the higher amount of fluid being washed down along the leading edge tip.

However, Stanton numbers show an increase from $X/S = 7$ on up to the leading edge tip which can be retraced to the inclination of the streamlines and a higher velocity component directed to the endwall. The fact that cooling effectiveness levels are slightly diminished in comparison to the blowing rates $BR = 0.24$ and $BR = 0.30$ for the better part of the running length is explained with the lack of cooling air being led above the endwall downstream of the injection. The increased momentum of the injected secondary air leads to a deeper penetration into the primary flow. Where primary flow is directed onto the endwall it is already mixed with a great part of the cooling air. This applies to the results of the repeated measurements as well which feature nearly identical cooling effectiveness levels like the results at $BR = 0.30$ downstream of running lengths $X/S > 4$. Cooling effectiveness at similar values of the blowing rates $BR = 0.24$ and $BR = 0.30$ is achieved from $X/S = 6$ to $X/S = 7.5$ in the symmetry plane. Downstream of $X/S = 8.5$ all cooling secondary air is swept away.
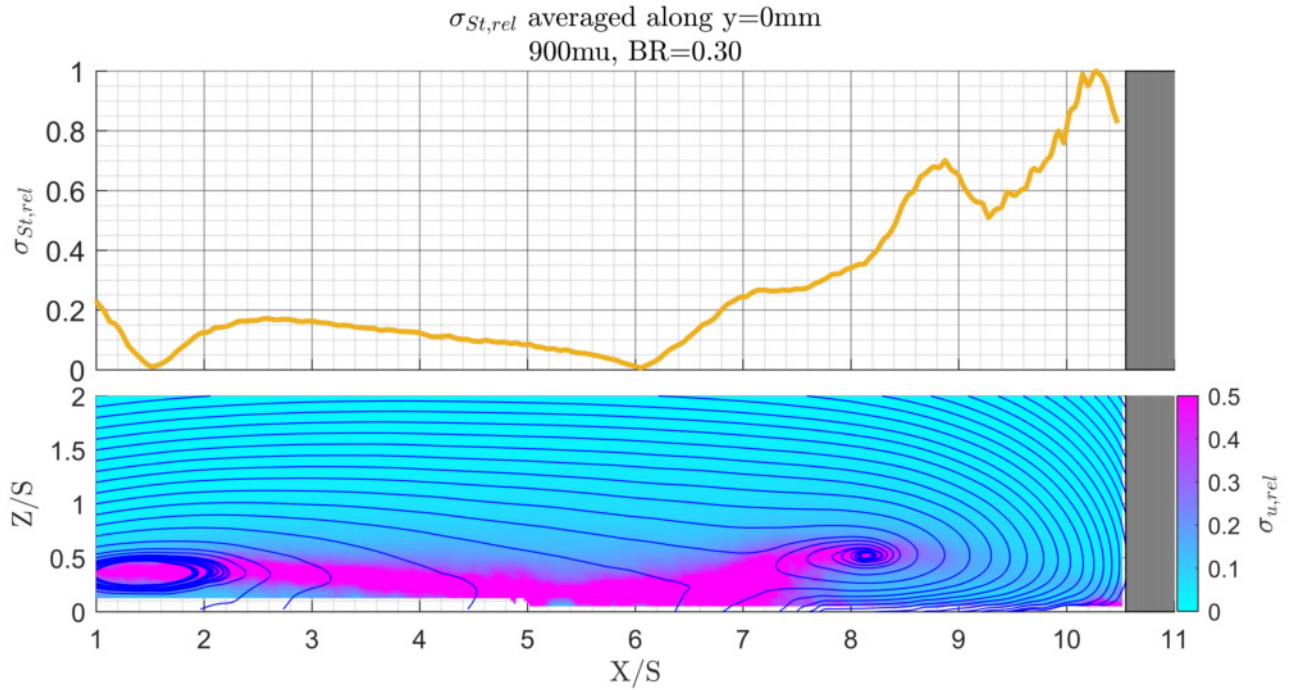
**Figure 5.23:** Normalized standard deviation of Stanton numbers and normalized standard deviation of absolute velocity in the symmetry plane at the blowing rate $BR = 0.30$
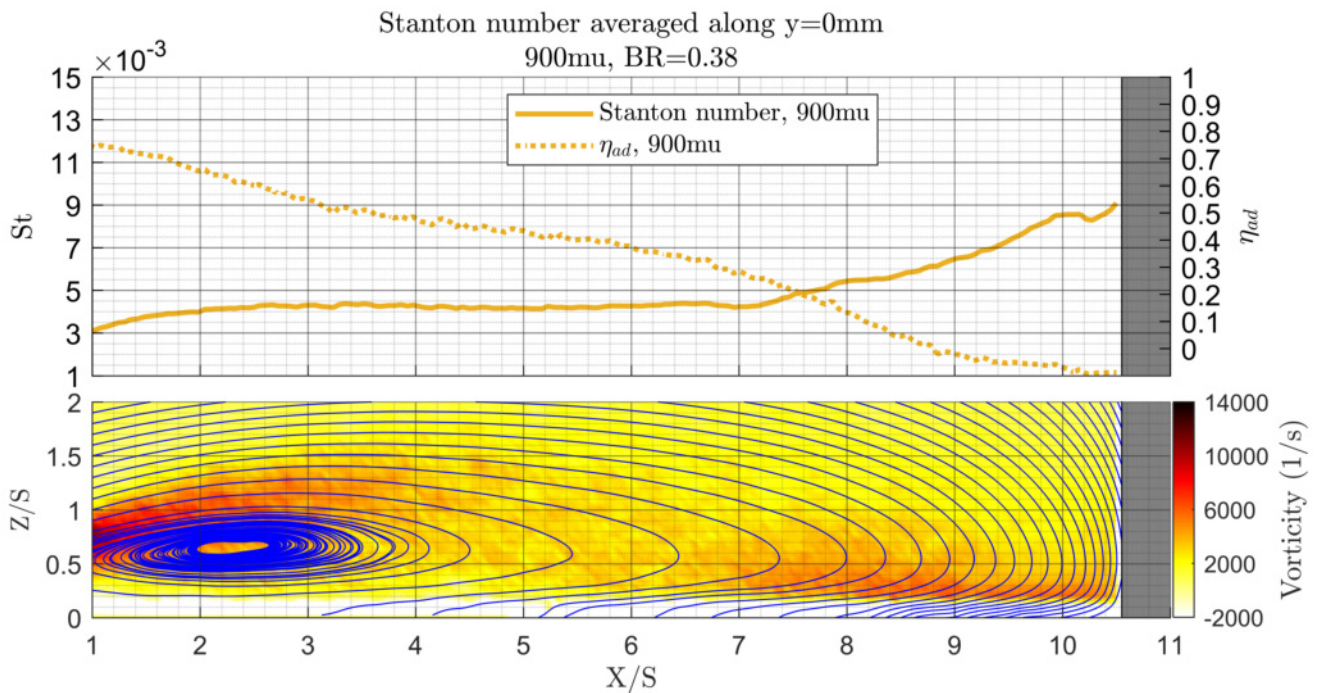


**Figure 5.24:** Stanton number along the stagnation line for the blowing rate $BR = 0.38$ combined with streamlines from the aerodynamic measurements below

From the depiction of temporal deviations regarding Stanton numbers and the absolute velocity in figure 5.25 it is obvious that the only vortex structure is situated downstream of the slot. The typical fluctuations associated with the secondary vortex

and expressed in a local maximum of Stanton number deviations are not observable. A region of elevated fluctuations in Stanton numbers is found from $X/S = 7$ on, rising to a maximum value in front of the leading edge. Again, this location is not coincident with increased deviations in the velocity field, but with the highest overall heat transfer coefficients. High fluctuations in the absolute velocity are visible up to $X/S = 8$ at the height of the vortex downstream of the slot which is indicated by the streamlines. Whereas at lower blowing rates the highest velocity fluctuations propagate towards the endwall they remain at a nearly constant height at the blowing rate $BR = 0.38$. This is attributed to the result of the intensified and stable reverse flow. Single vortices forming from detachments in the turbulent flow after the slot injection are present above this reverse flow which can be concluded from the inspection of instantaneous PIV recordings.
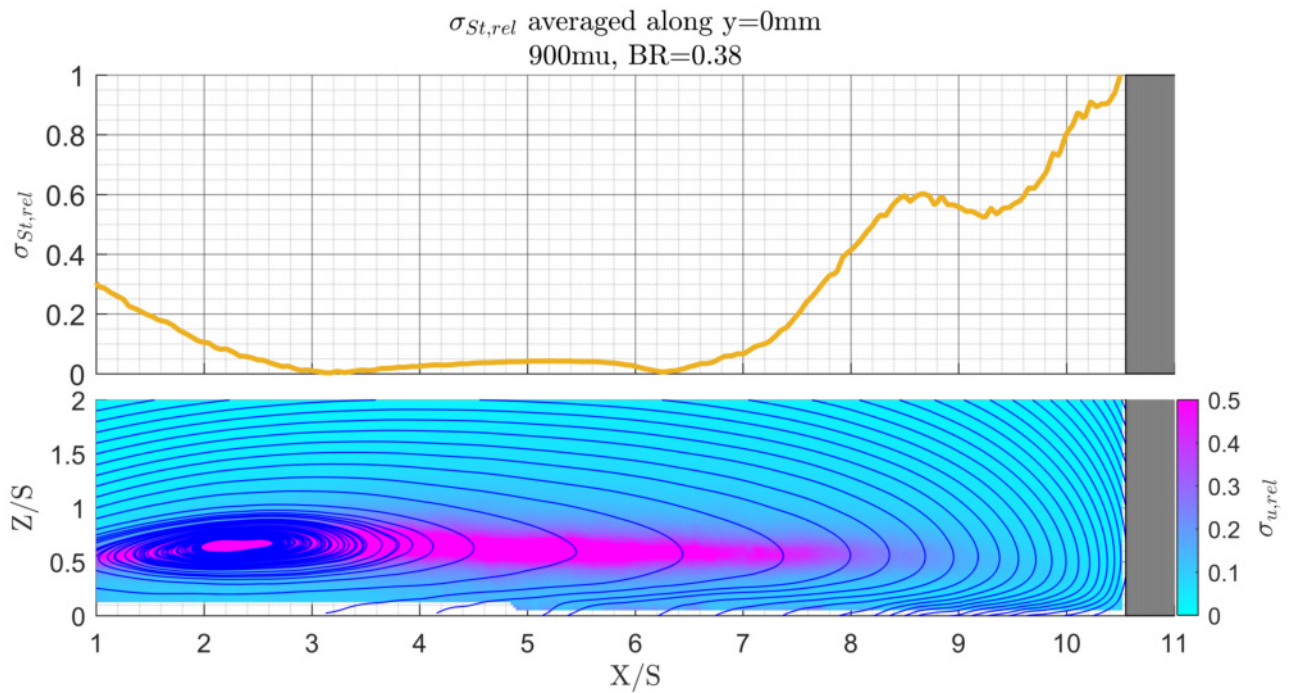


**Figure 5.25:** Normalized standard deviation of Stanton numbers and normalized standard deviation of absolute velocity in the symmetry plane for blowing rate $BR = 0.38$

# 6 Conclusions

The following chapter serves to recapitulate the main conclusions drawn from the investigation of various integration times and the measurements at different blowing rates. Results from the variation of integration times are connected to the future application at the LSTR and the interaction between the aerodynamics and the endwall heat transfer is summarised.

## 6.1 Conclusions from the variation of integration times

The variation of integration times shows that the camera output signal can influence the adiabatic results significantly if no correction is applied. Raw signals obtained with the camera show an intensifying fixed-pattern noise which propagates throughout the evaluation procedure for the adiabatic results. This leads to high-frequency oscillations along the direction of pixel columns in the focal plane array and subsequently in the surface data. Besides, the average levels of adiabatic heat transfer coefficients and cooling effectiveness obtained at an integration time of $50\,\mu s$ also differ from the reference at $900\,\mu s$, especially in regions of notably lower surface temperatures (compare figure 4.5).

In case a one-point NUC is applied to the raw images at lowered integration times, the adiabatic results can be brought into good accordance with the reference integration time. This is owed to the calibration method which matches surface temperature data and camera input data from the surface radiation only at the locations of the reference thermocouples. This way, high-frequency spatial changes in the response of single pixels cannot be considered properly which makes an additional NUC necessary. Both the spatial oscillations and the total deviation from the reference are diminished and a discrimination of adiabatic results at different blowing rates is possible with the lower integration times. The application of an additional low-pass filter to the adiabatic surface data such as shown with the median filter further improves the correspondence with the reference data at $900\,\mu s$.

It is shown that the contribution of the camera output signal to the total uncertainty of the adiabatic heat transfer coefficient rises with decreased integration time. In particular, this relative contribution rises as much 30 % for the heat transfer coefficient in comparison to the contributive fraction at the reference integration time for a blowing rate of $BR = 0.24$. For the cooling effectiveness this gain reaches up to 40 % at distinct locations of lower surface temperatures. Practically, if the contribution of the camera output signal to the total uncertainty of adiabatic heat transfer coefficients was 10 % at $900\,\mu s$ a rise to 13 % could be estimated at $50\,\mu s$, given all other uncertainties (including temperature data) and the setup are identical. In this context it is also recommended to obtain 1000 frames at each set temperature in order to reduce the statistical deviation of the average camera output signal for a single pixel and increase the signal-to-noise ratio.

## 6.2 Conclusions for the heat transfer coefficient

From the combination of heat transfer measurements on the endwall and aerodynamic measurements in the overlying flow a series of interactions can be observed. The flow configurations vary with differing blowing rates of the secondary air. A horseshoe vortex can be visualised explicitly at all blowing rates except from the highest one. A secondary and a tertiary vortex are not evident from the time-averaged aerodynamic measurements alone, but their existence is suggested by the distribution of the adiabatic results on the endwall and by instantaneous PIV recordings. The attributes of this vortex structure associated with the impact on the endwall heat transfer and acknowledged in the cited literature can be identified in the present measurements as well.

Generally, the impact of the flow configuration on the endwall heat transfer can be summarized as follows:

- Heat transfer to the endwall is particularly dependent on the structure of the horseshoe vortex, the secondary vortex, the tertiary vortex and the corner vortex. Whereas the horseshoe vortex is found to be a stable flow characteristic in the time-averaged aerodynamic results, the secondary and the tertiary vortex are only indicated by the bended course of the streamlines. They are, however, found in instantaneous images from the aerodynamic measurements.

- Typical bands of local maximums and local minimums in heat transfer coefficients wrapped around the airfoil are detected at those blowing rates which feature a horseshoe vortex in the aerodynamic measurements.

- The locations of local maximums are coincident with positions between the secondary vortex and the horseshoe vortex at all blowing rates that show a horseshoe vortex. Elevated heat transfer in this region is associated with an inrush of fluid from above the vortex structure onto the endwall. This is caused by a recurrent transition of the vortex structure in front of the leading edge. It is identified in a series of instantaneous PIV recordings in the reference case and it is also visualised exemplarily at the blowing rate $BR = 0.24$.

- Local minimums are found to be coincident with the reverse flow beneath the horseshoe vortex.

- The bands of local maximums and local minimums have bigger streamwise distances to the airfoil contour at lateral displacements from the symmetry plane. This is attributed to the guidance of the horseshoe vortex branches on either side of the airfoil.

- The highest heat transfer coefficients are found directly in front of the leading edge at all blowing rates investigated. This is caused by portions of the primary flow that are washed down onto the endwall. A possible influence of the corner vortex and the resulting stagnation point of the boundary layer on the leading edge surface cannot be determined.

A variation of the blowing rate shows the following changes in the impact on the heat transfer to the endwall:

- The horseshoe vortex core steadily moves upstream with rising blowing rates. In all cases with secondary air injection the vortex is located farther upstream than in the reference case. This movement corresponds to the shift of the local maximums and minimums of the heat transfer coefficients with varied blowing rates.

- From the interrogation of the streamline topologies it is also evident that the horseshoe vortex core is displaced to greater heights above the endwall with rising blowing rates.

- An area of low pressure comparable to a dead-water zone forms downstream of the slot injection and expands in streamwise direction with higher blowing rates. This is accounted for by the perpendicular injection and the growing momentum of the secondary air at higher blowing rates causing a blockage of the primary flow. At the highest blowing rate vortices are generated on either side which is also confirmed by CFD simulations following the experiments in this work.

- At short running lengths and farther upstream of the vortex structures heat transfer is elevated in regions with high streamwise velocity and with high velocity components directed onto the endwall. The blowing rate $BR = 0.11$ exhibits a smaller streamwise velocity near the endwall than the reference case. In conjunction with a small amount of cooling secondary air this results in lower heat transfer than in the reference case. In contrast, the blowing rate $BR = 0.24$ shows smaller velocity components in the streamwise direction as well, but velocity components perpendicular to the endwall are present in an area of local reattachment. This increases heat transfer coefficients above the levels attained at the reference case.

- At the highest blowing rate said vortex structures are not detectable. A strong reverse flow featuring little temporal fluctuations forms near the endwall while unstable single vortices generated by the injection are located above. They are only present in instantaneous PIV recordings.

- Heat transfer to the endwall is augmented compared to the reference case only at the two intermediate blowing rates $BR = 0.24$ and $BR = 0.30$. Heat transfer coefficients at these blowing rates are similar to the reference case in the regions upstream of the vortex structures and directly in front of the leading edge. On account of the upstream shift of the vortex structures heat transfer is significantly higher at these blowing rates in the vicinity of the vortices.

Wiemer [13] concluded in his work that the highest absolute uncertainty in heat transfer coefficients is present in regions of the highest heat transfer coefficients. From the findings of this work it can be added that the temporal deviations in heat transfer coefficients are highest at those locations where high heat transfer coefficients are present. These locations are associated with temporally unstable flow configurations such as the inrush of fluid near the secondary vortex. The corner vortex near the airfoil junction is also expected to account for high fluctuations in endwall heat transfer coefficients, but its presence cannot be confirmed ultimately in this work.

An exact transfer of the results obtained in the heat transfer measurements to the application at the LSTR is difficult. It is expected, however, that the characteristic vortex structures described in this work and also confirmed by Thrift et al. [49] in a scaled vane cascade occur at the rotor of the LSTR. The horseshoe vortex is found to form in cases where a boundary layer flow in streamwise direction is present. Furthermore, it is expectable that the vortex structure vanishes above a critical blowing rate as well. As the flow from the cavity guides the secondary air more tangentially to the streamwise direction the vortex structures might be pushed away with rising momentum of the secondary flow like it is suggested by Thrift et al. [50]. On top of that, a blockage of the primary flow by the injected secondary air is not expected due to the lack of channel walls. Vortices forming on either side of the slot at high blowing rates cannot appear along a continuous cavity. The implications of the stator-rotor interaction for the endwall heat transfer described by Blair [27] need to be considered as well.

## 6.3 Conclusions for the cooling effectiveness

The implications for the cooling effectiveness levels with increasing blowing rates found in the present experiments are the following:

- Cooling effectiveness levels are found to increase with the secondary mass flow. At the lowest blowing rate $BR = 0.11$ the secondary flow does not penetrate into the primary flow, keeping the flow above the endwall tangential and decelerating it. The small amount of coolant is not sufficient to reach cooling effectiveness levels attained at higher blowing rates downstream of half a slot width after the injection. At blowing rates higher than $BR = 0.24$ there is no additional benefit in cooling effectiveness and values remain in the range found at $BR = 0.24$. A more homogeneous distribution of the cooling film is not found at blowing rates above $BR = 0.24$, either.

- The general course of cooling effectiveness levels is in accordance with the cited literature, showing a steady decrease towards the airfoil. It is found that the reverse flow beneath the horseshoe vortex is responsible for vanishing cooling effectiveness levels as it seems to sweep most of the residual secondary air away and is mostly fed by the primary flow.

- Raising the momentum of the secondary flow results in a deeper penetration into the primary flow. However, as it can be seen from the results at the highest blowing rate $BR = 0.38$ this does not imply that a shielding of the endwall from primary flow is impossible. The massive reverse flow present from downstream of the slot up to the airfoil is supplied by secondary and primary flow and prevents the primary flow from a direct impact on the endwall. Only right after the slot injection do cooling effectiveness levels drop below those found at the other blowing rates by around 15 % which is attributed to the high momentum perpendicular to the streamwise direction.

Negative values for the cooling effectiveness at the highest blowing rate occur in the region in front of the leading edge where most of the present fluid stems from the primary flow being washed down onto the endwall. These implausible results are assumed to be caused by an insufficient temperature range for the calibration of the reference thermocouples. Primary flow temperatures are up to $15\,^{\circ}$C lower than the lowest temperature recorded by one of the reference thermocouples. This leads to improper temperature assignments at locations between the thermocouples where calibration coefficients are scattered across the pixel array. At the flow channel used for the measurements in this work an active heating of the primary flow is not possible. Besides, all reference thermocouples are situated in regions around the airfoil where the hot secondary air is present and keeps surface temperatures well above the primary flow temperature. This issue is solved with additional measurements repeated at a blowing rate of $BR = 0.38$. These measurements are conducted at a higher ambient temperature (and higher primary flow temperature, accordingly), reducing the temperature difference between the impinging primary flow and the lower limit of the calibration range for surface temperatures from $13\,^{\circ}$C to $6.5\,^{\circ}$C (compare section 4.4.2). Corresponding results of the cooling effectiveness feature deviations to the initial measurements of up to 10 % right after the slot injection, but physically plausible cooling effectiveness levels approaching zero are found near the leading edge.
What is more, the secondary air temperature measured in the plenum might not reflect the actual temperature at the exit of the slot due to heat transfer inside the slot. As the heating plate constitutes the downstream boundary of the slot heat flux is directed towards the secondary air flow if the set temperature of the heating plate is lower than the secondary air temperature. Heat flux towards the heating plate is existent if the temperature differences are reversed. This either elevates or reduces the secondary air temperature at the exit of the slot. According to equation 2.5 the dimensionless wall temperatures $\Theta$ determined at the specific set temperatures are calculated to higher values if the secondary air temperature is overestimated. Vice versa, $\Theta$ remains at lower values in case the secondary air temperature is underestimated. A rough estimation of Nusselt correlations shows that the secondary air temperature can drop around $1\,^{\circ}$C at a blowing rate of $BR = 0.24$ due to heat transfer inside the

slot. The secondary air temperature is assumed at 55 °C at the entrance to the slot while a notional temperature at the heating plate wall of 30 °C represents the lowest set temperature chosen for the experiments. On the contrary, with a supposed heating plate wall temperature of 75 °C the rise of the secondary air temperature is estimated to as much as 0.9 °C. All other bordering walls including the injection module itself are assumed adiabatic and the flow through the slot is assumed to be homogeneous in this case. These improper temperature assumptions from the measurements are owed to the construction of the setup. Although these are only rough estimates, said temperature differences will also have an influence in future applications at the LSTR. In figure 3.2 the path of the secondary air to the exit of the cavity can be seen. It is obvious that heat is transferred to or from the secondary air flow if a temperature difference exists between the flow and the slender edge of the hub side endwall which will be part of the heating plate.

For a future application at the LSTR some recommendations can be summarised:

- At the LSTR an application with hot secondary flow is planned as well, but primary flow temperatures can also be elevated above the ambient temperature. This way, the lowest temperature conceived by the reference thermocouples is definitely lower than or equal to the primary flow temperature. Surface temperatures in regions where fluid from the primary flow is washed down onto the endwall and consequently reducing surface temperatures are not extrapolated from the calibration range. Another solution to this issue could be to exclude the lowest set temperatures from the regression in the evaluation procedure. However, a compromise has to be found between a reduced number of nodes for the regression and the stability of the determination of $\eta_{ad}$.

- Increasing the primary flow temperature influences the regression for the determination of the cooling effectiveness positively. At the lowest set temperature where temperature data and camera output signals are acquired positive heat flux values can be obtained. As explained in section 4.3.2 placing the data pairs of heat flux and surface temperature on both sides of the abscissa reduces the uncertainty in the determination of the cooling effectiveness. This is achieved in the present setup only at locations with surface temperatures well above the secondary air temperature.

- Placing reference thermocouples inside the heating plate in the vicinity of the leading edge helps to capture regions where surface temperatures might drop due to the impact of cold primary flow.

- A calibration of the complete heating plate with all thermocouples and their connections installed can be performed. In addition to this calibration, an exact determination of the thermal conductivity of the used auxiliary wall is desirable. This would ultimately reduce the contribution to the total uncertainty of the adiabatic results.

- Measurements of the secondary air temperature should be conducted as close as possible to the exit from the cavity in order to adequately capture the aforementioned heat input or heat loss to the secondary flow. An installation of thermocouples in the stator endwall (the yellow part in figure 3.3) would be advantageous.

# 7 Summary and Outlook

At the institute GLR the investigation of heat transfer to the rotor endwall with respect to a variation of sealing air mass flows through the stator-rotor cavity is planned at the LSTR. In the present thesis preliminary investigations are done in a flow channel equipped with a symmetrical airfoil serving as a rotor blade substitute and an upstream slot for secondary air injection simulating the sealing air inlet.

## Summary

Thermal measurements on the endwall in front of the airfoil are conducted with reduced integration times of the infrared camera used for the acquisition of surface temperatures and at varied blowing rates of the secondary air flow. Results of the thermal measurements are expressed in adiabatic quantities, namely the adiabatic heat transfer coefficient and the adiabatic cooling effectiveness which are obtained with the in-house evaluation procedure *HTCVal1.7*.
Both high-resolution distributions of heat transfer coefficients on the endwall surface and courses in the streamwise direction at different lateral positions are presented. The influence of reduced integration times on the uncertainty of adiabatic results is quantified. Flow field visualisations upstream of the leading edge are derived from aerodynamic measurements using PIV. Characteristics of the flow field in a reference case without secondary air injection are compared to literature and related to the heat transfer measurements. The flow field at varied blowing rates is examined and conclusions are drawn as for the influence of flow characteristics on the endwall heat transfer.

A reduction of the integration time to $50\,\mu s$ is chosen as a comparable integration time for applications at the LSTR. It is based on the geometric dimensions of the rotor endwall, the rotational speed at the design point and an estimation of the spatial resolution in previous measurements on the stator endwall. The reference data are recorded at $900\,\mu s$, a value frequently used in previous works and matching the present temperature range. An average over a total of 1000 frames is used for the evaluation process. The uncertainty contribution to adiabatic results stemming from surface temperatures is raised in comparison to the reference at $900\,\mu s$ in regions with high spatial gradients of local heat transfer coefficients. At a blowing rate of $BR = 0.24$ it is found to be homogeneously distributed across the observed area in front of the airfoil and a rise compared to the uncertainty contribution at the reference integration time is seen in regions of predominantly lower surface temperatures. Generally, an increase of the relative contribution to the uncertainty of heat transfer coefficients can be estimated to 30 % at some locations whereas a corresponding rise for the contribution to cooling effectiveness uncertainty reaches up to 40 %. Adiabatic results of the heat transfer coefficient at $50\,\mu s$ integration time correspond well to the reference at $900\,\mu s$ mainly within the range of two times the measurement uncertainty stemming from surface temperatures alone.

Blowing rates of the secondary air are determined with respect to the approximate sealing air mass flow at the design point of the LSTR. In this variation endwall heat transfer is put in context with the findings from aerodynamic measurements. Flow field visualisations show characteristic vortex structures in front of the leading edge with a distinct horseshoe vortex in the time-averaged data. A secondary and a tertiary vortex are indicated by the course of streamlines in the time-averaged results, but can definitely be found in several series of instantaneous PIV recordings. Endwall heat transfer distributions are brought into accordance with the flow characteristics. From inspections of instantaneous recordings typical transitions of the vortex structures described in literature are detected. An inrush of fluid from above the tertiary vortex is directed onto the endwall as part of the transition which elevates heat transfer and results in a band of local maximums of heat transfer coefficients. A stable reverse flow is found beneath the horseshoe vortex, coinciding with a local minimum in heat transfer. It is located prior to a region of constantly rising heat transfer coefficients towards the leading edge related to primary air being washed down onto the endwall.
Said vortex structures are found at all blowing rates investigated except from the highest one. Instantaneous PIV recordings at the blowing rate $BR = 0.24$ exemplify the transition of the vortex structures in cases with secondary air injection. Higher blowing rates also result in higher momentum of the secondary flow and a deeper penetration into the primary flow due to the perpendicular injection from the slot. The injected secondary air demonstrates an obstacle for the approaching primary flow and produces an area of reverse flow downstream of the injection. It spans the whole running length to the leading edge at

the highest blowing rate, resulting in a boundary layer flow with velocities in negative streamwise direction so that the vortex structure is not able to form. All vortex structures shift upstream with rising blowing rates which is confirmed by the upstream displacement of the typical distribution of heat transfer coefficients. The horseshoe vortex is also slightly lifted above the endwall at higher blowing rates. Elevated heat transfer coefficients are seen in regions where fluid previously deflected by the injection is redirected onto the endwall and where velocities near the endwall are raised. Cooling effectiveness levels mainly scale with the secondary mass flow. The vortex structures extinct residuals of the cooling secondary air film as it is swept away by the reverse flow beneath the horseshoe vortex. Highest overall cooling effectiveness levels related to the respective secondary mass flow are found at a blowing rate of $BR = 0.24$ which also features the highest overall heat transfer augmentation compared to the reference case without secondary air injection.

## Outlook

An outlook on further improvements regarding heat transfer measurements and aerodynamic measurements at the flow channel include the following issues:

- A new specimen of the heating plate should be finished in advance to other measurements. On the edges of the currently used heating plate separations of the auxiliary wall from the underlying aluminium structure are visible that affect the effective thermal conductivity in this region. The thermal conductivity of the auxiliary wall itself should be determined with more accuracy prior to the installation in a new heating plate.

- Heat transfer measurements with injection from an angled slot can be performed to improve the comparability to the geometry at the LSTR. A corresponding design for an injection module with the slot inclined to $30°$ is drafted and included in the appendix. The concept allows for an installation where the entrance to the slot can be aligned with the downstream wall of the plenum so that the direction change for the flow is as kept as small as possible. Length-to-width ratios and the inclination can be adapted to other values and it is producible in the in-house workshop.

- The mass flow meter for the secondary air flow should be re-calibrated by the manufacturer as several years have passed since the last calibration and the measurement uncertainty reaches well up to $10\%$ of the measured value. What is more, a defective calculation of the primary mass flow by the standard orifice is found. The source of this error can be narrowed down to the influence of possible contaminations and accompanying geometric changes or to the use of inaccurate parameters in the mass flow equation for this particular design.

- Additional measurements of the pressure distribution in the flow channel upstream of the measurement section can contribute to further CFD validations. Particular investigations of the boundary layer upstream of the measurement section might furthermore enable to put the heat transfer measurements and the aerodynamic measurements in context to the findings from CFD simulations as the precise knowledge of boundary conditions is advantageous for the numerical examination.

Regarding future measurements at the LSTR the following subjects from the learning process in the scope of this thesis have to be considered. Additional recommendations are summarised in the conclusions in section 6.3.

- Conducting the heat transfer experiments at generally elevated primary flow temperatures and set temperatures of the heating plate shifts the calibration of surface temperatures into regions of reduced sensitivity related to camera output signals. This approach allows for a reduction of uncertainties in surface temperatures, especially at low integration times. It is shown that the lowest surface temperatures occurring on the unpowered heating plate needs to be captured by the calibration range which is best achieved with an elevated primary flow temperature. The first data acquisition point should be set with an unpowered heating plate while both the primary flow and the secondary flow remain at their respective mass flows and temperatures to account for changes in the transmission coefficient in the optical path.

- With the knowledge of flow characteristics forming in front of the leading edge attained in this work reference thermocouples in the instrumented rotor endwall installed at the LSTR can be placed in such way that the region where primary air is washed down is properly captured.

- The usage of a technique to merge infrared images taken at different integration times like the one presented by Gazzini [40] can be tested. The levels of camera output signals seem to be sufficient at the integration time $50\,\mu s$ in the present

work and they can further be raised in experiments performed at generally higher temperatures. Intensities reaching the camera are therefore not expected to drop in an application at the LSTR. Pixel shifts in the camera images caused by the rotating endwall could be corrected with methods of convolutions used by Gazzini [40].

- An alternative way to detect the reference thermocouples as geometric references in the evaluation procedure should be considered. In the present setup recordings taken at a high integration time serve to point out the distinct locations at which the data pairs of camera signals and temperature values are matched. This works for all integration times as the position of the camera does not change during the acquisition. Regarding an application in a rotating system other methods like the correlation of measurement images with images of an ideal reference point might be helpful.

# Bibliography

[1]   International Civil Aviation Organization. *Forecasts of Scheduled Passenger and Freight Traffic: Medium-Term Passenger and Freight Traffic Forecasts*. 2013. URL: https://www.icao.int/sustainability/pages/eap_fp_forecastmed.aspx.

[2]   W. J. G. Bräunling. *Flugzeugtriebwerke. Grundlagen, Aero-Thermodynamik, ideale und reale Kreisprozesse, Thermische Turbomaschinen, Komponenten, Emissionen und Systeme*. 3. vollst. überarbeitete und erw. Auflage. Berlin, Heidelberg: Springer Verlag, 2009.

[3]   W. Lazik, T. Doerr, S. Bake, R. Bank, and L. Rackwitz. "Development of Lean-Burn Low-NOx Combustion Technology at Rolls-Royce Deutschland". In: *Proceedings of ASME Turbo Expo 2008: Power for Land, Sea and Air* 3 (2008), pp. 797–807. DOI: 10.1115/GT2008-51115.

[4]   H. D. Baehr and K. Stephan. *Wärme- und Stoffübertragung*. 9. aktualisierte Auflage. Berlin, Heidelberg: Springer Vieweg, 2016.

[5]   J. H. Spurk and N. Aksel. *Strömungslehre. Einführung in die Theorie der Strömungen*. 8. überarbeitete Auflage. Berlin, Heidelberg: Springer Verlag, 2010.

[6]   R. J. Moffat. "$h_{adiabatic}$ and $u'_{max}$". In: *Journal of Electronic Packaging* 126.4 (2004). DOI: 10.1115/1.1827265.

[7]   M. Gritsch, S. Baldauf, M. Martiny, A. Schulz, and S. Wittig. "The Superposition Approach to Local Heat Transfer Coefficients in High Density Ratio Film Cooling Flows". In: *Proceedings of ASME Turbo Expo: Power for Land, Sea, and Air* 3 (1999), pp. V003T01A048. DOI: 10.1115/99-GT-168.

[8]   E. R. G. Eckert. "Analysis of Film Cooling and Full-Coverage Film Cooling of Gas Turbine Blades". In: *Journal of Engineering for Gas Turbines and Power* 106.1 (1984), pp. 206–213. DOI: 10.1115/1.3239536.

[9]   B. Laveau, R. S. Abhari, M. E. Crawford, and E. Lutum. "High Resolution Heat Transfer Measurements on the Stator Endwall of an Axial Turbine". In: *Journal of Turbomachinery* 137.4 (2014), pp. 0410051–04100510. DOI: 10.1115/1.4028431.

[10]  P. Stephan, K. Schaber, K. Stephan, and F. Mayinger. *Thermodynamik - Grundlagen und technische Anwendungen. Band 1: Einstoffsysteme*. 19. Auflage. Berlin, Heidelberg: Springer Vieweg, 2013.

[11]  M. Vollmer and K. Moellmann. *Infrared Thermal Imaging - Fundamentals, Research and Applications*. 2. Nachdruck 2013. Weinheim: Wiley-VCH Verlag, 2010.

[12]  C. Steinhausen. "Definition und Anwendung des Datenanalyseprozesses für Wärmeübergangs- und Filmkühleffektivitätsmessungen am Large Scale Turbine Rig (LSTR)". MA thesis. Darmstadt: TU Darmstadt, 2015.

[13]  S. Wiemer. "Influence of varied inflow conditions on Heat Transfer and Film Cooling Effectiveness at the hub side endwall of an axial turbine and assessment of measurement uncertainty". MA thesis. Darmstadt: TU Darmstadt, 2016.

[14]  M Ochs, T Horbach, A Schulz, R Koch, and H.-J. Bauer. "A novel calibration method for an infrared thermography system applied to heat transfer experiments". In: *Measurement Science and Technology* 20.7 (2009), p. 075103. DOI: 10.1088/0957-0233/20/7/075103.

[15]  A. Schulz. "Infrared thermography as applied to film cooling of gas turbine components". In: *Measurement Science and Technology* 11.7 (2000), pp. 948–956.

[16] M. Raffel, C. E. Willert, S. T. Wereley, and J. Kompenhans. *Particle Image Velocimetry - A Practical Guide*. Second edition. Berlin, Heidelberg: Springer Verlag, 1998.

[17] H. Süße and E. Rodner. *Bildverarbeitung und Objekterkennung. Computer Vision in Industrie und Medizin*. Wiesbaden: Springer Vieweg, 2014. DOI: 10.1007/978-3-8348-2606-0_2.

[18] B. Wieneke. "Stereo-PIV using self-calibration on particle images". In: *Experiments in Fluids* 39 (2005), pp. 267–280.

[19] R. J. Goldstein and R. A. Spores. "Turbulent Transport on the Endwall in the Region Between Adjacent Turbine Blades". In: *ASME Journal of Heat transfer* 110.4a (1988), pp. 862–869. DOI: 10.1115/1.3250586.

[20] S. Friedrichs. "Endwall Film-Cooling in Axial Flow Turbines". PhD thesis. Cambridge University, 1997.

[21] M. B. Kang, A. Kohli, and K. A. Thole. "Heat Transfer and Flowfield Measurements in the Leading Edge Region of a Stator Vane Endwall". In: *Journal of Turbomachinery* 121.3 (1999), pp. 558–568. DOI: 10.1115/1.2841351.

[22] T. J. Praisner and C. R. Smith. "The Dynamics of the Horseshoe Vortex and Associated Endwall Heat Transfer—Part I: Temporal Behavior". In: *Journal of Turbomachinery* 128.4 (2006), pp. 747–754. DOI: 10.1115/1.2185676.

[23] S. P. Lynch and K. A. Thole. "The Effect of Combustor-Turbine Interface Gap Leakage on the Endwall Heat Transfer for a Nozzle Guide Vane". In: *Journal of Turbomachinery* 130.4 (2008), pp. 041019–041019–10. DOI: 10.1115/1.2812950.

[24] D. G. Knost and K. A. Thole. "Adiabatic Effectiveness Measurements of Endwall Film-Cooling for a First-Stage Vane". In: *Journal of Turbomachinery* 127.2 (2005), pp. 297–305. DOI: 10.1115/1.1811099.

[25] N. D. Cardwell, N. Sundaram, and K. A. Thole. "The Effects of Varying the Combustor-Turbine Gap". In: *ASME Journal of Heat transfer* 129.4 (2007), pp. 756–764. DOI: 10.1115/1.2720497.

[26] S. W. Burd, C. J. Satterness, and T. W. Simon. "Effects of Slot bleed Injection over a Contoured End Wall on Nozzle Guide vane Cooling Performance: Part II - thermal Measurements". In: *Proceedings of ASME Turbo Expo: Power for Land, Sea, and Air* 2000-GT-0200 (2000). DOI: 10.1115/2000-GT-0200.

[27] M. F. Blair. "An Experimental Study of Heat Transfer in a Large-Scale Turbine Rotor Passage". In: *Proceedings of ASME Turbo Expo: Power for Land, Sea, and Air* 4.195 (1992), V004T09A012. DOI: 10.1115/92-GT-195.

[28] H. D. Joslyn and R. P. Dring. "The Relative Eddy in Axial Turbine Rotor Passages". In: *Proceedings of ASME Turbo Expo: Power for Land, Sea, and Air* 1.83 (1983), V001T01A010. DOI: 10.1115/83-GT-22.

[29] H. D. Joslyn and R. P. Dring. "Three-Dimensional Flow in an Axial Turbine: Part 1—Aerodynamic Mechanisms". In: *Journal of Turbomachinery* 114.1 (1992), pp. 61–70. DOI: 10.1115/1.2927998.

[30] A Krichbaum, H. Werschnik, M. Wilhelm, H.-P Schiffer, and K Lehmann. "A Large Scale Turbine Test Rig for the Investigation of High Pressure Turbine Aerodynamics and Heat Transfer With Variable Inflow Conditions". In: *Journal of Turbomachinery* (2015), pp. V02AT38A032. DOI: 10.1115/GT2015-43261.

[31] A. Neubauer. "Inbetriebnahme der Waermeuebergangs-Messtechnik am Large Scale Turbine Rig (LSTR)". Bachelorthesis. Darmstadt: TU Darmstadt, 2014.

[32] R. de Oliveira Schneider. "Inbetriebnahme eines Windkanals zur Untersuchung von Wärmeübergangsphänomenen in filmgekühlten Gebieten". •. Darmstadt: TU Darmstadt, 2015.

[33] T. Fox. "Experimentelle Untersuchung des Wärmeübergangs im Endwandbereich einer Schaufelumströmung unter dem Einfluss von Kühllufteinblasung". Diplomarbeit. Darmstadt: TU Darmstadt, 2016.

[34] T. Ostrowski. "Experimentelle Validierung der Wärmeübergangsmesstechnik für den Large Scale Turbine Rig". MA thesis. Darmstadt: TU Darmstadt, 2013.

[35]  P. Roth. "Auslegung und Konstruktion einer Messstrecke zur Etablierung von Wärmeübergangsmesstechnik". Bachelorthesis. Darmstadt: TU Darmstadt, 2015.

[36]  T. auf dem Kampe, S. Völer, and F. Zehe. "A Model for Cylindrical Hole Film Cooling—Part I: A Correlation for Jet-Flow With Application to Film Cooling". In: *Proceedings of ASME Turbo Expo 2015: Turbine Technical Conference and Exposition* 134.6 (2012). DOI: `10.1115/1.4006306`.

[37]  H. Unbehauen. "Klassische Verfahren zum Entwurf linearer kontinuierlicher Regelsysteme". In: *Regelungstechnik I: Klassische Verfahren zur Analyse und Synthese linearer kontinuierlicher Regelsysteme, Fuzzy-Regelsysteme*. Wiesbaden: Vieweg+Teubner, 2007, pp. 185–290. DOI: `10.1007/978-3-8348-9196-9_8`. URL: `https://doi.org/10.1007/978-3-8348-9196-9_8`.

[38]  MathWorks Matlab 2017b. *Matlab Documentation: Imfindcircles*. URL: `http://de.mathworks.com/help/images/ref/imfindcircles.html`. last called on 1st April, 2018.

[39]  C. Brandstetter. "Strömungsvermessung in rotierenden Turbomaschinenkomponenten mit Stereoscopic Particle Image Velocimetry". Diplomarbeit. Darmstadt: TU Darmstadt, 2010.

[40]  S. Gazzini, R. Schädler, A. I. Kalfas, and R. S. Abhari. "Infrared thermography with non-uniform heat flux boundary conditions on the rotor endwall of an axial turbine". In: *Measurement Science and Technology* 28.2 (2017), p. 025901. DOI: `doi:10.1088/1361-6501/aa5174`.

[41]  W. Nitsche and A. Brunn. *Strömungsmesstechnik*. 2. aktualisierte und überarbeitete Auflage. Berlin, Heidelberg: Springer, 2006.

[42]  A. Rowland. *Physics of Digital Photography*. IOP Publishing, 2017. Chap. Image quality. DOI: `10.1088/978-0-7503-1242-4`. URL: `http://dx.doi.org/10.1088/978-0-7503-1242-4`.

[43]  G. Bittlinger, A. Schulz, and S. Wittig. "Film Cooling Effectiveness and Heat Transfer Coefficients for slot Injection at High Blowing Ratios". In: *Proceedings of the ASME Turbo Expo: Power for Land, Sea, and Air* 4 (1994), pp. V004T09A032. DOI: `10.1115/94-GT-182`.

[44]  K. F. Milidonis and D. P. Georgiou. "Film cooling effectiveness in the region of the blade-endwall corner junction with the injection assisted by the recirculating vortex flow". In: *International Journal of Heat and Mass Transfer* 83 (2015), pp. 294–306. DOI: `10.1016/j.ijheatmasstransfer.2014.11.067`.

[45]  J. Eitenmüller. "Experimentelle Untersuchung der Statorzuströmung einer Axialturbine unter Anwendung der Particle Image Velocimetry". Master Thesis. Darmstadt: TU Darmstadt, 2016.

[46]  R. J. Goldstein and R. A. Spores. "Turbulent Transport on the Endwall in the Region Between Adjacent Turbine Blades". In: *Journal of Heat Transfer* 110.4a (1988), pp. 862–869. DOI: `10.1115/1.3250586`.

[47]  W. J. Devenport and R. L. Simpson. "Time-dependent and time-averaged turbulence structure near the nose of a wing-body junction". In: *Journal of Fluid Mechanics* 210 (1990), pp. 23–55. DOI: `10.1017/S0022112090001215`.

[48]  T. J. Praisner and C. R. Smith. "The Dynamics of the Horseshoe Vortex and Associated Endwall Heat Transfer—Part II: Time-Mean Results". In: *Journal of Turbomachinery* 128.4 (2006), pp. 755–762. DOI: `10.1115/1.2185677`.

[49]  A. A. Thrift, K. A. Thole, and S. Hada. "Effects of Orientation and Position of the Combustor- Turbine Interface on the Cooling of a Vane Endwall". In: *Journal of Turbomachinery* 134.6 (2012), pp. 061019–061019–10. DOI: `10.1115/1.4004817`.

[50]  A. A. Thrift and K. A. Thole. "Influence of flow injection angle on a leading-edge horseshoe vortex". In: *International Journal of Heat and Mass Transfer* 55.17-18 (2012), pp. 4651–4664. DOI: `10.1016/j.ijheatmasstransfer.2012.04.024`.

[51]  W. A. Eckerle and L. S. Langston. "Horseshoe Vortex Formation Around a Cylinder". In: *ASME. Turbo Expo: Power for Land, Sea, and Air* 1 (1986), pp. V001T01A109. DOI: `10.1115/86-GT-246`.

[52]  J. Jeong and F. Hussain. "On the identification of a vortex". In: *Journal of Fluid Mechanics* 285 (1995), pp. 69–94. DOI: `10.1017/S0022112095000462`.

# A  Data sheets

# VITRON CVD Zinc Sulfide

VITRON's polycrystalline ZnS is produced by a Chemical Vapor Deposition process (CVD). Two grades of ZnS are available:

**Regular grade (FLIR) Zinc Sulfide** is a cost-effective polycrystalline optical material and has high fracture strength. The material is used in the 7 – 12 µm band. Typical applications are windows, lenses and domes. It is available in large sizes and is moderately priced.

**Multispectral grade (CLEAR) Zinc Sulfide** is treated after growth with a special process to eliminate microscopic voids and defects which occur in the regular grade material. The material is usable in the visible to infrared region from 0.45 – 12 µm.

Classical polishing or Single-Point-Diamond-Machining enables the production of optical components with flat, spherical and/or aspherical and diffractive surfaces. Antireflection coatings can be applied to further improve the transmission.



*Typical delivery in form of blanks:*   Ø   5 – 500 mm
☐   5 – 500 mm
ct   0.8 – 25 mm

### Index of Refraction (@ 20°C)

| λ [µm] | n(λ) |
|--------|------|
| 0.46 | 2.459 |
| 0.50 | 2.419 |
| 0.66 | 2.342 |
| 0.80 | 2.313 |
| 1.00 | 2.292 |
| 3.00 | 2.257 |
| 4.00 | 2.252 |
| 5.00 | 2.246 |
| 6.00 | 2.239 |
| 7.00 | 2.232 |
| 8.00 | 2.223 |
| 9.00 | 2.212 |
| 10.00 | 2.200 |
| 11.00 | 2.186 |
| 12.00 | 2.170 |
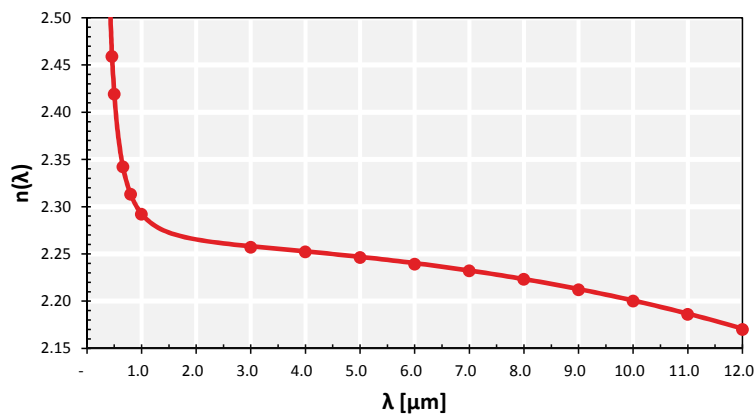


### Sellmeier-Coefficients (@ 20°C)

| | |
|---|---|
| A | 8.39193 |
| $B_1$ | 0.14383 |
| $C_1$ | 0.24211 |
| $B_2$ | 3.28701 |
| $C_2$ | 36.71026 |

$$n^2(\lambda) = A + \frac{B_1}{\lambda^2 - C_1^2} + \frac{B_2}{\lambda^2/C_2^2 - 1}$$

### Optical Properties

| Optical Properties | FLIR | CLEAR |
|---|---|---|
| Bulk Absorption Coefficient (@ 10.6 µm) | < 0.2 x cm$^{-1}$ | < 0.2 x cm$^{-1}$ |
| Thermo-Optical Coefficient dn/dT | 41 x 10$^{-6}$ K$^{-1}$ (@ 10.6µm) | 54 x 10$^{-6}$ K$^{-1}$ (@ 0.66 µm) |
| Refractive Index Inhomogeneity | < 100 x 10$^{-6}$ (@ 10.6µm) | < 20 x 10$^{-6}$ (@ 0.66 µm) |

**VITRON**
**Your Material Specialist**

# VITRON CVD Zinc Sulfide

## Transmission

| λ [µm] | FLIR [%] | CLEAR [%] |
|--------|----------|-----------|
| 0.46 | 0.0 | 65.0 |
| 0.50 | 0.0 | 67.0 |
| 0.66 | 0.0 | 69.0 |
| 0.80 | 0.0 | 70.0 |
| 1.00 | 0.0 | 71.0 |
| 3.00 | 35.5 | 72.2 |
| 4.00 | 56.0 | 72.5 |
| 5.00 | 65.0 | 73.0 |
| 6.00 | 56.0 | 73.4 |
| 7.00 | 68.0 | 73.7 |
| 8.00 | 71.2 | 73.9 |
| 9.00 | 71.6 | 74.0 |
| 10.00 | 71.7 | 74.1 |
| 11.00 | 57.3 | 61.5 |
| 12.00 | 46.1 | 61.0 |



Thickness: 5.0 mm

## Material Properties
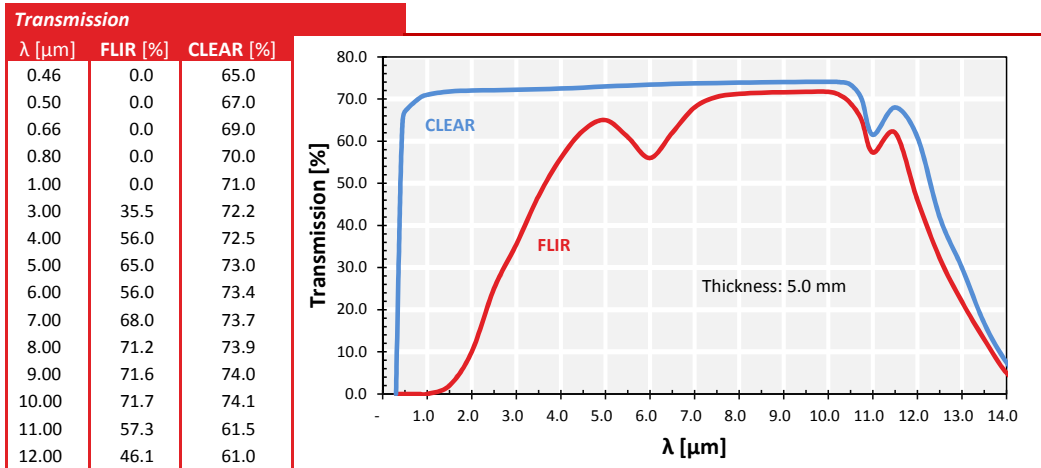
| Material Properties | FLIR | | CLEAR | |
|---------------------|------|------|-------|------|
| Density | 4.08 | g·cm$^{-3}$ | 4.09 | g·cm$^{-3}$ |
| Thermal Expansion (@ 20°C ) | 6.8 | x 10$^{-6}$ K$^{-1}$ | 6.5 | x 10$^{-6}$ K$^{-1}$ |
| Specific Heat Capacity | 0.469 | J·g$^{-1}$·K$^{-1}$ | 0.527 | J·g$^{-1}$·K$^{-1}$ |
| Thermal Conductivity | 16.7 | W·m$^{-1}$·K$^{-1}$ | 27.2 | W·m$^{-1}$·K$^{-1}$ |
| Young's Modulus | 74 | GPa | 88 | GPa |
| Modulus of Rupture | 103 | MPa | 69 | MPa |
| Poisson's Ratio | 0.27 | | 0.27 | |
| Hardness (Knoop) | 210-240 | Kg·mm$^{2}$ | 150-165 | Kg·mm$^{2}$ |

## Chemical Properties

VITRON's CVD Zinc Sulfide is chemical inert and not hygroscopic. It is resistant to highly reactive atmospheric gases.

## Typical Forms of Supply

Semi-finished:     Cut To Size Blanks (CTS), Sufficient Material To Yield (SMTY), Generated Lens Blanks

Other shapes by customer request

Optical components:     Windows, Lenses, Prisms and other optical parts according to customer specification

AR/AR coatings on customer request

**VITRON**
**Spezialwerkstoffe GmbH**
Maua
Am Naßtal 5
D-07751 Jena

Phone:     +49-(0)3641-2 88 1-30
Fax:     +49-(0)3641-2 88 1-55
Email:     kontakt@vitron.de
Internet:     www.vitron.de

**VITRON**
**Your Material Specialist**

# Polytec EP 601

| Eigenschaften im flüssigen Zustand | Methode | Einheit | Technische Daten |
|---|---|---|---|
| Chemische Basis | - | - | Epoxid |
| Anzahl Komponenten | - | - | 2 |
| Mischungsverhältnis nach Gewicht | - | - | 100:35 |
| Mischungsverhältnis nach Volumen | - | - | - |
| Topfzeit bei 23°C | TM 702 | h | 4 |
| Lagerstabilität bei 23°C | TM 701 | Monate | 12 |
| Konsistenz | TM 101 | - | Niederviskos |
| Dichte Mischung | TM 201.2 | g/cm³ | 1,15 |
| Dichte A-Part | TM 201.2 | g/cm³ | 1,17 |
| Dichte B-Part | TM 201.2 | g/cm³ | 0,95 |
| Viskosität Mischung 84 s⁻¹ bei 23°C | TM 202.1 | mPa·s | 460 |
| Viskosität A-Part 84 s⁻¹ bei 23°C | TM 202.1 | mPa·s | - |
| Viskosität B-Part 84 s⁻¹ bei 23°C | TM 202.1 | mPa·s | - |

| Eigenschaften im gehärteten* Zustand | Methode | Einheit | Technische Daten |
|---|---|---|---|
| Farbe | TM 101 | - | Farblos/transparent |
| Härte (Shore D) | DIN EN ISO 868 | - | 80 |
| Betriebstemperatur max. dauerhaft | TM 302 | °C | -55 / +125 |
| Betriebstemperatur max. kurzfristig | TM 302 | °C | -55 / +220 |
| Zersetzungstemperatur | TM 302 | °C | +280 |
| Glasübergangstemperatur ($T_g$) | TM 501 | °C | +73 |
| Thermischer Ausdehnungskoeffizient ($<T_g$) | ISO 11359-2 | ppm | . |
| Thermischer Ausdehnungskoeffizient ($>T_g$) | ISO 11359-2 | ppm | . |
| Thermische Leitfähigkeit | | W/m·K | . |
| Elastizitätsmodul | TM 605 | N/mm² | 3 500 |
| Zugfestigkeit | TM 605 | N/mm² | 65 |
| Zugscherfestigkeit (Al/Al) | TM 604 | N/mm² | 37 |
| Bruchdehnung | TM 605 | % | 2,9 |
| Wasseraufnahme 24 h, 23°C | TM 301 | % | 0,2 |
| Brechungsindex @λ=633nm | - | - | 1,5645 |

**\***Die Daten wurden an Proben ermittelt, die bei 150°C gehärtet wurden. Die Eigenschaften können durch die Wahl der Härtetemperatur z.T. beeinflusst werden.

# Makrolon® GP
## Massivplatten aus Polycarbonat

**S** Covestro S-Line, die Standard-Produktlinie, ist ein Sortiment aus zertifizierten Qualitätsprodukten, die bewährte Lösungen bei vielen Anwendungen bietet.

**Lichtdurchlässigkeit:** Testmethode nach DIN EN ISO 13468-2. Die angegebenen Dicken sind nicht alle standardmäßig erhältlich. Bitte fragen Sie für nähere Informationen an. Die angegebenen Werte sind Richtwerte.

| Lichtdurchlässigkeit in % | 0,75 | 1 | 1,5 | 2 | 3 | 4 | 5 | 6 | 8 | 10 | 12 | 15 |
|---|---|---|---|---|---|---|---|---|---|---|---|---|
| Makrolon® GP clear 099 | 90 | 90 | 89 | 89 | 88 | 87 | 87 | 86 | 85 | 83 | 82 | 80 |
| Makrolon® NR clear 099 | | 83 | 83 | 82 | 82 | 80 | | | | | | |
| Makrolon® GP white 130 | | | | 40 | 30 | 23 | 18 | 13 | | | | |
| Makrolon® GP white 150 | | | | 60 | 50 | 40 | 33 | 28 | 20 | | | |

**Verfügbare Abmessungen:** Makrolon® ist in den Dicken 0,75 – 15 mm und in den folgenden Maßen erhältlich, andere Maße, Farben und Plattenstärken sind anzufragen.

**Farben:**
Makrolon® GP clear 099
Makrolon® GP white 130
Makrolon® GP white 150

Makrolon® NR clear 099
Makrolon® FG clear 099

**Formate (Standard):**
2.050 x 1.250 mm
3.050 x 2.050 mm

**Dauergebrauchstemperatur:** Die Dauergebrauchstemperatur liegt bei ca. 120 °C.

**Brandschutzklassifizierung (*):**

| Land | Standard | Klassifizierung | Dicke | Farbe |
|---|---|---|---|---|
| Deutschland | DIN 4102 | B1 (Innenbereich) brennend abtropfend | 1 – 6 mm 2 – 3 mm | GP clear 099 GP white 150 |
| | DIN 5510-2 | S3 SR2 ST1 | 2 – 8 mm | GP clear 099 |
| Frankreich | NF P 92-501&505 | M2 | 1 – 15 mm | GP clear 099 |
| | NF F 16-101&102 | F1 | 0,75 – 15 mm | GP clear 099 |
| Europa | EN 13501-1 | B s1 d0 B s1 d0 B s2 d0 | 1 - 3 mm 1 – 6 mm 1 – 6 mm | GP white 150 GP clear 099 GP alle Farben außer 150 |
| USA | UL94 | V2 HB V0 | 0,75 – 1,4 mm ≥ 1,5 mm ≥ 10 mm | GP alle Farben GP alle Farben GP clear 099 |

**Glühdrahttest, IEC 60695-2-12, in °C (*):**

| | 0,75 | 1 | 1,5 | 2 | 3 | 4 | 5 | 6 | 12 |
|---|---|---|---|---|---|---|---|---|---|
| Makrolon® GP clear 099 | 850 | 850 | 800 | 800 | 850 | 960 | | 960 | 960 |
| Makrolon® GP white 130 | | | | 900 | 960 | 960 | | | |
| Makrolon® GP white 150 | | | | 960 | 960 | | | | |

(*) Brandzertifikate sind produktspezifisch und teilweise zeitlich begrenzt gültig, bitte überprüfen Sie in dem betreffenden Zertifikat immer die Gültigkeitsdauer und -umfang. Das Brandverhalten von Polycarbonat-Platten kann durch Alterung und Bewitterung beeinflusst werden. Die Brandklassifizierung wurde entsprechend den Vorgaben der jeweils angegebenen Brandschutznormen an neuen, unbewitterten Polycarbonat-Platten getestet.

This is a technical engineering drawing (Siemens PLM template) with the following labels and dimensions visible:

30°
0,5
10
45
20
10
5
45
130
Ø6
Ø3,4
5
5
29
10
15

SIEMENS

TITLE: schlitzeinblasung_schraeg_teil1

FIRST ISSUED: 07.06.2018
DRAWN BY: Völzel
CHECKED BY:
APPROVED BY:

SIZE: A4
DRG NO.: dwg1
SHEET REV: A
SCALE 1:1.2
SHEET 1 OF 1

THIS DRAWING HAS BEEN PRODUCED USING AN EXAMPLE
TEMPLATE PROVIDED BY SIEMENS PLM SOFTWARE

ALL DIMENSIONS IN MM

ALL DIMENSIONS IN MM

**SIEMENS**

| TITLE | schlitzeinblasung_schraeg_teil2 | | |
|---|---|---|---|
| FIRST ISSUED | 07.06.2018 | | |
| DRAWN BY | Völzel | | |
| CHECKED BY | | | |
| APPROVED BY | | | |

| SIZE | DRG NO. | | SHEET REV |
|---|---|---|---|
| A4 | dwg2 | | A |

SCALE 1:2     SHEET 1 OF 1

30°

62

20

10

5

70

60

10

Ø6

Ø3,4

5

130

15

10

5

R5,2

# B  Adiabatic results

## B.1  Distribution of Stanton numbers
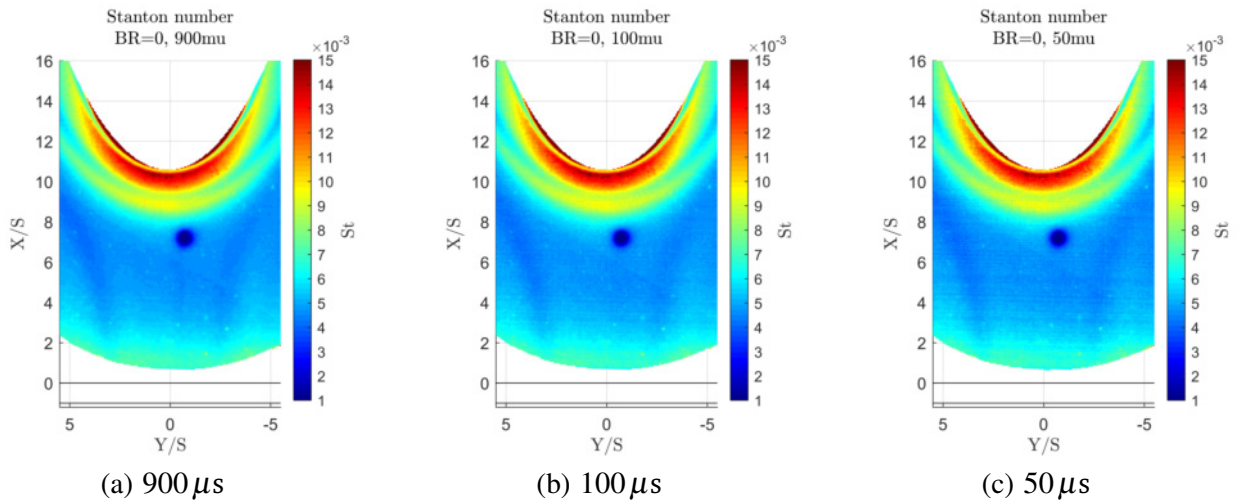


(a) $900\,\mu s$      (b) $100\,\mu s$      (c) $50\,\mu s$

**Figure B.1:** Reference case without secondary air injection, $BR = 0$



(a) $900\,\mu s$      (b) $100\,\mu s$      (c) $50\,\mu s$

**Figure B.2:** $BR = 0.11$
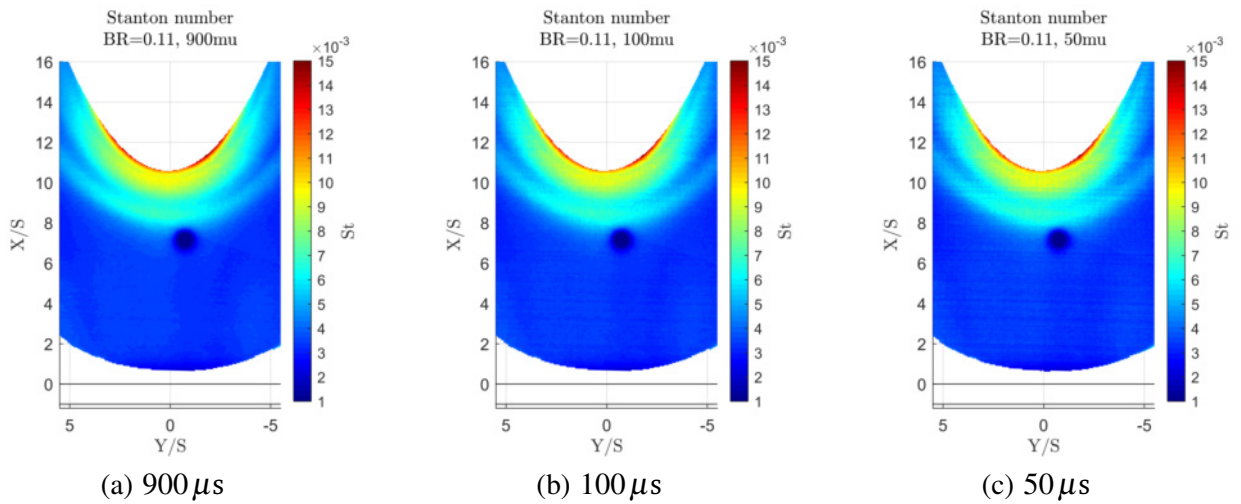
(a) $900\,\mu s$          (b) $100\,\mu s$          (c) $50\,\mu s$
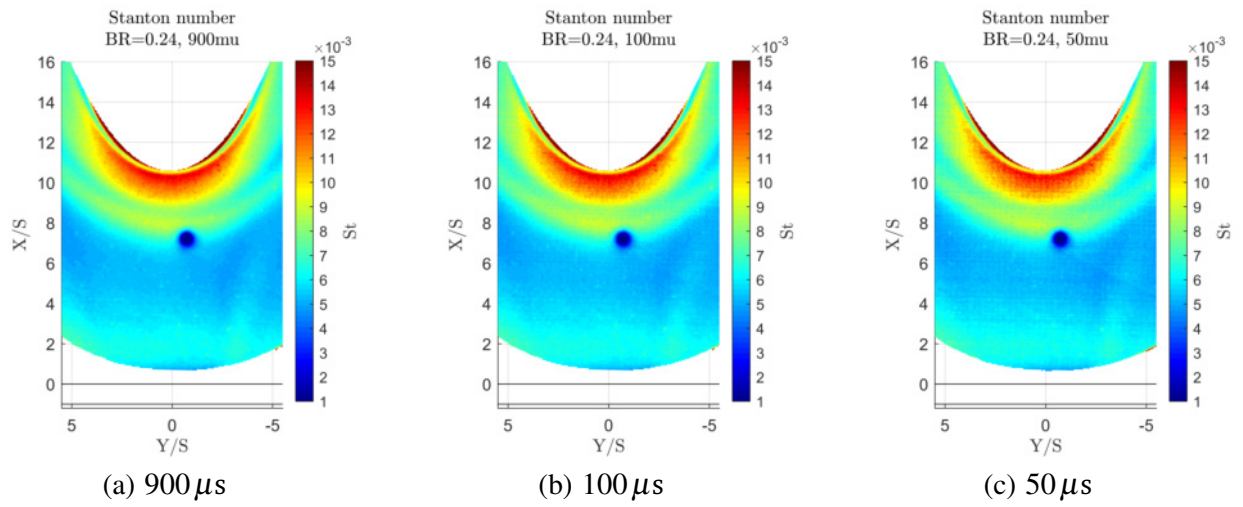
**Figure B.3:** $BR = 0.24$
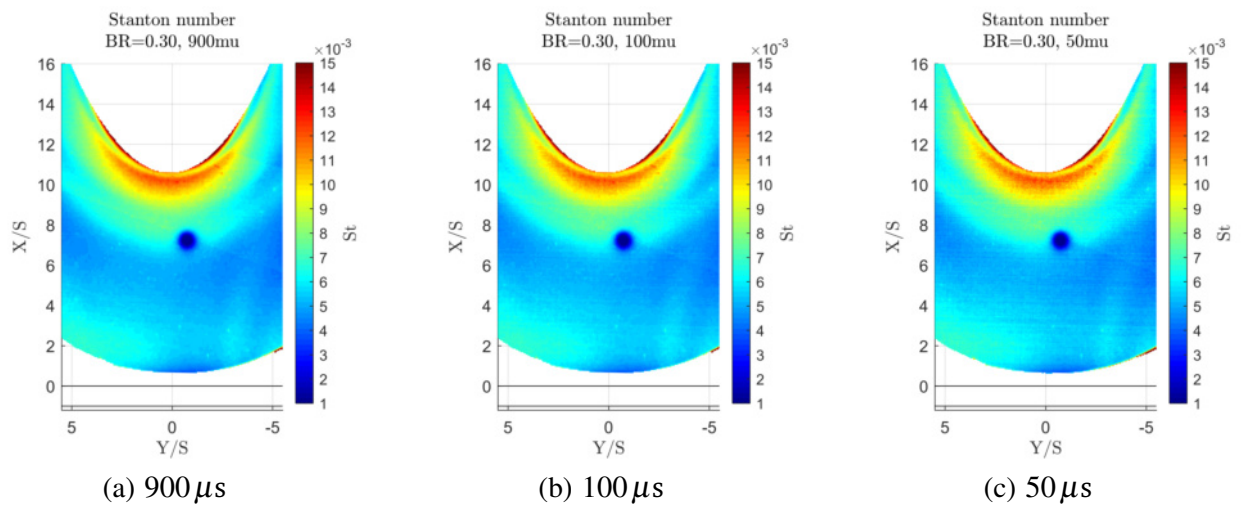


(a) $900\,\mu s$          (b) $100\,\mu s$          (c) $50\,\mu s$
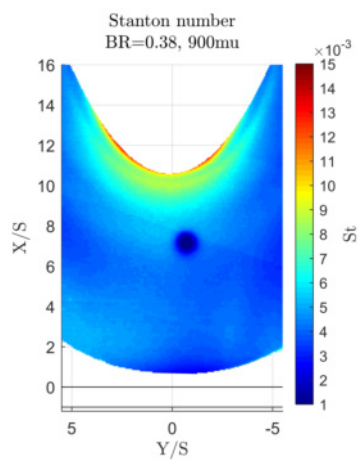
**Figure B.4:** $BR = 0.30$
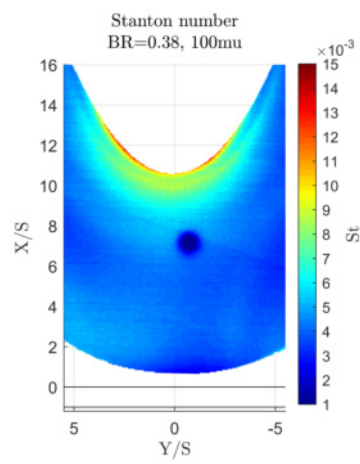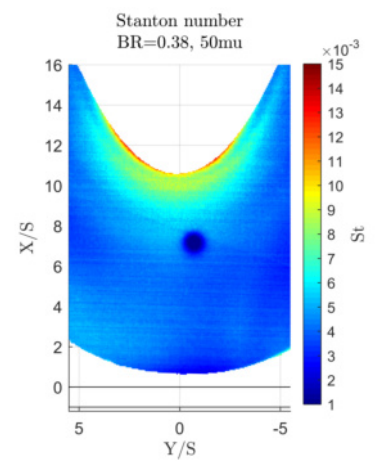
(a) $900\,\mu s$  (b) $100\,\mu s$  (c) $50\,\mu s$

**Figure B.5:** $BR = 0.38$

## B.2 Distribution of Cooling effectiveness



(a) $900\,\mu$s

(b) $100\,\mu$s

(c) $50\,\mu$s
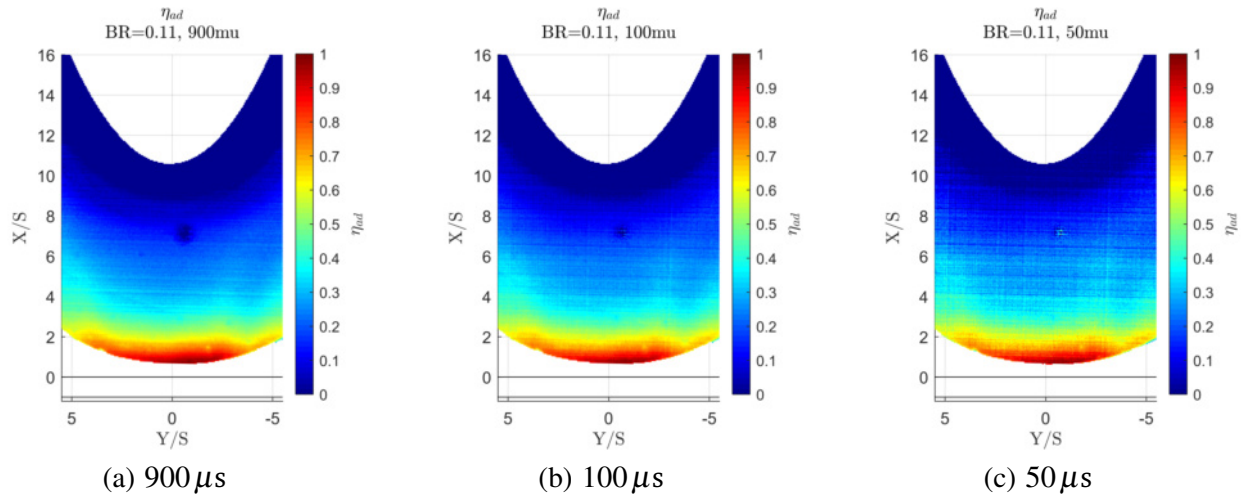
**Figure B.6:** $BR = 0.11$
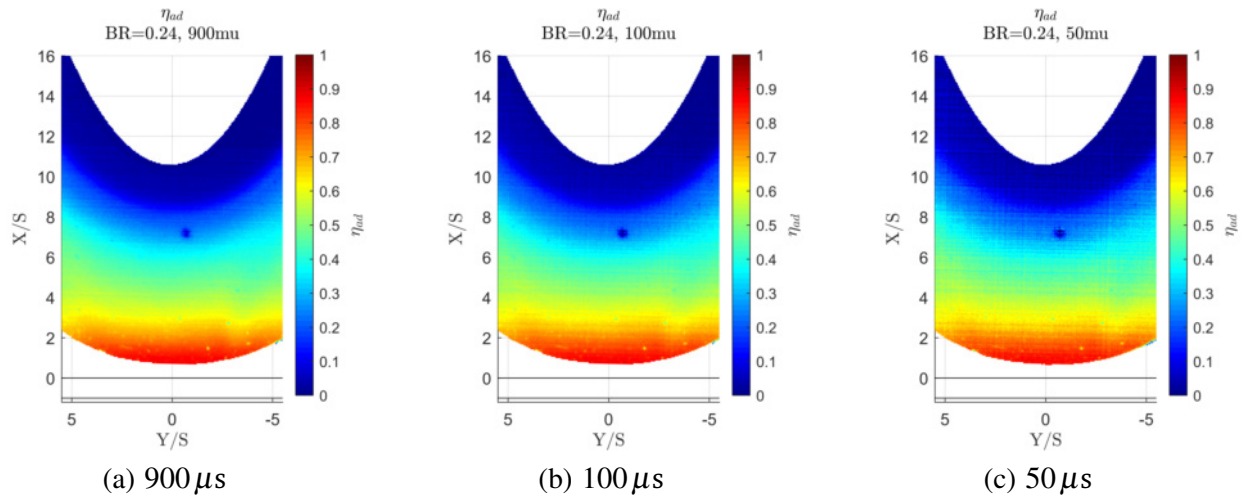


(a) $900\,\mu$s

(b) $100\,\mu$s

(c) $50\,\mu$s
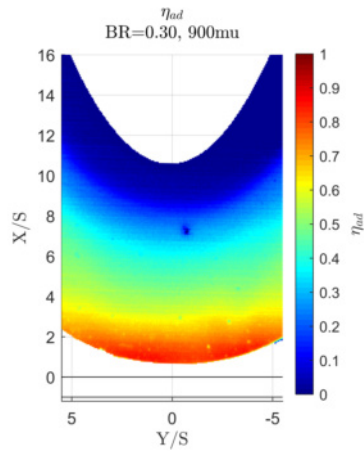
**Figure B.7:** $BR = 0.24$
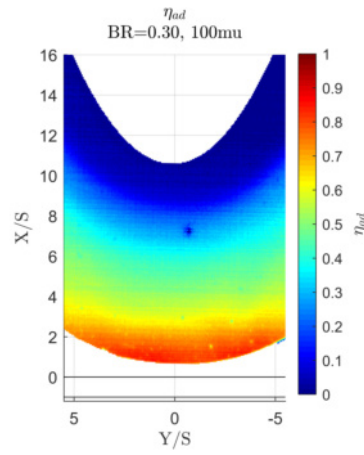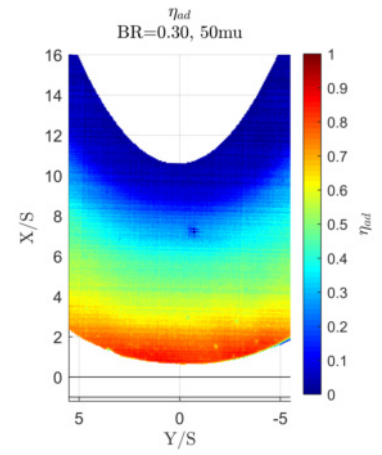
(a) $900\,\mu s$      (b) $100\,\mu s$      (c) $50\,\mu s$

**Figure B.8:** $BR = 0.30$
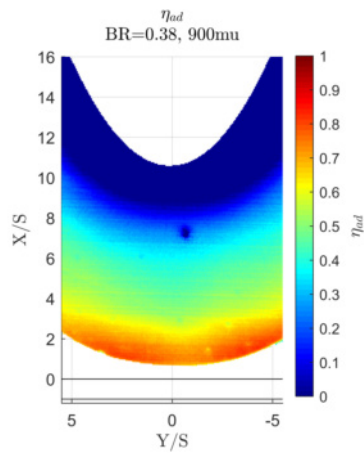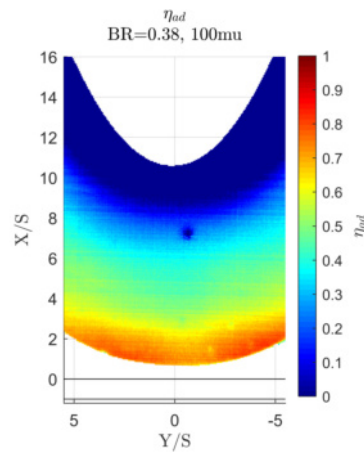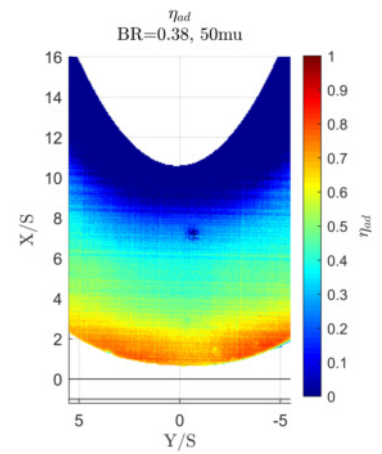


(a) $900\,\mu s$      (b) $100\,\mu s$      (c) $50\,\mu s$

**Figure B.9:** $BR = 0.38$

## B.3 Lateral positions
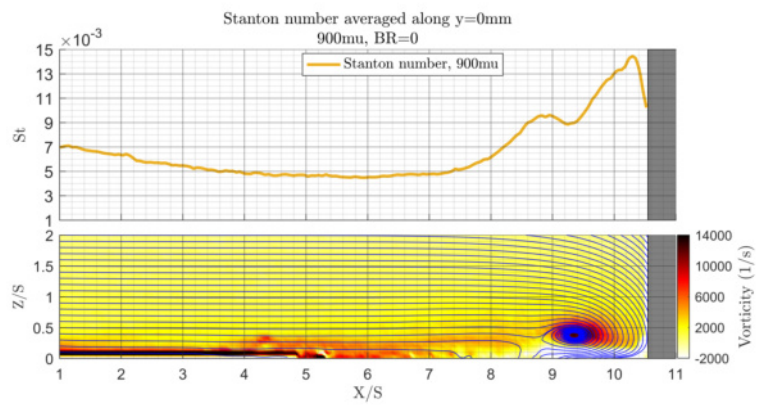
(a) $Y/S = 0$
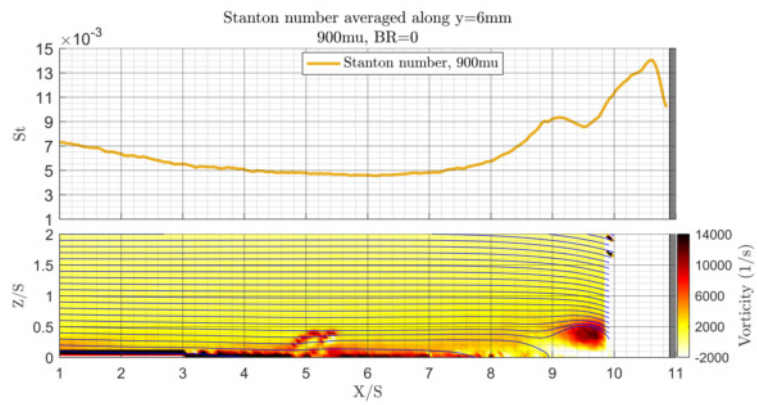


(b) $Y/S = 1.5$
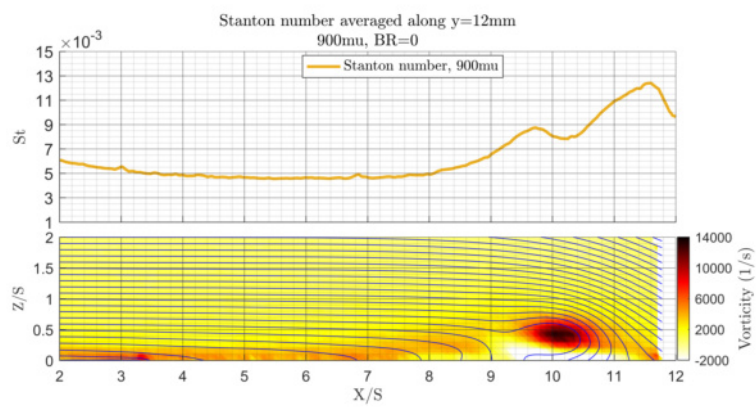


(c) $Y/S = 3$

**Figure B.10:** $BR = 0$
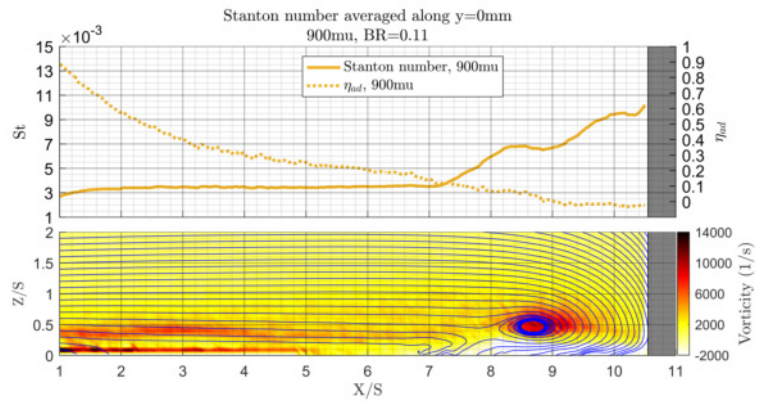
(a) $Y/S = 0$
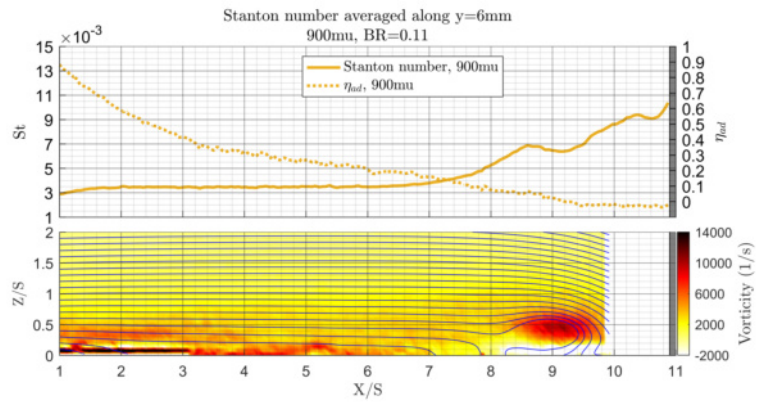


(b) $Y/S = 1.5$
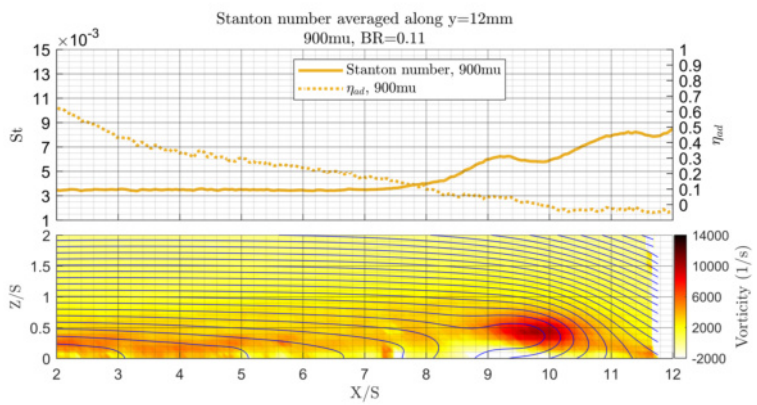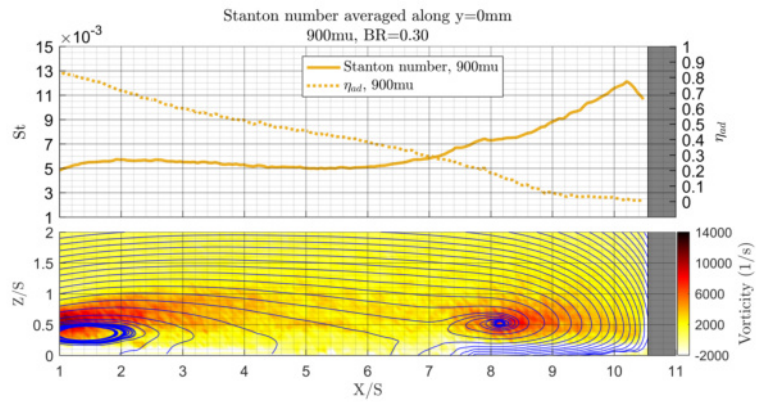


(c) $Y/S = 3$

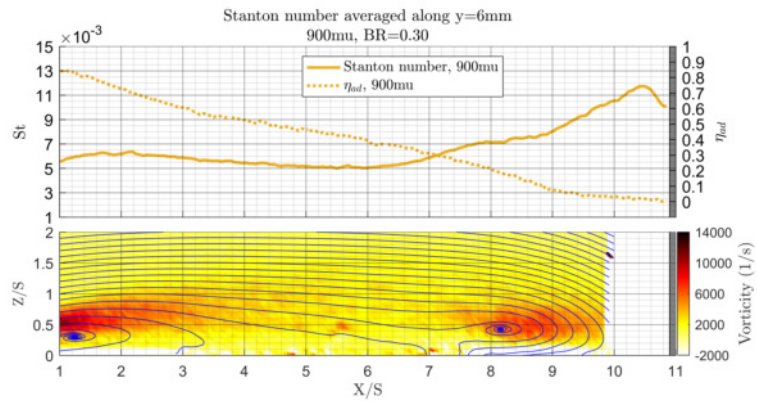**Figure B.11:** $BR = 0.11$
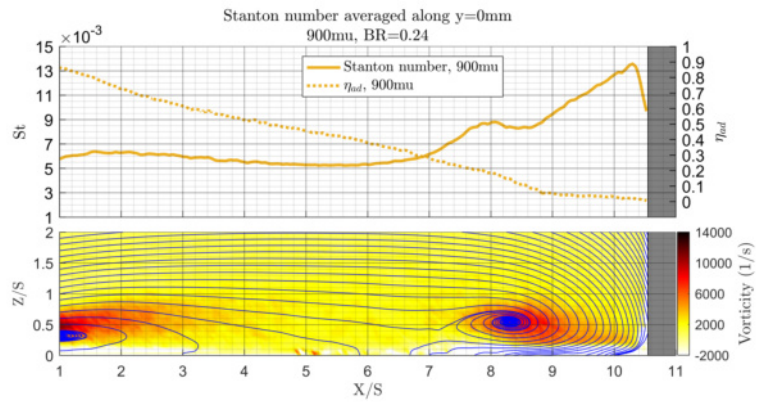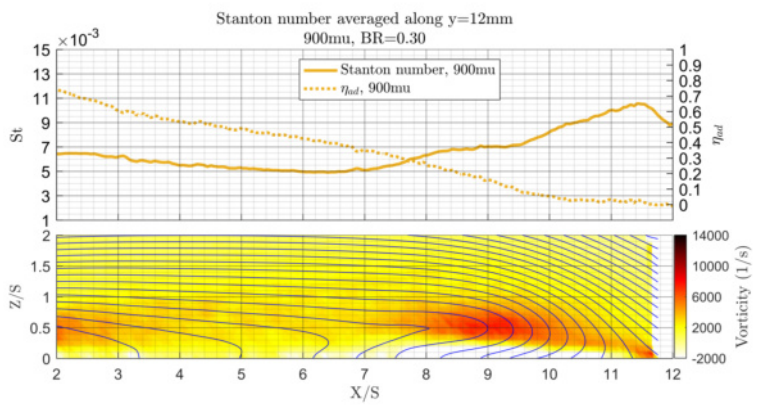
(a) $Y/S = 0$
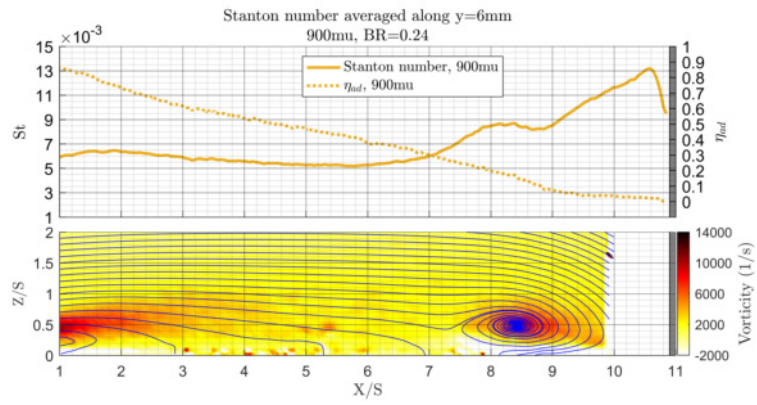


(b) $Y/S = 1.5$
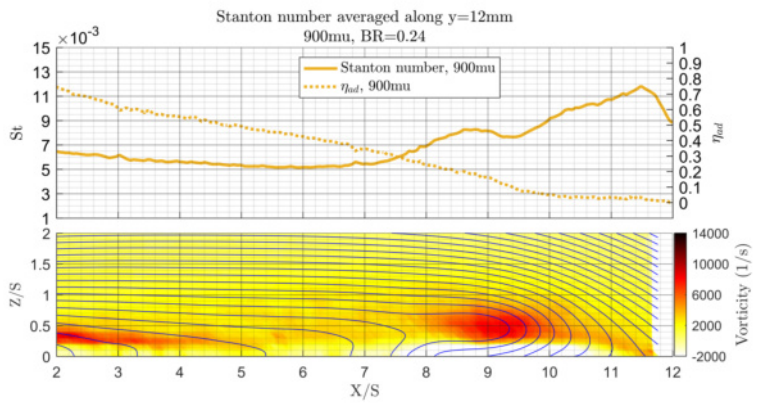


(c) $Y/S = 3$

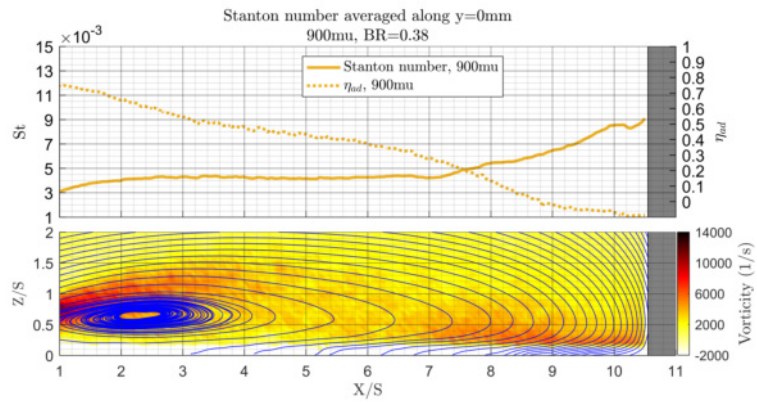**Figure B.12:** $BR = 0.24$

(a) $Y/S = 0$
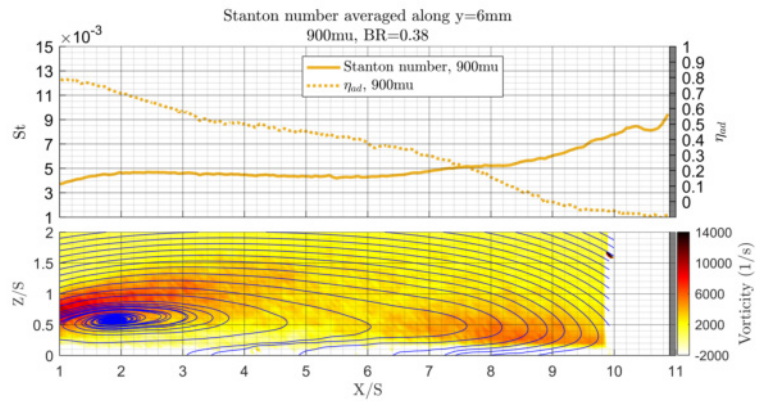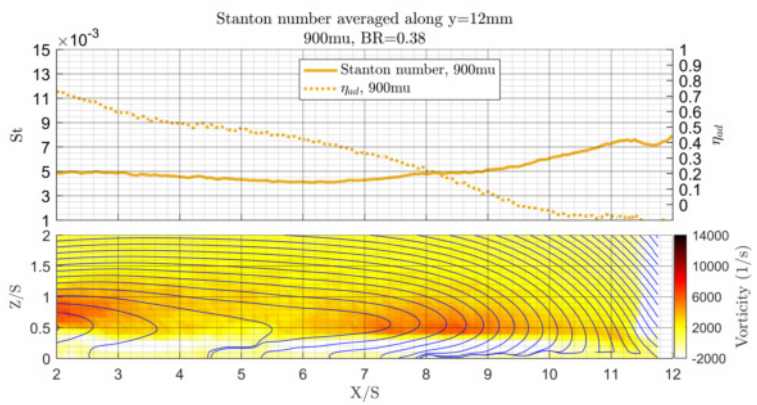


(b) $Y/S = 1.5$



(c) $Y/S = 3$

**Figure B.13:** $BR = 0.30$

(a) $Y/S = 0$



(b) $Y/S = 1.5$



(c) $Y/S = 3$

**Figure B.14:** $BR = 0.38$

# C Operating manual for heat transfer measurements at the flow channel

## Starting

1. Turn on test bench computer (in the same rack like the pressure scanner PSI9116).

   a Start NI Max.
   b Start *Main_V8.6_bronkhorst_flowmeter* in C:\users\student\KWK_Steuerung.

2. Turn on IR computer

   a Start NI Max.
   b Start VI *MAIN_HTPlate_CV_20180116* in E:\IR_Messungen_Voelzel\Heizfoliensteuerung.
   c Start *FLIR Research 64bit*.

3. Turn on the IR camera

4. Check connections

   a Pressure scanner and network switch (rear side of the rack)?
   b Measuring boards occur among connected network devices in NI Max?
   c FLIR IR camera connects to *FLIR Research 64bit* via Gigabit Ethernet adapter (Camera\Connect or View\Startup Dialog)?
   d Connect the power plug to the relay of the flow heater and activate the relay.
   e Connect the secondary air tubes to the compressed air supply.
   f Turn on the main switch and the power supply to the blower at the frequency converter.

5. Turn on the power supply units for the heating foils.

## Operating

1. Primary flow

   a Make sure no loose parts can be drawn in by the blower!
   b Start the ball valve in *Main_V8.6_bronkhorst_flowmeter* and make the setpoint 100 %.
   c Start the main flow and make the setpoint $1000 \frac{1}{\min}$ for two minutes. After that, set it to the desired speed.

2. Secondary flow

   a Open the valve for the secondary air supply.

3. IR camera and heating plate

   a Adjust path for saved files (in Edit record settings above the screen).

b Set desired number of frames in the same window (Note that the setting for the number of frames applies to all integration times in total. Enter a value of 1000 to acquire 500 frames per integration time if two integration times are activated in the settings.)

c Edit the name of the recording sequence in the same window. This has to be repeated and adjusted between each set temperature (name it *BR05_Tset30* for example).

d Adjust preset integration times (Camera\Control\Presets).

e Change to second filter *Open* in the drop-down menu.

f Edit the path for saved temperature recordings in *MAIN_HTPlate_CV_20180116*. This has to be repeated between each set temperature (name it BR05_Tset30 for example).

g Adjust the set temperature of the secondary flow in *MAIN_HTPlate_CV_20180116*. Do not power the flow heater if no secondary flow is running.

h Position the camera above the optical access to the flow channel. Make sure that no reflection of the objective can be seen in the recordings.

i Adjust the focus of the camera with the help of contrast between the reference thermocouples and the heated secondary flow.

4. Data acquisition

   a Make sure all thermocouples in the heating plate remain at a constant temperature and that the secondary mass flow is held constant at the setpoint (fluctuation in the compressed air supply might occur).

   b Activate the data acquisition in *MAIN_HTPlate_CV_20180116*.

   c Start a recording in the camera software.

   d Deactivate the data acquisition in *MAIN_HTPlate_CV_20180116* and proceed to the next set temperature.

   e Repeat the steps 3.c, 3.f, 4.c and 4.d for all set temperatures.

   f Check in between if reference thermocouples can be detected in the measurement images by manually adapting the script reference_image_circles_test.m. Make sure to consign the path to an appropriate reference image in which at least five thermocouples can be identified. These reference images can be any images acquired with a high integration time as they are only used to spot the locations of the reference points.

## Shutting down

1. Make all temperature setpoints $0\,^{\circ}\text{C}$.
2. Make the setpoint for the primary flow blower $0\,\frac{1}{\text{min}}$.
3. End all running VIs.
4. Shut down IR camera and the camera software (in case data are already exported).
5. Turn off relay for the secondary air flow heater and pull the power plug.
6. Turn off the power supply units for the heating foils.
7. Close the valve at the connection to the compressed air supply and draw the connector.
8. Turn off the frequency converter.

## Export of recordings

1. Select desired recording (saved as .ats movies) from the file menu in the camera software.
2. Select the desired integration time above the screen (Preset integration times 0,1,...) and make sure the camera signals are selected instead of temperatures.
3. Export the movie via File\Export as TIFF movie (16 bit depth) to the desired path.

## Processing with *HTCVal*

1. Create .txt files with the following structure for infrared recordings and temperature data:

Name of the file which is entered in the function Import Data Load.m
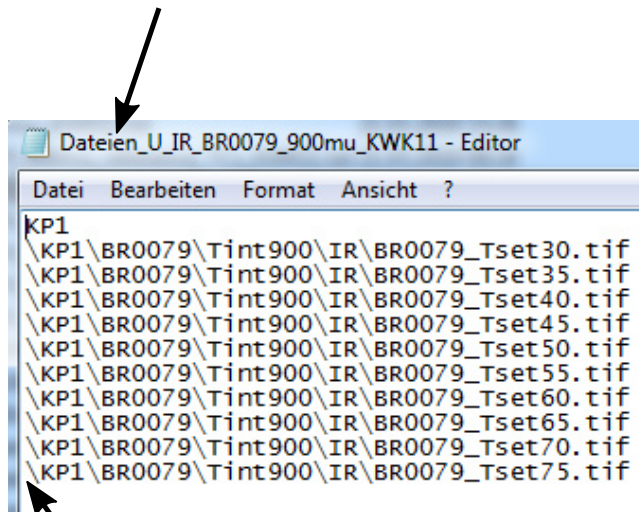


File structure to the single recordings (exported from the camera software), starting from the root path which is entered in the function Parameter general.m

2. Make further adjustments in the functions Parameter_general.m and Import_Data_Load.m as regards paths to the .txt files and the names of the measurements.